TRIBOLOGICAL CHARACTERISATION AND MODELLING OF PREMIUM TUBULAR CONNECTIONS

by

Fiona Stewart

A thesis submitted to Plymouth University in partial fulfilment for the degree of

DOCTOR OF PHILOSPHY

Copyright Statement

Thesis Title

TRIBOLOGICAL CHARACTERISATION AND MODELLING OF PREMIUM TUBULAR CONNECTIONS

by
Fiona Stewart

A thesis submitted to Plymouth University in partial fulfilment for the degree of

DOCTOR OF PHILOSPHY

School of Marine Science and Engineering
Faculty of Science and Technology

In collaboration with
Hunting Energy Services

October 2014

Abstract

Premium tubular connections (sometimes referred to as rotary shouldered thread connections), are commonly used to complete a production string in a well in the oil and gas industry. These are attached to threaded pipe ends using a bucking unit and a pre-defined torque value. The torque value is calculated using the coefficient of friction between the two surfaces and a well-known torque equation. The existing technology relies on the coefficient of friction approximated by interpolation, or extrapolation, of empirical data. This may become inaccurate due to the variation of surface finish and/or operation conditions and lead to over or under torque of the connections. A failure such as a leaking connection can result in high financial implications as well as environmental ones. The project was aimed to develop a bench test which adequately represents field conditions. This benchmark test was then used to investigate how CoF was affected by changes in the main variables so that these variables can be better controlled.

Therefore, a propriety laboratory test system was developed to allow measurements of friction and galling under these conditions and to examine the sensitivity of friction to initial surface topography, contact pressure, sliding speed and lubricant type. Samples were produced to represent variables which were possible within the oil and gas industry. A set of data was produced to identify the different frictional values for each combination of variables. The results showed that the initial surface topography and the burnishing in repeated sliding have significant effects on friction.

In order to understand the correlation between the effects of initial surface roughness and burnishing during the sliding process on the coefficient of friction, a theoretical approach was taken to produce a mathematical model whichutilised the data from the laboratory testing. This gave predictions of the wear, roughness and friction with sliding distance. This data was then compared to the physical testing and found to be in line with the results. The results helped to understand how friction is related to external circumstances in the operation of premium tubular connections.

Table of Contents

Table of Figures

Table of Tables

Acknowledgements

I would like to express my sincere gratitude to my supervisor, Dr. Huirong Le, for his paramount expertise, patience, assistance and motivation. Without his support and understanding, my journey through my Ph.D. project would not have been possible. His commitment and dedication to the advancement of the tribology world is inspiring and outstanding.

I would like to thank Hunting Energy Services and J.F.E. Steel Corporation for the opportunities this project presented and for the vital financial support they provided during the four years. I would personally like to thank Andrew Leech for the assistance, commitment and knowledge he provided. Thanks are also due to Alun Roberts and Dr. Bostjan Bezensek, who without their expertise and encouragement, the project would not have taken shape as well as it did. Dr. Bezensek's Finite Element Analysis gave a good setting for the initial research.

Thanks are due to my second and third supervisors Dr. Ming Dai and Dr. Sanjay Sharma for their continued guidance and expertise during the second half of the project. Special thanks to Prof. Neil James for allowing me to continue my project at Plymouth University and for his interest and support during the process. Thanks to the Graduate School at Plymouth University for their advice and support during the project. Thanks to the School of Marine Science and Engineering administration staff, especially Barbara Fuller who worked particularly hard to ensure my transfer from the University of Dundee was as smooth as it could be. Special thanks are also due to the library staff

who supported me in obtaining essential resources which allowed my project to proceed.

My eternal gratitude is due to my parents, Dorothy and David Stewart, who without them none of this would have been possible. Their support and guidance has been fundamental during this four year journey. Their love, help, advice and financial assistance has been fundamental in the success of the project. Sincere thanks and appreciation goes to Robbie Crossan for his continued encouragement and for agreeing to move to the other side of the country in pursuit of my dreams. His support and love during my study was invaluable. Thanks also to my sisters, Elaine and Mairi Stewart, who provided encouragement and support during the journey.

Thanks are also due to the staff in the Mechanical Engineering and Mechatronics department at the University of Dundee for their assistance and back-up during the first 18 months of the project. Their support provided me with a solid foundation for the project. Thanks to the technical staff for their continued support in the manufacture of the test rig.

Appreciation also goes to Steven Clark for his assistance in the project during his summer placement in 2010. Thanks are also due to Dr. Ruth Mackay for her continued support during my study. Her advice and encouragement was essential to my success. Thanks also to Dr. Richard Rothwell for his guidance and help during the project. Learning from his experiences was invaluable in helping me through the most difficult parts of my Ph.D. Thanks too to Johnny

(Shiyang) Qu for his assistance during his work placement which was very helpful.

Thanks to the technical department at Plymouth University for their continued support and assistance. In particular to Terry Richards, for his advice and invaluable assistance; his willingness to support me was remarkable. Thanks are also due to Gregory Nash for his technical assistance and expertise during the project. Also thanks to Dr. Richard Cullen for the support and assistance he provided during my initial move to Plymouth University.

Thanks also go to the technical and academic staff at the University of Cambridge for their assistance in the use of the Zygo Interferometer and for the Tribology Course I attended during September 2010. Their advice and assistance provided me with a set of high quality data that, in the initial section of my project, I would have otherwise been unable to obtain. Thanks go especially to Prof. John Williams for his help with the journal paper, and during the project development. His ideas and assistance were exceptional.

Thanks are also due to Dr. James Bowen from the University of Birmingham who provided me with the use of the nano-hardness testing technology which would have otherwise been very difficult to obtain.

Author's Declaration and Word Count

At no time during the registration for the degree of Doctor of Philosophy has the author been registered for any other University award without prior agreement of the Graduate Committee.

This study was financed with the aid of funding from a Knowledge Transfer Partnership between Hunting Energy Services and The University of Dundee, as well as funding from Hunting Energy Services and J.F.E Steel Corporation in return of experimental results.

The following paper was accepted for publication.

Publications (or presentation of other forms of creative and performing work):

- Characterisation of friction and lubrication regimes in premium tubular connections; Stewart F, Le HR, Williams JA, Leech A, Bezensek B, Roberts A.; Tribology International.; 2012; Issue 53: pp 159 - 66.
- Modelling of Surface Burnishing and Friction in Repeated Make-up Process of Premium Tubular Connections; Stewart F, Le HR, Tribology Letters, Pending 2014
- Presentation at Plymouth University Marine Science and Engineering post-graduate seminar

Word count of main body of thesis:

Signed : Fiona Stewart

Date : 18th September 2014

Chapter 1 : Introduction

1.1 Fundamentals of tribology

Tribology is the study of wear, friction and lubrication. This “study of the interaction between surfaces in contact” incorporates physics, chemistry, materials science and mechanical engineering **(1, 2)**. Although the idea of tribology has been around for centuries, the word was fabricated when Jost's Department of Education and Science Report was published in 1966. Its definition became "the science and technology of interacting surfaces in relative motion and of related subjects and practices" **(3)**. The report was in response to the increase in failures of machinery due to the wear of moving parts. As manufacturing procedures improved and technology developed, the costs associated with machinery wear started to become a significant burden. Both wear and friction are linked to energy and material losses, and the costs associated with these will reduce potential profit **(4)**. The findings of the report concluded that reducing wear significantly, by means of optimising design and operation, could save an estimated £500 million annually in the United Kingdom **(1)**.

The attention to tribology was important because it gave an appreciation of "how the surfaces interact when they are loaded together in order to understand how a system works”. The scope of the subject broadened but the main aspects of friction, lubrication and wear remain the leading subjects of interest **(5)**.

1.1.1 Definition of friction

The term “friction” originates from the Latin word *frictiō* meaning rubbing **(6)**. The idea of friction has been around since the Stone Age, where the application of friction was used to light fires and then more recently in transportation including rollers, wheels and sleds **(7)**. Vehicles with wheels date back to 3000 to 2000 B.C. These are examples of how friction is minimised as a benefit by using wheels as opposed to sliding an object directly over the ground. From ancient Egypt, 2000 B.C. to 500 B.C., there is archaeological evidence of drills, potter's wheels, the application of lubricants and transporting heavy objects by means of sleds **(3)**. All of these use characteristics of tribology to make the execution of tasks easier or quicker.

Studies performed to understand friction date back to France in the 1560s during the Renaissance **(8),** and also to work done by Leonardo da Vinci in the 1500s. Da Vinci stated that the friction force $\boldsymbol{F}$ was proportionally related to the normal force $\boldsymbol{W}$.

$$\boldsymbol{F} \propto \boldsymbol{W} \qquad \textbf{(1.1)}$$

Da Vinci’s work was the first methodical approach concerning dry friction. His conclusions were that the area of contact between two surfaces has no effect on the friction associated with them and secondly that if the load of an object doubles, the frictional force also doubles **(9)**. These laws were restated by Guillaume Amontons in the early 18th century, and the law that the coefficient of friction (CoF) is the ratio of the horizontal force, $\boldsymbol{F}$, necessary to cause motion to the weight $\boldsymbol{W}$ of a block, was generated **(10)**. He also stated that friction is

independent of the apparent contact area. Further research by Leonhard Euler in the 1740s and 1750s established theories concerning the normal and frictional forces of an object on an inclined plane. He stated that the frictional force was determined by the object's weight and the angle of the slope. He also introduced the current symbol for coefficient of friction μ and his work initiated more studies into kinetic friction.

Experimental work by Charles Augustin de Coulomb in 1785 confirmed Amontons' theory that the frictional force was directly proportional to the normal force pressing two surfaces together, and he also defined the difference between static and dynamic friction **(7)**. Coulomb also studied the effect of surface roughness on the friction and his work proved that friction was not defined by the size of the objects in contact but on the roughness value of the surfaces. He also was able to confirm that CoF is not dependent on the load **(11)**. In the 1830's, Arthur Jules Morin performed experiments to prove, and add to, Coulomb's theories. He confirmed that friction is proportional to the normal force exerted on a body; that friction depends on the nature of the surfaces in contact; and that within limits, the friction is independent of the velocity **(12)**.

1.1.2 Point contact and contact pressure

Heinrich Hertz's work in 1882 **(13)** was the first on elastic contact between two bodies of circular arc geometry. It gave an understanding of line contact between these two entities (as shown in Figure 1-1) and the relationship between the normal load applied to the system and the area of contact that occurs when the two objects are pressed together by normal force, P.

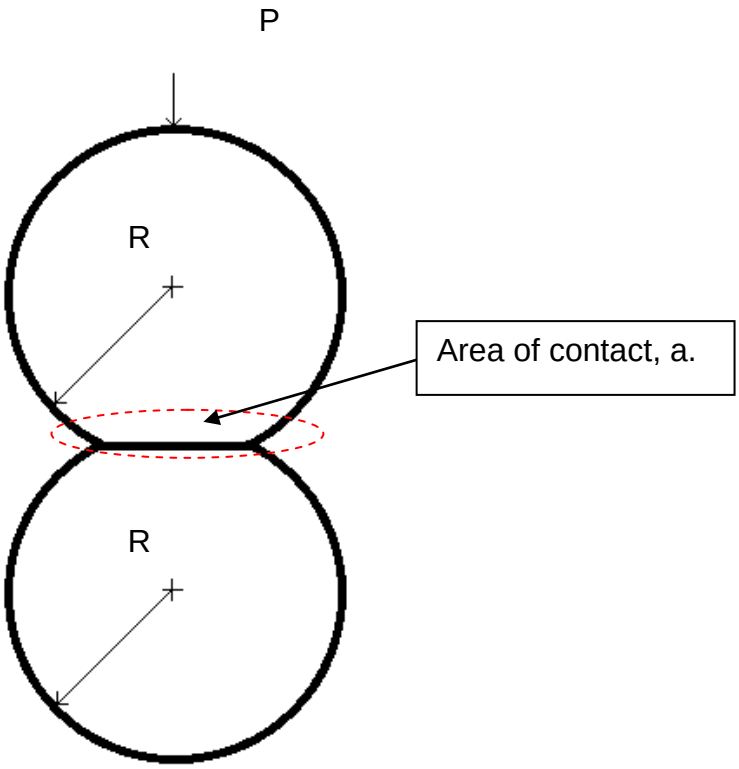

Figure 1-1: Contact of two cylinders

This relationship is most commonly known as Hertzian contact and the area of contact, $\boldsymbol{a}$, is determined using the following equation.

$$\boldsymbol{a^2 = \frac{4PR'}{\pi E^*}} \qquad \textbf{(1.2)}$$

Where $\boldsymbol{P}$ is the normal load applied to the system, $\boldsymbol{R'}$ is the reduced radius and $\boldsymbol{E^*}$, the contact modulus for the system is calculated using the equations below.

$$\boldsymbol{\frac{1}{R'} = \frac{1}{R_1} + \frac{1}{R_2}} \qquad \textbf{(1.3)}$$

$$\boldsymbol{\frac{1}{E^*} = \frac{1 - {v_1}^2}{E_1} + \frac{1 - {v_2}^2}{E_2}} \qquad \textbf{(1.4)}$$

Where $\boldsymbol{E_1}$ and $\boldsymbol{E_2}$ are the elastic moduli for materials 1 and 2 respectively, and $\boldsymbol{v_1}$ and $\boldsymbol{v_2}$ are the Poisson's ratio values for both materials. Hertz's (also known as Hertzian) theory was restricting because it is only true for smooth, elastic, frictionless surfaces; meaning that it is an idealised case and cannot be true for engineering components. Therefore this is only used to estimate the contact pressure in the cylinder-to-cylinder contact in order to identify the contact regime in Chapter 2.

1.1.3 Line contact and contact pressure

Early work by Bush et al analytically compared theories concerning elastic contact of rough surfaces **(14)**. Typically, a rough surface was represented using a statistical model based on the assumption that the surface was represented by paraboloids of the same principal curvature and had random heights. The deformation of the model was then analysed using classical Hertzian contact **(15)**. Both line and point contact was considered by Hertz and by doing so the stresses and surface displacement were investigated **(1)**. Line contact considers what happens between surfaces in two dimensions whereas point contact adds the third dimension. The pressure at point x is considered to be equal to:

$$\boldsymbol{p(x) = p_0\sqrt{1 - x^2/a^2}} \qquad \textbf{(1.5)}$$

Where a is the distance along the x-axis between the origin and the edge of the contact; and x is equal to the distance along the same axis to the point being investigated.

By considering line contact, the pressure of the two-dimensional system was obtained by assuming that the pressure at the edges of the contact is equal to zero and that the maximum pressure occurs in the centre of the face. From this assumption, the load per unit length can be presumed to be equal to the area under the curve of the pressure between +a and –a. This can also be obtained by integrating the pressure between the two values with respect to the distance in the x axis being investigated. This means that:

$$\frac{W}{L} = \int_{-a}^{+a} p(x)dx \tag{1.6}$$

As the maximum pressure is known to exist at the centre, a value can be obtained by using the equation:

$$\frac{W}{L} = \int_{-a}^{+a} \sqrt{(1 - x^2/a^2)}\, p_0 dx = \frac{\pi}{2} p_0 a \tag{1.7}$$

Rearranging this gives the peak pressure to be equal to:

$$p_0 = \frac{2W}{L\pi a} \tag{1.8}$$

The mean pressure over the contact line is equal to $W/2aL$, which means that the peak pressure can be calculated using the expression:

$$p_m = \frac{\pi}{4} p_0 \tag{1.9}$$

This gives a starting point for considering an equation for the value of load and pressure described in Chapter 2.

Frank Bowden and David Tabor's work in 1954 gave reason for the inconsistency between Guillaume Amontons' theorem that the friction is independent of the apparent contact area, and John Desaguliers' idea that

adhesion occurred in the friction process **(16, 17)**. They found that the differences were in how the contact was defined. Bowden and Tabor's work was based on the idea that the sliding process between the two surfaces was purely plastic, in contrast to Hertz's elastic contact ideas. Their work was based upon Hertzian elastic theory, however this time it was assumed that the asperities were plastically deformed during the contact process. This is more accurate under high contact pressure as in the current premium tubular connections but will require detailed surface topography as input.

1.1.4 Coefficient of friction

Friction is present in everyday life; in some cases, having a greater friction can be beneficial, like in the brakes of a car; and in others it can cause energy loss and be detrimental to the workings of a system. For example, in an internal combustion car engine if there is insufficient oil between the piston rings then friction will be high. This means that the moving parts will grind against one another causing damage to the surfaces and unnecessary wear leading to the need for premature replacement of engine parts. Friction occurs between solids, as well as between liquids and gases. Fluid friction (the term used to cover both liquids and gases) is known as drag. Between two solids, this friction can be classified as either kinetic or static. Static friction applies to motionless objects and kinetic friction to objects in relative motion. Friction is not a standard value for a particular type of material, but is related to the conditions of the system in which a material finds itself in. There are many different parameters which affect CoF and even slight variations to the surface properties can have a large effect

on the coefficient. The CoF changes depending on the conditions in which it is in. Lubrication can reduce CoF and also decrease the wear rate.

CoF is defined as “the dimensionless ratio of the friction force F between two bodies to the normal force N pressing these bodies together” **(18), (19)**. This is a measure of how much resistance the surface generates compared to the normal force pushing the surfaces together. Therefore, CoF can be calculated by measuring the normal force and tangential force (frictional force) for a sliding movement of two surfaces where this is equal to:

$$\boldsymbol{CoF = \frac{Tangential\ Force}{Normal\ Force}} \qquad \textbf{(1.10)}$$

Figure 1-2 is a simple set-up to measure CoF. This normal force is proportional to the weight of the object for a certain slope. It is found that the friction force, F, is also proportional to the weight of the object, i.e. the heavier the object, the higher the friction force preventing it from slipping back down. Since CoF is a dimensionless ratio of the friction force (tangential to the slope) to the normal force (perpendicular to the slope), the value is independent of the size of the body.

However, the surface conditions can have significant effects on the value. The CoF is not a material property but is a function of the system in which the materials are used **(20)**. The CoF for one system with two particular materials may not have the same value if the roughness varies or a coating is present.

This creates a subject matter with a large number of unknowns, meaning that even with the extensive research carried out; the reasons behind the behaviour are not always fully understood.

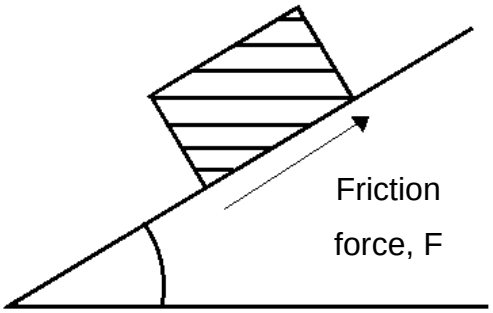

Figure 1-2: Friction force on an inclined plane

1.2 Premium tubular connections

1.2.1 Definition and application

There are three processes that occur during the life of an offshore well. These are: well construction, well completion, and well intervention **(21)**. Well construction is the erection of the well, including determining the location. Initially, geologists are employed to locate a well by means of studying surrounding rocks and surface features and by using satellite imaging. In the past decade, improvements in technology have made this process much faster and more accurate. Traditional methods of oil location include examining the sedimentary basin **(22)**, because it is here where the build-up of hydrocarbons occurs at a considerably faster rate than the neighbouring areas. **Figure 1-3** illustrates a schematic diagram of a hydrocarbon well. The gas and oil have formed in pockets under the surface by trapped decayed organic materials which sank to the bottom of the sea millions of years ago.

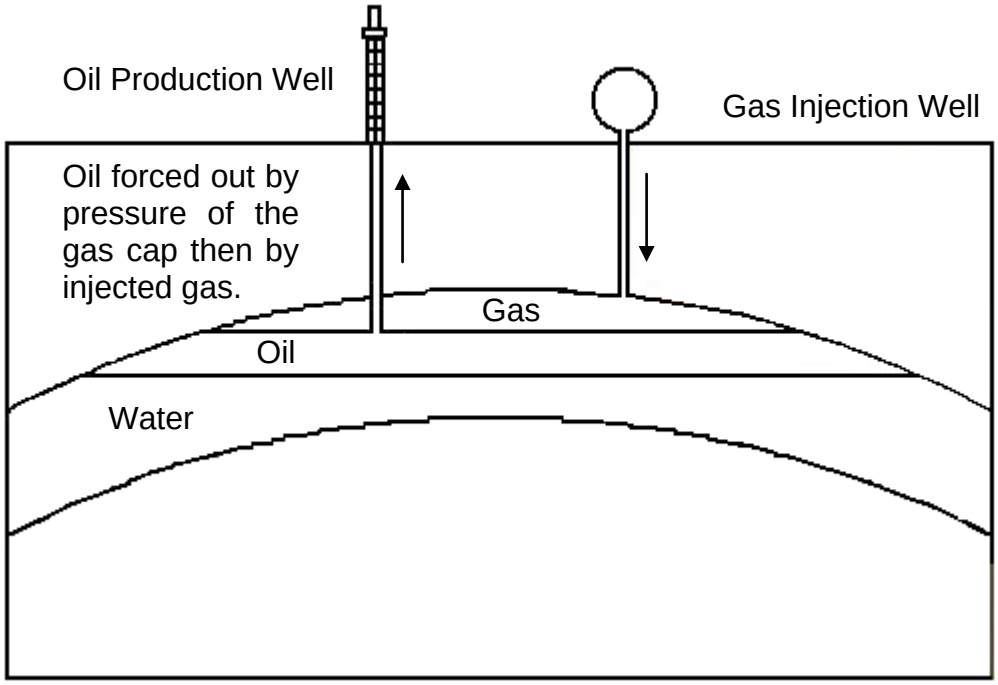

Figure 1-3: Simplified schematic of the location of oil and gas offshore

After a suitable well has been identified and located, the environment that it is in is defined. The depth of the pockets of oil, the hardness and nature of terrain that needs to be drilled through and whether it is on or offshore contribute to the selection of drill bits used to allow penetration of the well. The drilling process is an extensive progression starting with a very small drill bit. The well is opened up gradually and during this time, fillers and casings are added to maintain a robust cavity for the drill string to be positioned inside the well. **Figure 1-4** shows a simplified diagram of a well structure. The first hole is created using the largest size drill. A depth for each bore is calculated from the formation pore pressure and the fracture pressure. The pore pressure is the pressure that is expected during formation, and the fracture pressure is the pressure that causes ruptures in the well. These calculations are done accurately to ensure that the maximum depth is drilled before the concrete is pushed into the bore to

seal the sides of the well. Drilling each level as deep as possible means that production can begin earlier, thus providing a greater profit for the drilling company. It is however important to ensure that the value is calculated accurately, as drilling too deep means that if the collapse pressure is exceeded then the well may be inoperable and the time and money spent in drilling will have been wasted. Blowout occurs when the pressure is below the formation pore pressure and leakage can occur where the pressure is above the fracture pressure, therefore it is important to set the balance right to ensure that the well is operated as efficiently as possible. After the well has been completed to this stage, the production string can be installed ready for oil and gas production.

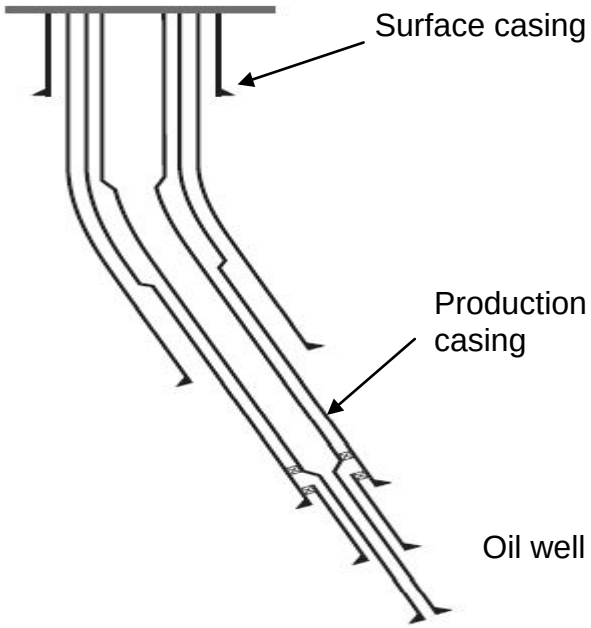

Figure 1-4: Schematic of an example drilling well with casings

Well completion is the process of providing a well with a pipeline it requires in order to make it ready to transport the hydrocarbons to the surface **(23)**. This is the step between drilling the bore hole and the beginning of production of the oil

and gas **(24)**. The type of well is determined by the location of the hydrocarbons, these can either be vertical or horizontal.

A conventional natural flowing well is shown in **Figure 1-4**. To produce a well, a large hole is drilled in the sea bed, which begins with a very large diameter at the top and reduces in size as the well deepens. This allows the well sides to be reinforced with concrete to prevent collapse of the side walls. A series of pipes and couplings (tubing) are attached in a string, inside the well which has already been completed. This is done using a casing packer fluid, cement, a perforated casing, and a packer to ensure the sides of the well do not collapse preventing the removal of hydrocarbons from the well. The tubing (premium tubular pipe and connection) is run from the well floor to the well head. At the well head, pressures are maintained and reported by the ‘Christmas trees’. The ‘Christmas tree’ gets its name from the number of valves and fittings added onto it, as it is like a set of decorations. These fittings and valves are used to control the flow and prevent leakage; the devices on the tree can be remotely controlled and operated safely.

The actual production pipeline consists of pipes, pipe connections, crossover subs and valves etc. Each pipe connection is usually made up of a threaded pipe end and a coupling. The pipe end is a male connector and the coupling (so called ‘box’) end is a female connector. To complete the well, these connections are fastened together in a bucking unit. Each pipe and coupling connection (be it a valve, crossover sub or coupling) has a pre-defined torque value associated with it. It is with this process where the CoF becomes a major issue.

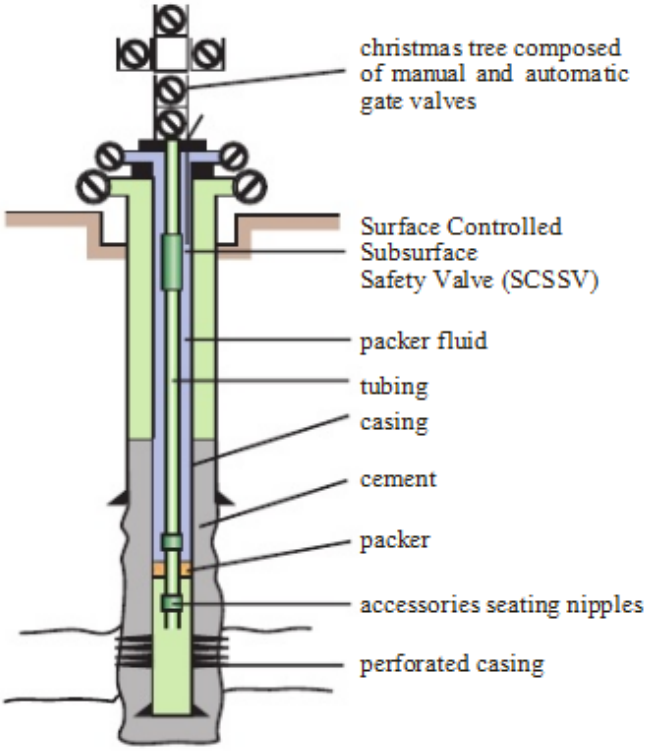

Figure 1-5: Completion string of a well without artificial lift (25)

Figure 1-6 shows one type of premium tubular connection. This figure comprises of two pipe sections of identical design and one coupling. The cross-sectional image of the connection shows how the pipes and coupling fit together. Tubing is run down a casted well in order to complete a string ready for production. The hydrocarbons flow through the production pipe and connection and therefore they are required to have a sufficient seal at very high temperatures and pressures. Pipe sections are connected together with couplings on either end. These are “made-up” by screwing them together using a predefined torque value. This torque value is pre-determined using an estimated CoF.

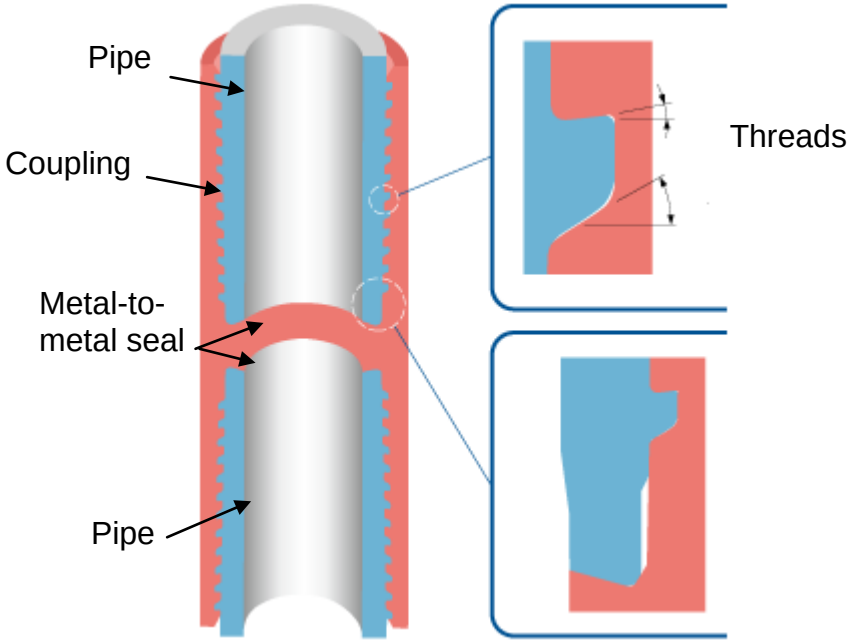

Figure 1-6: Premium tubular connection – coupling with two pipes attached (26)

The pipeline is assembled by fastening a pipe into a coupling (in the process known as make-up) using a bucking unit. Two different versions of these machines are used onshore (see **Figure 1-7**) and offshore due to space utilisation however they work in exactly the same way. An onshore assembly connects the coupling to the pipe horizontally. Offshore, the pipes are run down the well and each pipe is connected to the coupling at the well head.

Figure 1-8 shows a premium tubular connection model made up of two pipe ends and one coupling section. A sectional view of the coupling illustrates the arrangement shown in more detail.

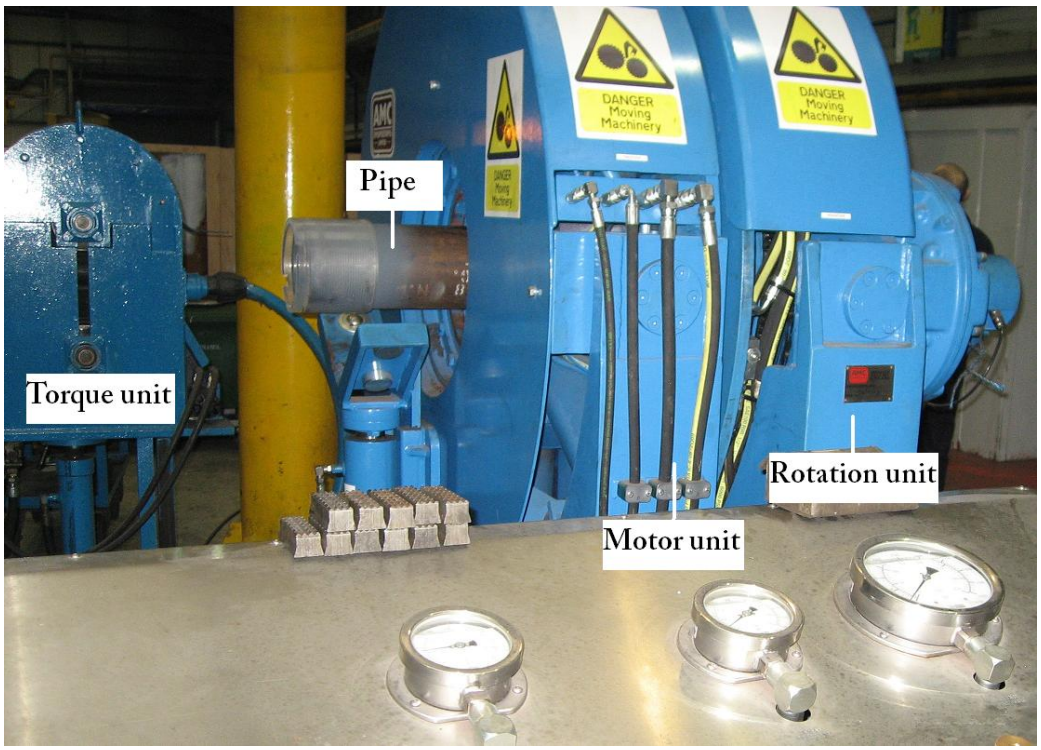

Figure 1-7: Bucking unit used for make-up of connections in machine shop

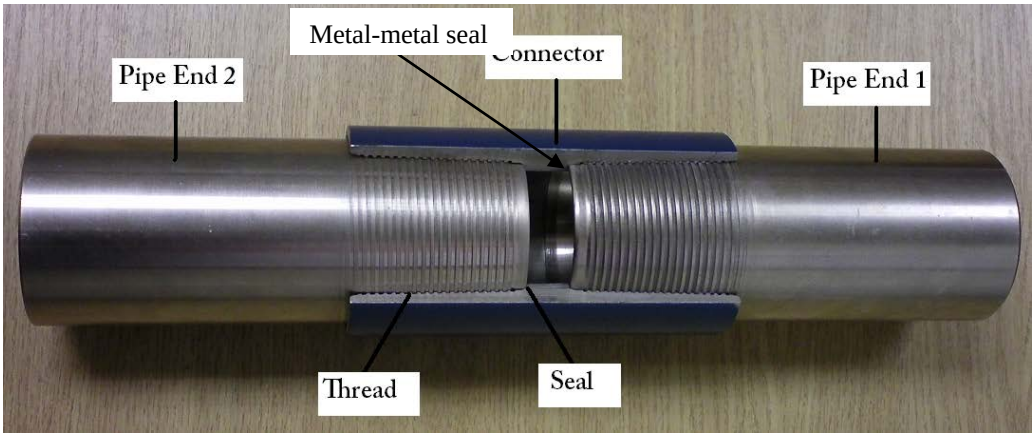

Figure 1-8: Premium tubular connection elements

During the service life of a completion string, premium tubular connections may be subjected to both high internal and external pressures. Throughout this period, the connection may also be subject to severe loading conditions including bending, tension and compression at elevated temperatures. For

premium tubular connections to work effectively in such harsh environments, the connection not only needs to have sufficient strength, but also relies on the amount of pre-load in the metal-to-metal seal. To maintain the pressure effectively during the connection's service life, it is critical that the correct amount of torque is applied during assembly; thereby overcoming thread interference and generating the required strain energy in the seal. Seal pre-load is determined by connection geometry, applied torque and the frictional properties of the contacting surfaces.

A small proportion of connections fail during their working life. Approximately two thirds of drilling failures were caused by loose connections **(27)**, where the majority of losses were caused by galling of threads. Research in the Wall Street Journal concluded that a gas leak in the North Sea in 2012 had cost its owners billions of dollars due to lost production, replacement of connections and unplanned well intervention **(28)**.

The value of fastening torque used to make-up a connection is vital to create a proficient seal between the coupling and pipe. As the pipeline is secured using a pre-defined value of torque, this is the main parameter responsible for ensuring no leakage occurs. The continued search for oil has resulted in deeper wells being drilled. The resulting increase in the pressures and temperatures mean that the connection is exposed to increased stresses. It is at this point that the value of torque becomes most critical. An insufficient value of torque will mean that there is a poor seal in the connection and leak paths can easily form. On the opposite side of the spectrum, if the connection is over-torqued,

the seal begins to plastically deform, making the connection susceptible to damage and creating leak paths within the connection. When the connection is exposed to high pressures and high temperatures, the material finds itself close to its yield strength, either in tension or compression. This gives opportunity for leaks to occur, with severe leakages in connections costing a significant amount due to loss of profit. An example of this is in the Total well platform off the coast of Elgin, UK. Experts have reported that the cost of closing a well per day amounted to $1.5 million, with a response call adding another $1 million to the loss daily **(29)**. The best way to prevent this from happening is to ensure that the torque value is calculated correctly and accurately. To do this, the CoF has to be known for all materials, make-up speeds, contact pressures, lubricants, material properties, surface roughness and other such variables. The current method of obtaining the CoF is very expensive and requires a large scale operation along with some interpolation and extrapolation of data to acquire all necessary values.

The pipe end of the connection is usually peened using a locally available peening material. This peening process produced a surface with irregular craters on the surface, and was performed because it was found that the lubricants used during assembly stuck much more effectively during the sliding process than a plated surface. It also gave a much more isotropic surface rather than the unidirectional plated surface, where the lubricant could squeeze out from the surface much more easily. The media used to peen the steel surfaces included ceramic particles, stainless steel particles, aluminium oxide particles

and also glass particles. This research focussed primarily on the ceramic peened, stainless steel and aluminium oxide peened surfaces.

1.2.2 Role of friction in a premium tubular connection

The friction coefficient is a very important parameter involved in the make-up of Oil Country Tubular Goods (OCTG) systems. The pipe and box sections are screwed together using a pre-defined value of torque. This torque value is calculated using Duggan's torque equation **(30)**. Duggan's torque method was based upon a nut sliding on a bolt. The equation gives the relationship between the tightening torque and the equivalent end load. It is based on the idea that "when a bolt is tightened, some of the effort goes in pre-loading the parts (i.e. the bolts are stretched and the connected members are compressed), and some goes into overcoming friction both at the threads and at the annular surface of the bolt head or nut whichever turns" **(30)**.

$$T_{Dug} = \frac{P_r d_m}{2}\left(\frac{l + \pi d_m \mu sec\beta}{\pi d_m - \mu l sec\beta} + \mu_c \frac{d_c}{d_m}\right) \qquad \textbf{(1.11)}$$

Where,

P_r	Connection seal preload
d_m	Mean pin thread diameter
l	Lead
μ	Coefficient of friction on the thread
μ_c	Coefficient of friction on the shoulder
β	Thread load flank angle

d_c Average collar diameter (0.5 x nib thickness)

The loading flank contributes approximately half of Duggan's torque value because the force on the seal is equal to the force on the loading flank. As shown in the equation above, the CoF has a large effect on Duggan's torque. It is noted that the CoF on the shoulder μc can differ from that on the thread μ.

This equation was derived by considering the forces acting on an inclined plane of a bolted joint, which in the case of the premium tubular connection is the helix angle of the thread; giving the total torque required at the threads. This value was then added to the torque needed to overcome friction at the annular bearing surface of the nut or bolt, i.e. the seal of the coupling in the premium tubular connection.

This is used along with the API RP 5A3 test to acquire CoF from the test sample. The additional torque caused by the conic shape of the connection is not incorporated into the equation and has to be calculated separately because it is not associated with the seal pre-load. By executing the test until yielding occurred, the pre-load value was then extracted from the geometry and yield strength, allowing CoF to be estimated. To achieve the wide combinations of sizes, weights and grades of connections, extrapolation was used as these full scale tests were not viable to be done for all combinations. The main issue with interpolating and extrapolating the results to obtain values for every combination is the unpredictable effects of contact pressure, operating speed and surface conditions. These effects are not linear and do not always correlate.

1.2.3 Current methods for acquiring coefficient of friction

The American Petroleum Institute (API) Recommended Practice (RP) 5A3, 3rd Edition test protocol provides industry standard methods for testing threaded connections in the oil and gas industry. From this procedure an estimate for the friction coefficient in premium tubular connections has been obtained **(31)**. The test apparatus is made up of a nut and a bolt (bolt shown in **Figure 1-9**). This contains three sections: a motor, a torque transducer and a rotation transducer. Rotation and torque are provided to the samples by the motor. The torque transducer resists rotation and from this an output signal is produced. The angle of rotation is calculated using the output signal from the rotational transducer, where the output signal is proportional to the angle through which the specimen is rotated. Both the torque and rotational signals are recorded so that there is one-to-one correlation between the data points. This is used to calculate the CoF for the system. The test apparatus has geometry which is significantly different from the premium tubular connection being modelled and this means that there are discrepancies between the values calculated and the real values experienced. The load on the shoulder is estimated from the tension of the bolt, which is inaccurate. A face-to-face contact is expected on the shoulder so that the contact pressure is much lower than the line contact in the seal of a premium connection. Furthermore the form of the thread in a premium connection is far from standard thread form. Therefore some discrepancy is expected in the distribution of axial load.

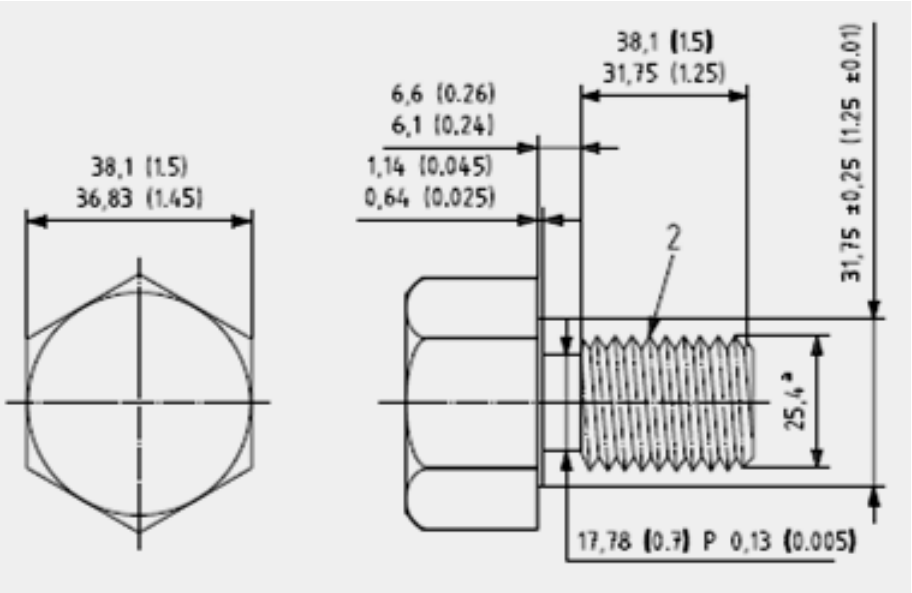

Figure 1-9: API RP 5A3 (3rd Edition) test piece(31)

Values for the contact pressure on actual premium tubular connections were taken from robust FE Analysis performed by Hunting Energy Service's (HES) Research and Development department. The finite element analysis looked at the localised pressures on individual nodes, on both the thread and seal surfaces. Although the nodal pressure values on the threads can be large, there is no cause for concern regarding yielding of the joints. The section where the yielding most likely takes place, if any, is within the seal area where very high localised pressure values are used to maintain seal engagement as shown in **Figure 1-10**. Localised yielding is not a catastrophic problem for the integrity of the structure, but it may cause galling or seizure in the seal contact area and hence lead to leakage pathways for pressurised oil/gas.

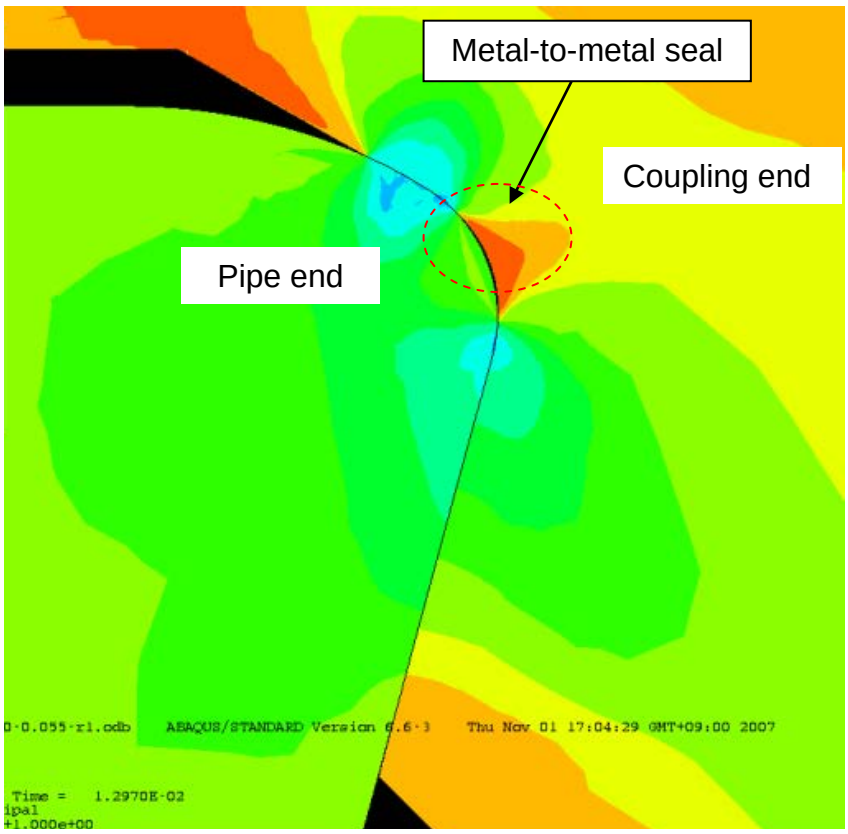

Figure 1-10: The Manufacturers FE analysis of seal during make-up (32)

The API test only gives on average a pressure of 20 – 69 MPa (3 – 10 ksi) in the threads and 206 –413 MPa (30 – 60 ksi) on the loading collar. The true values in a premium connection are approximately 690 – 2070 MPa (100 – 300 ksi) on the seal and 138 – 690 MPa (20 – 100 ksi) on the thread **(32)**. This API test generates a thread CoF between 0.05 – 0.07 which is considerably lower than the true value observed in premium connections for the same lubricant **(31)**. This is because the contact pressure in API test is much lower compared to that in the seal of premium tubular connections. This may improve the effect of hydrodynamic lubrication and reduce the risk of galling in API test and hence reduces the CoF. Observations of scrapped connections in the field showed that galling is a usual cause of concern.

1.2.4 Effect of surface wear and burnishing on CoF

“Wear is the progressive damage of a surface, involving material loss” (1), which is caused by the contact experienced by two surfaces in relative motion. It is an unavoidable cohort of friction and occurs in some form each time two surfaces are in contact with one another. A lubricant can be applied between two surfaces during contact in order to reduce the wear. Lubrication between two surfaces creates a gap between them and this means that less material loss will occur. Miscalculated and unappreciated wear can lead to major consequences in engineering and it is important that those designing the moving parts are aware of the problems. It is not only the replacement of parts, which in itself can be significant, but also the length of time that it takes to replace them. This replacement process is usually accompanied by machine downtime resulting in lost production and therefore less profit.

The wear rate is the volume of wearing surface lost per unit sliding distance per unit time. In dry contact, the wear rate is dependent on the normal load, the sliding speed, the initial temperature, and the thermal, mechanical and chemical properties of the materials in contact. As the complexity of wear is so vast, there are no situations which are entirely understood and no collective method which can be applied to every case. Minor changes in circumstances that connections experience can have a major effect on both the wear and the coefficient of friction of that system. A simple way, used by Williams **(1)**, to differentiate between mild and severe wear is to examine where the wear rate increases rapidly with a rising contact pressure. The jump in wear rate is usually very noticeable and this typically provides a clear distinction of the result of severe

wear as opposed to mild wear. Depending on the material types involved in the contact, and the circumstance to which the surfaces are subjected, influences the conditions in which this occurs.

It is important to note that the CoF depends on both the properties of the surfaces in contact and the dynamics of the conditions which the surfaces are under **(33)**. Coulomb **(34)** was the first to recognise that the surface roughness of an object has an effect on the friction between two objects **(35)**. Work done by Nayak **(36)** on Gaussian, non-isotropic random surfaces, produced a useful method of representing the surfaces by equations. It was confirmed that the CoF is dependent on the surface roughness value and interface properties in research done by Bengisu et al **(33)**. The authors managed to relate the macro-scale friction force to the micro-scale forces produced at the areas of true contact between the surfaces.

Further work by Menezes et al **(37)** demonstrated that value for the average CoF in a system is dependent on the mean slope of the surface profile, however it is not affected by the surface texture of any type of material. Studies by Sedlacek et al **(38)** found that in dry testing, the CoF is lower when roughness is higher; yet in systems with lubrication, the CoF is lower when roughness is lower. The contradiction in these observations is owing to the different friction mechanisms in dry or lubricated contact conditions.

1.3 Current Research in Tribology of Tubular Connection

Regulatory bodies are abundant in the oil and gas industry to ensure that safety regulations are adhered to as it is the primary concern. In order to comply with the regulations, there are a number of standards and specifications which designs have to satisfy to permit operation down well. In the current environment, tubing designs are well within the limits to withstand the existing environmental conditions that they are exposed to, however as the search for oil and gas goes deeper, the environment becomes more severe. In order to ensure that designs remain safely within the limitations; companies have to examine and scrutinise a wider scope of variables, therefore the tribology field becomes an essential area in the fuller understanding.

1.3.1 Tribology in premium tubular connections

Bradley et al **(39)** noted the importance of the design being critical to the reliability of premium tubular connections and threaded casings in High Pressure High Temperature (HPHT) environments. The authors' work included an analysis of the types of thread, thread interference, thread forms, crest-root designs, seals and service design. The analysis showed that due to the wide availability of designs and the requirement of a safe environment, it was important that testing of connections was done accurately and effectively.

As the cost of International Organisation for Standardisation (ISO) testing based on the ISO 13679 protocol **(40)** is extremely expensive, it is becoming increasingly important to attain results for as many different aspects as possible to reduce costs and the lengths of testing time. An alternative method of testing,

on a much smaller scale would therefore benefit any company significantly. "Modified" ISO testing is already used to prove that components meet the specified criteria at a reduced cost. These "modified" tests reduce the number of samples required but increase the number of results gained from testing. This is done by combining tests looking at different aspects of the internal and external pressures, with and without bending using the same samples. By constructing alternative cost-effective test rigs, gaps in testing could be easily filled. There are a minimum number of tests for combinations of materials which need to be completed using these ISO tests and therefore interpolation was used to fill the gaps and extrapolation used to obtain results outside of conventional limitations. Having a laboratory based test rig allows every combination to be tested economically but thoroughly.

The main issue in OCTG failures is in connections, where approximately two thirds of all failures are caused primarily by the connection **(41)**. Guangjie et al carried out work on premium tubular connection testing using finite element analysis **(27)**. Guangjie et al split the torque of the system into two main sections: the friction torque and the deformation torque. The deformation torque is the one used up when deforming the surfaces of the pipe and coupling of the connection. Similar to the premium tubular connections examined in this project, the deformation torque was negligible compared to that of the frictional torque. In this work the friction torque was obtained by the equation:

$$\boldsymbol{T_{FR}} = \sum_{\boldsymbol{K}} \int_{\boldsymbol{S_K}} \mu \boldsymbol{\sigma_{nn} r dS_K} \qquad \textbf{(1.12)}$$

Where$\boldsymbol{r}$ is the radius at the integration point, $\boldsymbol{\sigma_{nn}}$ is the normal contact stress, μ is the friction coefficient obtained from the thread compounds characteristics and $\boldsymbol{S_K}$ is the contact surface number $\boldsymbol{K}$. The integral is applied to each contact surface while the summation is to combine the contributions of all surfaces to the total torque. This allows for the definition of different CoF for each contact pair. The work looked at the distribution of the equivalent stresses, normal contact force and of friction in the system. Repeated make-up and break out of connections affects the taper and this could reduce the pitch diameter of the pipe end connection.

This concept is similar to Duggan's equation **(30).** Duggan's torque equation permits different CoF value to be defined for the shoulder and the thread to reflect the different contact regimes, but assumes a constant CoF within each section. Guangjie's equation is applied in Finite Element Analysis which provides continuous stress distribution in the system so that the torque applied to each element can be combined. This approach allows for the system to be split into as many sections of contact as necessary. Within each section the friction coefficient can be regarded as a constant or a continuous function of the pressure, if known. Therefore, Guangjie's equation is most useful in cases where the friction coefficient is sensitive to contact pressure. Nevertheless, the pre-requisite for this approach is that the friction function is pre-determined.

An attempt was made to understand friction and the forces associated with tightening conical threaded connections by Baragetti et al **(42)** in 2003. The author acquired results by friction testing a full connection. Strain gauges were

fitted to locations of the connection which were understood to give values for axial shoulder pre-load $(\boldsymbol{Q_{up}})$ and the friction parameter $(\boldsymbol{K_{up}})$ was calculated from the equation below using the pre-defined torque value $(\boldsymbol{M_{up}})$ used to make-up the connection. This method was advantageous because it allowed the friction to be investigated in real life conditions; nevertheless due to the costs associated with it, repeated testing could not be undertaken easily and economically and there was a limit to how many conditions could be investigated.

$$\boldsymbol{M_{up} = K_{up} Q_{up}} \qquad \textbf{(1.13)}$$

Wittenberghe et al attempted to make modifications to existing pipe and coupling assembly designs in order to improve fatigue life **(43)**. The reduced fatigue life was due to the issue of localised stress concentrations initiating cracks particularly in the thread roots. In order to achieve a better fatigue life, they endeavoured to change the distribution of load by spreading it more evenly. In order to do this, they needed to perform testing to understand the locations of maximum stress. The testing procedure was primarily done using fatigue experiments. Two-dimensional Finite Element modelling was done for the connection as a secondary test. The testing procedure comprised of a universal test machine set up to perform four-point bending tests. This was more beneficial than a three point bending test as it applied only normal loading to the material and therefore all damage was caused by the normal stresses **(44)**. Through repeating the test after alterations had been made, their work was successful and an improvement in the fatigue life was made. It was established that under axial load, the section with highest stress concentration was located

at the last engaged thread of the pipe, and that this was triggered due to irregular dispersal of load, which is different to where the maximum stress was found in the Finite analysis used to establish the maximum stresses in the design. However, it has to be noted that in the premium tubular connections investigated in this project, the main loading is carried by the seal and distributed to all the threads.

1.3.2 Friction and metal-on-metal contact

An understanding of metal-on-metal contact is imperative in many industries. Meng et al **(45)** researched the mechanics and lubricating regimes of metal-on-metal contact in an artificial human hip joint. This is dissimilar to a premium tubular connection, however there are similarities between the two. Noted in their work was the importance of controlling the surface roughness to allow metal-on-metal contact between two surfaces to be successful. The work concluded that by increasing the contact area (in this case by increasing the variation rate of the radius of curvature or the size of internal bearing surface) then the contact area would increase, consequently reducing the contact pressure, and therefore sequentially increasing the film thickness. This is similar to that of the premium tubular connection, if the area of contact increased, then the contact pressure would decrease therefore producing a more even film thickness.

1.3.3 Friction and surface roughness

Bengisu et al **(33)** developed a friction model which considered deformation and adhesion of surface asperities. The paper looked at "true contact" between

surfaces and related the micro-scale forces to the macro-scale friction force. The work was more accurate because it also looked at all areas of contact between the surfaces and also allowed for the resultant normal forces produced by the contact on the slopes of the asperities. Until this point no other research had looked at this in any great depth. The stick-slip phenomenon is a reaction which occurs in dynamic systems where the objects slide over one another in an unsteady manner. This occurs when the sliding force is not as high as the static friction and the samples will not slide over one another until the driving force is high enough to exceed it. This is most common when the surface roughness is very high and the authors found that the surface roughness plays an important role in the stick-slip motion. It was also found that machined surfaces have the higher tendency to display stick-slip effects than that of non-stationary roughness surfaces e.g. shot blasted surfaces as used in the majority of samples tested in this project.

1.3.4 Friction and metallurgy

An investigation into the effect of sliding speed on friction and wear behaviour was completed by Shafiei and Alpas **(46)**. The authors' work investigated the frictional behaviour of nickel within an argon atmosphere. Although the testing conditions were different to those used in this project, some of the procedures and ideas are similar. The samples used were thick sheets of electrodeposited nickel and these were polished using a diamond suspension to give a consistent surface roughness for each test. Both nano-crystalline and micro-crystalline samples were tested and compared. Values for CoF and wear of the samples were measured using an off-the-shelf pin-on-disc tribometer. This test

method was satisfactory because the authors were not trying to simulate real-life conditions but were investigating the significance of speed. An optical interferometric surface profilometer was used to examine the wear mark. The wear volume and wear rate were calculated using already existent equations. It was found from the experimentation that for nano-crystalline structures, a large increase of speed caused an increase in CoF. The authors' assumed that protective tribo-layers formed on the material surface and these were responsible for the lower CoF at reduced speeds. At the higher speeds, the fragments of material removed during sliding were much smaller. This meant that the smaller particles did not fill the gaps as well as the larger ones and a defensive layer was not generated, resulting in a higher CoF. For the micro-crystalline samples, the CoF was impartial to the increased sliding speed.

Farhat et al **(47)** looked at the effect of grain size on CoF and wear of nano-crystalline aluminium. The authors' concluded that CoF increases with initial contact and sliding distance, and then levels out to a constant value until sliding ceases. CoF was also found to be dependent on grain size: as the grain size decreased, CoF decreased. Another outcome of the investigation was that CoF was higher when sliding was carried out in a vacuum. This was because when a test is undertaken in a vacuum there is an increase in the metallic contact and this increases CoF value **(48)**. The wear of the system was found to follow a similar pattern to CoF; as the sliding distance increased, the wear volume initially increased sharply, and after a certain sliding distance, the rate of growth of the grain size slowed.

1.3.5 Friction and surface topography

Coulomb **(34)** was the first to recognise that the surface roughness has an effect on the friction between two objects **(35)**. His work was based upon the idea that friction was due to the "work done in dragging one surface up the roughness on surfaces becoming interlocked" **(1)**. However, this was discredited in the early 19th century by Leslie **(49)** as he exposed the idea that if friction is only based on overcoming gravity, then no average change in the value of elevation of the moving body could result in no friction occurring. This cannot be true as it has already been proven that some level of friction, even if it is miniscule, always exists. Leslie concluded that some surfaces in contact could be moving up whilst others had to be sliding down, which provided an explanation for the fluctuation of friction.

Work by Greenwood and Williamson **(50)** in the 1960s investigated contact between "flat" surfaces. Previous research had already proven that all "flat" surfaces were rough on some level. This meant that the true contact was smaller than assumed when the two surfaces appeared to be fully in contact. The work concluded that the pressure did not affect the separation between the two surfaces significantly and there was no change in the separation distance between them when the load was changed. This gave a reason for the inability to achieve a complete gas-tight seal when using metal-to-metal contact. The authors also concluded that surfaces which have been "bead-blasted" (i.e. peened) fit Gaussian distribution very well.

The Greenwood and Williamson (GW) model is one of the most established methods used to predict the ratio of asperity contact. Although changes have been made to this model throughout years of investigation, the fundamental features are still widely used and relevant. Greenwood and Williamson's model was based on the idea that the height of asperities from the mean plane of the surface has a normal distribution **(51)**. All asperities on the surface were assumed to be spherical with a constant curvature of $\boldsymbol{K_s}$. The surface is represented by a matrix of height values which were obtained through statistical analysis. The method works on the assumption that the asperities deform elastically, and that each asperity is not affected by the deformation of the features around it. However this theory was based on elastic contact mechanics for rough surfaces. It is expected that the contact in the seal of a premium connection would be quite different. Some plastic deformation of the asperities would occur due to the considerable contact pressure.

Jackson and Green **(52)** modelled the elastic contact between rough surfaces using three very different approaches. The research carried out was to compare closed form elastic rough surface contact with deterministic models. Closed form models are those in which the output is obtained by entering data directly into formulae without changing the input every time. Deterministic models are where the value is acquired by using the final output as the input values for the next phase of the test, i.e. no random values can be created. This method is very time consuming, and therefore if accurate values can be achieved using the closed form method, then this would be adequate. The authors concluded that the mesh resolution made a significant difference to the final values. In

every test type, the coarser mesh produced a pressure result which had a difference of about one order of magnitude smaller compared to that of the finer mesh. This is thought to be caused by the interval between the nodes in the model. In the coarser model, the force is distributed across a larger area. However in the finer model the same force is located across a much smaller surface and therefore as the pressure is equal to the force divided by the area, the contact pressure is affected accordingly. In each test, the calculated contact area is smaller for the finer mesh and larger for the coarser mesh, which is in line with the difference in pressure. For each of the types of test and for each size of mesh, the predicted contact area is directly proportional to the load applied. This proves that even though the foundations of the model types are very different, the outcome remains the same.

Similarly Zavarise et al **(53)** looked at the relationship between the resolution of a model and the prediction of the mechanical response of the contact between surfaces. It was concluded that in cases where random process theory is applied, the results of the test rely heavily on the lower cut-off length of a system. Random process theory is where the initial variables are known, but for each iteration the process does not use the final reading from the previous phase of the test, therefore creating uncertainties in the resultant values. To obtain these results, the authors used an entirely numerical approach to model the topography of the surfaces using statistical models. The materials represented by these matrices were a zirconium alloy and a stainless steel. It was shown that as the lower cut off reduces to zero, the slope of the real contact versus normal load curve decreases to zero for all contact models. The

relationship between the preciseness of the model and other properties of the solution were identified, but the main conclusion drawn from this set of experiments was that the prediction of contact is extensively dependent on the deformation regime used in the model and it is the plasticity index which is of upmost importance.

Sedlacek et al **(38)** looked at the impact that the surface fabrication has on the roughness, friction and wear of steel plates. The tribo-testing performed on the samples used a pin-on-disc measuring device with a ball-on-disc contact. The surfaces of every test sample underwent a series of checks prior to testing to ensure that the quality of the surface was consistent. The surface checks were done using profilometers to check the main roughness parameters including average surface roughness, root mean square roughness, skewness, Kurtosis, core peak-to-valley height, reduced peak height and reduced valley depth. The authors' reasons for testing these in particular were because these show the greatest differences in values. The effects of different types of surface treatments were also investigated and various grades of milled, turned, polished and ground surfaces were examined. Both dry and lubricated tests were undertaken and different sliding speeds were also tested. The main conclusions were that in dry tests, there was a lower CoF when the roughness was very high. However this is only true in severe conditions. In lubricated test set-ups, CoF is lower when the roughness is low. It was also found that when the sliding speed was higher, the friction was smaller for both dry and lubricated tests. The more negative Kurtosis is, the lower the friction is for lubricated tests.

Carbone **(54)** produced a "slightly corrected" method where all spheres were not of equal curvature. This created asperities whose curvature changed with varying heights. This method was directly compared with the theories by Bush, Gibson and Thomas (BGT) **(14)**. The BGT method is a more complicated technique with a considerable number of calculations involved. Although this makes the process very expensive and time consuming, it does provide a more accurate result than the GW method. BGT works by executing an arrangement of multi-asperity theories. By this method, the true contact area is found to be linearly correlated to the applied load. Carbone attempted to produce a method that would be as accurate as the BGT method, but was based upon the theories of GW. The initial change made was to make the asperities spherical but not of equal radius; therefore the sphere curvature was dependent on the height. The new model produced results similar to the BGT findings, and it was also found that the linear relationship between the contact area and the load was a result of the varying asperity curvature.

Nayak **(36)** concluded that for random, isotropic, Gaussian surfaces, the information required to evaluate the behaviour is contained within “the power spectral density of the profile in an arbitrary direction”. The height above the plane reference of the surface is defined as $\boldsymbol{z}(\boldsymbol{x},\boldsymbol{y})$**,** where $\boldsymbol{z}$ is a random variable and $(\boldsymbol{x},\boldsymbol{y})$ are the Cartesian coordinates in the reference plane. The power spectral density, $\boldsymbol{\phi}$, is the Fourier transform of the autocorrelation factor, $\boldsymbol{R}$, where these are defined to be:

$$R(x,y) = \lim_{\substack{L1\to\infty \\ L2\to\infty}} \left(\frac{1}{4L_1L_2}\right) \int_{-L1}^{L1}\int_{-L2}^{L2} z(x_1,y_1).z(x_1+x,y_1+y)dx_1dy_1 \qquad \textbf{(1.14)}$$

$$\phi(k_x,k_y) = \frac{1}{4\pi^2}\iint_{-\infty}^{\infty} R(x,y)exp[-i(xk_x+yk_y)]dxdy \qquad \textbf{(1.15)}$$

For isotropic surfaces, similar to the surfaces considered for modelling in Chapter 5, the autocorrelation factor depends only on the value of $r = (x^2+y^2)^{1/2}$ and not of the polar angle, $\theta = tan^{-1}(k_y/k_z)$ which simplifies computation.From the equations above, the probability distribution of summit heights, spectral density of summits and the probability distribution of the mean curvature of the summits can be obtained. A method for the accurate calculation of these values allows a comparison between surfaces and additional statistical analysis of the distribution and curvature. This gives a more substantial understanding of how the surface structure differs.

Greenwood **(55)** provided an extension to Nayak's work and concluded that most surfaces are only slightly elliptical. The author showed that elastic theory can explain the effect that the contact area and load have on one another. It was noted that the product of the principal curvatures of the asperities is more important than the sum or mean, in the process of measuring the shape of them. This is because this value can be used to differentiate between maximum points and saddle points, i.e. localised maxima which are a result of smaller asperities. This technique is useful because it can be used to locate where the peaks are on a surface during modelling, however this complicates the data computation. It then becomes important to distinguish whether or not the

method supplements the already existent techniques in return for a far more arduous one, or if a simplified one actually produces results that are sufficiently accurate.

Work by Buczkowski et al **(56)** took the analysis one step further and looked at anisotropic surfaces. Their work concluded that there was a linear relationship between the applied elastic load and the contact area. This is similar to what is assumed for isotropic surfaces. In both circumstances, as the load increases, the surfaces are pushed closer together and as long as the gap between the surfaces reduces with increasing load, the contact area will increase too. Although not investigated by the authors for the apparent isotropic surfaces, the contact stiffness for an anisotropic surface was also found to be proportional to the normal load. The authors stated the significance of the elastic modulus which was used to investigate the material properties of both surfaces in contact. In cases where the surfaces have similar material properties, i.e. where the Young's modulus and Poisson's ratio values are different from one another especially in the cases where one surface is much more elastic than the other, the contact (also known as the effective contact modulus) is ***E**** (the plane-strain modulus). In the case where the materials are the same, the contact modulus is half of this value.

1.3.6 Lubrication regimes

There are four main types of lubrication: solid lubrication, boundary lubrication, mixed-film lubrication and hydrodynamic lubrication **(57)**. **Figure 1-11** shows the relationship (according to Stribeck) between the friction coefficient and the

lubrication regimes with a lubricant. In the production of the graph, the load and velocity were kept constant while the viscosity was varied **(58)**. It was found that the lowest friction coefficient is between the elasto-hydrodynamic and hydrodynamic lubrication region, which is expected because it is at this point that the full load is carried by the lubricant. The elasto-hydrodynamic lubrication involves some elastic deformation in the contact area due to the hydrodynamic pressure. The minimum friction depends on the materials, contact pressure and initial surface roughness. The highest friction coefficient shown was observed during the boundary lubrication phase. This is where the contact load is solely carried by the boundary layer on the asperity contacts. Often in some cases, this provides areas of asperity contact which have a thin lubricant film around the asperities. The friction is a combination of the shearing of the boundary layer and the lubricant. This is called ‘mixed’ lubrication. The graph was ciphered using the results of experiments in which the load and speed were varied in a similar way to the work by Thurston **(59)**.

1.3.6.1 Hydrodynamic lubrication

The likelihood of hydrodynamic lubrication is low for the make-up of a premium tubular connection, however the initial hypothesis for the project gave rise to the possibility that due to the low contact pressure in some thread sections such as the conical surfaces, the surfaces could experience hydrodynamic lubrication. It was thought that this may explain the low overall CoF used in the API calculation of torque during the make-up procedure.

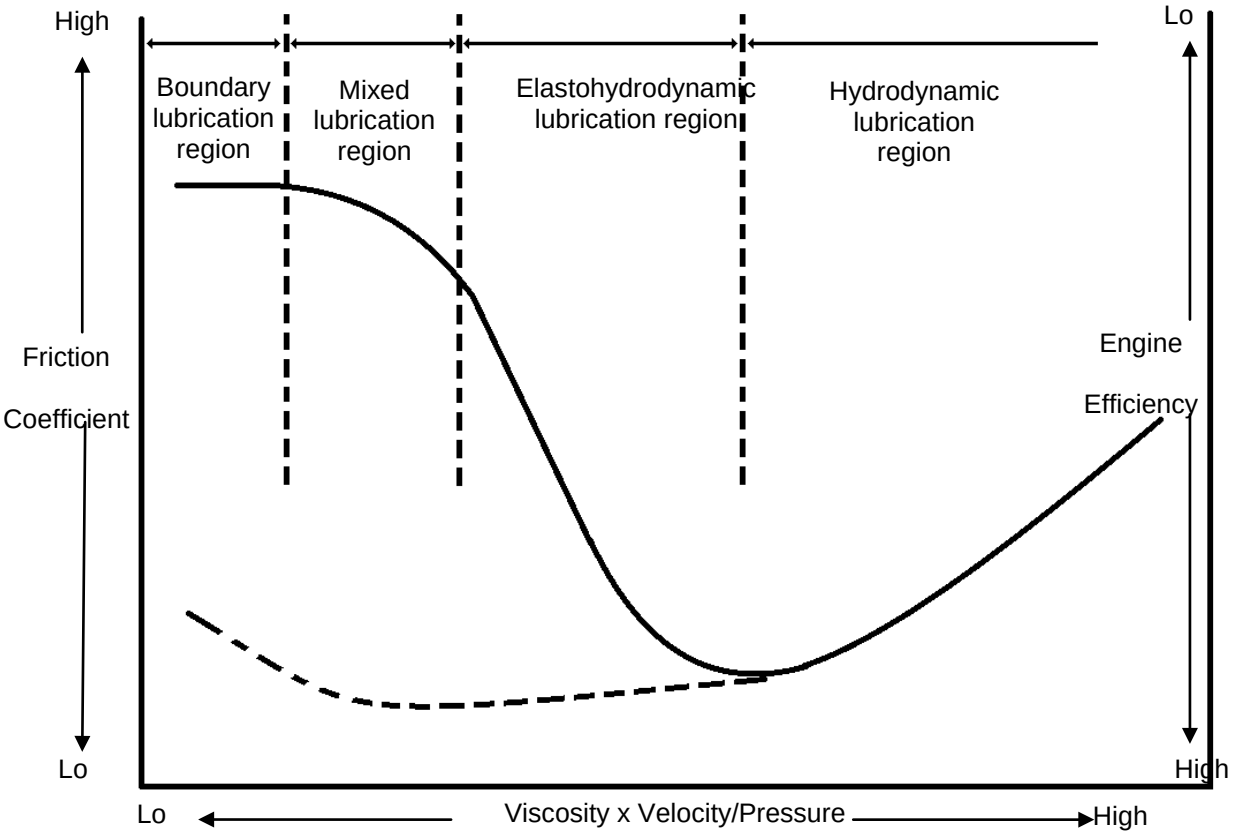

Figure 1-11: Stribeck curve and friction modification relationship (58)

Hydrodynamic lubrication is where a lubricant film completely separates two surfaces that are in contact. It can occur in situations where the hydrodynamic pressure is sufficiently high to carry the external pressure. The viscosity and velocity can both have an effect on any hydrodynamic lubrication. A simplified schematic of hydrodynamic lubrication is shown in **Figure 1-12**. Sample (a) shows a diagram where the surfaces are separated by the lubricant, resulting in limited direct contact between the two. In the case of sample (b), the lubricant has been forced out and the surfaces are in direct contact with each other. This is a slightly exaggerated example, but the differences in the coefficient of friction between the two tests can be significantly large. If one fluid can be forced out from between two surfaces easier than another, then the more viscous lubricant

would theoretically create a higher hydrodynamic lubrication effect. Where the two surfaces fully converge, i.e. no hydrodynamic lubrication is taking place; the amount of material removed by wear will be significantly higher than where the two samples are separated by the thin layer.

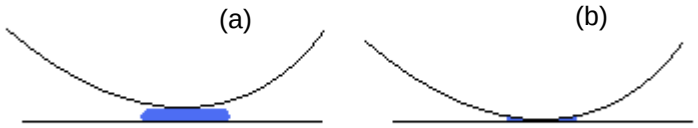

Figure 1-12: (a) Surfaces separated by lubricant (b) Surfaces in direct contact

Qasim et al **(60)** modelled the piston skirts in an engine, looking at the effect of the surface roughness on the lubrication of surfaces at initial engine start-up. The hydrodynamic film thickness used in the paper was expressed as:

$$\boldsymbol{h = C + e_t(t)cos\theta + \left[e_b(t) - e_t(t)\frac{y}{L}cos\theta\right]} \qquad \textbf{(1.16)}$$

Where the piston skirts angle is defined by equation $\boldsymbol{\theta = {}^{x}/_{L}}$, $\boldsymbol{x}$ and $\boldsymbol{y}$ are coordinates of the position, $\boldsymbol{L}$ is the piston skirt length, and $\boldsymbol{e_b}$ and $\boldsymbol{e_t}$ are the acceleration term of piston skirts bottom and top eccentricities respectively. The hydrodynamic load is carried by this minimum film thickness. The work concluded that the peak minimum film thickness is found immediately before combustion and does not change significantly during engine activation when the engine start-up speed is low.

Teodoriu et al **(61)** looked at friction considerations in rotary shouldered threaded connections; another name for a premium tubular connection. The accepted value of CoF according to the API Standards is 0.07-0.08 and was

obtained through laboratory experiments carried out on different types of metal particle-containing thread compounds. The lubricants used in the experiments contained variant amounts of zinc, lead and copper, which is similar to the constituents of Lubricant B described later in section 2.4. The Farr **(62)** equation used to compute the make-up torque **(M)** between the pipe and coupling of a connection is shown:

$$M = F_v\left(\frac{P}{2\pi} + \frac{R_p}{cos\beta}\mu_{th} + R_s\mu_s\right) \qquad \textbf{(1.17)}$$

Where F_v is the tension force required in each bolt, $P$is the thread lead, R_p is the average mean radius from axis of bolt out to point where load is applied to thread surface, R_s is the mean radius of the nut face, or shoulder and β is half of the thread angle measured on a plane through the axis.

This equation is similar to that used by Duggan (c.f. Eqn 1.6) in the way that the torque is highly dependent on the friction coefficient. Similar to Duggan's equation, the dimensions of the threaded connection are used in the calculation. In Duggan's it is the diameter that is used and in Farr's it is the radius. Although the two are very similar, the main difference is in the order of some of the terms. Two different CoF values are used in the calculation of torque, these are the μ_s, the CoF in the shoulder and μ_{th}, the thread CoF.

Jeng **(63)** looked at the effect on friction with changes in height and orientation of asperities on a surface. Experiments were carried out using a pin-on-disc set-up on samples which represented a range of heights and directions with arithmetic average surface roughness (R_a) values between 0.48 and 14.67 µm.

As previously stated, the accuracy of such a set-up can be slightly unreliable when it comes to comparing different testing procedures due to possible differences in the speed and contact pressure. The overall effect can be compared satisfactorily and a general trend can be achieved for tests performed using the same equipment. The results showed that as the load increased, CoF decreased. The research also concluded that by increasing the speed, CoF reduced too. A final conclusion of the work was that as the height of the surface asperities reduced, so too did CoF. This effect of the orientation and heights of the surface asperities was much larger when the load applied during contact was higher.

The research of Qiao et al **(64)** showed the effect of PTFE (Polytetrafluroethylene) particles on CoF. PTFE is known to produce one of the lowest values of friction of any type of material. PTFE lubricants are often used in a contact system to reduce CoF. This works by reducing the adhesion experienced by the samples when they are in contact, i.e. preventing them from sticking to one another. A comparison was made between the addition of PTFE particles to a PEEK (Polyetheretherketone) powder mixed with nano or micrometer Al_2O_3 (Aluminium Oxide). An Amsler friction and wear testing device, which consisted of a rotating ring and a sample, where a load was applied downwards (see **Figure 1-13**) was used to obtain wear data. The wear volume was measured by weighing the sample between tests. This was then used to calculate the wear coefficient ($\boldsymbol{w}$) and friction using the following equations.

$$w = \frac{V_s}{X.L} \quad (1.18)$$

$$\mu = \frac{M}{R.L} \quad (1.19)$$

Where V_s is the measured volume loss, X is the sliding distance, L is the applied load, and R is the radius of the steel ring.

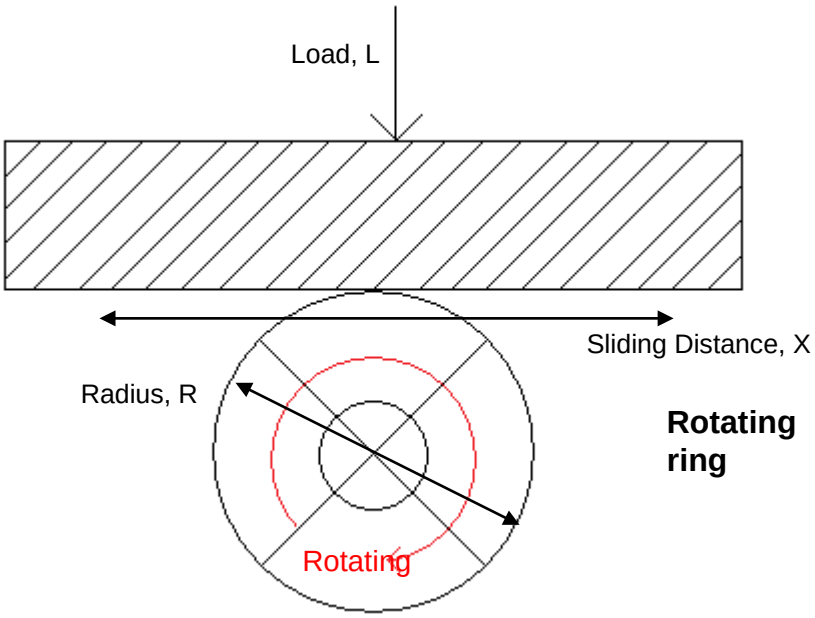

Figure 1-13: Amsler friction and wear test rig schematic

Some of the earlier work on modelling hydrodynamic lubrication in rough surfaces dates back to the 1960s in work done by Ralph Burton **(65)**. His work entailed using a Fourier series type approximation to model the surface roughness **(66)**. When the nature of the surface roughness was established to be random, stochastic approaches began to be used to create a representation of the surfaces in question. Work by Christensen (communicated by Christopherson) **(67)** stated that the value of the maximum pressure depends on the pressure coefficient of viscosity multiplied by the equivalent Young's

modulus. Their work also concluded that at very large pressures, additional load caused a much larger effect than at lower pressures. This is different from the assumptions used in this project as in this case the pressure in the system was assumed to be directly related to the load (see Equations 1.4 to 1.10). Some of their experiments use balls instead of the cylinders (as used in their compared theory) and therefore a direct comparison between the experiments is not possible.

Work done by Ahmed and Sutcliffe **(68)** looked at identifying surface features of shot blast steels in cold rolling. Their work produced algorithms which identified several surface features from a three-dimensional profile of a sample. The profile was obtained from the three-dimensional images and these were converted into a matrix which described the surface. The algorithms established the position of the pits on the surface and also identified the location of the roll marks. This created a system to estimate the lubrication conditions that the surface would be exposed to in order to speculate how much oil would be trapped in features on the face of the material and what effect it would have on the lubrication. The control of the surface finish can be easily monitored using this technique, providing a quantifiable approach to inspecting the quality of surfaces.

1.3.6.2 Boundary lubrication

Boundary lubrication is where the surfaces are so close together that the load is mainly carried by the asperities with an ultrathin boundary layer **(58)**. Conventional boundary layers are thought of as solid layers, of which the shear strength is directly proportional to contact pressure giving rise to a constant

coefficient of friction independent of viscosity or sliding velocity as shown in **Figure 1-11**. More recent studies suggest that the properties of boundary films may be more complex than this **(69, 70)**. The properties of the boundary layers depend on the tenaciousness of the films' ability to adhere to the surface and the details of the surface topography. Single molecular layers, such as paraffin oils, can provide reductions under low contact pressure, but may be depleted under higher pressure **(17)**. More complex surface films such as $CaCO_3$ in n-dodecane colloidal solution are very much dependent on the applied pressure **(71, 72)**. There exists a 'shakedown' limit. When loads are in the acceptable 'shakedown' or elastic regime, the coefficient of friction falls with increasing load. Above the 'shakedown' limit, the coefficient of friction increases owing to a contribution from ploughing deformation. The coefficient of friction increases rapidly with the severity of galling or scuffing which leads to direct metal-to-metal contact **(73-75)**.

1.4 Knowledge gaps

With the current and future environments that premium tubular connections are expected to withstand, including high pressures and temperatures, the expectations of the connections will only increase. The main uncertainty in current piping research is in the prediction of CoF. Even with the magnitude of pioneering research presented in this chapter, a method of inputting accurate CoF for a premium tubular connection does not currently exist. API uses a set value for every connection, without considering alterations in surface roughness after initial make-up or in the changes in sliding speed. A method of prediction would be very beneficial to the current industry in the future. Currently there is

limited appreciation for a method of calculation of CoF. However, as environments become more challenging, future generations will benefit from this type of research and altering working practices will not seem so costly or time-consuming. Therefore, there is a need for laboratory research which provides a method for obtaining values for CoF as well as the wear of the surfaces. Thus providing foresight into how the connection reacts to being torqued up more than once, or at different speeds.

There are three distinctive sections in a premium connection. According to the FEA studies shown above **(32)**, the highest pressure occurs in the seal section. This is a line contact as shown in **Figure 1-10**. The pressure is above 600 MPa which is above the ‘shakedown’ limit so that the lubricant is almost completely squeezed out of the contact area **(75)**. The dominant lubrication regime is believed to be boundary lubrication, which is insensitive to sliding speed. The surface of the seal is usually burnished in the manufacturing process so that it is smoother than other sections. Some plastic deformation is expected in this section. Observations in the field also indicate that the surface is burnished after repeated make and break. Another section is on the loading flanks of the threads. The loading flanks usually have negative angle in a premium connection as shown in **Figure 1-6**. The design of premium connections is to ensure that the load is distributed to all threads engaged so that the contact pressure is in the order of 150-500 MPa. This is somewhere below the ‘shakedown’ limit. The surface of the pipe is usually peened so that it is commonly rougher than other sections. In this case, the contact area was notably larger and the contact pressure smaller so that the lubricant film in the

contact area is allowed to escape through the roughness troughs, leading to a large fraction of asperity-to-asperity contact. Hence, the friction is a combination of boundary lubrication and hydrodynamic lubrication which is more sensitive to sliding speed. The contact pressure on the conical surfaces is the lowest so that the surface asperities are not removed as quickly as in other sections. It was initially thought that this section would experience an elasto-hydrodynamic lubrication effect due to the small pressure it experienced. However, it is not possible to separate three different sections using full size physical tests. The lubrication mechanism of each section is not well understood.

It is important to note that it is not only the contact pressure that determines CoF, but also the details of the surface topography. It is also important to observe that the surfaces are modified during sliding and repeated make-up as observed in the field. It is not fully understood how quickly this happens and to what extent that this changes the CoF. Therefore there is a need to develop a micromechanical model to understand the relationship between asperity wear and the implications on the asperity contact, and to establish a friction model that takes into account the role of lubricant distribution.

1.5 Project aims and objectives

The project was sponsored by Hunting Energy Services (HES), an oil services company who specialise in premium tubular connections used in the completion string in the oil and gas industry. HES's OCTG department provides pipe casing and premium tubing. Premium tubing is usually connected via premium connections which consist of a threaded section and a metal-to-metal seal. The

metal-to-metal seal provides a liquid and gas tight connection to allow hydrocarbons to be transported through the connection back to the rig platform. The threads ensure that the seal is maintained during the high-temperature, high-pressure environments in which the connections are exposed to during production.

The initial aim of the collaborative project was to produce a laboratory tool to measure friction and galling under a wide range of contact conditions, which mimicked contact conditions in three different sections of a premium connection to help understand the observations of the role of tribology in the field. The scope of this project started with the design and manufacture of a test rig based on existing techniques in order to obtain a range of measurements for CoF with varying sliding velocity, contact pressure, surface roughness and materials in contact. Test pieces were manufactured to represent the surfaces in contact for testing purposes. These samples were exposed to the same procedures that the pipes and couplings experience in manufacture, producing surfaces that were comparable with real products. The project was then extended to develop a model which could predict the surface roughness, friction and wear of surfaces without such a large amount of physical testing. This reduction of physical testing has the potential to reduce costs if the outcomes of the mathematical modelling are accurate.

Chapter 2 Design for Measurement of Friction

2.1 Determining the coefficient of friction

2.1.1 Pressure regimes

Contact pressure is an important consideration in the design of a friction test device. In a premium tubular connection, the most important locations, where connection contact pressure is of the most interest, are on the seal where the pin and coupling meet, on the thread cone, and on the thread loading flank. The contact pressure at each of these sections has a different magnitude and using Finite Element Analysis **(32)**, the values of each have been estimated.

A premium tubular connection which consists of a metal-to-metal seal relies on the torque from make-up to seal the connection and prevent leakages. The torque values are calculated using Duggan's **(30)** equation relying on accurate measurements of CoF. An under-torqued connection will not provide a sufficient seal to prevent leakages from occurring when the pipe is used to extract the oil from the well. An over-torqued connection is one in which the value used in make-up is too high and therefore the seal is plastically deformed. This can result in the occurrence of leak paths in the connection. At current well depths, the pressures and temperatures that the connections are subjected to are high; though these are well within the yield strength of the materials in question. Therefore minor differences in calculated and actual CoF cause limited problems and will not cause concern. However as the oil reservoirs are depleting and drilling has to occur at deeper depths, then miscalculations of

CoF can lead to issues if connections are made-up with the wrong value of torque, especially in the case where it is over-torqued. From Finite Element Analysis (FEA) it was shown that the highest pressure in the connection occurs on the seal section. To simulate the three different values of contact pressure, three modifications of a custom-built friction tester were made. Alterations in the sample dimensions and the size of load cell used meant that results for such a large range in pressures could be obtained.

2.1.2 Current methods of measuring CoF

Sacher **(76)** defined CoF as “an intrinsic property of the two interfacing, interacting surfaces and serves as a measure of their micro and macro roughness, inter and intra molecular forces of attraction and repulsion and their visco-elastic (polymer deformation) properties. As such, the area of contact, duration of contact before movement, velocity of movement, pressure etc. are contributing factors to CoF results obtained and also to the inconsistency of the values observed when different friction testers, sensors and/or protocols are employed” **(77)**. CoF is therefore a parameter which is dependent on the surface features and characteristics of the two materials in contact. This means that CoF can be measured for any arrangement of surfaces and lubricants but not necessarily representative of the operational conditions concerned. There are various established methods for measuring CoF however, depending on the test arrangement and situations being investigated, some provide more reliable results than others.

Commercially available machines which can measure and record friction and wear properties are available to buy off-the-shelf. These are offered as pre-assembled devices and are widely obtainable. Many of these machines have their own remit, however the results are not always representative of the conditions concerned and the test rigs themselves have limited range of contact load and speed. These test procedures have been created to estimate different tribological properties for different types of systems. In order to gain reliable test results, a test method which demonstrates the conditions in which the real system is exposed to needs to be present. Therefore, modifications of testing procedures are necessary in a large number of cases.

2.1.2.1 Four-ball test

One common technique used for measuring CoF is the four-ball test procedure (shown in **Figure 2-1 (78)**). Although this method can provide a value for CoF of a system, it is used predominantly in the assessment of lubricants under severe loading conditions **(79)**. The test is made up of four steel ball bearings; three placed on one layer inside a cup, and the fourth held in a chuck above, providing equal loading on the other three. The lubricant is applied over the top of the three ball bearings in the cup. A top sample is rotated and a load is applied vertically. There are different variations of this set-up which provide a range of loading and lubrication systems. For example, to study boundary lubrication, the ball bearings inside the cup are fixed to the base to generate contact in three small round areas.

Alterations in the loading and speed applied to the system can be easily made. In some commercially obtainable products, a temperature control is also available to understand the conditions that occur in hot or cold environments.

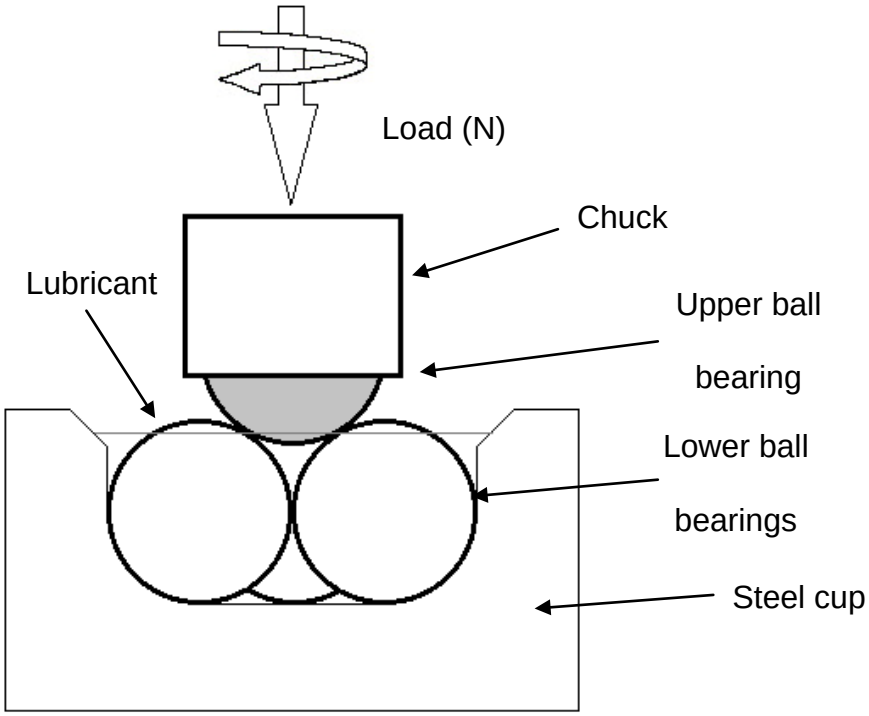

Figure 2-1: Four-ball friction test machine

2.1.2.2 Pin-on-disc

The pin-on-disc test is a common method for determining wear properties in a system. In this test, the pin is held stationary and the disc is rotated beneath it generating a circumferential wear track on the disc **(79)**.

There are different methods of arranging the test rig and it depends on the type of test required as to how it is assembled. **Figure 2-2** shows the pin-on-disc test with (a) the pin on top and (b) the pin on the bottom. In each test, a load is applied perpendicularly to the disc surface and the disc is rotated to create a circular wear mark, however the assembly of the parts can drastically vary the

results of the test. When the pin is on top (a), the removed material remains on the surface of the disc and as the number of cycles becomes greater, this volume of debris increases and causes abrasive wear. In the case where the pin is on the bottom (b), the debris removed in the wear process falls off due to gravity. This means that the wear test is not identical in both situations as there is abrasive wear occurring. This makes it imperative that when CoF results are being compared from external practices, the type of test is known to give a fair and reliable comparison. Another disadvantage of the test is that if the pin and disc are not aligned properly, the pressure applied on the surface will not be accurate and this has the ability to cause variances in testing procedures.

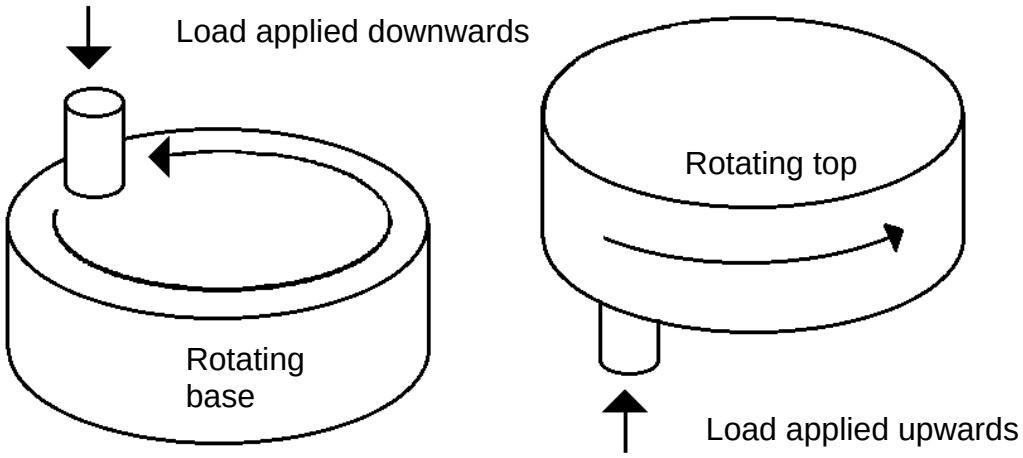

Figure 2-2: Pin-on-disc test (a) pin on top (b) pin on bottom

Podgornik et al **(80)** reviewed various laboratory friction test methods. It was established that the simplest and most extensively used procedure for general friction testing was the pin-on-disc technique. However, to obtain a new contact surface each time, the location of the pin had to be adjusted for each test making the testing procedure very time consuming. Further, a rounded pin is

required in order to generate a high contact pressure representative of premium connection. Consequently the contact pressure can change significantly when there is wear on the rounded pin. There are also discrepancies in sliding speed and sliding distance between the test and the connection during make-up. The operating sliding speed of commercial pin-on-disc machines usually ranges between 0.05 and 10 m/s **(81)**, which is significantly higher than the speed concerned with a premium tubular connection assembly make-up, which is within the range of 3 mm/s to 50 mm/s **(82)**. Another issue is that the sliding distance in these tests is at least tens of metres each run which is much larger than what occurs in tubular connections.

2.1.2.3 API test method

As described in 0, the APIRP 5A3 (3rd Edition) document describes the recommended practice for obtaining frictional data in threaded connections **(31)**. The test rig contains a nut rotating on a bolt assembly (see **Figure 1-9**) where the bolt is rotated into the stationary nut until a specific pre-load is attained. CoF is extracted from the torque data and the estimated contact pressure from the angle of rotation. Although this is a widely used testing procedure for threaded components, it lacks comparativeness between external conditions including contact pressure and the material finish on the seal section. The contact pressure generated in this test method is only 200 to 400 MPa (30 - 65 ksi) on the loading collar and below 260 MPa (40 ksi) on the threads. This is significantly lower than the values of contact pressure on the threaded section of the connection which were estimated using FEA. In this project, the seal pressure was found to be between 689 – 2068 MPa (100 – 300 ksi) [see **Figure 2-3**]. The pressure was found to be different at two sections of the thread and

both were required to gain a full perspective of the contact pressures between the surfaces during make-up. The loading flank of the thread, i.e. on the leading edge of the thread was found to be subjected to 130 - 480 MPa (20 – 70 ksi). The cone of the thread was subjected to less than 130 MPa (20 ksi). Therefore CoF data obtained using this method may be representative of that for the cone and thread sections, but questionable for the seal due to the discrepancy in the contact pressure.

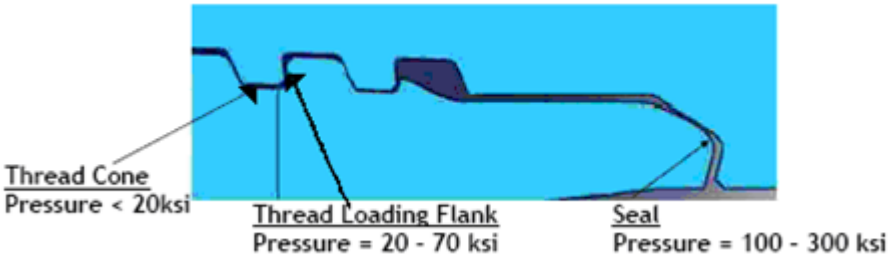

Figure 2-3: Locations of pressure in a premium tubular connection

2.1.2.4 Conical pin on box

Conical pipe-on-box tests with coincident tapers were used by Carper et al **(83)** to measure the friction coefficient. It is a line contact in circumference of the conical surfaces. The box was rotated whilst the normal load was increased linearly. CoF was obtained by measuring the axial force and the torque applied. To produce the necessary contact pressure, a large axial force was required and this meant that a large experimental device was needed. This is perhaps the most representative of the contact conditions in the seal but the cost is comparable to that of full size tests. Therefore the range of tests is very limited.

2.1.3 Design and construction of the test rig

Since CoF is dependent on the system being tested, it is imperative that the experiments carried out are representative of real contact conditions. The main parameters of interest are the velocity, sliding distance, contact pressure, surface conditions and lubricant which all have the potential to cause changes to CoF obtained.

Similar to work by Le et al **(73, 84)**, a reciprocal sliding test rig was designed and manufactured to obtain a sliding friction measuring device, capable of achieving a large range of pressures to simulate various sections of the surfaces in contact during the make-up of a premium tubular connection. As shown in **Figure 2-4**, two samples of pre-determined material type and surface finish were held in holders positioned perpendicular to one another. A circular contact between two cross cylinders is generated. The combinations, which include the sample types and lubricants used, were based upon circumstances that represent the actual field conditions which premium connections experience during oil production. The samples slide over one another linearly starting with a minimum pressure 0 MPa (0 ksi) and moving to maximum pressure (determined by angle of tilt table and type of samples) before returning back to zero. This was done using a motorised table which was controlled by a specifically written program in Aerotech Soloist, detailed in Appendix 1. **Figure 2-5** shows the configuration of the samples at the minimum and maximum pressures.

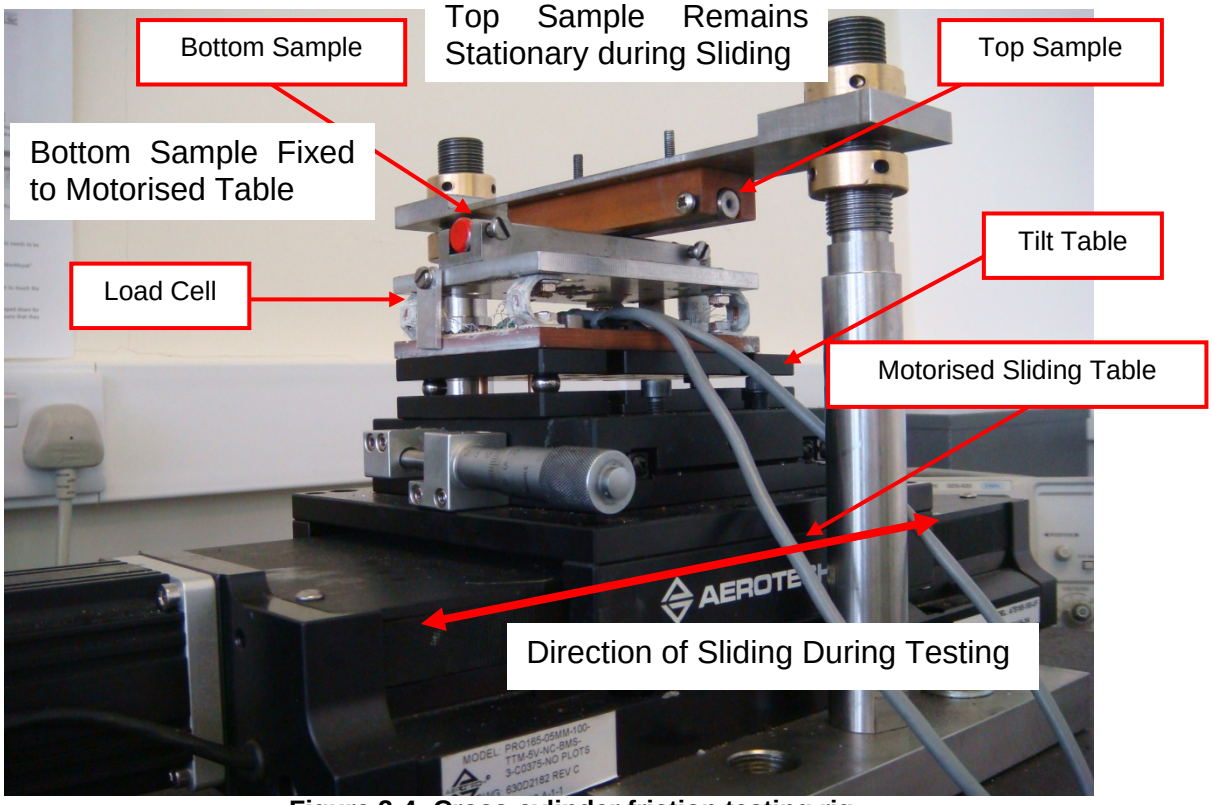

Figure 2-4: Cross-cylinder friction testing rig

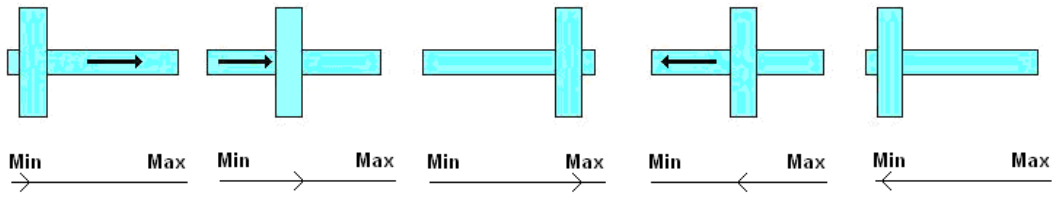

Figure 2-5: Sample configuration at minimum and maximum pressures

The test rig is comprised of a load cell, tilt table and motorised sliding table. The tilt table allows adjustment of the angle that samples are positioned to one another during sliding. The larger the angle, the higher the force and therefore contact pressure generated at the maximum pressure end of the cycle. This allowed for an easy adjustment of maximum pressure. Once the correct pressure had been obtained, the rig allowed the tilt table to be locked to

maintain the same contact pressure for future tests to ensure consistency and repeatability of testing.

Due to the large pressure range involved in a premium tubular connection, 20 MPa to 2 GPa (3 and 300 ksi), three different regimes were designed to allow the pressures to be investigated. Three sets of samples of different geometries were manufactured to represent the surfaces of the pipe-end and coupling sections of the connection. Each different regime employed a cross-cylinder configuration with curved test samples. The curved shape of the test samples meant that the contact was point contact. The 'pins' (see assembly in **Figure 2-4**) used in Regime 1 for pressures between 620 MPa – 2 GPa (90 and 300 ksi), were manufactured with a diameter of 12 mm and the 'coupon' samples (see **Figure 2-8**), used in Regime 2 and 3, were cut from actual pipe samples (see **Figure 2-5**). For Regime 2 the samples had a diameter of 120 mm and for Regime 3 samples with a diameter of 168 mm were used. The maximum pressure for both was achieved by applying a normal force of up to 500 N to the samples and load cell.

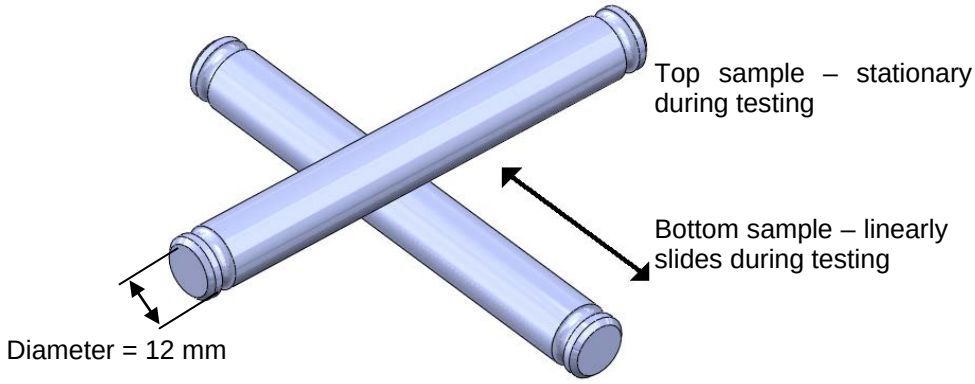

Figure 2-6: Regime 1 (P = 620 – 2000 MPa or 90 – 300 ksi) perpendicular pin test

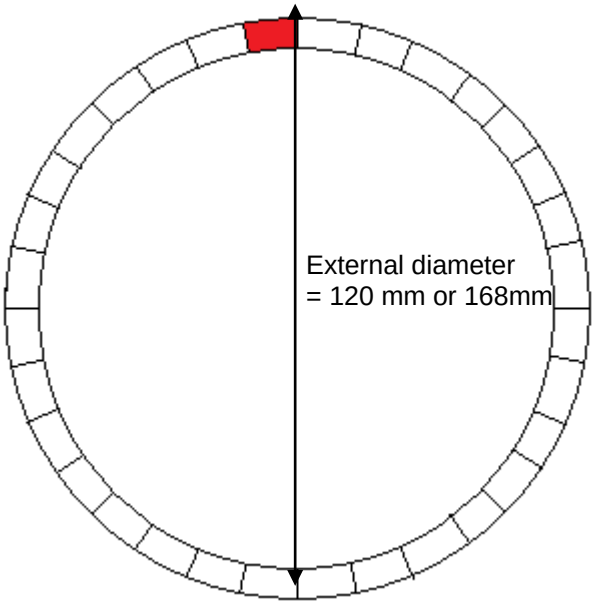

Figure 2-7: Coupon samples cut from pipe

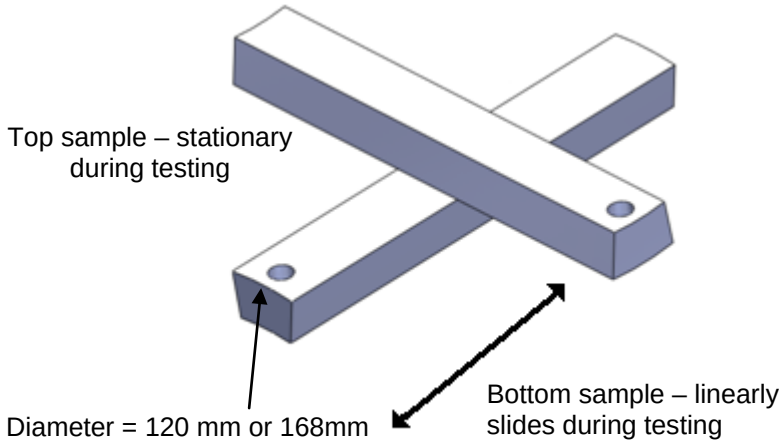

Figure 2-8: Regime 2 (P = 137 – 448 MPa or 20 – 65 ksi), perpendicular coupon-on-coupon test

2.1.3.1 Load to pressure conversions

CoF is determined by obtaining values for the normal and tangential forces when two surfaces slide against one another. To allow comparison of the friction coefficient, a value of the contact pressure is required. Hertzian contact **(1)** theory was used to calculate the contact pressure between the two samples.

In general, the pressure is quantified as the force divided by the sample contact cross-sectional area. Due to the complexity of the shape of the area of contact in the test assembly, a more complicated formula had to be used to calculate this pressure value. The two curved surfaces in contact create a shape that can be compared to a semi-elliptical form. This pressure distribution can be extended into the third dimension, and so the analysis made applicable to the contact of two spheres (according to Williams **(1)**), giving the contact pressure to be:

$$p(x) = p_0\sqrt{1 - \left(x^2/a^2\right)}$$

$$p(r) = p_0\sqrt{1 - \left(r^2/a^2\right)}, \text{ where } r^2 = x^2 + y^2 \qquad \textbf{(2.1)}$$

Where a is the radius of the contact circle, p_0 is the peak pressure, and x, y and z are Cartesian coordinates of the area of interest. W, the total load on the contact spot, is calculated using:

$$W = \int_0^a 2\pi r p(r)\, dr = \frac{2}{3} p_0 \pi a^2 \qquad \textbf{(2.2)}$$

The mean pressure, $p_m = W/\pi a^2$, and rearranged gives an expression in terms of the peak pressure.

$$p_m = \frac{2}{3} p_0 \qquad \textbf{(2.3)}$$

The deflections of the surfaces, both inside and outside the contact area (due to pressure loading) are consistent with:

$$\text{When } |r| = a \ , \ w_{z1} + w_{z2} = \Delta - \frac{r^2}{2R}$$

$$\text{When } |r| > a \ , \ w_{z1} + w_{z2} > \Delta - \frac{r^2}{2R} \qquad \textbf{(2.4)}$$

provided that $\boldsymbol{a}$ is satisfied by the equation below.

$$a^3 = \frac{3WR}{4E^*} \tag{2.5}$$

$\boldsymbol{R}$is the reduced radius of contact, as defined below, which takes the radii of both surfaces in contact into consideration.

$$\frac{1}{R} = \frac{1}{R_1} + \frac{1}{R_2} \tag{2.6}$$

The laboratory set-up with cross-cylinder coupons or pins meant that to calculate the reduced radius, the direction of the radii of both samples had to be taken into consideration. To comply with the equation, the radii of both surfaces should be in line with one another and in the same direction; this is not true for the experimental procedure as they are fixed perpendicularly. However, as $\boldsymbol{R_1}$ and $\boldsymbol{R_2}$ are of equal value, the radius of either can be used in the equation. The magnitude of the other surface, in this case $\boldsymbol{R_2}$, can be considered as being very large, i.e. infinite and therefore one of the radius values does not partake in the calculation of the reduced radius, and consequently $\boldsymbol{R = R_1 or R_2}$ and $\boldsymbol{E^*}$ is the contact modulus. The contact modulus is an expression of the elastic properties (i.e. Young's modulus $\boldsymbol{E}$ and Poisson's ratio $\boldsymbol{v}$) of both materials. The order of the materials used in the equation makes no difference to the calculation and the subscript numbers can be assigned to either surface. The simplest way to express this is in terms of the elastic modulus of the material because it is proportional to the elastic modulus for plane strain conditions. The equation below takes a combination of springs in series into consideration and uses the relationship between this and the elastic modulus to give a suitable value.

$$\frac{1}{E^*} = \frac{1 - {v_1}^2}{E_1} + \frac{1 - {v_2}^2}{E_2} \quad \textbf{(2.7)}$$

During contact, the area where the samples touch can increase (or in some cases decrease), that can result in a change in pressure. The contact pressure, $\bar{p}$, can therefore be defined by:

$$\bar{p} = \frac{W}{\pi a^2} \quad \textbf{(2.8)}$$

Table 2-1 shows the corresponding load for every pressure range using each of the test set-ups. These values were obtained using equation 2.8. As all tests were undertaken using chrome steel samples (L80), the material properties of such were used in the calculation. The values underlined are the corresponding loads required for each set-up to achieve the required pressure. As shown in the table, three different set-ups were needed in order to obtain the required pressures using measureable forces. Pressure level 3 was attained using the Regime 2 technique with the small coupon samples and large load cell; and pressure levels 4, 5 and 6 were achieved in Regime 1, using the pin-on-pin combination and large load cell. Pressures 1 and 2 were acquired using the larger coupons and a smaller load cell which could measure significantly lower forces.

Table 2-1: Pressure to load conversion

Pressure Level	Contact Pressure (ksi)	Contact Pressure (MPa)	Load (N) (for Regime 1)	Load (N) (for Regime 2)	Load (N) (for Regime 3)
1	3	20.68	0.00044	0.044	0.18
2	10	68.95	0.01643	1.64	*6.79*
3	30	206.84	0.443667	*44.37*	N/A
4	90	620.53	*11.98*	1197.90	N/A
5	150	1034.21	*55.46*	5545.84	N/A
6	300	2068.42	*443.67*	44366.74	N/A

The samples were fixed into the clamps and then assembled into the test rig; they were then lowered to allow contact with one another. They were adjusted to produce an initial zero reading for normal and tangential forces, however the two samples were in contact. Soloist IDE provided by Aerotech Inc. is a PC controller program which instructs the movement of the motorised table. It was utilised to provide linear travel of the table which created sliding between the two test samples. The tilt table provided a varying angle of incline between the sample holders, which altered the load exerted on them. As the motorised table moved linearly, the load increased along the sample (as shown in **Figure 2-9**) generating a tangential force that was measured using a custom built load cell. CoF was calculated using the equation below where $\boldsymbol{F}$ is the frictional (or tangential) force and $\boldsymbol{N}$ is the normal force acting perpendicular to the direction of sliding.

$$\boldsymbol{CoF} = \frac{\boldsymbol{F}}{\boldsymbol{N}} \qquad \textbf{(2.9)}$$

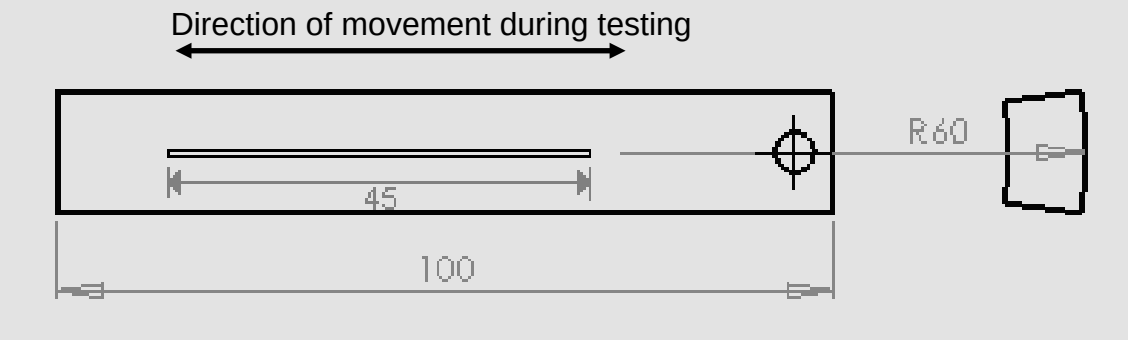

Figure 2-9: Sample length

To achieve the required pressures, loading adjustment from 0 to 500 N was set. The manual stage could be adjusted linearly so that the bottom sample clamp position could be moved. This allowed several tests to take place on the same sample (see **Figure 2-10**). For each peened sample, three tests could be undertaken which allowed a greater amount of data to be obtained without increasing the cost of the project.

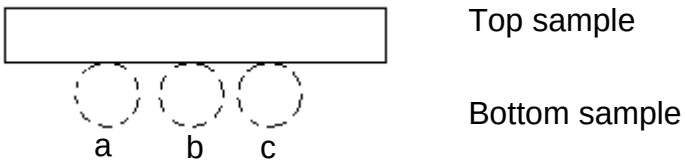

Figure 2-10: Schematic of test apparatus when adjusting the location of contact for multiple testing

For each pressure range, a sliding distance was calculated to ensure that the maximum force necessary was reached. This length was calculated to be 45mm which generated a maximum force of 500 N.

As the pressure range of 20 – 2000 MPa (3 – 300 ksi) proved too large for one sample configuration, three separate regimes were used to generate the required pressures. The first regime achieved the highest range of pressures (see configuration in **Figure 2-11**) which were associated with the connection

seal. This used a pin-on-pin arrangement and pressures between 206 – 2000 MPa (30 – 300 ksi) [Regime 1] were generated using a normal force of 5-500 N. Following high pressure tests, it was found that the test data was only valid and reliable for pressures between 620 – 2000 MPa (90 – 300 ksi) due to the initial period of acceleration of the motorised table. This unreliable residual strain was removed from the results before plotting CoF graphs. The tilt table provided a variable incline for the horizontal surface of the load cell. Test pins/coupons were placed in a sample holder perpendicular to one another; the motorised table slid the samples at a right angle to create an area of contact from which CoF could be calculated.

The load cell was designed to provide both normal force and tangential force output voltages, and these were used to calculate CoF. The angle of incline of the samples altered the force exerted on the two samples during the increase in sliding distance. As the angle of incline increased, the higher end of the sample became higher up in the test set-up and therefore this meant that the force increased proportionally. The stiffness of the set-up comes directly from the strength of the load cell legs, therefore creating a method of altering the maximum allowable pressure during the testing. A larger angle of incline created a higher normal load between the two samples, allowing adjustment in the test set-up. The Aerotech motorised table with controller is capable of speeds of up to 100 mm/s and moves a linear distance of up to 45 mm (see **Figure 2-9**). For each set of tests, velocities of 3 mm/s, 15 mm/s and 50 mm/s were evaluated. The sliding distance was maintained for every test to ensure

that the maximum pressure was kept consistent. Regime 1 is representative of connection seal engagement, from initial contact to shoulder abutment **(82)**.

Regime 2 (shown in **Figure 2-8**) employed a perpendicular coupon-on-coupon configuration which produced a lower pressure range i.e. 137 – 448 MPa (20 – 65 ksi). The samples were held in clamps positioned perpendicular to one another; the view shown in **Figure 2-11** shows the set-up before any load was applied. The section of the coupon that is visible is the side that experiences the higher pressures during the test. The forces generated in this set-up were similar to that of Regime 1. However due to the larger radius of the sample and therefore larger contact area, the contact pressure range was lower (from **Figure 2-11**) and provided CoF results for pressures between 137 – 483 MPa (20 -70 ksi).

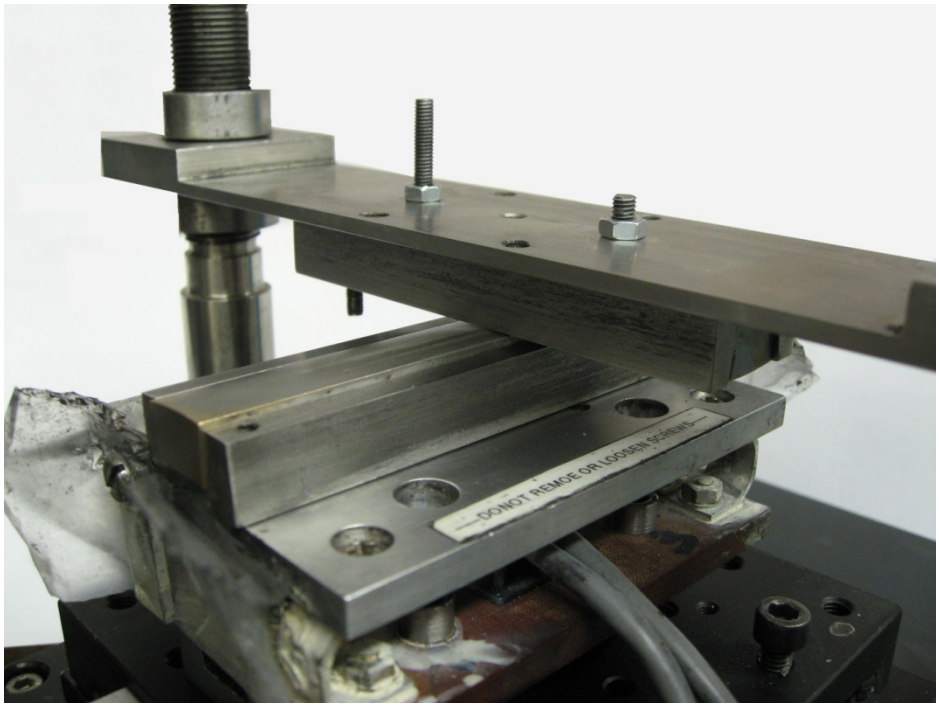

Figure 2-11: Regime 2 friction test set-up

Regime 3 used a similar coupon-on-coupon set-up to Regime 2. However, the coupons were cut from a larger diameter pipe, producing samples with a larger radius and thus the contact area between the samples during testing increased again. Although the contact pressure required between the samples was slightly larger compared with repeating Regime 2 for the very low pressures, the force that had to be applied to the sample to create such a pressure was not within the limits obtainable by the existing load cell and so another one had to be created. The new load cell had to be manufactured to produce more accurate results at very low forces and pressures. Two initial attempts were made to manufacture the load cell to withstand the required pressure range and the final design is shown in **Figure 2-12.**

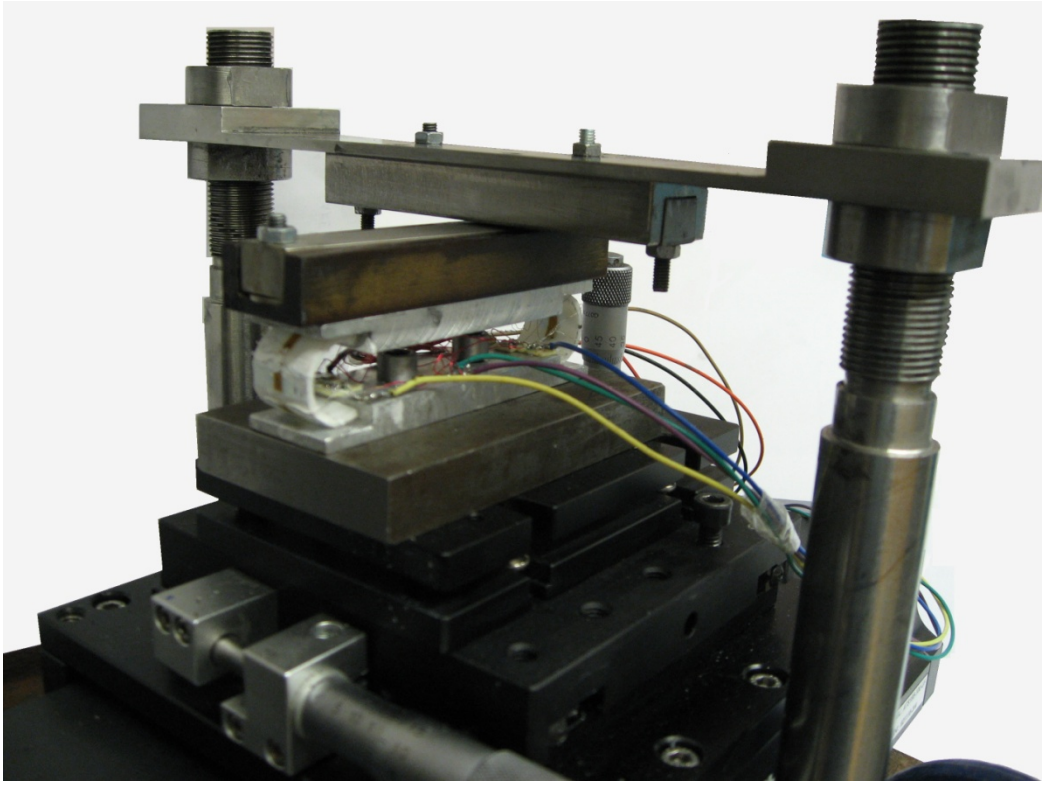

Figure 2-12: Regime 3 friction test set-up

2.1.4 Load cells

2.1.4.1 Large pressure load cell

Both load cells were of similar design. The large pressure load cell had four fixing points, which made calibration and reducing the effect of crossover more difficult compared to the same process in the two-legged small pressure load cell. Crossover was an effect caused from minor differences in the load cell legs' thicknesses and other unavoidable defects. The crossover effect meant that even when a load was applied to the middle of the top plate, registering what should have been equal loading on each leg; different values of voltage were measured. This irregularity in values meant that something had to be done to counteract these issues and this was done during the data processing of strain gauge readings.

Both load cells consisted of an arrangement of strain gauges, which could be assembled into tension or compression depending on how the equipment was loaded. **Figure 2-13** shows the location of the eight strain gauges in the low pressure load cell, and half of the strain gauges on the high pressure one. In the case of the high pressure load cell, four strain gauges were positioned on each of the four load cell legs. When a normal load was applied to top plate, gauge (a) stretched in tension and gauge (b) experienced a value of equal magnitude of compression in the opposite direction. This meant that in order to verify that the geometry and position of the legs was accurate, the two should be equal in magnitude and opposite in sign when a force was applied to the top plate. This extends to the other legs too as it should experience the same loading on gauges (e) and (f), provided that the weight was positioned in the middle of the

load cell. These strain gages were arranged in one full bridge to measure the normal force. Gauges (c) and (d) were used to measure the force in the tangential direction when the linear motor applied a force in the horizontal direction. In this case, gauges (c) and (d) recorded equal magnitude and opposite sign values of strain as did gauges (g) and (h). Therefore strain gage c, d, g, h were arranged in another full bridge to measure the tangential force. The same can be said of the other set of gauges on the two extra legs on the large pressure load cell. As the bottom plate was held down, the top section was distorted by the movement.

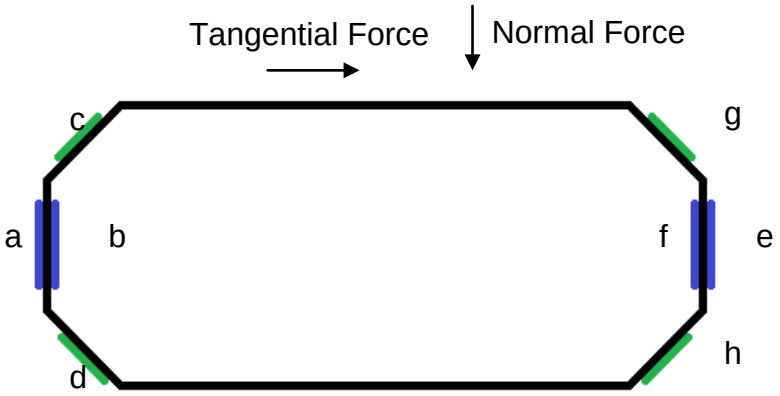

Figure 2-13: Load cell strain gauge positions

Before manufacture, an initial assessment had to be done to ensure that the load cell could withstand the forces required to achieve the contact pressures between the surfaces. This evaluation also ensured that the load cell was produced from an appropriate material. To do this, Finite Element Analysis performed using ANSYS and SolidWorks predicted the strains involved when applying the force to the top surface of the leg. It was also imperative that enough strain was produced in the load cell to ensure that it would register a response to the testing process. The load cell was chosen to be made from

Dural, an aluminium, copper and magnesium alloy. Its benefits included high strength and low weight composition.

For the large pressure load cell (see **Figure 2-14**), a force was applied to the face of the leg. For these initial tests, it was assumed that the force was applied to all four legs equally and therefore the maximum 500 N force was split between the four legs evenly. The 125 N force was applied evenly on the surface and the maximum strain on the central node (where the strain gauge was applied) was 2.414 µ-strain.

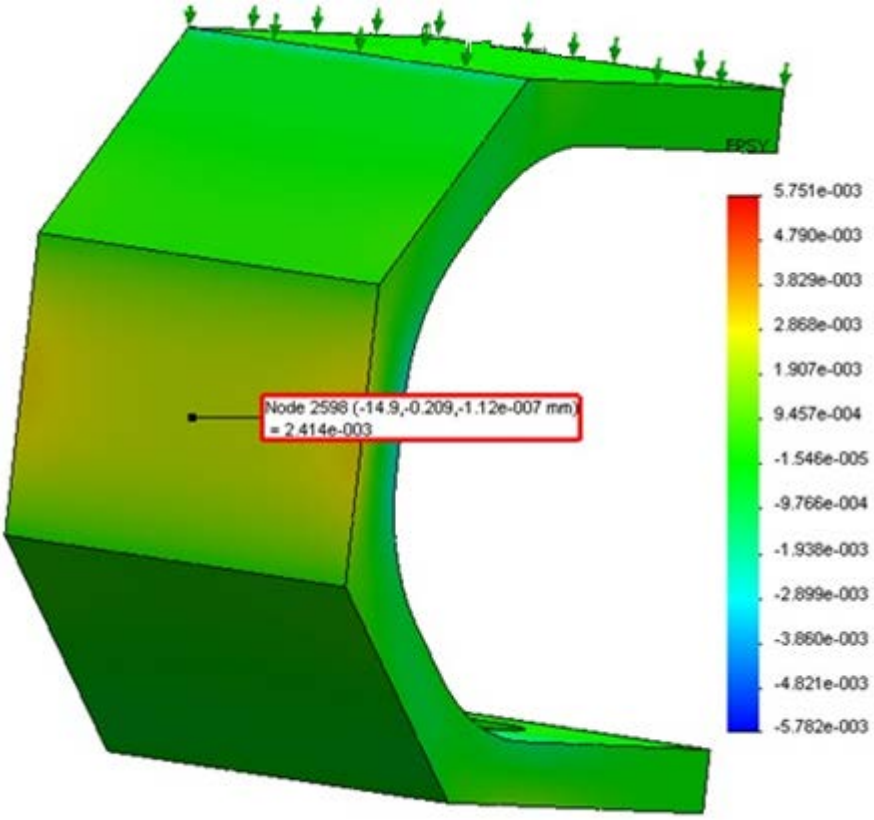

Figure 2-14: Analysis of the load cell generated in SolidWorks

The results are similar to the simple calculation findings. Dural has a modulus of elasticity of 73 GPa and at the maximum force (i.e. of 500 N split evenly

between four legs), the contact pressure for each leg was calculated to be approximately 200,000 Pa, and the strain on each leg at maximum pressure was 2.73 μ-strain. This is based on four legs with contact area between leg and top plate of 25 mm by 25 mm.

2.1.4.2 Small pressure load cell

The first attempt for obtaining low pressures was to use a more delicate test rig, machined from a single section of Dural as a shown in **Figure 2-15**. This was produced from a very high quality CNC machine, however the thickness of the legs and the effect that crossover had on the output voltages, meant that this method could not be used. The load cell collaborated with the test rig effectively and the normal force could be extracted from the rig successfully, however there was a large crossover in the tangential force. This made the rig unusable because all of the legs gave inaccurate readings. It was therefore decided that the number of legs should be reduced to eliminate some of the crossover effects.

To combat the problem, two high density polyethylene half-rings were used. These were already shaped (as shown in **Figure 2-16**) and therefore were suitable, as the required load could be supported within the elastic region and did not buckle or plastically deform. The strain gauges were mounted onto the rings in a similar fashion to that of the large load cell and the rig was set up in the same way as before.

To ensure that the contact pressure between the samples was within the limits required, the largest samples were manufactured from the largest pipe

available. In an ideal situation, the pipe size would preferably have been larger. Nevertheless, the available pipe samples were deemed to be acceptable. To achieve the contact pressure range between 20.68 MPa to 68.9 MPa (3 and 10 ksi), a force of 0.18 to 6.79 N was applied to the surface.

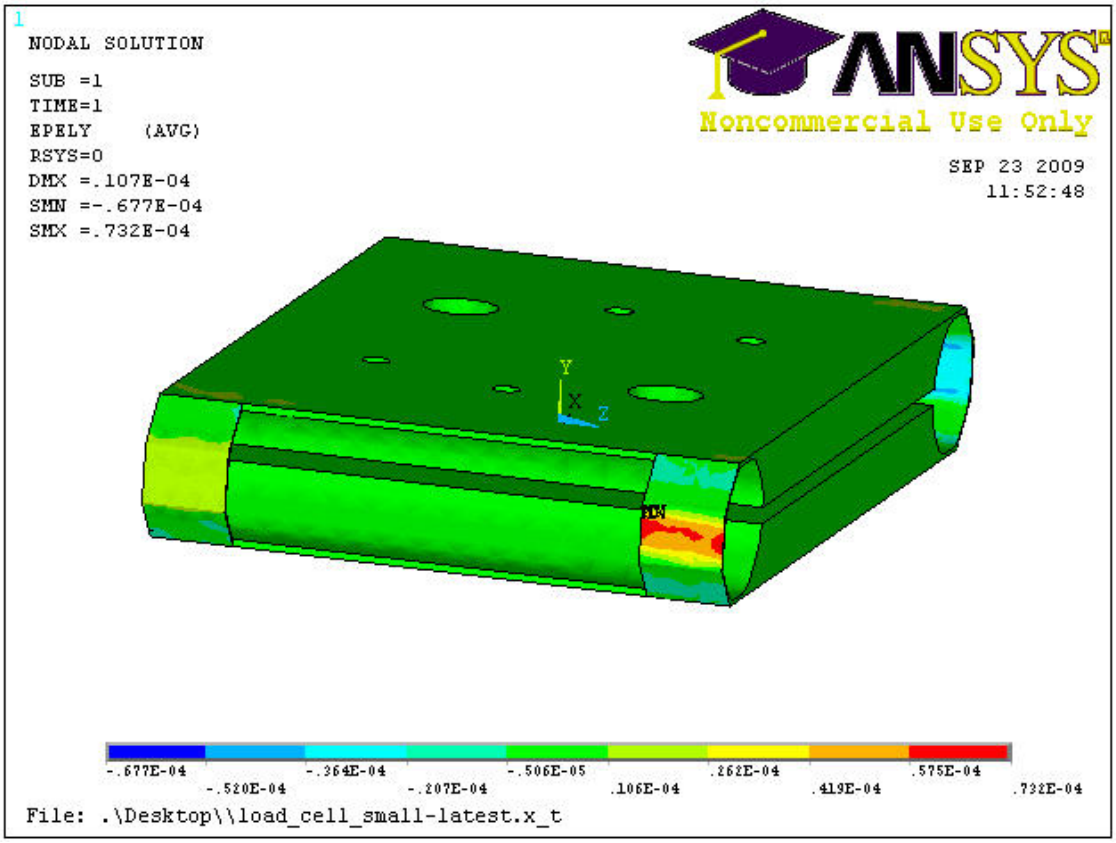

Figure 2-15: Regime 3 - attempt 2

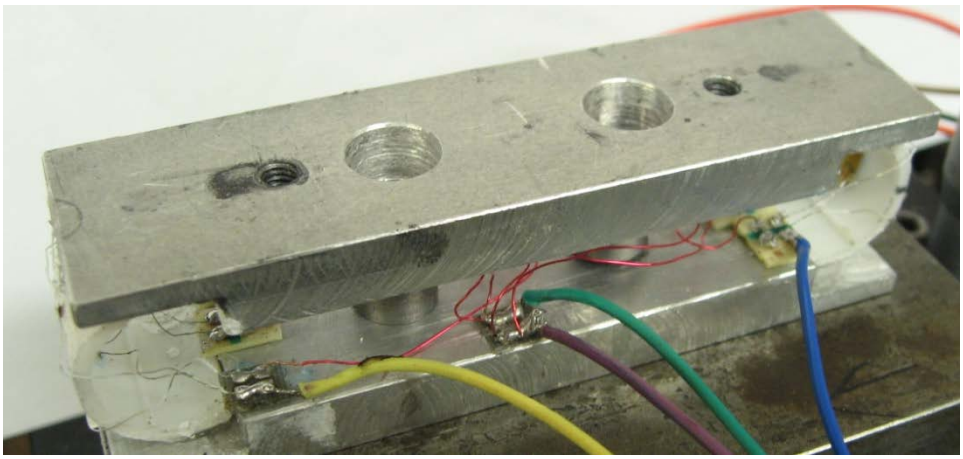

Figure 2-16: Small pressure load cell

2.2 Calibration of load cell

Both the normal and tangential voltages had to be calibrated separately in order to determine the forces they corresponded to. The normal force was calibrated by measuring the normal and tangential voltage outputs when a known mass was placed on top of the load cell (shown in **Figure 2-17**).

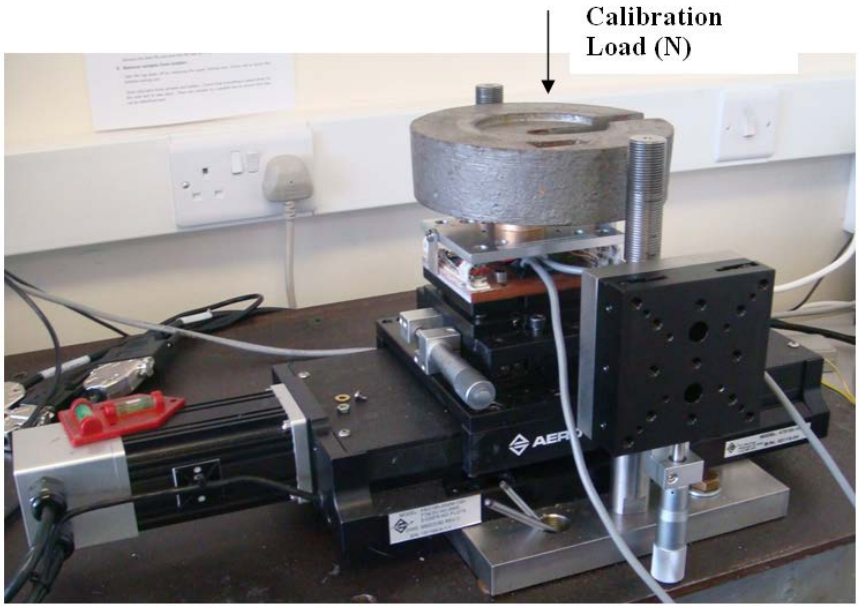

Figure 2-17: Load cell - normal force calibration set-up

If the legs of the load cell were perfectly symmetrical, applying a normal load would produce only a normal voltage, and the tangential voltage would be zero at the central position (a) on the top plate. However, even with the high precision machinery used to manufacture them, the legs still harnessed unavoidable imperfections. A very slight difference in one leg causes a crossover between the normal and tangential forces, making it necessary that a correctional calibration factor had to be determined.

To find the calibration equation for the system, masses were placed on different positions of the load cell. If the legs had been identical, the tangential voltage would be equal at positions b-d (left) and c-e (right) on the load cell (shown in **Figure 2-18**). However as the two values were different, the discrepancy needed to be taken into consideration. The normal voltages were measured for a number of different masses, and this allowed a correctional factor to be determined.

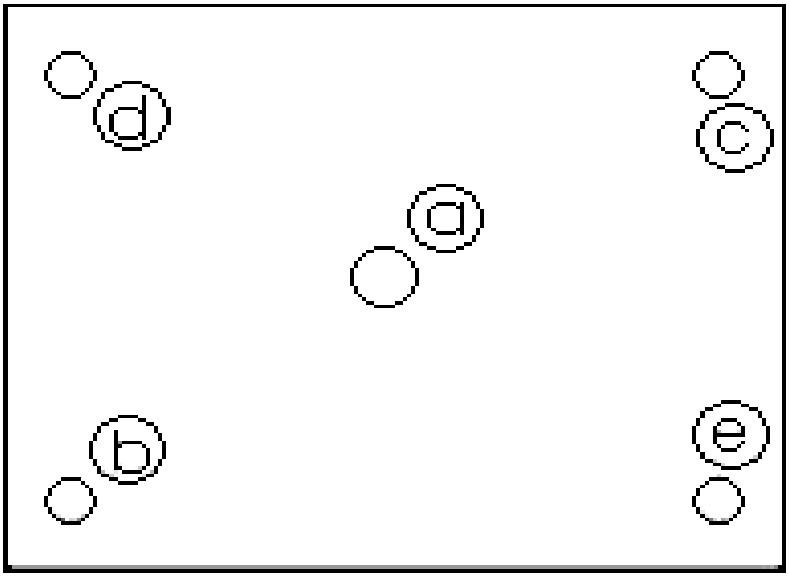

Figure 2-18: Load cell – top plate loading locations

On the top plate of the load cell, the masses were applied to the centre of the face and the four corners. The weight (N) against the voltage (V) was plotted for the three positions, as was the crossover for the system. As shown in **Figure 2-19**, the crossover increased as the weight was shifted from the right to the left-hand side of the load cell.

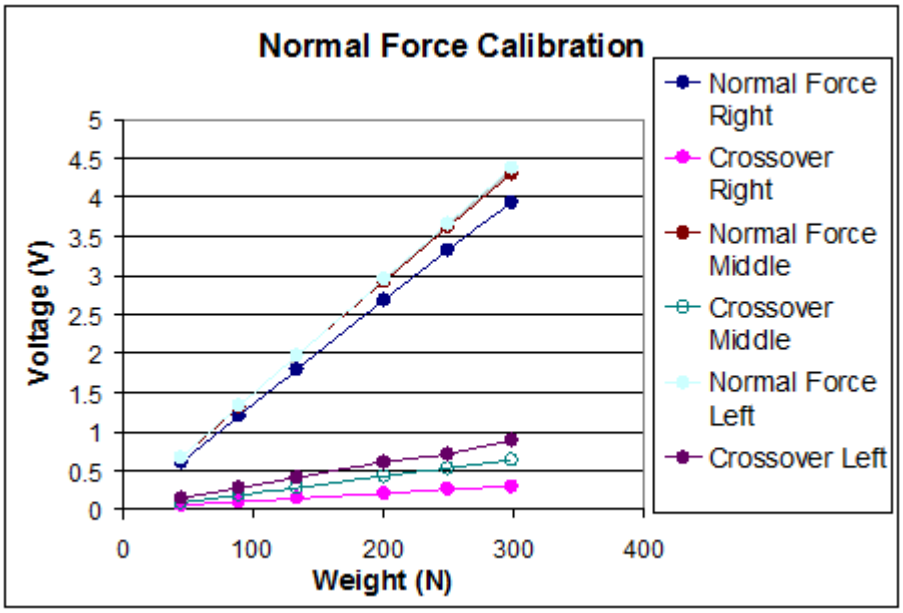

Figure 2-19: Normal force calibration and crossover to tangential

The curves were fitted using linear relationships to extract the reciprocal of the slope $\boldsymbol{K_n}$, so that the normal force could be calculated from the output voltage using the following equation:

$$\boldsymbol{F_n = K_n V_n} \qquad \textbf{(2.10)}$$

Where $\boldsymbol{F_n}$is the normal force, and $\boldsymbol{V_n}$ is the voltage reading on normal channel.

Figure 2-20 shows the variation of the conversion factor $\boldsymbol{K_n}$ along the sliding distance. The quadratic fit for the conversion factor was determined to be:

$$\boldsymbol{K_n = 10.164\left(s/L\right)^2 - 17.856\left(s/L\right) + 76.221} \qquad \textbf{(2.11)}$$

Where $\boldsymbol{s}$ is the coordinate along the sliding direction, and$\boldsymbol{L}$ is the sliding distance of each stroke.

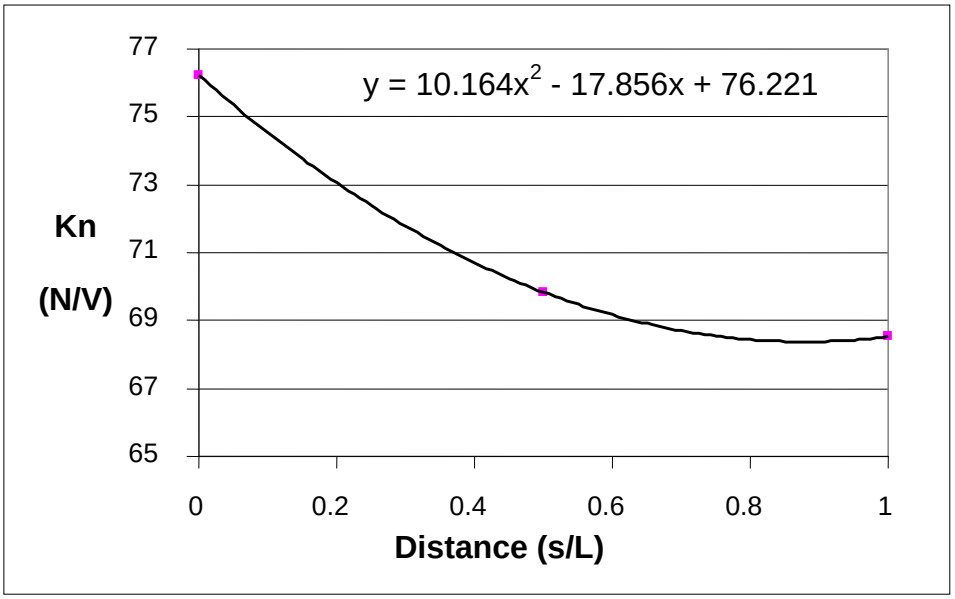

Figure 2-20: Variation of normal force correction factor along sliding distance

The same process (see **Figure 2-21**) was repeated to obtain the crossover factor $\boldsymbol{K_c}$ which is related to the location along the sliding direction:

$$\boldsymbol{K_c = -0.0009\left(s/L\right)^2 + 0.0028\left(s/L\right) + 0.0009} \qquad \textbf{(2.12)}$$

This was used to work out the crossover voltage $\boldsymbol{V_c}$; using the crossover factor $\boldsymbol{K_c}$, sliding distance $\boldsymbol{s}$ and normal force $\boldsymbol{F_n}$ predetermined by the calibration process.

$$\boldsymbol{V_c = K_c F_n} \qquad \textbf{(2.13)}$$

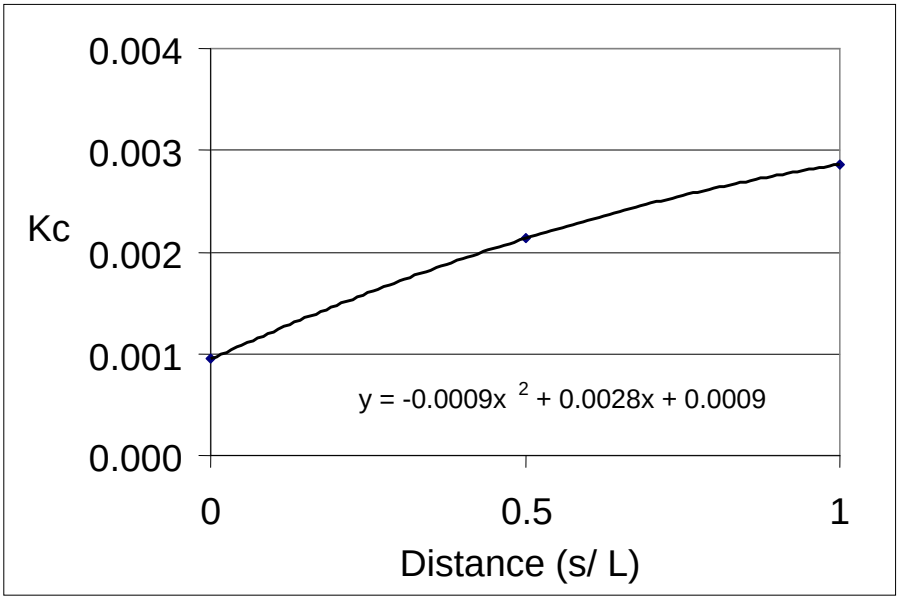

Figure 2-21: Crossover to tangential output voltage

These calibration factors were applied to the data obtained from testing, providing a credible and reliable set of results.

To calibrate the tangential force, the setup shown in **Figure 2-22** was used. The load cell was held vertically so that the weight could be applied in the tangential direction. This meant that the load applied was parallel to the top plate of the load cell. This calibration process was similar to that of the normal component, however in this case the masses were suspended from a rope attached to a screw on the load cell. The mass was suspended from two locations on the top plate to record the difference in the voltage reading, and therefore the effect of positioning in the tangential direction. Similar to the normal voltage procedure, when the tangential load was applied, a voltage in the tangential was registered.

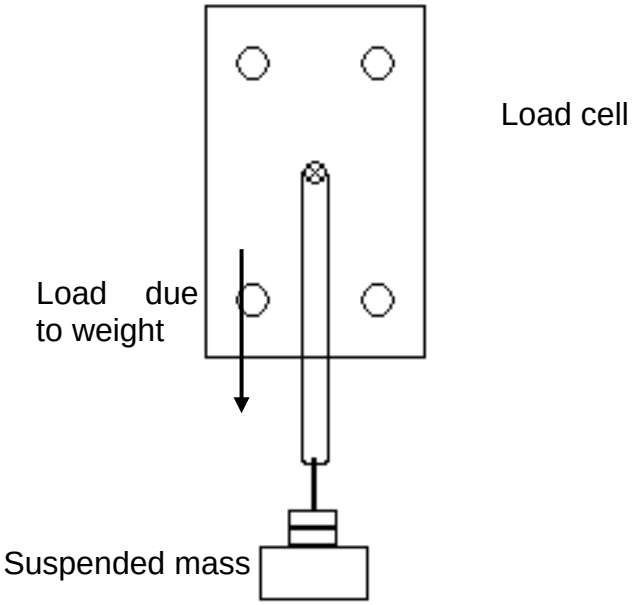

Figure 2-22: Schematic of tangential force calibration set-up

As shown in **Figure 2-23**, the slope of the linear range (up to 100 N) was 0.11 so that the reciprocal of the slope was $\boldsymbol{K_t = 9.05}$ $(\boldsymbol{N/V})$.Taking into account the effect of crossover from normal force, the tangential force was derived using the forumla:

$$\boldsymbol{F_t = K_t(V_t - V_c)} \qquad \textbf{(2.14)}$$

Where $\boldsymbol{V_t}$ is the voltage reading on the tangential force channel, and $\boldsymbol{V_c}$ is the crossover voltage from the normal force channel.

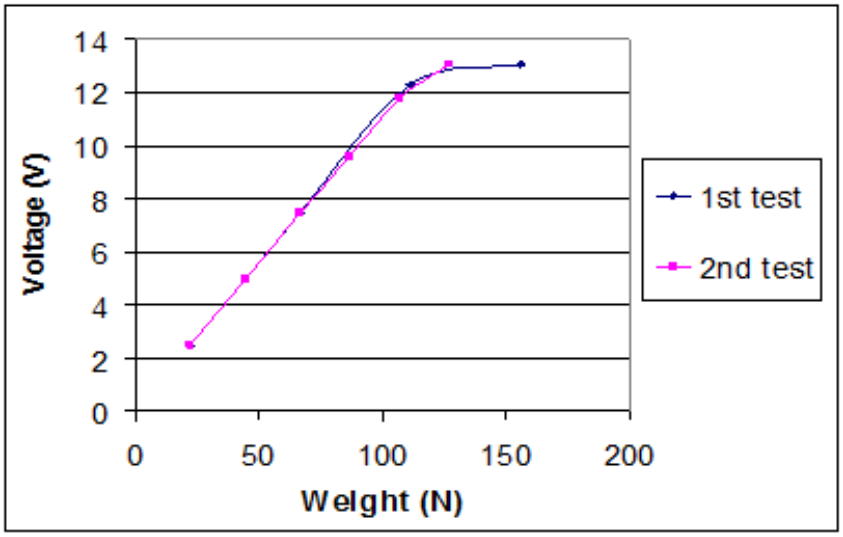

Figure 2-23: Tangential force – calibration function

2.3 Peening of samples

2.3.1 Peening process

Peening, or shot blasting, is carried out on samples to produce an isotropic surface. This ensures that the material topography is equal in both directions. The pipe section of the connection is peened during the manufacturing process. The type of peening media used depends on the country where the process is being performed. The samples used in the friction test were peened to the same standard as that of the actual pipe-end surface. Zirconia ceramic, stainless steel and aluminium oxide peening media were used to allow representation of materials used in the respective parts of the world.

The current method of shot blasting does not have a predetermined duration, position or direction associated with it and therefore there are inconsistencies in the finishing method. Shot blasting is undertaken in a chamber where the

peening media is blasted at the surface using a moveable gun. The distance from the gun's position to the surface that is being treated is not defined, and therefore it can be presumed that there are discrepancies between different operators' techniques. Slight changes in blasting angle or distance can alter the way that the beads impact the surface. In the case of the ceramic peened surface, a direct hit will produce a more isotropic pattern than that of an askew one. Work by Higounenc **(85)** shows the complexity of the effect of the shot peening characteristics on the final surface. There are various ways in which the peening process can be undertaken and this can result in a number of different features on the surfaces of the samples. It is therefore beneficial to ensure that the peening process is standardised to ensure that all samples are as similar as possible. This is difficult however because the angle of peening, distance between gun and sample, blasting velocity of media and, most importantly, the length of time that samples are peened for, all effect the surface quality.

2.4 Lubrication in friction tests

During the make-up process, a lubricant is applied to the two surfaces in contact. This is done with the intention to provide sufficient sliding between the two surfaces, and to prevent galling from occurring. The lubricant used is dependent upon the material type of the pin and coupling surfaces. A comparison between three different lubricants was completed during the project. The main lubricant (Lubricant A) under investigation is a proprietary synthetic formula which was specifically designed to prevent galling of surfaces during make-up. The other two lubricants are of industry standard. Lubricant B

contains large metal particles such as lead and nickel and the other, Lubricant C, is an environmentally friendly substance which contains PTFE particles. It is noted that Lubricant C did not stick well to the surfaces, and was easily removed during testing.

Table 2-2: Properties of Lubricants

Properties	Lubricant A	Lubricant B	Lubricant C
Base oil	Lubricating Greases, Calcium Hydroxide	Lubricating Greases	Petroleum distillates, Calcium Compounds
Viscosity	50,000 cP (50 Pa.s)	N/A	N/A
Additives	Non-metallic nano-particles	Metallic particles (Inc. graphite, lead, zinc, copper)	Non-metallic particles (graphite)
Penetration	N/A	310 – 340	300 – 340
Weight/ Gallon	N/A	15.8 lbs/gallon	10.4 lbs/gallon

2.5 Testing Procedure

To provide a suitable representation of the two surfaces of the connection during the make-up process, three cycles of the two samples sliding past one another were completed. Due to the shape of the two surfaces being opposite conically, there are limitations to where lubricant can become trapped in comparison to the helical shape in the thread of the real connection. Therefore the lubricant used in each experiment was reapplied between cycles to ensure that the full effect of lubrication was felt for each section of the test.

Three different lubricants were used during testing; however the main results were obtained using Lubricant A. This allowed a range of results to be attained to provide a comparison for changes in make-up velocity, contact pressure, surface roughness and peening media used to alter the surfaces.

Lubricant A was designed to be safer to use and more environmentally friendly. Its primary function was galling resistance which, when combined with the bronze plated chrome steel coupling, reduces the likelihood of defects on the surface triggering leaks. The lubricant contains PTFE particles, has corrosion protection properties, and also removes the need to clean the surfaces between make-ups and break-outs.

Lubricant B and Lubricant C were both commercial industry lubricants. Lubricant B was the most widely used but contained harmful particles including lead and nickel. It was generally used with a copper plated chrome steel coupling and a peened chrome steel pin-end pipe similar to the test set-up of Lubricant A. The stiction properties of Lubricant B were relatively high and it was not as easily removed from the surface compared to Lubricant C during testing. Lubricant C was an environmentally friendly lubricant with similar properties to Lubricant B, however did not contain harmful particles. There we reissues with galling of surfaces for this lubricant however, and these detriments were deemed to outweigh the benefits.

2.6 Repeatability

To ensure repeatability and comparability by using the same samples, the design of the sample holders provided the possibility for rotation of the pins and coupons in all three regimes. The design allowed three tests to be undertaken on each sample. The data from each sample was compared and collaborated to produce the final results. To ensure the tests were comparable, the two surfaces in contact had to have the original surface topography. As illustrated in Chapter 3, the initial stroke during the test removed the peaks from the surface. This higher surface roughness value induced a slightly greater CoF compared to that of the final cycles where the surface was smoother. This meant that it was critical to ensure the surface roughness of all samples was comparable to allow reliable data to be obtained.

Chapter 3 Surface Measurements

3.1 Measurement of roughness of surfaces

Topography defines the features of a surface. Appreciating topography of a surface is fundamental in understanding tribology **(86)**. It is also of significant value in understanding the fatigue resistance **(87)**. Surface roughness is one of the most dominant characteristics which affects the friction and wear of a system. As it affects the surface mechanics of a set-up so significantly, measures have to be put in place to make sure it is controlled in manufacturing processes. This ensures repeatability during testing and, most importantly, maintains some kind of conformity in real-life situations where the value of CoF is imperative to the success in operation.

An object's surface roughness can be measured using various techniques, including profilometers and various types of microscope. There are numerous techniques available, and the technique deployed depends on the type of surface, the quality of roughness measurement required and primarily, the budget of the project. The most expensive methods can be extremely accurate and useful, but the expense may outweigh the benefits. Measurement can be done with or without contact between the device and the surface in question. Rough surfaces are often considered to be unattractive due to the adverse consequences of fatigue strength and wear resistance, as well as the displeasing appearance that is produced **(88)**.

3.1.1 Surface roughness measurement terms

The most common surface roughness values acquired during testing include the arithmetic average roughness ($\boldsymbol{R_a}$) and the root mean square average roughness ($\boldsymbol{R_q}$). Other notable values are the Skewness ($\boldsymbol{R_{Sk}}$) and Kurtosis ($\boldsymbol{R_{Ku}}$). The arithmetic average roughness is most commonly used to measure the roughness of machined surfaces **(89)**. It is informative for determining the difference in the height profile of a surface. It is generally used to assess manufacturing techniques. The arithmetic average surface roughness, also known as the centre-line average **(1)**, is calculated using simple statistical formulae to calculate the average height of a set of datay_i.

$$\boldsymbol{R_a = \frac{1}{n}\sum_{i=1}^{n}|y_i|} \qquad \textbf{(3.1)}$$

The root mean squared average roughness represents the standard deviation of the surface height. It is more useful for representing the optical finish of the profile. It is essential in the calculation of the Skewness and Kurtosis. The formula for calculating the r.m.s roughness value is:

$$\boldsymbol{R_q = \sqrt{\frac{1}{n}\sum_{i=1}^{n}(y_i - \overline{y})^2}} \qquad \textbf{(3.2)}$$

The Skewness and Kurtosis values are related to the root mean square roughness. The Skewness is calculated using the third root of the same expression and Kurtosis is estimated using the fourth root **(89)**. The Skewness is an accurate definition of how symmetrical the data is about the central line **(90)**. Symmetrical data has a Skewness value close to zero. The value for Skewness is used to determine how capable the surface is in carrying a load; it also shows how porous the surface is, and is good for identifying the

characteristics of irregular machining processes. The value of skew can become non-zero when the peaks of a rough surface are removed, if the troughs of the surface are not altered at the same time **(1)**. The Skew value can be calculated using the following equation:

$$R_{sk} = \sqrt[3]{\frac{1}{n{R_q}^3}\sum_{i=1}^{n}\left(Z_i - \overline{Z}\right)^3} \qquad \textbf{(3.3)}$$

Kurtosis is defined as the "degree of peakedness of a distribution" **(90)**; it defines whether the height data is peaked or flat compared to the normal distribution. Surfaces with normal or Gaussian distribution have a Kurtosis value of 3 **(91)**. The value depends upon both the peak and the tails of the distribution of height data. Kurtosis is calculated using the equation:

$$R_{ku} = \sqrt[4]{\frac{1}{n{R_q}^4}\sum_{i=1}^{n}\left(Z_i - \overline{Z}\right)^4} \qquad \textbf{(3.4)}$$

3.2 Methods of measuring the surface roughness

3.2.1 Contact methods

Contact methods of measuring roughness include using a traditional stylus profilometer and using an atomic force microscope **(92)**. Both methods use a stylus technique, where the nib of the stylus is drawn across the surface. In the profilometer method, a very low force is applied and the surface roughness is measured across one dimension, i.e. along a straight line of the surface. This method is relatively inexpensive; however the main disadvantage is that, particularly for soft materials, it can scratch the surface during testing thus changing the roughness and surface properties. These are available both as

large set-ups and handheld devices; therefore the chosen type depends on the requirements of the user. This method can be inaccurate due to the surface area of the measurement being relatively small. Depending on the overall size of the surface under investigation, the measurements it may not include all features of the surface. This technique is much more suitable for surfaces with isotropic structure and peaks and troughs of equal depth. The surface roughness value will be significantly distorted and features on some sections of the surface will not be accurately represented by the outcome value. To improve accuracy, a high number of measurements need to be taken along the surface. This can improve the precision of the result though it is very time consuming, and costs can be relatively high.

The atomic force microscope is a variation on the Binnig and Rohrer invention of the scanning tunnel microscope (STM) **(93)**. The STM uses the technique of scanning a sharp tip over a sample surface and measuring the force from the deflection of springs. This is done by applying a voltage difference to the tip to ensure that the surface and the device are close enough together. The theory is based upon "tunnelling", a quantum mechanics effect where electrons that characteristically should not have been able to move through a barrier, because the electrons have insufficient energy in them, have been able to do so. In quantum mechanics theory, electrons act as waves and therefore do not stop suddenly but peter out quickly. If the obstacle is thin enough, some of these electrons appear to be on the other side of the barrier. This phenomenon is called tunnelling. In the case of the STM, the barrier is the air between the tip and the sample. The current in the tip allows control of the distance between

sample and tip to be maintained **(94)**. As the surface heights alter, the current changes; the results of these are exhibited as an image. The output of the STM produces a height matrix of the surface which can be used to calculate the roughness of the material. The main issue with STM is that it can only be used for metal substrates. Alterations to this technique were made to produce an atomic force microscope (AFM) which could investigate any type of material.

The atomic force microscope **(95)** is a contact method which uses a similar procedure to the STM, although instead of using a current to recognise peaks or troughs it uses a probing tip. The tip is attached to a cantilever spring and the angle between the two changes to trace the shape of the surface. The tip is very fine and can react to microscopic features on the surface as it is designed to respond to atomic forces **(96)**. The device can then identify surface properties and produce a set of measurements, including the roughness values in nanometres.

3.2.2 Non-contact methods

Non-contact methods are becoming increasingly more favourable because this technique removes the possibility of damaging a surface during measurement. This technique uses optical sensors to measure the height of the asperities on a surface. Three-dimensional images are created by stacking individual two-dimensional layers on top of one another to create a replica surface. This is executed by the device automatically and thus when reassembling the layers together, the risk of human error is reduced. This type of measurement takes longer than the contact types, however within one reading the entire area of the

surface is recorded. To do the same thing using a contact method would be far more time-consuming, and the user of the device would have to locate the next position of every line. By using only a two-dimensional device, there is a chance that important sections of the surface could be missed out. The main disadvantages of the three-dimensional method are the expense and maintenance of the machine. Regular checks need to be done to maintain the accuracy and the replacement of essential lenses, should they become damaged, have large costs associated with them.

Laser scanning confocal and optical confocal microscopy are two of the most common methods of non-contact profiling. They each have similar techniques, however they use different light sources and receivers to create the image of the surface and to store the data. The method used most commonly depends on the accuracy required from the images, the types of samples being investigated and, primarily, on the budget. Similar to other types of three-dimensional microscopy, a confocal microscope recreates an image of the surface point by point **(97)**. The word confocal means "having a common focus or foci" **(98)**. It is where the device focuses on only one common point and rejects the background 'noise' from outside the focal plane. To create the same focus point, the pinhole only allows certain light beams through onto the detector (shown in **Figure 3-1**). The laser confocal method **(99)** uses a laser beam and a detector which has a pinhole in front of it. In contrast to a typical microscope, where the device observes as far into a surface as it can; the confocal microscope perceives an image one layer at a time. The depth of each layer is determined by the user. The laser is shone onto a beam splitter, and

this light is shone onto a focal plane. The beam then projects back into the direction of the pinhole and only light which is in focus is detected. This detected light is then processed and an image of the required surface is created. As the "image" is a matrix of surface heights, other useful values can easily be obtained from it. This technique is useful for acquiring sharp images with fine detail because there is no unfocussed light impairing the image quality.

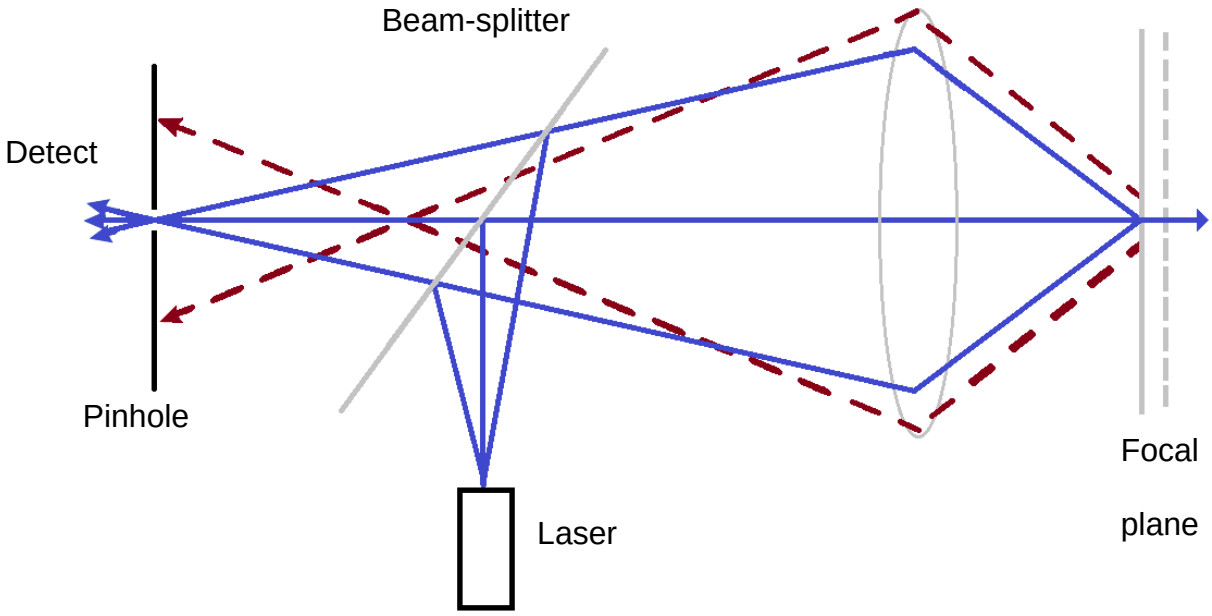

Figure 3-1: Confocal laser microscope (97)

A Scanning Electron Microscopy (SEM) creates an image of the surface using high-energy electrons. A beam of high-energy electrons are directed at the sample and each type of material reacts to the electrons differently, giving off a range of signals. It is these differences in electron reaction which allow the user to establish which element types are present. This technique is used to gain more information about the surface quality and structure (topography), chemical make-up, and crystalline structure of the material. Although this method has

many advantages, the surface roughness cannot be measured using the device. The accelerated electrons contain a considerable quantity of kinetic energy and when these hit the sample they slow down, producing a number of signals which can be picked up by the detector. Signal types include secondary electrons, backscattered electrons, cathodoluminescence, auger electrons and characteristic x-rays **(100)**. During the SEM process (**Figure 3-2**), electrons are blasted at the anode using an electron gun and these electrons pass through the anode, directing them onto the magnetic lens. Current is applied to the magnetic lens, creating a magnetic field. The electron beam passes through the spinning coils and electron detector onto the sample. The beam can either pass through the sample, missing all atoms within; collide with sample electrons to create secondary electrons; or meet the nucleus of the sample atoms, producing backscattered electrons. Each type of material produces a different number of backscattered and secondary electrons, and the detector counts this to identify the material type in the sample. It should also be noted that SEM imaging is a non-destructive testing process, i.e. there is no reduction in sample volume after testing; the testing process has to be undertaken in a vacuum.

3.3 Surface roughness measurement techniques

The value of CoF in a system depends highly on the characteristics of the contacting surfaces. These contacting surfaces are dependent on the surface roughness value, therefore it was important to ensure that this parameter was kept constant during the tests. The roughness of each sample was measured to ensure test consistency.

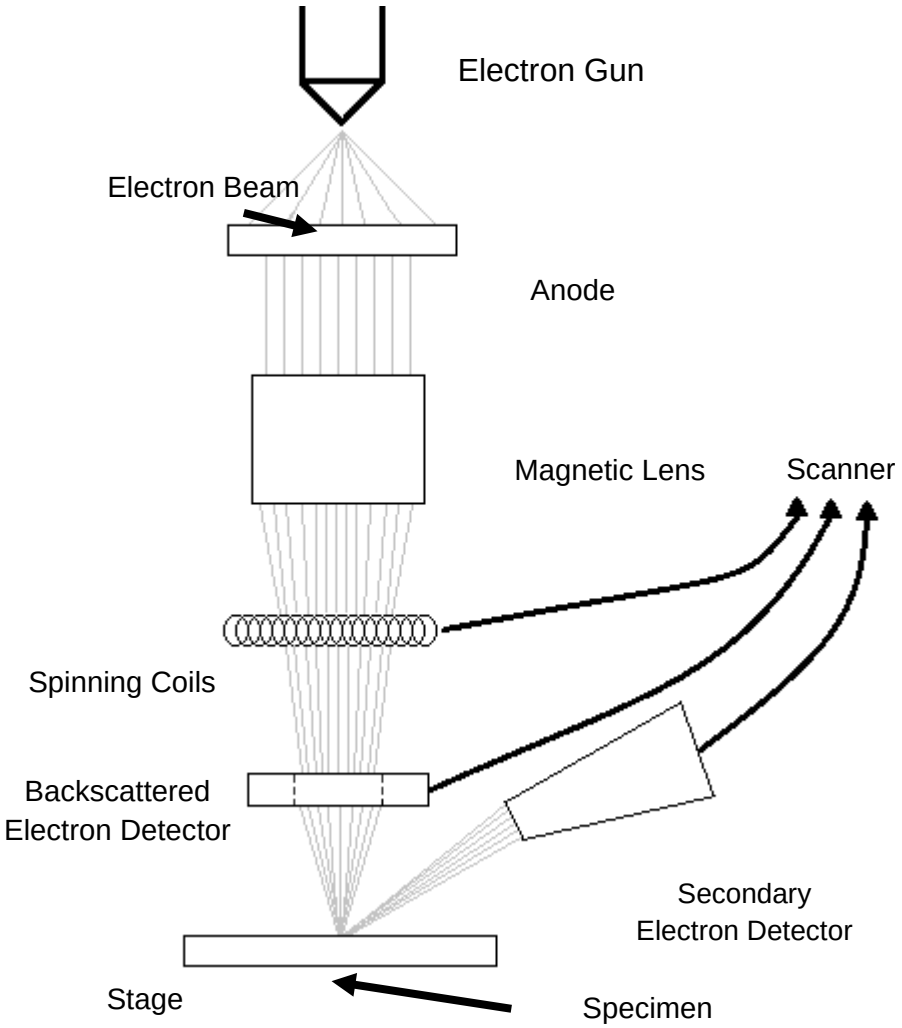

Figure 3-2: Scanning Electron Microscope set-up (re-drawn from(101))

3.3.1 Two-dimensional roughness measurements

3.3.1.1 Veeco Dektak Profilometer

The initial surface roughness values were recorded using a Veeco Dektak profilometer. Veeco's Dektak^3 ST Surface Profiler (shown in **Figure 3-3**) was used to measure the surface roughness of all test samples prior to testing. Before the test samples were placed into the friction and wear rig, nine measurements were taken on each surface to obtain an average for each sample. It was assumed that the value of surface roughness made a difference to CoF. Therefore the roughness of each surface was measured prior to testing

so as to reduce the effect of external influences. Any samples that had a roughness value outside the given tolerances were re-machined and/or re-coated/re-plated, and rechecked. The main disadvantage of the Dektak was that it was very outdated. The limited capability meant that the outputs were restricted to arithmetic average roughness and root mean square roughness. The measurements were only performed in two dimensions and Kurtosis and Skewness were not calculated. In order to enhance the accuracy, several measurements had to be taken across each sample. In the three-dimensional roughness measuring devices, an area of the surface is measured; as opposed to a line being measured in two-dimensional tests. This means that it is much easier to miss out features of the sample if two-dimensional test is being used. As with all projects, there are limitations to the budget. Therefore all available equipment was used to obtain the most accurate test results.

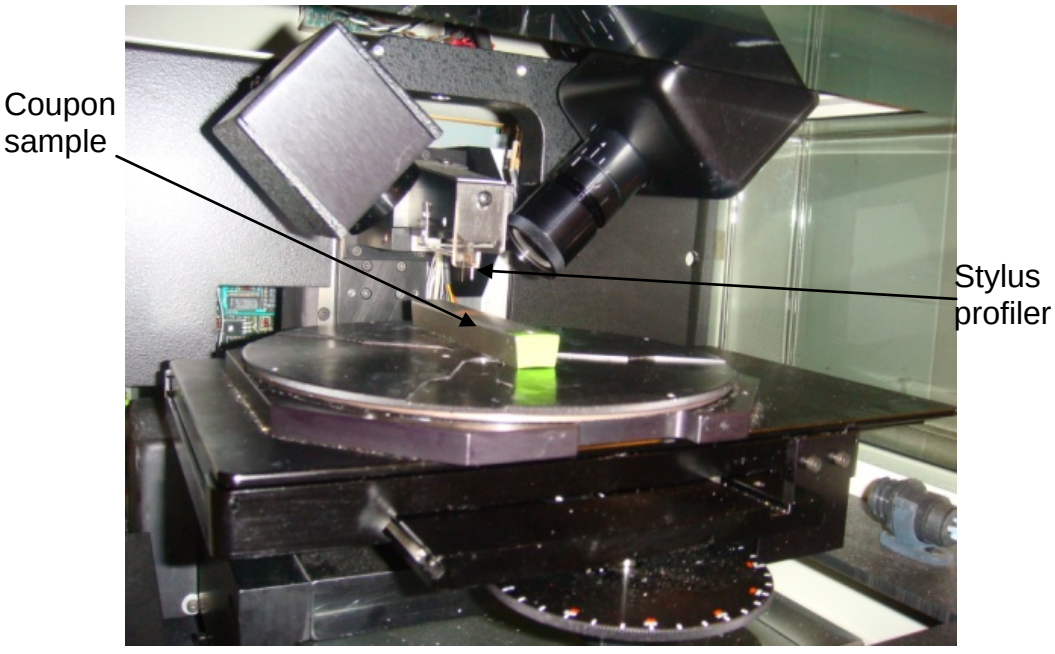

Figure 3-3: Veeco Dektak surface profilometer

3.3.1.2 Brown and Sharpe handheld Pocket Surf 3

Surface roughness values were measured on premium tubular connections in HES using a Brown and Sharpe handheld profilometer (shown in **Figure 3-4**). Test samples were manufactured to represent the roughness which corresponded to the real connection. This handheld profilometer was a more compact and portable version of the Dektak. It used the same contact method to trace the profile of the surface. Measurements were only available in two dimensions, these being in one dimension along the surface and the height profile of the surface. The distance along the sample was much smaller than that of the Dektak, thus it measured less of the profile. The Pocket Surf 3 gave outputs of arithmetic average roughness ($\boldsymbol{R_a}$), maximum roughness depth ($\boldsymbol{R_{max}}$) and the average maximum height of the profile ($\boldsymbol{R_z}$). It did not have the capability to produce the root mean square average roughness, and therefore Kurtosis or Skewness. Consequently, it was only the arithmetic average roughness that was comparable with the values taken from the Dektak.

Figure 3-4: Pocket Surf 3 (Brown & Sharpe)

3.3.2 Three-dimensional roughness measurements

For that reason, a more accurate three-dimensional profile of the surface topography needed to be made. This was initially done using the Zygo Interferometer (OMP-0347K shown in **Figure 3-5**) in the University of Cambridge, and more recently using the Olympus LEXT Laser Confocal Microscope in Plymouth University.

Optical interferometry is the study of measuring distances using the interference of light waves. Interferometers are very precise, accurate machines which use a light source and mirrors to create an image of the surface profile. The output is a measure of the interference. A beam is split into two halves and an optical light is directed at a piece of glass coated with silver (known as the beam-splitter); half of the light passes through and half reflects back. The silver coated glass material acts as a cross between a mirror and a piece of glass. One beam shines onto a mirror and then onto a screen or camera and the other beam shines on or through the surface being measured then onto a second mirror and back through the beam splitter, and finally back to the same screen or camera.

Due to the shifting distance and direction that the second beam travels to the first beam, it becomes out of phase with the first beam. The two beams meet up on the screen or camera and here they interfere with one another. Dark and light areas are produced from the phase difference between the images. Light areas are created at sections where the two beams have been added together (which is defined as constructive interference) and dark areas are created where the beams have been subtracted from each other (destructive

interference). The pattern produced from the interference data provides the information that can be accurately measured. One disadvantage of the interferometer is that it gives the best results and images when the material is shiny. Duller materials, particularly the manganese phosphate bathed carbon used in some of the tests, do not generate as good an image when compared to other surfaces.

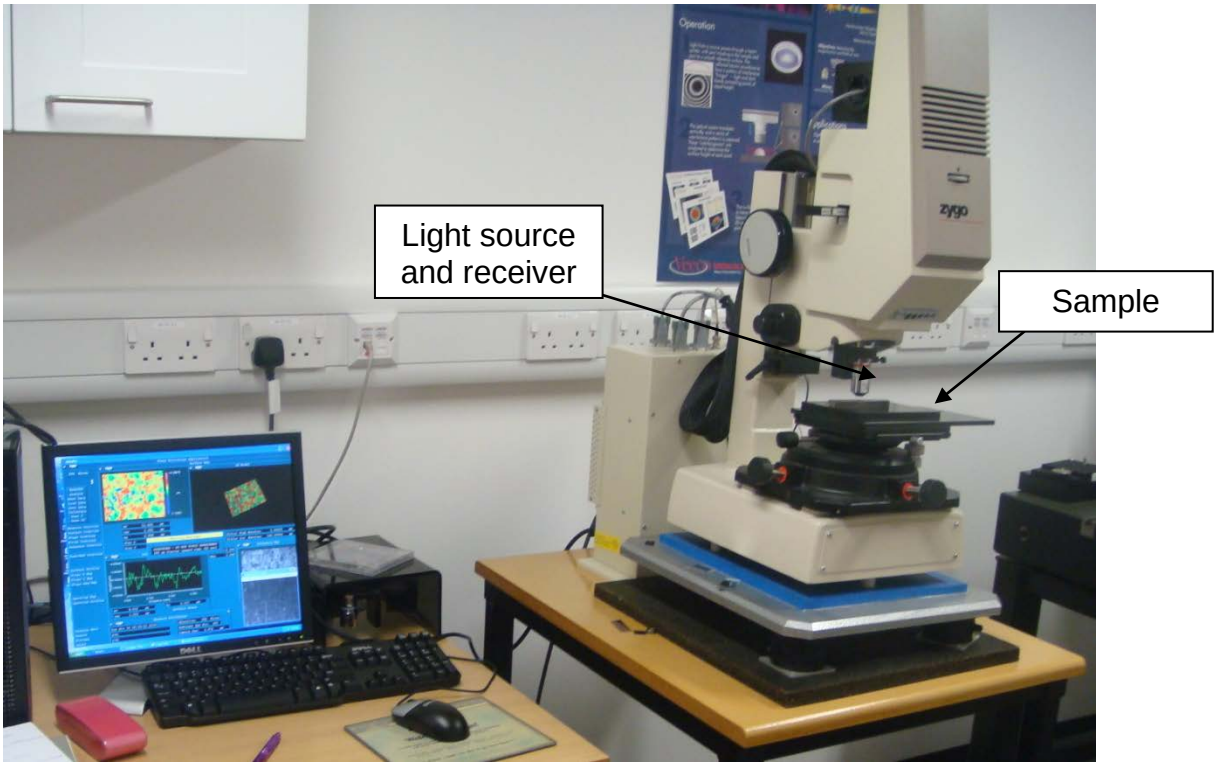

Figure 3-5: Zygo Interferometer (OMP-0347K)

3.4 Peening media and sample images

The word "peen" is of Scandinavian origin, it comes from the Danish "pene" which means to beat (out) **(98)**. Processes such as shot blasting (or peening) are generally used for opposing crack formation and growth, by inducing a compressive residual stress layer around the surface of a material **(1)** i.e. stresses within the structure which are not subjected to the external

compressive forces. Small particles of a chosen material are propelled onto a surface through a gun using air pressure. Peening plastically deforms the surface of the material alleviating it from some of the localised stresses associated with the situation in which it is placed in **(102)**. A peening technique was used to refine the surface of the pipe section of the connection. This peening practice produces an even surface, removing the machining lines and leaving an isotropic surface. As the connection pieces are relatively thick, it is only the surface which deforms during the peening process, and therefore it does not lose its shape.

3.4.1 Peening media

Since local materials are used to peen surfaces, different materials are utilised in various parts of the world. An assortment of materials was used for shot peening, including ceramic and metal particles. The peening media was examined under a microscope to observe the differences between the size and shape of the particles. Finer stainless steel peening media (**Figure 3-6)**, ceramic (**Figure 3-7**) and coarser stainless steel (**Figure 3-8**) media types were available for inspection.

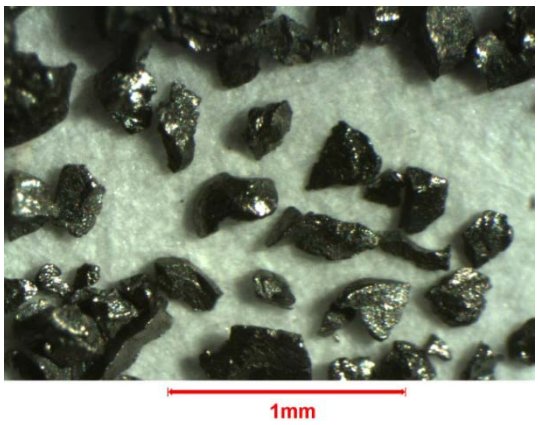

Figure 3-6: ≤0.2mm stainless steel peening media

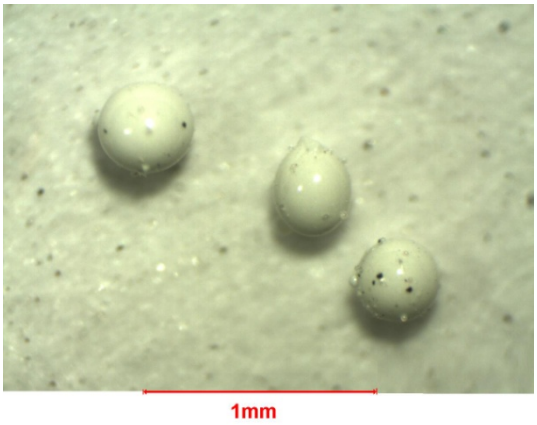

Figure 3-7: Ceramic peening media

Figure 3-8: Coarser stainless steel peening media

The shape and size of the individual peening medium can be seen in the above images. The ceramic media is of spherical character compared to the coarse and fine stainless steel. The ceramic material is made from a composition of Zirconium Oxide ($\boldsymbol{ZrO_2}$), Silicon Oxide ($\boldsymbol{SiO_2}$) and Aluminium Oxide ($\boldsymbol{Al_2O_3}$) particles. The general make-up of the composition is approximately 60-70wt% $\boldsymbol{ZrO_2}$, 28-33wt% $\boldsymbol{SiO_2}$ and less than 10wt% $\boldsymbol{Al_2O_3}$ **(103)**. The composition of the finer stainless steel particles is approximately 30wt% Chromium (Cr), up to 2wt% Silicon (Si), up to 2wt% Manganese (Mn), up to 3wt% Carbon (C) and up to 4wt% Molybdenum (Mo), leaving the remaining 59wt% of material to be Iron (Fe). The finer stainless steel particles are the smallest size available of this material (the particle sizes are below 0.14 mm in size) and are designed to improve the quality of the surface finish and reduce the blasting time.

To shot peen a material, a set of media is blasted at a surface using a high pressure air gun. The shot peening media size, structure and shape plays a huge part in the surface structure of the final product, as does the distance and direction that peening is done. The ceramic media is spherical in shape and its composition has very few sharp edges or corners. This results in the majority of troughs being circular.

The stainless steel media is larger in size to that of the ceramic material. This resulted in larger craters on its surface. The stainless steel peening media was quite sharp and contained various different sizes of particles. The profile of the peened surface therefore had a wide range of different sizes of troughs.

3.4.2 Surface roughness of peened samples

Table 3-1 shows the equivalent arithmetic average surface roughness (Ra) values for the pin (shown in **Figure 3-9** (a)) and coupon (shown in **Figure 3-9** (b)) samples, manufactured for testing for ceramic peened, coarse stainless steel peened, aluminium oxide peened and finer stainless steepened tests.

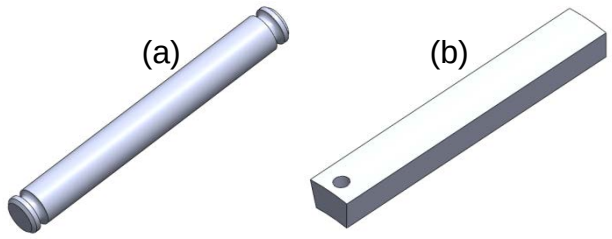

Figure 3-9: Geometry of the samples for used in tests (a) Pin (b) Coupon

Table 3-1: Peening media and roughness of coupon or pin

Surface Peening	Coupon		Pin	
	Ra (µm)	Ra (µinch)	Ra (µm)	Ra (µinch)
Ceramic	1.60±0.23	65.17±5.97	1.52±0.12	62.18±4.72
Coarser Stainless steel	1.18±0.19	48.16±7.49	0.81±0.11	33.06±4.33
Aluminium Oxide	2.88±0.34	117.59±13.39	2.45±0.22	99.92±8.66
Finer Stainless Steel	0.92±0.11	37.48± 4.33	1.15±0.31	46.94±12.21

The stainless steel peened coupons and pins had a lower arithmetic average surface roughness than those measured on the premium tubular connection. The procedure for peening was supposed to be similar to that of the process used in everyday manufacture. Microscopic images of the surfaces showed the

main characteristics of each peening media. On these images, the craters and machining marks were clearly visible. Images of each of the different surfaces were also taken using the 3D Zygo interferometer (in the University of Cambridge). The images show a three-dimensional representation of the surface and the main characteristics of the peening media can be seen in the images for each of the surfaces.

Figure 3-10 shows both a two-dimensional and three-dimensional image of the finer stainless steel peened sample surface, and it is evident that the smaller particles created a much smoother surface finish. The roughness of this surface was also lower than that of the coarse stainless steel peened surface due to the difference in size of the blasting media. The finer stainless steel peened coupon had an Ra value of 0.92 µm and the coarse stainless steel, had an Ra of 1.18 µm. The coarse stainless steel peened surface is shown in **Figure 3-11**. The machine marks are visible in both three-dimensional images. These machine marks are most likely present due to under-peening of the surface i.e. an insufficient time spent blasting.

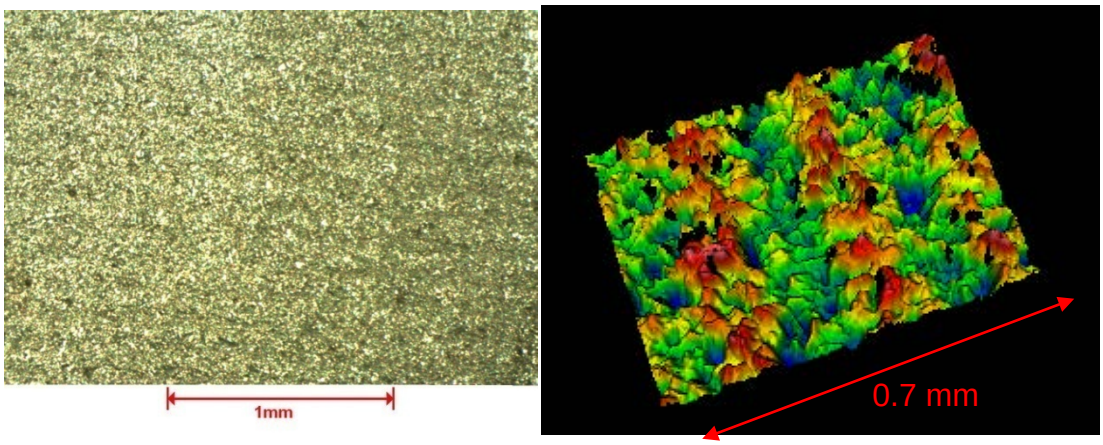

Figure 3-10: Finer stainless steel peened chrome

The coarser stainless steel peened sample image (see **Figure 3-11**) shows that the machine marks are visible and the peening marks were less prominent than expected compared to that of the ceramic peened surface (see **Figure 3-12**). The large peening media size was shown very distinctively on the aluminium oxide peened sample image. In comparison, the ceramic peening media was much smaller than the aluminium oxide peened media and this resulted in larger cavities on the surface. The finer stainless steel (**Figure 3-10**) peened sample surface was similar to stainless steel peened; however the surface is slightly smoother due to the smaller particle size.

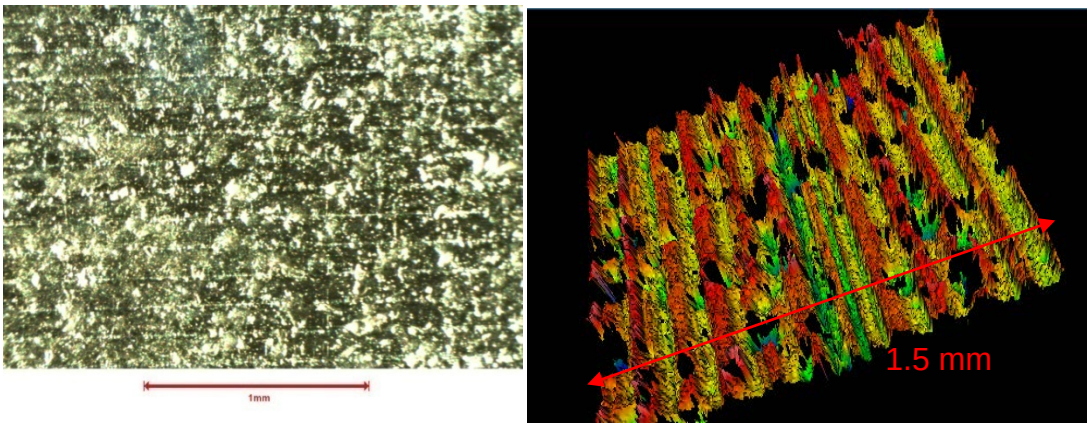

Figure 3-11: Coarser stainless steel peened chrome

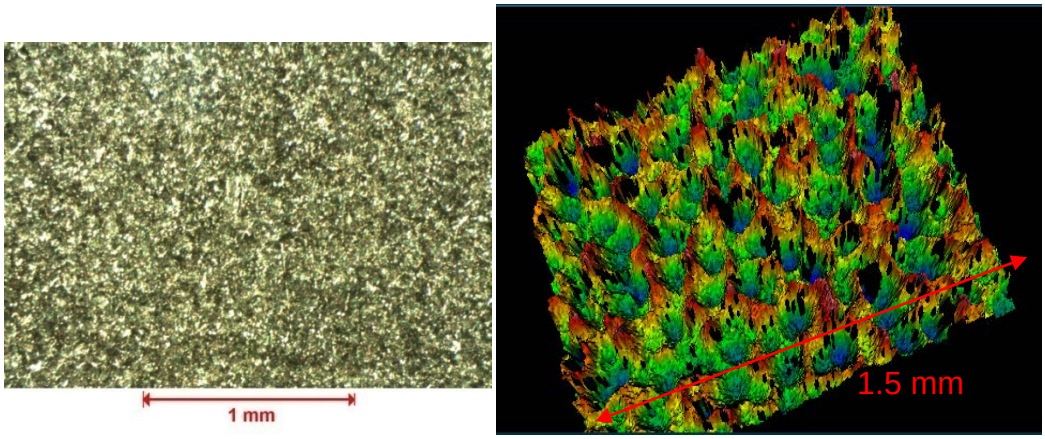

Figure 3-12: Ceramic peened chrome surface

Ceramic peening (see **Figure 3-12**) of chrome caused large interconnecting craters which are approximately 100 – 200 µm in diameter. The stainless steel peening caused large craters, 150 – 200 µm in diameter, though the machine marks on the surface were still present. The largest craters were created by the aluminium oxide peening process which gives a much higher surface roughness (Ra) value thereby reducing the stability of CoF. **Figure 3-13** shows the surface of the aluminium oxide peened coupon, the large craters can be seen on the three-dimensional microscope image.

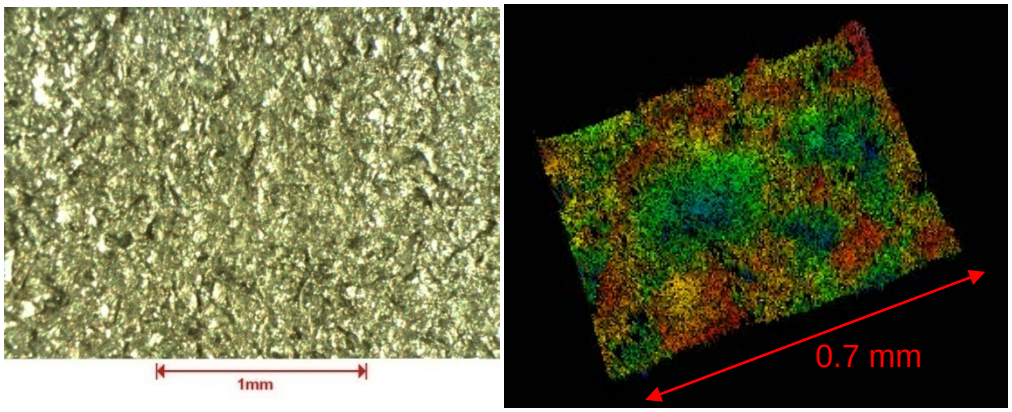

Figure 3-13: Aluminium oxide peened chrome surface

The as-machined roughness of the carbon samples was similar to that of the chrome samples and lies in the direction of the machine marks (see **Figure 3-14**). Bronze plate (shown in **Figure 3-15**) and copper-plate treatments slightly increase the surface roughness of the sample, however this plating does not affect the surface topography as much as peening. A comparison between the surface roughness values for each of the materials is shown in **Figure 3-16**.The roughness of the as-machined carbon samples lies in the machining direction.

Manganese phosphate treatments result in a porous coating on the sample. This significantly increases the roughness of the sample.

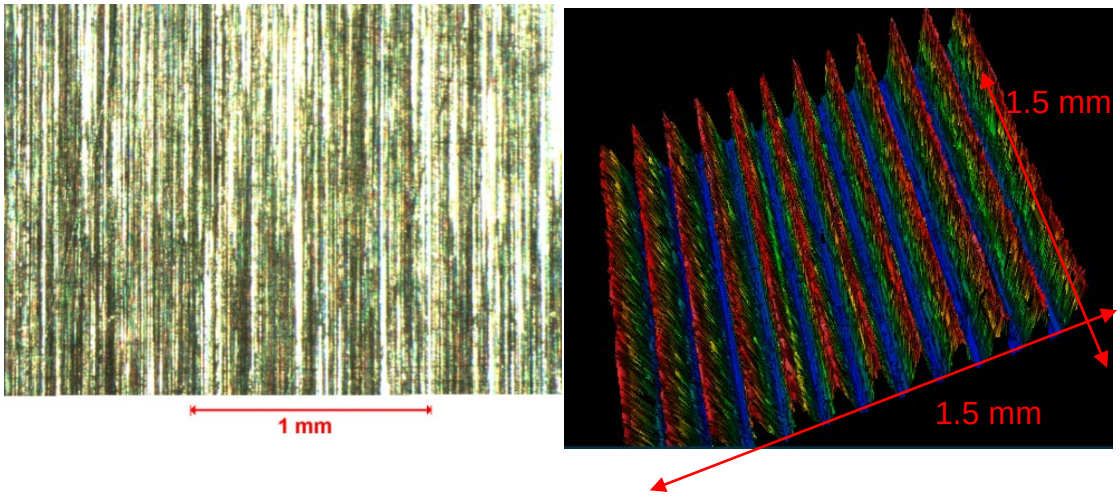

Figure 3-14: As-machined chrome steel

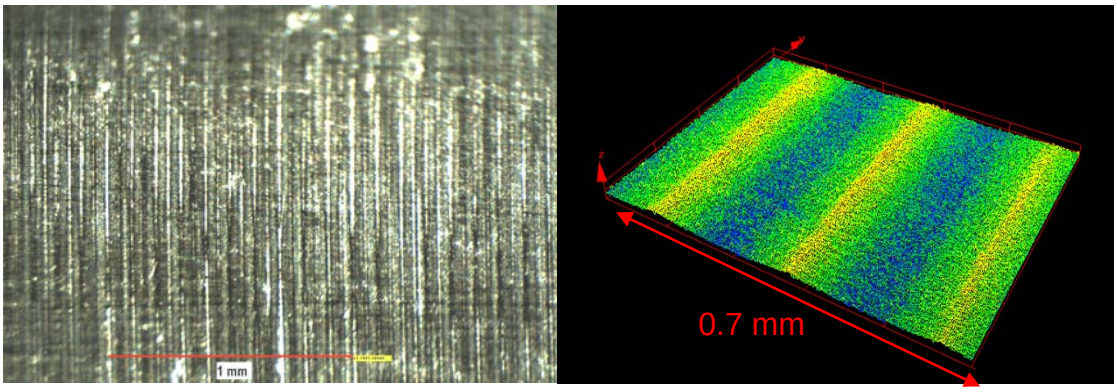

Figure 3-15: Bronze plated surface

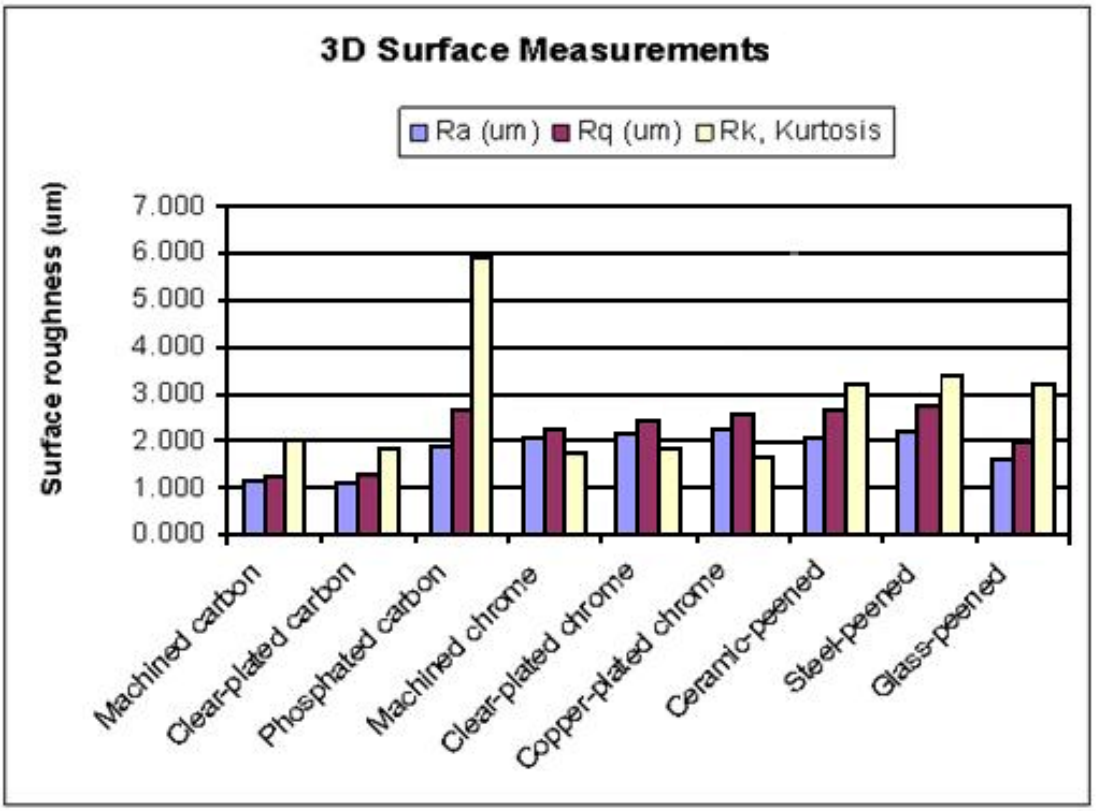

Figure 3-16: Coupon samples - surface roughness measurement values

The machine marks on the as-machined carbon sample (shown in **Figure 3-17**) are visible; as are those on the as-machined chrome sample. On the manganese phosphate coated carbon steel sample (shown in **Figure 3-18**), the machine marks remained visible after they had been bathed in manganese phosphate however some of the sharper asperities were smoothed out. The coupons and pins manufactured to carry out CoF testing are representative of the real products. This means that the CoF tests are reliable, and are comparable with actual situations.

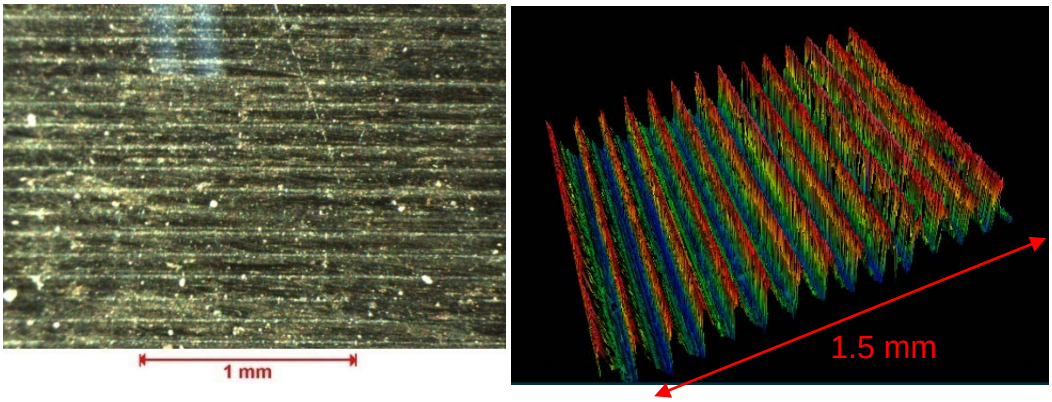

Figure 3-17: As-machined carbon steel surface

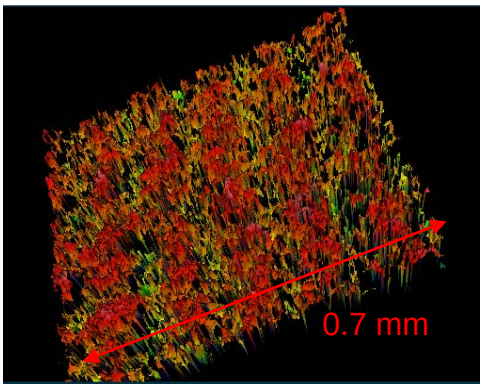

Figure 3-18: Manganese phosphate carbon steel surface

3.5 Microscope surface images

To investigate how the sample surfaces reacted during testing, microscope images of the surfaces were captured after 15 mm/s friction tests. Plated and peened samples are shown for each combination. Using the testing procedure described in Chapter 2, the wear marks shown below were produced by the contact between the surfaces during testing. On the top sample (sample (b) in each of the figures below), a circular mark was created. This occurred because the top sample was stationary during testing and the bottom sample moved back and forth over the top one. This is similar to what happens in making-up

the premium tubular connection. The bottom sample (sample (a) in each of the figures) experienced a linear wear mark along the 45 mm length of contact. The directions of travel are identified on the samples below by the arrows. On the peened samples, the machining marks which were a result of the manufacturing procedure are visible; this shows that the peening process only changes the surface topography but the structure of the material is intact.

3.5.1 Visual outcome of the bronze plated and peened samples after testing

3.5.1.1 Bronze plated – ceramic peened wear marks

Figure 3-19 shows the bronze plate and ceramic peened surfaces after the 15 mm/s friction test. The left hand (L) image shows the wear mark on the bronze plate surface. This wear mark is less prevalent compared to the mark on the surface during the stainless steel test. However it did not scratch the surface as much as during the stainless steel investigation (shown in **Figure 3-19**). In both peened samples, it is evident that machining marks on the plated samples made a difference to the wear on the peened surface. The peened surface in each case has a set of scratch marks along the sliding direction. These are caused by a combination of the peaks of machine marks on the plated surface and debris from the top surface being removed, leaving the deepest pits on the peened surface. This indicates that there is significant wear on the peened surface in both cases.

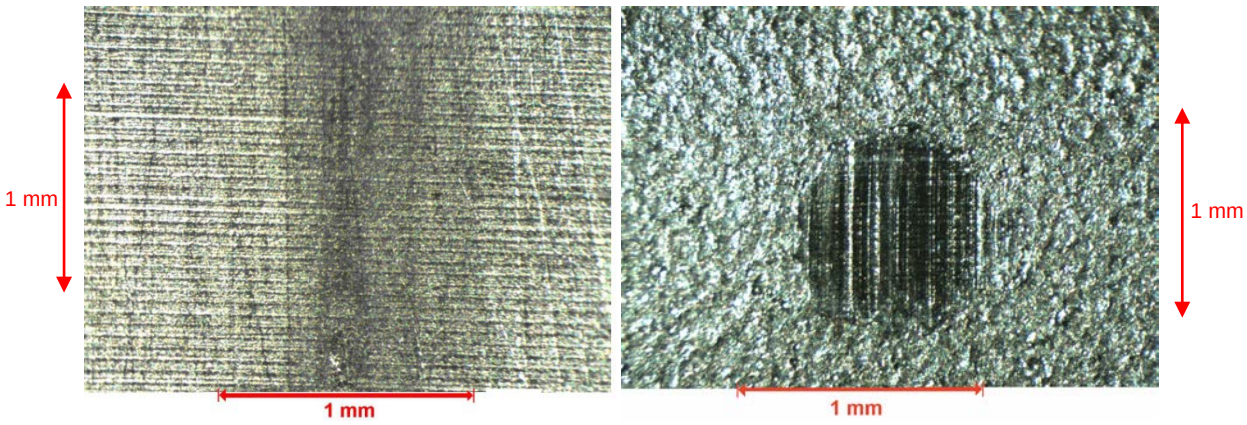

Figure 3-19: Surface images after test (L) Bronze plate and (R) ceramic peened chrome steel

3.5.1.2 Bronze plated – stainless steel peened wear marks

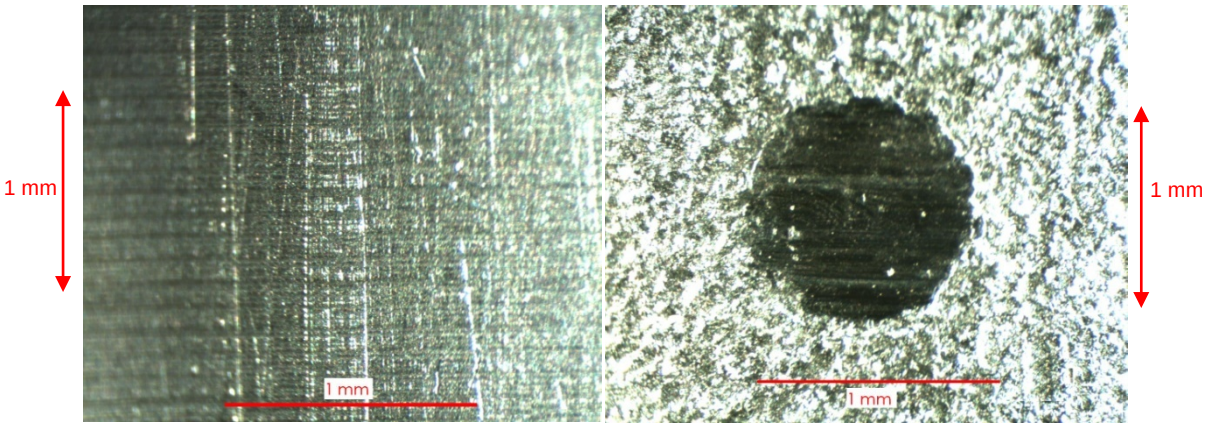

Figure 3-20: Surface images after test (L) bronze plated (R) stainless steel peened chrome steel bronze plated – aluminium oxide peened wear marks

The wear marks on the bronze plate surface for the aluminium oxide test (shown in **Figure 3-21**) are much more prevalent than on the ceramic or stainless steel tests. This is due to the higher roughness of the aluminium oxide peened surface. The wear marks on the peened surface are relatively deep compared to the other tests and the removal and build-up of material is apparent.

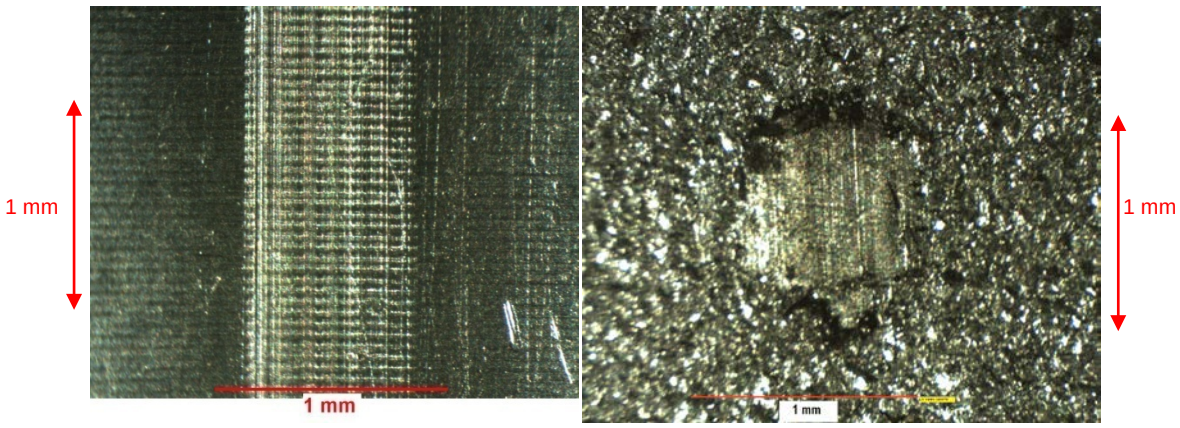

Figure 3-21: Surface images after test (L) bronze plate (R) aluminium oxide peened chrome steel

3.5.1.3 Bronze plate – finer stainless steel peened surface wear marks

Figure 3-22 shows the surfaces of the bronze plated and finer stainless steel samples after testing had occurred. The size of the wear mark this time was much larger. The wear mark on the finer stainless steel surface shows that more of the peened surface has been smoothed out during testing. The bronze plated surface was not affected the same way as in the other tests and this may be due to the peened surface roughness being smoother than the other samples. This confirms that the initial roughness of the peened surface has significant effect on the damage to the counterface. As described by Kapoor et al **(75)**, the plastic index increases with increasing surface roughness and hence the shakedown limit decreases leading to a higher risk of galling or scuffing.

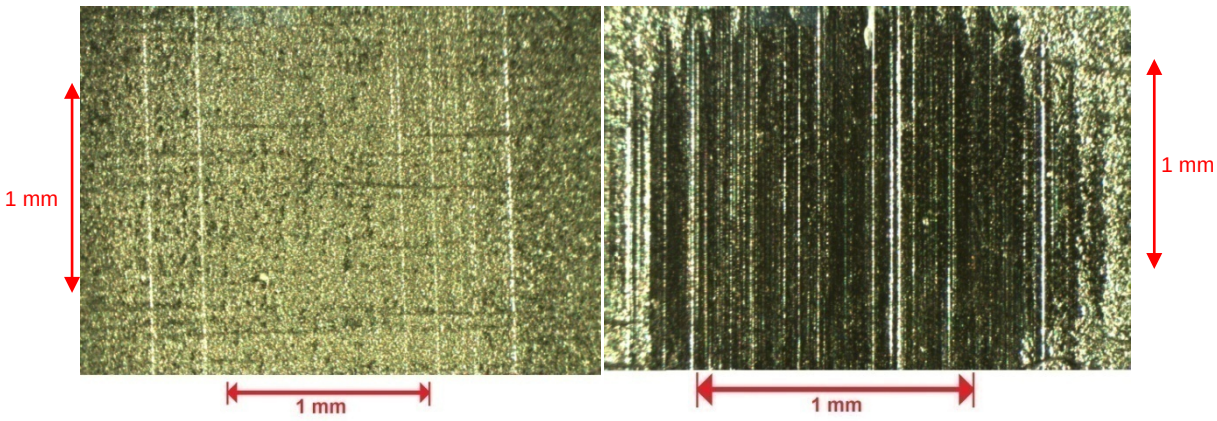

Figure 3-22: Surface images after test (L) bronze plate (R) finer stainless steel peened chrome steel

3.6 SEM imaging and composition analysis

SEM imaging was undertaken to improve the understanding of the surface structure. **Figure 3-23** shows the surface of the ceramic peened sample. The main structure of the surface is visible and the location of the ceramic peened holes can be clearly observed. The asperities created through peening are visible on the surface and these seem to be uniformly distributed. The width of the sample is approximately 2.5 mm.

Figure 3-24 shows an image with higher magnification of the surface structure. Where the surface has been blasted with the ceramic particles, there is a pile-up of material around the crater. There are various sizes of craters on the surface, some of which are spherical. The size of the craters depends on both the size of the peening media and the force with which they were blasted at the surface.

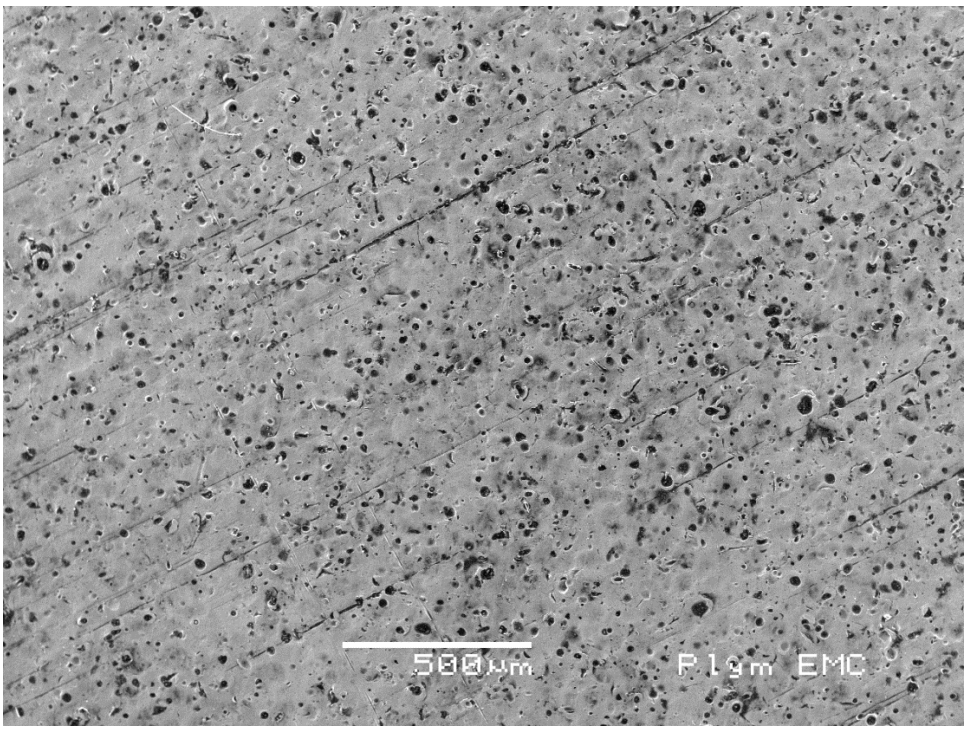

Figure 3-23: SEM image of ceramic peened surface - low zoom

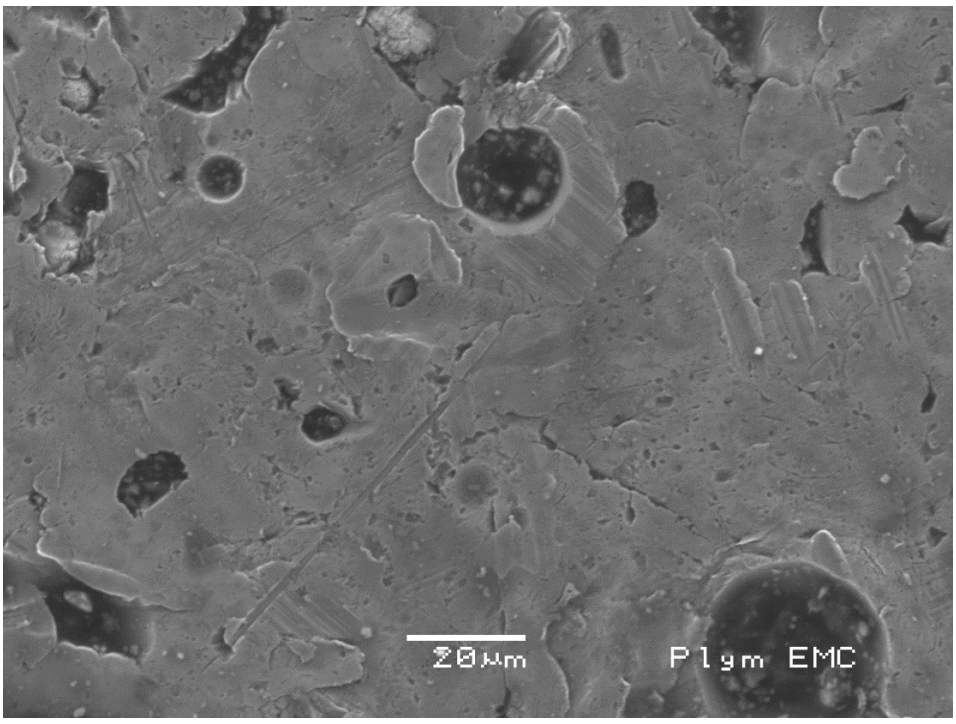

Figure 3-24: SEM image of ceramic peened surface - high zoom

Further SEM imaging was carried out on the ceramic peened surface prior to the frictional testing. The test included x-ray imaging and therefore information about the chemical composition of the material could also be obtained. This provided means for an investigation of the surface after testing to be undertaken so as to establish whether or not any transfer of material occurred during testing. **Figure 3-25** shows the ceramic peened surface and the locations where the ceramic media had made depressions on the surface. Prior to measuring, the samples were cleaned using a magnetic stirrer and acetone to ensure there was no contamination on the surfaces. The acetone would have removed any dust and foreign objects from the surface to ensure that it was free of contaminants.

The base material of the coupons is 13% chrome steel and the image below shows that the main material on the surface is iron, making up almost 79% of the material type. 13% of the material is made up of chromium which means that through peening, there is little of the chromium element removed. The zirconium, silicon and aluminium particles come from the peening media; left on the surface after shot blasting has taken place. **Figure 3-26** and **Figure 3-27** show two positions on the sample surface. In both, the main element is iron, with around a 13-14% of chromium and a small amount of the particles which make up the ceramic peening media, i.e. zirconium oxide, silicon oxide and aluminium oxide.

Figure 3-25: X-ray SEM Image of ceramic peened surface prior to friction testing

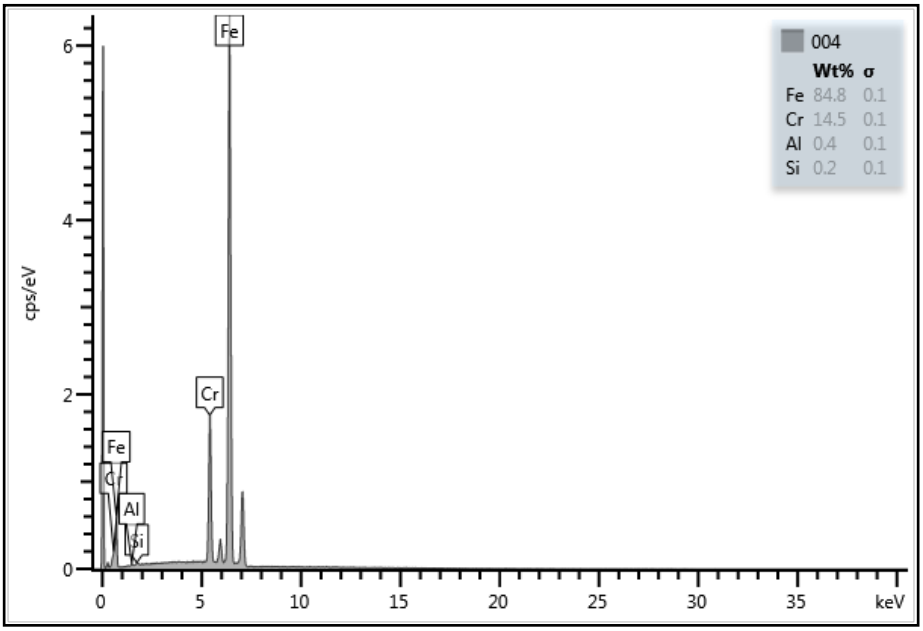

Figure 3-26: Chemical composition of ceramic peened surface prior to friction testing - Specimen 4

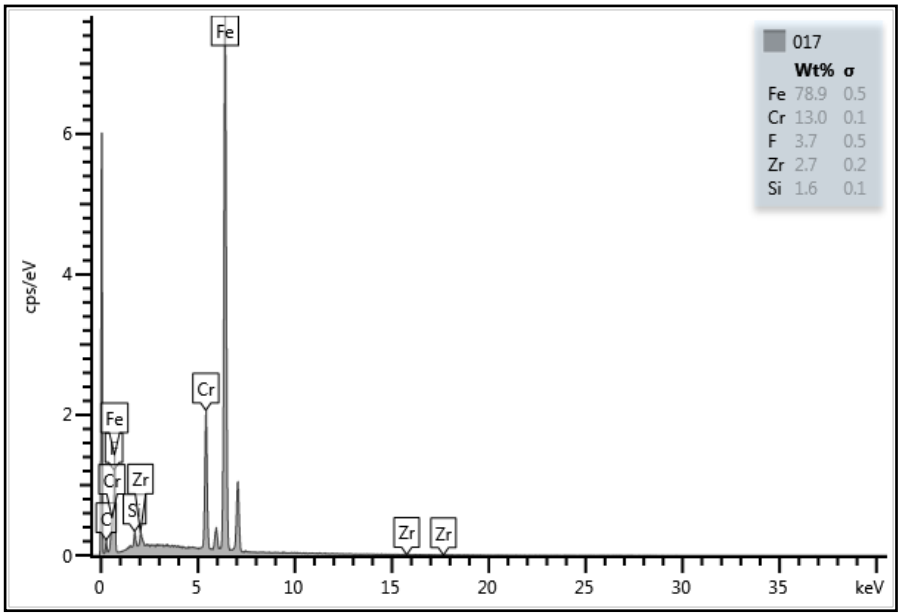

Figure 3-27: Chemical composition of ceramic peened surface prior to friction testing - Specimen 17

Figure 3-26 shows the corresponding graphs from the SEM image of the bronze plate (**Figure 3-25**). This shows the chemical composition of the bronze plate surface. Bronze plate is a 50% tin and 50% copper composition.

After the friction test was performed at 15 mm/s, SEM images were retaken on the surface. Similar to the measurements for the samples before testing, the surfaces were cleaned in acetone using a magnetic stirrer. The surfaces were not "wiped" after testing so any transfer should have been visible using the SEM. Removing the lubricant by wiping would have altered the surface and any transferred material would have been most likely removed. Nevertheless, there is a degree of uncertainty in using the acetone cleaner and ultrasonic bath; however without cleaning the surface, the main constituents of the

measurement would have been the lubricant. The SEM does not possess the capability to investigate liquids.

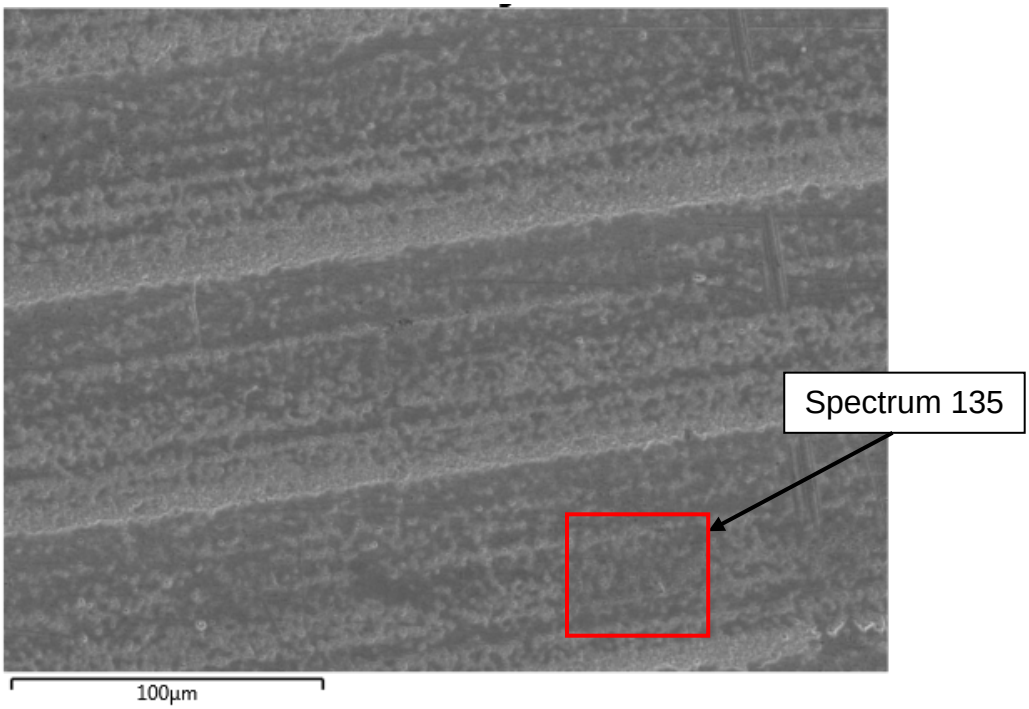

Figure 3-28: X-ray SEM Image of Bronze plate surface prior to testing

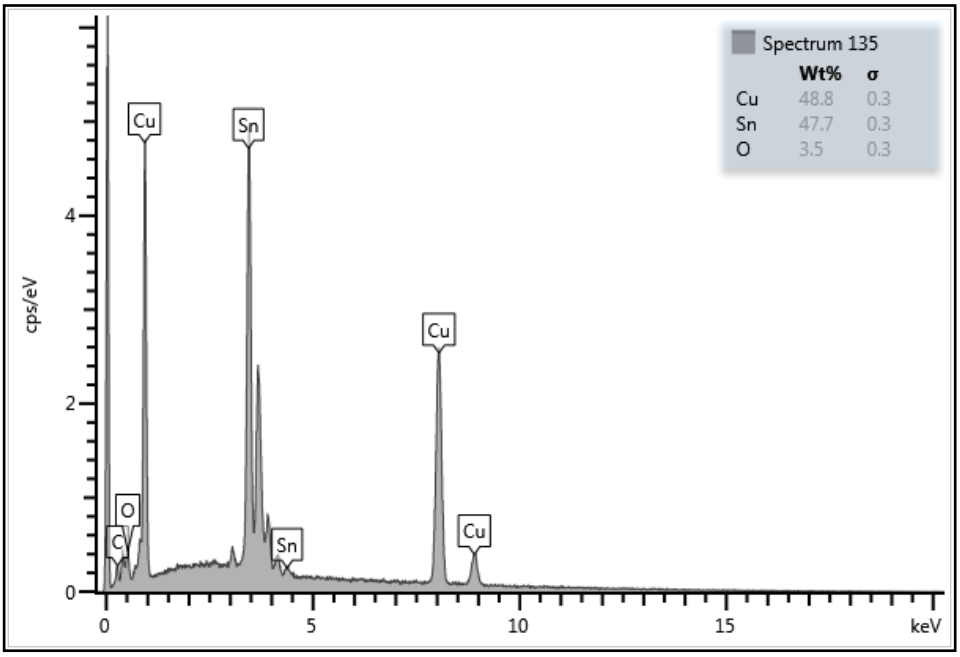

Figure 3-29: Chemical composition of bronze plated surface prior to testing

Figure 3-30 shows the image of the surface after friction testing. Wearing of the surface is present and the peening marks can still be seen. Although the surface has been worn, there is no evidence of transfer of material between the two surfaces. The composition for the material is shown in **Figure 3-31**. **Figure 3-32** shows the surface of the bronze plate sample after testing. The wear marks are more visible after testing, compared to the ceramic peened sample. However there is a similar outcome in that there is no transfer of material occurring. In each of the outcomes, the surface material percentage remained approximately the same as the untested sample surface, within error of measurements. Even in sections where the surface appeared different to the rest, it was still only a wearing of the original material, not a transfer from the other sample.

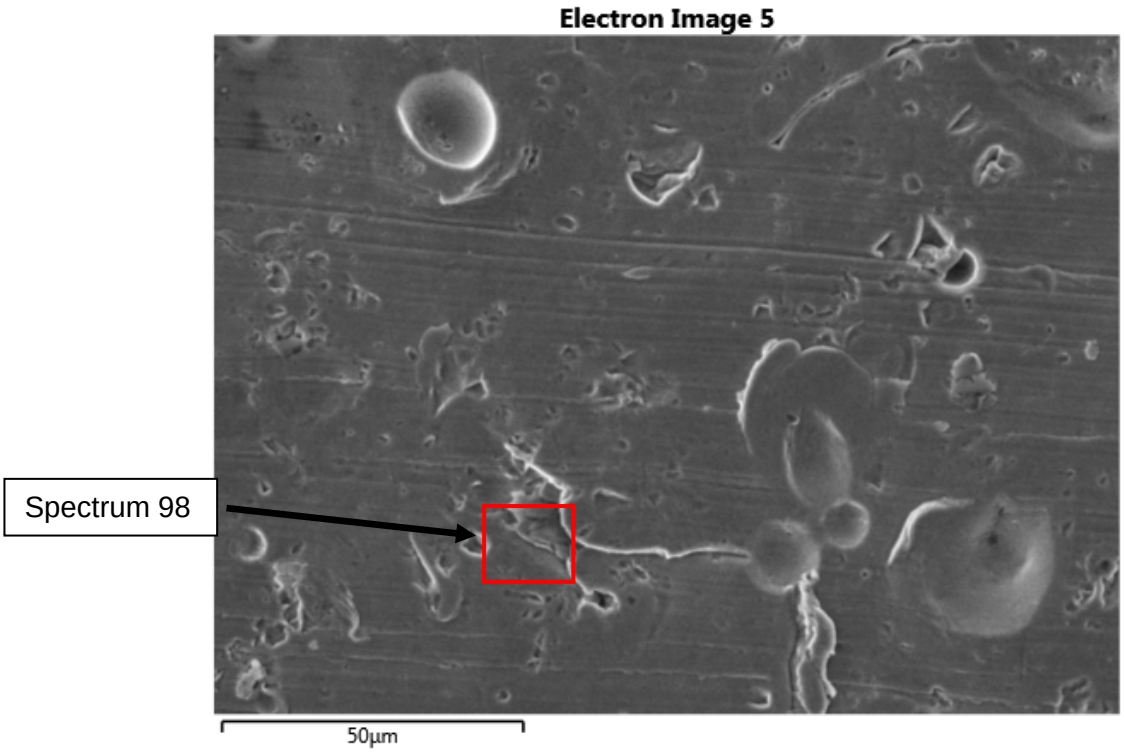

Figure 3-30: X-ray SEM Image of ceramic peened surface after friction testing

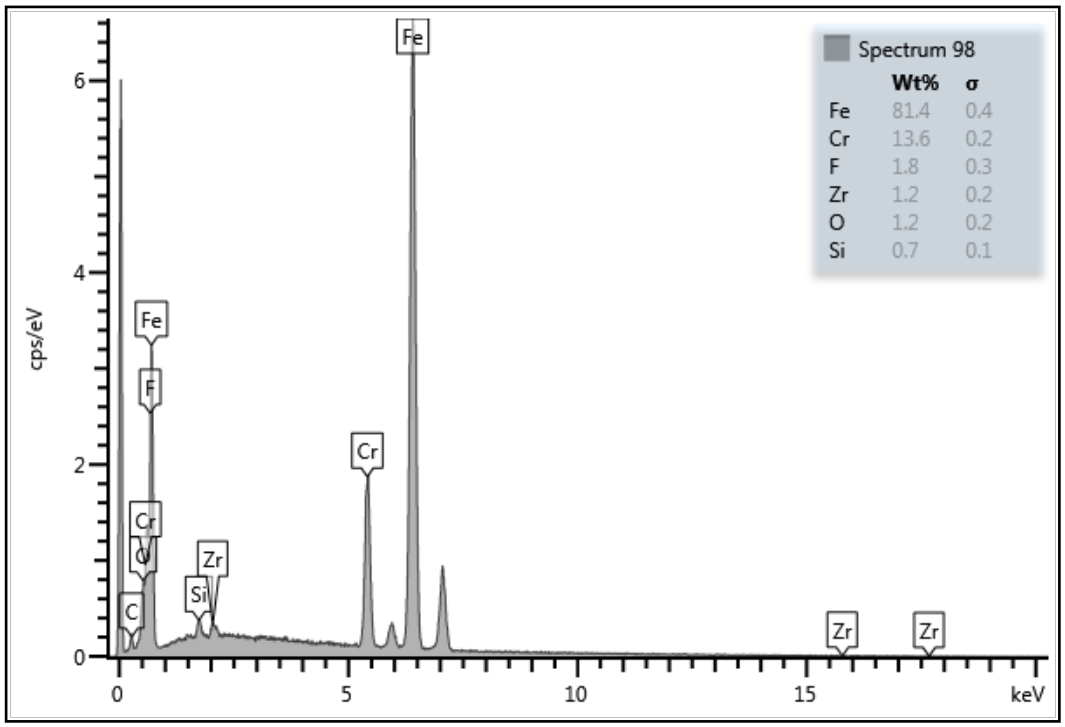

Figure 3-31: Chemical composition of ceramic peened surface after friction testing

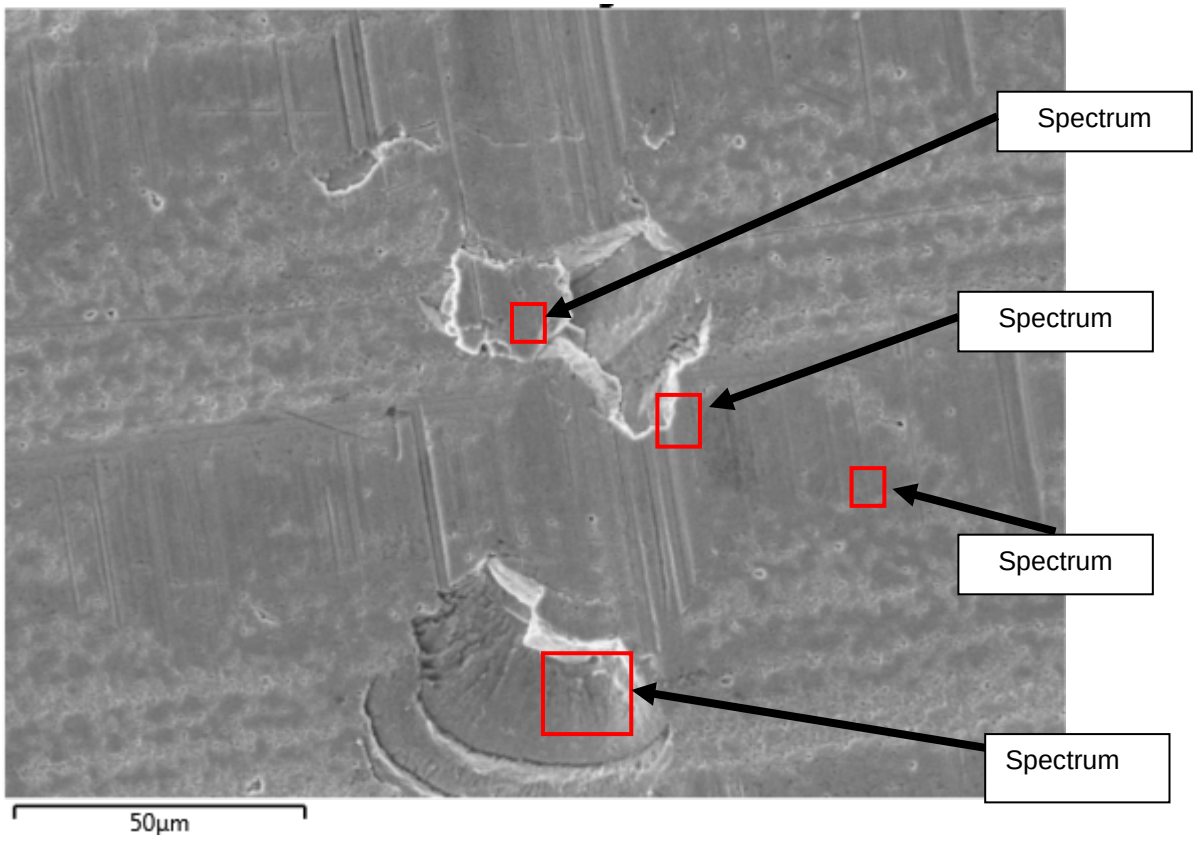

Figure 3-32: X-ray SEM image of Bronze plate surface after friction test

3.7 Hardness testing

To allow Archard's wear equation to be used, the hardness of each material had to be tested. As the coatings and peening depths were very thin, hardness tests were undertaken at Birmingham University using a nano-indenter (shown in **Figure 3-33**). The nano-indenter was specifically designed to apply forces of 0.1 to 500 mN and therefore a 3 mN force was applied to obtain the value of hardness for the coatings.

Table 3-2: Nano-hardness test results from University of Birmingham(104)

Material Type	Hardness (GPa)
Bronze plate	3.23± 0.74
Copper-plate	1.81± 0.29
Ceramic peened	2.57± 0.54
Stainless steel peened	2.83± 0.55

For each sample, one hundred tests were carried out. The values in **Table 3-2** show the mean and standard deviation for each surface finish of material. The hardness of the two peened surfaces was very similar. This was expected as these are predominantly the same material; the only difference being that the topography was changed by blasting different materials at the surfaces. The bronze plated surface had a much higher hardness value than the copper plated one, which was expected as bronze is known for its hardness and toughness.

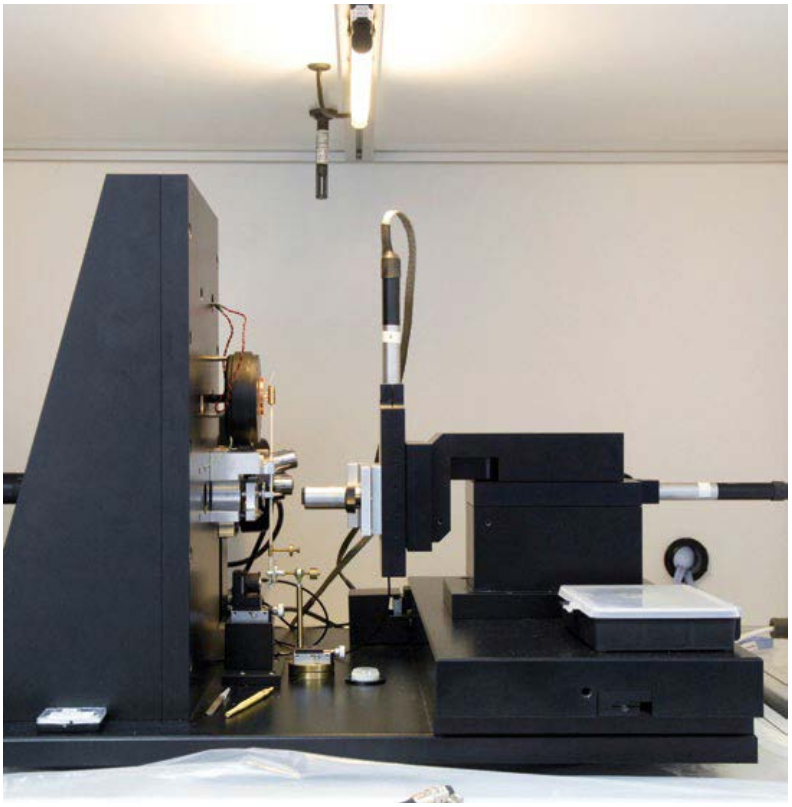

Figure 3-33: MicroMaterialsnano-testnano-indenter

Chapter 4 : Surface Topography Evolution and Coefficient of Friction

4.1 Test regimes

The intention of this research is to provide conclusions that can expose the general trend of how CoF is affected by changes in external circumstances during make-up of a premium tubular connection, in an oil and gas well. The main areas of concern were in the differences of CoF during sliding (or in this case, make-up of the connections) caused by changes in contact pressure, sliding speed, material properties, surface roughness values and lubrication. Changes in CoF had the potential to cause a problem because torque is calculated using the CoF value. To understand how each external circumstance affected the results, a set of combinations was pre-defined with the support of engineers from the manufacturer.

Using knowledge and results from previous laboratory tests, the list was developed to include the major circumstantial changes. It was known theoretically, according to Coulomb **(34)** and proven through an extensive number of experiments by Morin **(3)** that CoF did not change with varying sliding speeds. However, there is evidence to prove that this might not be entirely true and that this was primarily a fact in dry sliding conditions only. Work by Al-Samari et al **(105)** showed that CoF reduced with increasing sliding velocity. The authors' work also investigated the effect of surface roughness, normal force and relative humidity. Although the results were obtained using a pin-on-disc tribo-tester, there is uncertainty in the accuracy of the results. It was

found that generally, as the load increased, CoF decreased. This trend was true for the three speeds and for each load. The fastest velocity generated the lowest CoF in each case, which is in line with the outcomes of this project. It was also found that as the load increased, so too did the wear rate; therefore increasing the wear volume removed during contact. The trend of the results was similar to the work of Al-Samari et al.

To meet the objectives of the project, and to create a model capable of predicting friction, surface roughness and wear after make-up, the test results from Chapter 5 and surface measurements from Chapter 4 were used alongside tribological theory. The test rig was used to obtain quantitative results for CoF for the pre-defined combinations. Strain gauges were fixed to the rings of the load cell and calibrated accordingly, resulting in two output voltage values. The strain gauges continually recorded normal and tangential voltages experienced by the load cell, which were converted to forces. As CoF is calculated from the normal and tangential forces, this meant that when two samples were in contact with one another, and the motorised sliding table was in motion, there was a value of CoF associated with it. The testing process sampled both the normal and tangential forces constantly. This gave a large number of readings during the testing process, and therefore an average reading for each range of contact pressure (regime).Each test was run for three consecutive cycles under the same combination of conditions as would occur in repeated make-up of connections. It was noted that there was variation from cycle to cycle due to surface evolution which will be discussed in detail later.

To provide useful information to investigate the effect of the external circumstances, a table was drawn up which contained the data from all tests undertaken during the project. For each regime, an average reading was obtained from the data set. This CoF reading was an overall average for each range of contact pressure within the set. This provided a more straightforward approach to comparing the values during each range. However, it is important to note that this is a heuristic approach as it gave one measurement of CoF for each section, which can be used in the torque equation. The investigations produced data for three sliding velocities, three lubricants, three pressure ranges and five different peening media.

Table 4-1shows the results for each combination of external circumstances for Regime 1, with a pressure range between 620 – 2068 MPa (90 and 300 ksi). Table 4-2 shows CoF data for Regime 2, between 137 – 482 MPa (20 and 70 ksi) and Table 4-3 shows CoF values for Regime 3 between 20 – 69 MPa (3 and 10 ksi). Each of the regimes in the project produces CoF values much larger than that estimated from pipe connection make-up tests. Regime 1 illustrates the maximum localised pressures found at the seal during make-up. The greatest value is 2068 MPa (300 ksi), which is significantly higher than the yield stress of the L80 chrome steel material. This does not mean that leak paths will definitely occur because these high pressures are localised. During make-up, it is prevalent to ensure that there is adequate strain energy stored in the pin nib (ridge on the end face of the pipe section) to make sure that the connection is sealed. During the torqueing process, the seal and pin nib are in compression. Conversely, when the connection goes into tension, the strain

energy is necessary to ensure the two surfaces remain in contact and maintain a seal.

Connections can be exposed to both tension and compression and therefore there is a large variation in the pressure that they are exposed to. A comparison between the localised contact pressures during the internal compression (shown in **Figure 4-1**) and external tension shown in **Figure 4-2**) shows the significant difference between the stresses acting on the seal during make-up. These stresses are simulated using Finite Element analysis of the area of sealing between the pipe and coupling. The highest values of stress were located on the seal. The differences mean that to ensure no leak paths occur, a seal must not be broken after the torque has been applied. If the value of contact pressure reduces considerably during the make-up process then a seal will not be maintained; this has the opportunity to cause major problems when it comes to subsea operation.

The differences between the stresses during make-up mean that the connections need to seal in both tension and compression; therefore the accuracy of the connection dimensions needs to be precise. The torque value used to make-up the connection also needs to be determined accurately. Problems have occurred in the past due to the connections being contaminated, or an insufficient amount of lubricant applied during make-up. Although these failures are not caused by the design and are entirely due to the assembly of the connections offshore, this project provides an understanding of how differences in the lubrication or surface roughness can affect CoF. Unwanted

dust or dirt particles can result in an uneven surface which can produce scratch marks during make-up, hence increasing the wear rate. This may also increase CoF leading to a larger torque being required to make-up the connection properly.

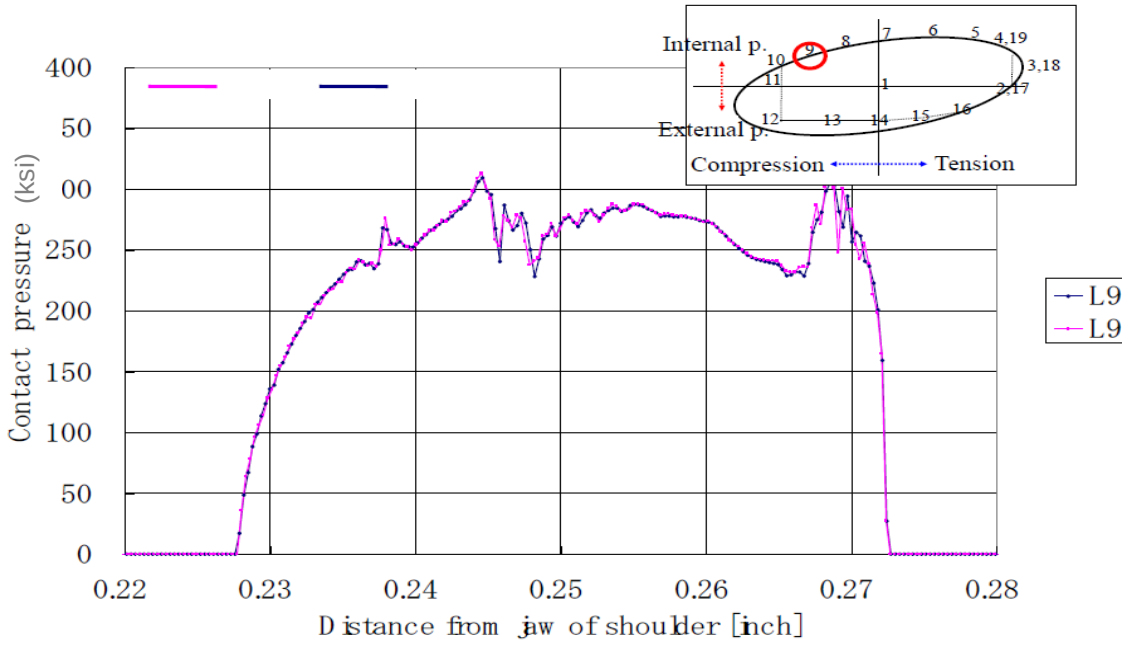

Figure 4-1: Contact stress during internal compression of connection during make-up (32)

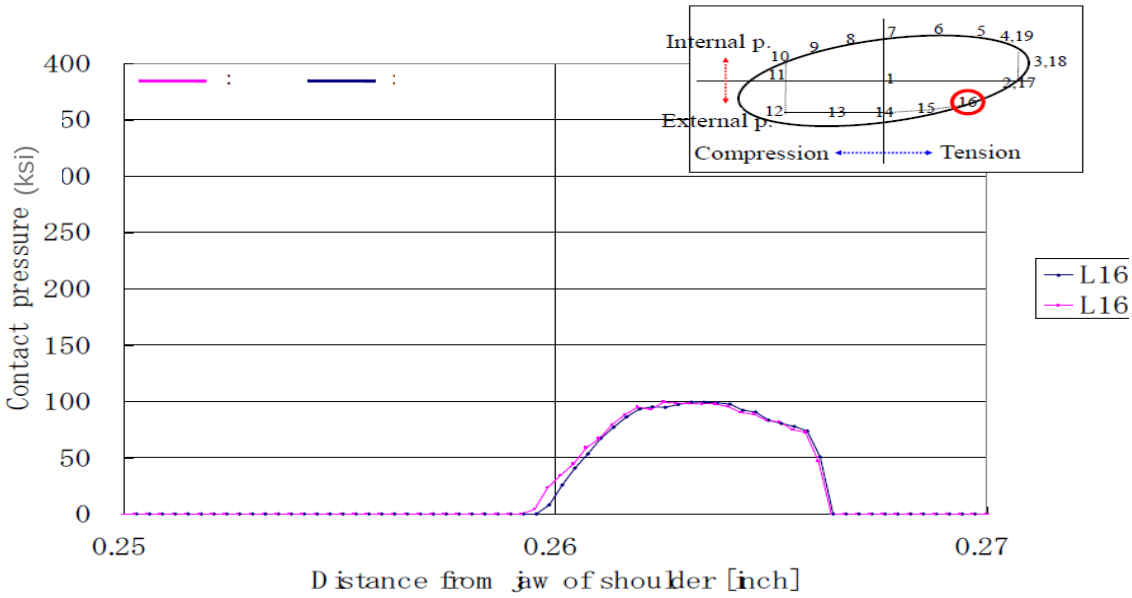

Figure 4-2: Contact stresses during external tension of connection during make-up (32)

High contact pressure tests were undertaken in Regime 1 where contact pressure values between 620 MPa – 2068 MPa (90 –300 ksi) were investigated. Finite Element analysis provided by the manufacturer supplied the limits of frictional testing undertaken in this project **(32)**. This regime represented those localised pressures experienced by the seal during make-up. The large localised stress is a result of the thin section of the pin nib. The pin nib and seal contact area are in compression during make-up, however when the connection moves into tension, the strain energy created in the pin nib is necessary to maintain seal contact **(106)**.

The internal pressure in normal testing on connections in the OCTG industry are in the region of 103 MPa (15 ksi) **(107)**, where the pressure testing has to be at least 1.5 times the working pressure. This 50% margin is initiated to ensure that designs can withstand pressures larger than what they are

designed to, in case of overload. This remains true for conditions where the internal pressure (or rated pressure) of a system is 69 MPa (10 ksi).The values of contact pressure investigated in this project are mainly based on localised maximum pressure. Although the average contact pressure may be significantly smaller than the values investigated here, small sections of the connection could experience this much larger pressure.

The Regime 2 tests are in line with the contact conditions in loading flanks of threads, where the average pressure is in the range of 137 – 482 MPa (20-70 ksi). The initial surface of the samples was rougher because they were cut from a turned pipe. This does reflect the surface finish on the pipe end thread. The CoF results are more sensitive to initial surface treatment and sliding speed (as shown in **Table 4-2**). Regime 3 tests were only conducted on one surface treatment due to the availability of test samples. The effect of sliding speed can be seen in **Table 4-3.** By directly comparing these results with those obtained by the American Petroleum Institute (API), there is no correlation. This is because the two test procedures are not comparable due to their geometrical differences. The results will be discussed in terms of surface treatment, sliding distance, sliding speed and lubrication below.

Table 4-1: Regime 1 CoF data summary

Regime 1				
Peening media	**Ra (µm) [µ inch]**	**Contact Pressure MPa [ksi]**	**Sliding Velocity (mm/s)**	**Lubricant A /bronze plated CoF**
As-machined chrome	0.7 [28]	620-2068[90-300]	3	0.127
			15	0.111
			50	0.117
Ceramic peened chrome	1.52 [62]	620-2068 [90-300]	3	0.147
			15	0.148
			50	0.139
Coarser stainless steel peened chrome	0.81 [33]	620-2068 [90-300]	3	0.150
			15	0.134
			50	0.150
Al_2O_3 peened chrome	2.45 [100]	620-2068 [90-300]	3	0.170
			15	0.180
			50	0.187
Finer stainless steel peened chrome	1.45 [47]	620-2068 [90-300]	3	0.142
			15	0.133
			50	0.121

Table 4-2: Regime 2 CoF data summary

Regime 2				
Peening media	**Ra(μm) [μ inch]**	**Contact Pressure MPa (Ksi)**	**Sliding Velocity (mm/s)**	**Lubricant A/ Bronze plated**
As-machined chrome	0.7 [28]	137 – 482 (20 – 70)	3	0.168
			15	0.147
			50	0.136
Ceramic peened chrome	1.0 [39]	137 – 482 (20 – 70)	3	0.145
			15	0.137
			50	0.139
Ceramic peened chrome	1.6 [65]	137 – 482 (20 – 70)	3	0.160
			15	0.157
			50	0.144
Finer stainless steel peened chrome	0.92 [37]	137 – 482 (20 – 70)	3	0.158
			15	0.143
			50	0.124
Medium steel peened chrome	1.18 [46]	137 – 482 (20 – 70)	3	0.155
			15	0.132
			50	0.152
Severe steel peened chrome	2.66 [90]	137 – 482 (20 – 70)	3	0.157
			15	0.163
			50	0.149
Al_2O_3 peened chrome	2.88 (118)	137 – 482 (20 – 70)	3	0.162
			15	0.155
			50	0.149

Table 4-3: Regime 3 CoF data summary

Regime 3				
Peening media	**Ra (µm) [µ inch]**	**Contact Pressure MPa [ksi]**	**Sliding Velocity (mm/s)**	**Lubricant A/ bronze plated**
Ceramic peened carbon	2.1 [82]	**20 – 69 [3 – 10]**	3	0.155
			15	0.162
			50	0.160

4.2 Effect of surface topography on CoF

By analysing the physical results obtained in this project, it was found that there is a general trend of CoF with surface roughness in both Regime 1 and 2 tests (c.f. **Table 4-1** and **4-2**). It is found that the CoF increases slightly with increasing surface roughness for tests undertaken using the Lubricant A and the bronze plated sample (see **Figure 4-4**). The results of this work show that the higher the arithmetic average surface roughness, the higher the CoF. There are however some exceptions to the rule.

The original conclusion behind this relationship between surface roughness and CoF is due to the size and shape of the peening media that was used to create a rougher surface. The area of the depressions on the material is dependent on the size of the peening media. The larger peening media, such as coarse stainless steel and ceramic beads, resulted in a surface which had larger troughs. The shape and hardness of the peening media also played some part in the value of CoF. The Metal Improvement Company **(108)** stated that the

hardness of the peening media should have the same or a greater hardness than the material being peened. It was found that the depth of the compressive layer was influenced by the peening media hardness, as well as other parameters such as the intensity of peening and the size of the particles. Sharp-edged hard particles, such as aluminium oxide, resulted in deep troughs and spikes. It was found that this caused severe galling on the counterface during sliding tests (c.f. **Figure 3-21**). It is believed that this is responsible for the significantly higher CoF.

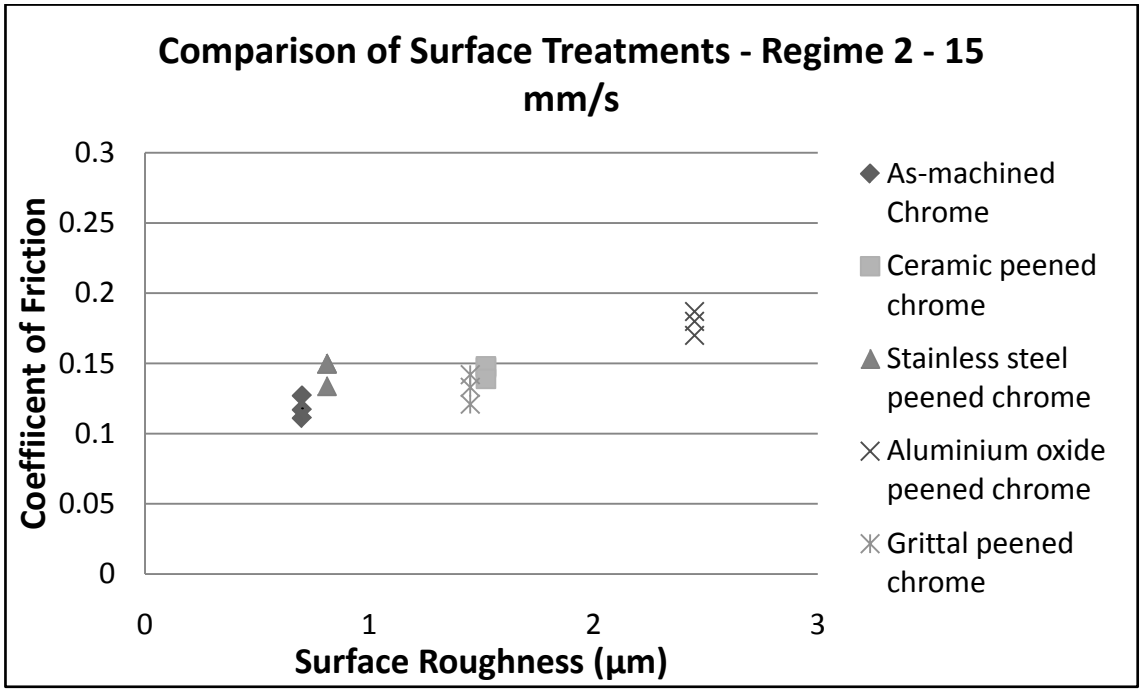

Figure 4-3: Effect of surface roughness on CoF for various surface treatments

Comparisons were also made between samples using the same peening media but with different surface roughness. Two samples were manufactured and tested: one with a lower than average surface roughness (approximately 1 µm) and another sample with a much larger surface roughness (2 µm). Both the arithmetic average and root mean square average roughness were larger in the

2µm sample; however the value is associated with the arithmetic average surface roughness. Although a full understanding of what caused a larger roughness in one sample is not known, it is believed that the rougher surface was subjected to a longer shot blasting duration.

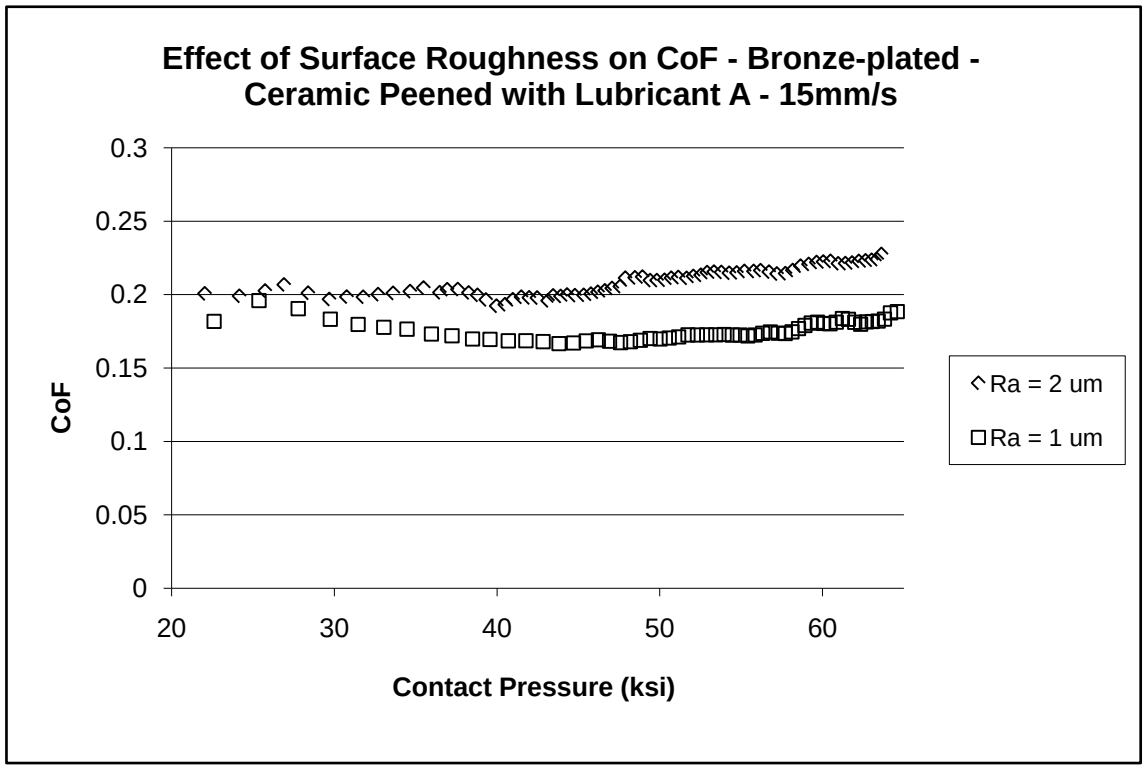

Figure 4-4: Surface roughness effect on CoF for the same surface peening process

In **Figure 4-4**, the surface roughness for one of the samples was approximately 1 µm and for the other 2 µm; all other variables were kept the same. This set of test results was from the third cycle so the sliding distance is between 180 mm and 225 mm. By then the initial surface spikes had been removed. For the higher surface roughness, CoF is dependent on the contact pressure; however the lower surface roughness is more stable across the pressure range. At the higher pressure end, CoF for the 2 µm sample increased significantly; this can possibly be explained by the lubricating regime during the test. Because of the

low sliding speed, the hydrodynamic effect is not significant. However some lubricant could be entrapped in the shot peened pits. At the higher pressure end in both circumstances, most of the lubricant will escape through the porous contact interface because the contact pressure between the two samples is highest at this point. In the 1 µm sample, the pits have a smaller diameter, decreasing the likelihood of the lubricant squeezing out. In the 2 µm sample there is more opportunity for the pits to join up, thus allowing faster leakage of the lubricant. This is supported by the experimental outcomes noted by Ford **(35)**. The author noted that during the numerical modelling of the elastic contact between rough surfaces, the shape of the asperities is taken to be non-spherical and asymmetric. This is in contrast to the Greenwood-Williamson model **(50)**. Nevertheless, the GW results are coherent with Ford's outcomes which concluded that where the asperities were larger, there was a faster lubricant spill out. An investigation into the effect of the direction of elongated asperities was done. It was found that CoF was higher when testing was undertaken in the direction of extended asperities, compared to situations where the asperity length was smaller. The main conclusion of Ford's experiment proved that CoF increased with increasing surface roughness; although the solutions were obtained purely using computer generated experimental data.

4.3 Evolution of surface roughness with sliding distance

To investigate the behaviour of the surface roughness during testing, a ceramic peened top sample with a bronze plate bottom sample test was undertaken with Lubricant A. These results were obtained using the Regime 2 testing procedure.

The testing procedure was identical to the previous test, however between each cycle the roughness of both surfaces were measured. For one ceramic peened surface, the initial surface roughness was approximately 2.7 µm and for the bronze plate surface, its value was also approximately 2.7 µm.

Figure 4-5 shows the arithmetic average surface roughness for the sample at different sliding distances. A roughness measurement was taken at the minimum and maximum pressure for each cycle. The change in topography and reduction in roughness is almost immediate. After the first loading cycle, it reduces to approximately 0.76 µm (30% of the initial value). A similar analysis was done for the bronze plated surface.

Figure 4-6 shows the surface roughness values taken on the bronze plated bottom sample at the same time as the ceramic peened surface shown above. There is limited change in the surface roughness value before and during the testing procedure. The first observation is owing to surface burnishing which occurs when the localised stresses are above the yield limit of the contact materials. It makes the surfaces appear smoother and usually reduces the surface roughness. The second observation is that scratch marks emerge because the counterface is sliding along the length of its surface. The area of interest is the same for both samples, however the ceramic peened surface pits are almost completely removed during testing because the contact is stationary on the fixed area. It is believed that this is responsible for the reduction in CoF after the first cycle. The spikes on the peened surface are worn very quickly under such high contact pressure so that there is less galling or direct metal-to-

metal contacts. Therefore CoF is reduced and stabilised after the first cycle. This will be discussed in detail later.

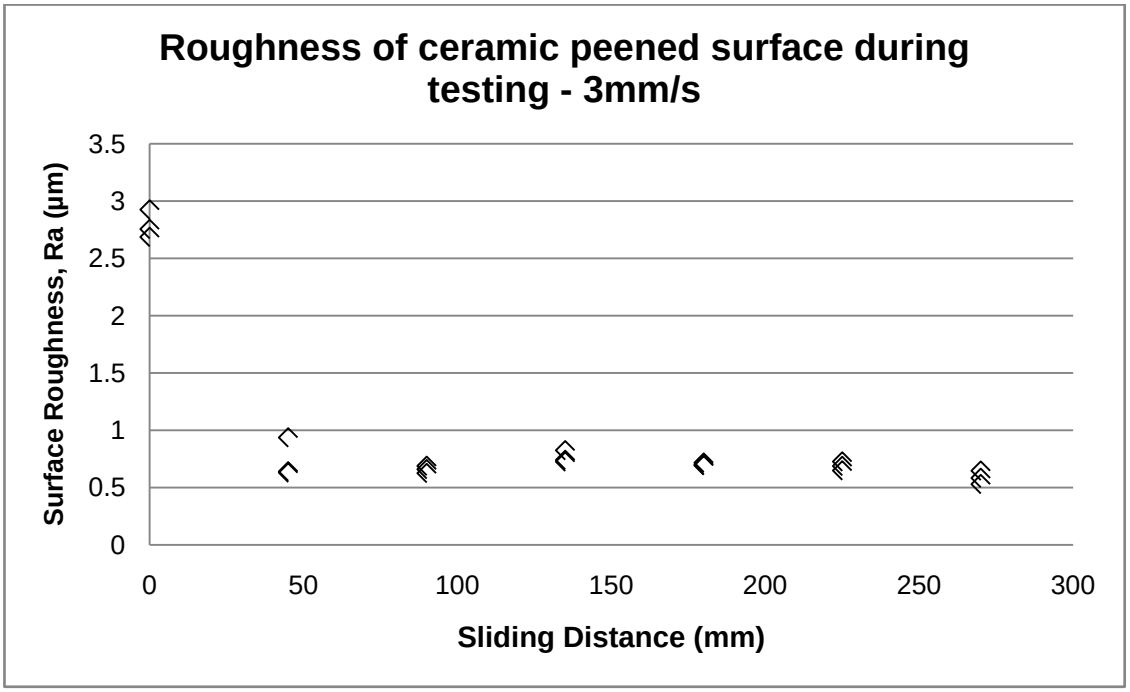

Figure 4-5: Surface roughness (Ra) values between cycles

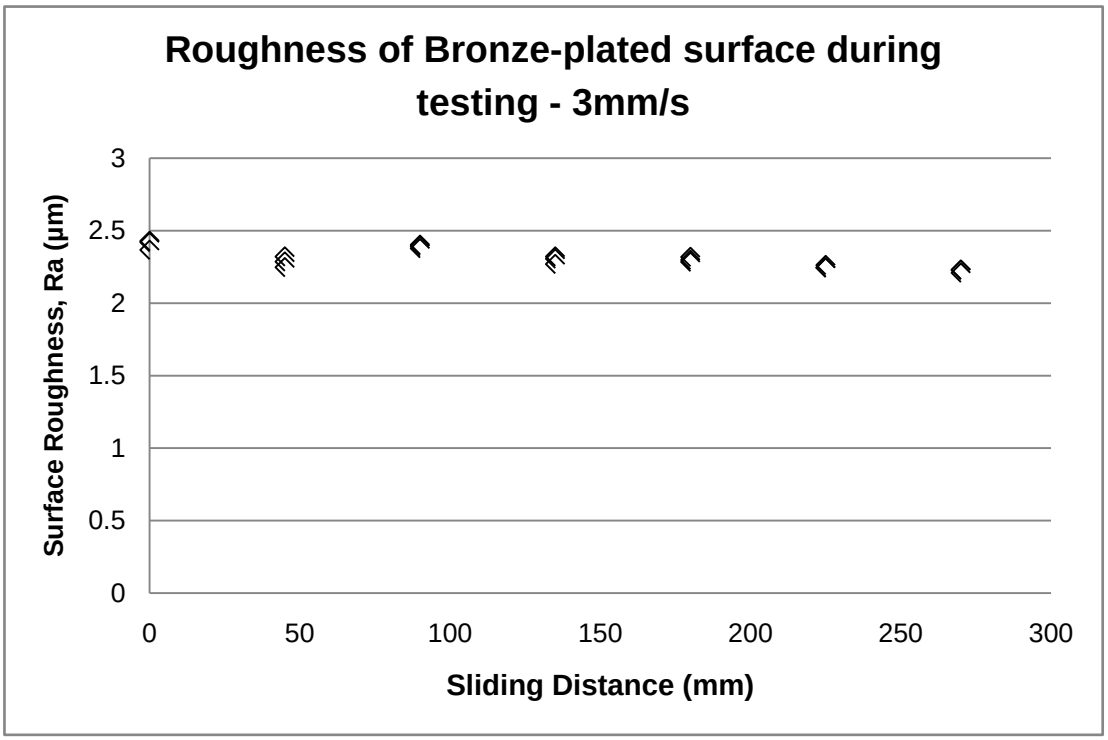

Figure 4-6: Surface roughness (Ra) values between cycles

4.4 Effect of sliding speed and contact regime on CoF

From the physical testing performed in this project, CoF reduces as the sliding speed of contact between the two surfaces increases. This is usually caused by hydrodynamic lubrication when there is a lubricant in contact. CoF depends on the conditions that a system experiences; this includes but is not limited to the material type, surface quality, lubrication, speed, pressure and the type of contact. If the same types of test are undertaken but the velocity of travel between two samples increases, then the dynamics of the contact changes. As the velocity increases, the samples move past one another more rapidly. When this happens, the shear stress of most metals will increase leading to a higher tangential force. Conversely, more lubricant will be entrained into the asperity-to-asperity contact so the hydrodynamic lubrication improves. The extent of reduction of CoF with increasing speed is low in Regime 1 (c.f. **Table 4-1**); however it does show to alter slightly for some combinations of surface conditions. This is much more prevalent in the Regime 2 results reported above (c.f. **Table 4-2**).

The three sliding velocities were selected to represent the tangential velocity of the connection during the make-up. The industry produces a range of sizes of connections from 2” 3/8 to 9” 7/8. It was important to establish whether the make-up speed affected the CoF experienced by the surfaces, to ensure that the value of torque was calculated accurately. The connection could be made up between 1 and 4 RPM. The sliding speed, $\boldsymbol{V}$, is equal to $\boldsymbol{V = \pi . d . n}$ (where $\boldsymbol{d}$ is the diameter and $\boldsymbol{n}$ is the rotation speed) and changes from 3 to 12.5 mm/s if made-up at 1 RPM.

Figure 4-7 shows the CoF values for Regime 2 which is the medium pressure range. This regime includes tests with contact pressure between 20 and 70 ksi (137 - 482 MPa). Similar to Regime 1, in most cases, an increase in sliding speed reduces CoF. The effect of sliding speed on CoF was relatively low for the three speeds investigated because the speeds are relatively similar. Larger differences in sliding speeds may have been more of an impact because there is an increased chance for hydrodynamic lubrication to be experienced by the surfaces over larger ranges. However, as the connection will not experience speeds higher than 50 mm/s, increasing it was outside the scope of the project.

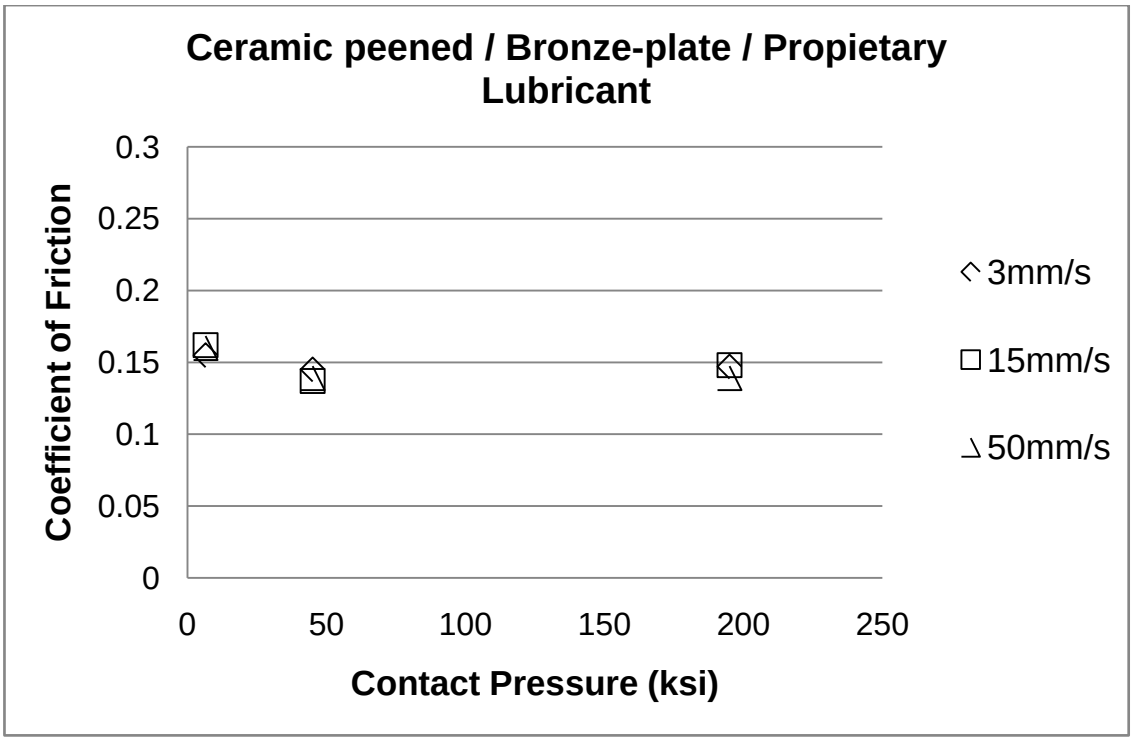

Figure 4-7: Comparison of three lubricants for Regime 2 tests

This shows a comparison between the three pressure regimes. The highest value of CoF occurs in Regime 3, within the lowest pressure regime. It was

expected that at the lowest pressure, there would be limited asperity-to-asperity contact, and therefore the load would be mainly carried by the lubricant. This could be due to the surface of those samples, which are not worn out as easily as those in Regimes 1 and 2 under higher contact pressure. CoF remains high in the second and third cycle, so the average of three cycles reported above becomes higher than those in Regimes 1 and 2. Whereas, in Regime 1 and 2 tests, the surface asperities were removed within the first cycle so that the CoF stabilises at a lower level.

Figure 4-7 also shows the effect of sliding speed on CoF in three different contact regimes. There was very little change between the CoF with modifications of speed at very low pressures shown in Regime 3. There is however a small reduction in CoF with increasing speeds in both Regimes 1 and 2.

According to Coulomb's and Amontons' laws of friction, the sliding frictional force is independent of sliding velocity **(3)**. This is predominantly true for cases of dry friction. Work done by Zwörner et al **(109)** looked at the effect of sliding velocity in point contact between different types of carbon compounds. The main outcome was that the frictional forces were independent of the sliding velocity even in instances of significantly lower speeds. The results were obtained using a friction force microscope which allowed the frictional forces to be investigated on a nano-scale. The research was based on the understanding that the tip moves with stick-slip type movement. During the slip section, the tip experienced very high speeds, and in the stick portion, it was stationary. It was

determined that as long as the slip movement of the tip of the microscope is faster than the sliding velocity, the friction will be independent of speed. It is important to note however, that this is only true when there is no lubrication between the two samples in contact. The velocities in Zwörner's tests are in the region of 50 to 800 times smaller than the velocity experienced by the surfaces during make-up of the connection, so this may explain the significant differences in CoF.

Investigation by Wang et al **(110)** showed that as the speed increased, both the wear rate and friction coefficient reduced. This was a consequence of the higher speeds producing a more efficient lubricating regime. This backs up the results experienced in this work, and the reason that in some tests CoF did not reduce may be because the efficiency of the lubricating regime did not improve. In the case of Regime 3, where the pressure was so low, an increase in speed did not make any difference to how the surface asperities reacted. This confirms that the hydrodynamic lubrication is not significant and that the mechanism is mainly boundary lubrication. It is noted that the surface roughness of the samples for Regime 3 tests is higher (c.f. **Table 4-3**) which facilitates side leakage during sliding. The effect of hydrodynamic pressure on the asperity flattening, or wear, is insignificant.

4.5 Effect of sliding distance on the CoF

The graphs in **Figure 4-8** to **Figure 4-10** show the effect of the sliding distance on CoF for a bronze plated surface with Lubricant A and ceramic peened arrangement. Initially, CoF is much higher than the average value and this

reduces as the sliding distance increases. At this point the CoF value levels out for the rest of the sliding distance. The initial surface roughness is significantly larger than the final roughness for the peened surface. The plated surface (bronze plated in this case) maintains a stable surface roughness throughout the entire testing method. The high CoF value in the first stroke of sliding is inferring the existence of galling and direct metal-to-metal contact.

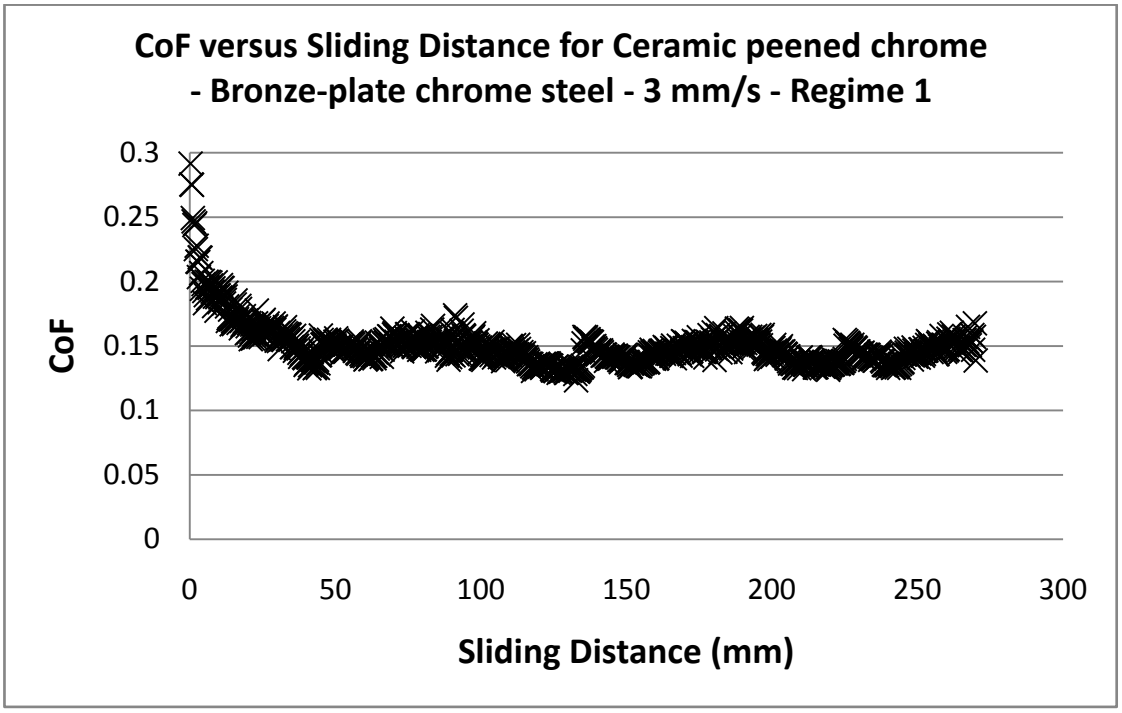

Figure 4-8: Effect of sliding distance on CoF at 3mm/s

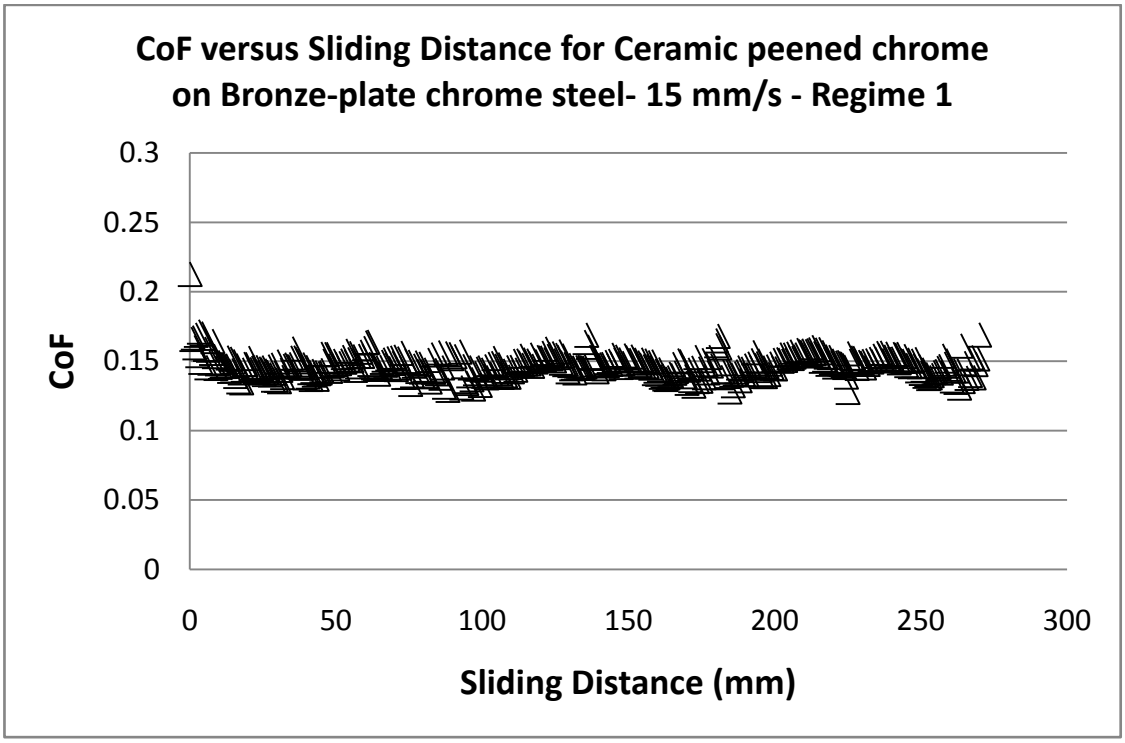

Figure 4-9: Effect of sliding distance on CoF at 15mm/s

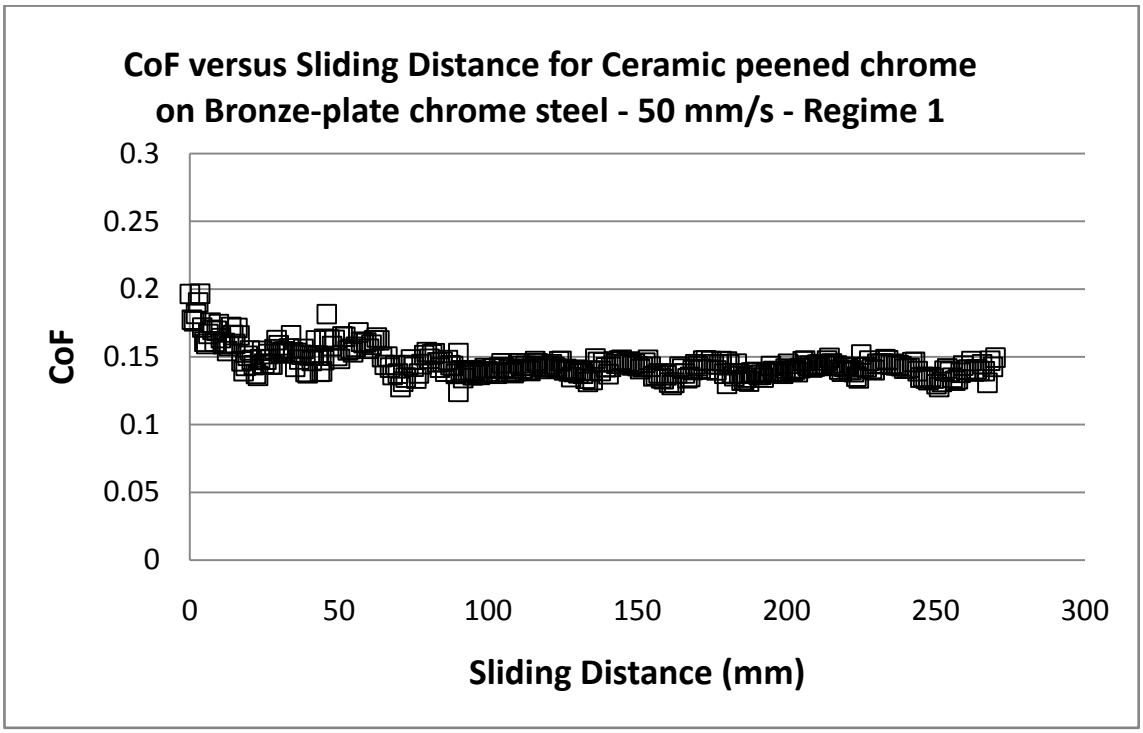

Figure 4-10: Effect of sliding distance on CoF at 50mm/s

This initial high CoF is much more dominant at the lowest speed. This is due to the fact that very little lubricant can be present in initial asperity contacts reducing the effectiveness of boundary lubrication. As the speed increases, a thin layer of lubricant can be entrained into the asperity contact improving the effectiveness of boundary lubrication. At each of the three speeds, CoF is higher for only a section of the first stroke, before stabilising for the remainder of the strokes; concurrently, the surface roughness reduces. Therefore, it is plausible to conclude that the lubrication improves as the sharp asperities are flattened. The general trend is similar to the work by Le et al **(111)** in the mixed lubrication regime in cold metal forming. Although the surface roughness in this case is much lower than that of the ceramic peened surface, there are similarities between the two. In the results of this project, the troughs become increasingly more isolated from one another and, compared with the linked valleys, the contact pressure in the valleys is much higher. However, it is assumed here that asperity crushing terminates when the asperity contact percolation is reached. Nevertheless, the only evidence to support this is that the initial surface roughness is very high; then after the first stroke and the subsequent strokes, the surface roughness levels out to a stable value. The bronze plated surface retains the same value of roughness after testing. From the surface images it can be shown (in Chapter 4 that the majority of this surface remains unchanged and only a thin wear mark is present on the surface after being tested. After the initial peened surface is burnished, the coefficient of friction is typical of the boundary lubrication mechanism.

For ceramic, coarser stainless steel and finer stainless steel peened surfaces, tested with the bronze plated surface and the Lubricant A, CoF values are similar. This is probably due to the fact that the surface roughness of each is comparable, and that the surface structure is relatively similar. In the case of the aluminium-oxide peened surface, the asperity diameter and depth is much larger than in the other cases. This means that the leakage of the lubricant during contact is more likely in the case of the larger connected troughs, therefore reducing the lubrication effect and increasing CoF. When the surfaces come into contact during the aluminium oxide test, the peaks on the surface are much higher and it is therefore considerably easier to scuff the counterface. The peaks on the peened surface are consequently in direct contact with the plated surface (c.f. **Figure 3-21**). The friction between the two surfaces is much larger than in the cases of lower surface roughness, as the asperities are in direct metal-to-metal contact.

4.6 Comparison of Lubricants

In addition to the experiments performed using Lubricant A (used during the majority of the project) additional testing was undertaken with two common industry lubricants, Lubricant B and Lubricant C. The properties were summarised in **Table 2.2**. A comparison of the three lubricants for a Regime 1 and Regime 2 test undertaken at 15 mm/s is shown in **Figure 4-11** and **Figure 4-12**.

Figure 4-11 shows the CoF results for Regime 1. The differences between the CoF values at this pressure range are minor. However, the larger CoF value is

for Lubricant A, which is of similar trend to Regime 2. In all cases, the CoF is initially higher and then decreases significantly. This is associated with surface burnishing explained in section 4.5. The initial high CoF was owing to galling due to the rough shot peened surface. Once the surface is burnished, the CoF becomes stable which is typical of boundary lubrication.

Figure 4-12 shows a similar overall CoF value for the two commercial lubricants compared to Lubricant A. Comparing the three, Lubricant B containing the metal particles has the lowest CoF. This could be caused by the fragments of metal filling gaps on the surface and producing more effective boundary lubrication. It is well known that metal particles such as lead or zinc have good stiction to steel surfaces and may generate a thin coating on the contacting surfaces avoiding direct metal-to-metal contact. Therefore Lubricant B provides effective boundary lubrication. Lubricant C contains a large amount of non-metallic solid lubricants which also generates a transfer layer on the peened surface. The CoF is similar to that of B. Although Lubricant A produces a higher CoF, it is stable after a short sliding distance. It is believed that the boundary additives would react with the fresh surface generated by mild galling. The CoF would have stabilised within the first make-up in a premium tubular connection and it does have the advantage of being environmentally friendly and less detrimental to the well.

It is noted that the decrease of CoF in Regime 2 is much slower than in Regime 1. This infers that the surface burnishing is slower in Regime 2 than Regime 1 due to the lower contact pressure.

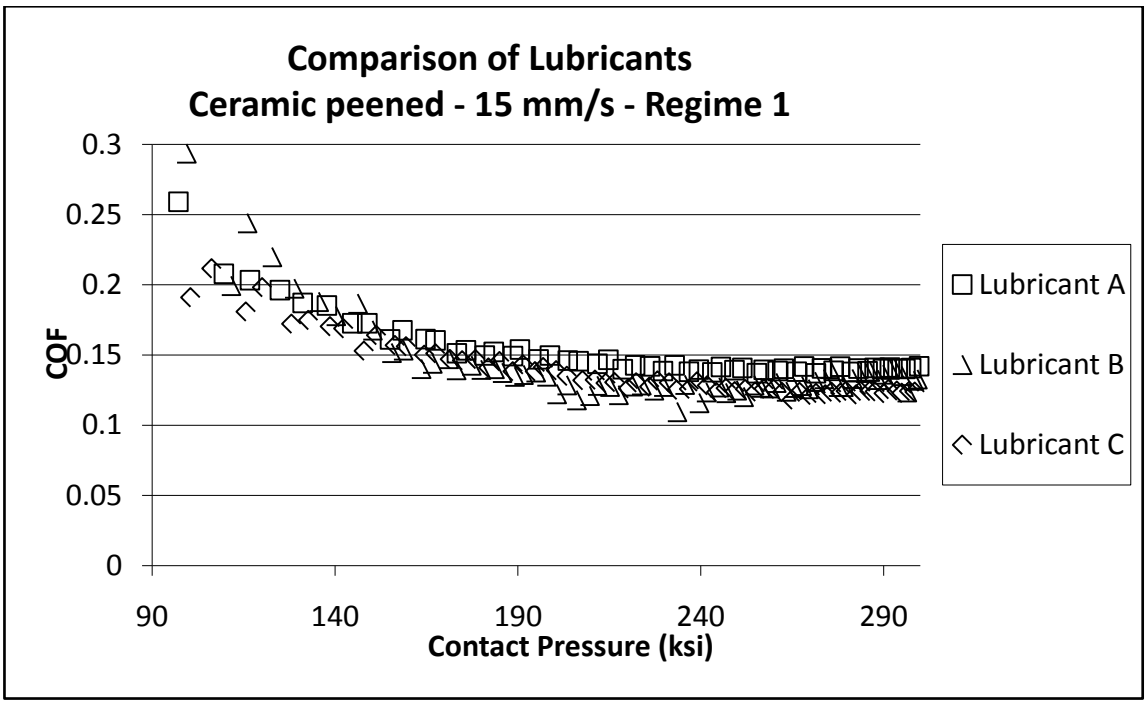

Figure 4-11: Comparison of lubricants for regime 1 test at 15 mm/s

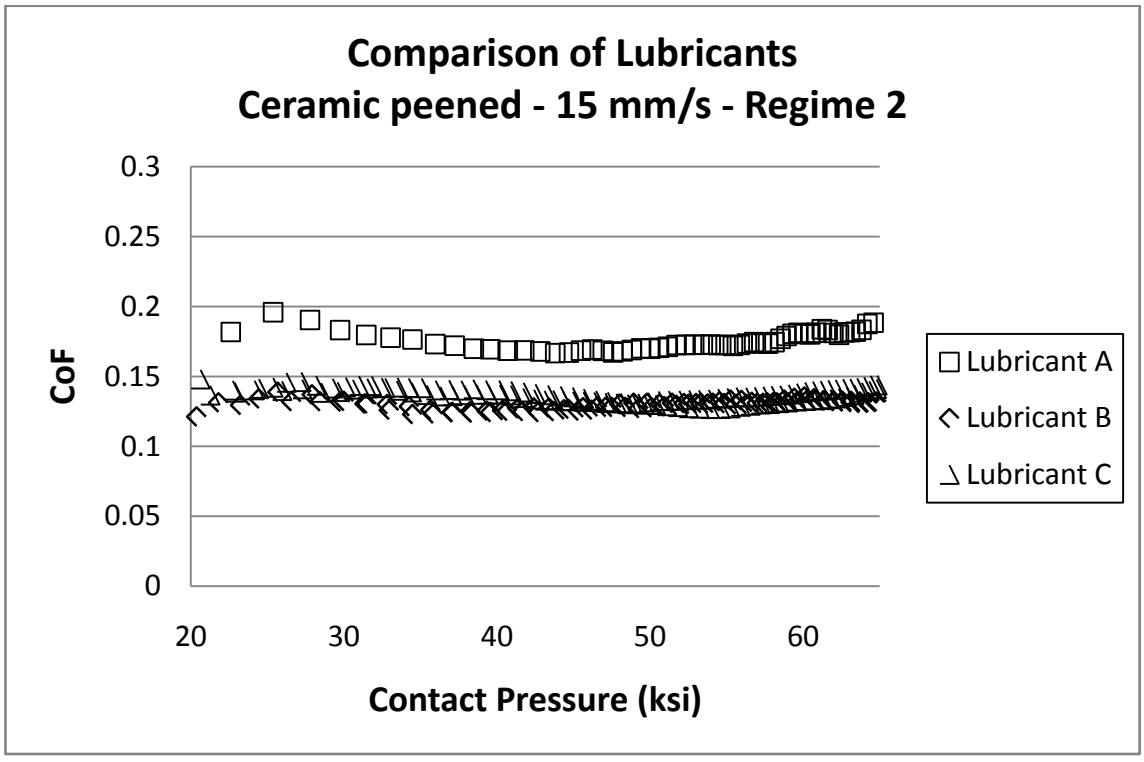

Figure 4-12: Comparison of lubricants for regime 2 test at 15 mm/s

4.7 Summary of CoF results

CoF tests were conducted in 3 contact regimes. The results showed that the lubrication regime is typical of boundary lubrication. Galling may have occurred at the beginning of sliding leading to a much higher CoF. However, the CoF stabilises while the peened surface is burnished. All peening media except aluminium oxide produce similar CoF value. The shot peened craters or pits store and distribute solid lubricant to the surrounding area which provides boundary lubrication in all contact regimes. Aluminium oxide peening causes deep craters and spikes which increase the risk of galling and hence increases the CoF significantly.

Chapter 5 : Modelling of Tribological Contact between Surfaces during Make-up Process

5.1 Modelling of tribological contact

One of the main objectives of the project was to develop a working model, capable of predicting the tribological behaviour of the contact between the surfaces in a premium tubular connection during the make-up process. In order to achieve this, some assumptions concerning the behaviour of the surfaces and generalisations regarding the material properties were also implemented. The friction, wear and surface roughness predictions from the modelling are presented. The solutions were validated using physical test results (found in Chapter 4).

To offer understanding of the experimental results, computer modelling is used as a method of cost efficiently simulating how variations in input affect the conclusions. Furthermore, they permit additional information to be added, allowing the estimation of supplementary results. If these methods can be corroborated, then the model can be used to predict outcomes in situations where a large scale physical test would be time and cost inefficient. Estimations using matrices of mathematical calculations have been around for centuries; however with the addition of large processing powers, computer simulations provide a much quicker and more accurate solutions. Computer modelling can be done in many different ways, including using software akin to MATLAB which manipulate matrices of data or by using Finite Element analysis (FEA) such as ANSYS or ABAQUS. The latter provides a solution where each point (or node)

in a model is defined by a series of equations and properties. A model was produced using the software to represent an object or surface of interest and at each point, a set of unknowns and equations are defined. These nodal calculations are subsequently computed to create a full scale model of results. Finite Element analysis can give very accurate results, however the computer processing power and memory required to obtain results in a reasonable time are very large. In order to obtain the most accurate models, each node in a simulation has to represent the subject.

Although useful, FEA can be time consuming and highly complex systems prove difficult to model. An alternative modelling method uses MATLAB (or Matrix Laboratory), which is a numerical computing program produced by MathWorks **(112)**. It is a software language that can provide an interactive setting in which programming, numerical computation and visualisation of matrices can be achieved. To obtain a solution, input data is entered as matrices. These matrices are processed by means of user-defined equations and all data is analysed to obtain an accurate solution to the problem. Instead of calculating only one value at a time (as done in traditional situations), the matrix allows a set of inputs to be computed. This is useful for situations where the values change or, in the case of material properties, where the height profile of a surface can be included in the calculation. The main disadvantage of this method is in the time taken to develop the program; however it does produce a far more accurate estimation of the project being investigated.

The three-dimensional surface readings obtained using the laser confocal microscopes (in Chapter 3) included a matrix of height profile. This meant that the roughness and surface profile after testing could be estimated using the correct equations and input of material properties. The surface profiles were measured both prior to, and after each cycle and following the frictional testing. These sets of data allowed experimental results to be compared with modelled data. In addition to this, the wear rate and wear volume could be estimated alongside to the coefficient of friction. This model has the capability to be very valuable in the future. It offers a potential tool which could be used by the operator, to understand and make appropriate changes to the torque value used during make-up, which would compensate for changes in operational conditions.

5.2 Wear model for surface burnishing

A wear model was created to allow the prediction of surface roughness variation, wear volume and actual wear area for a premium tubular connection. This model could be used to improve the calculation of torque for the make-up process in the oil and gas field. Connection make-up is where a pipe end is screwed into a coupling using a bucking unit which is controlled by a pre-defined torque value. In order to obtain this value, a CoF value is entered into a torque equation. The accuracy of CoF is significant because it is a major contribution in the torque computation equation (shown in Equation 1.11). However, since the current method of calculating the CoF does not take into account changes caused by the wearing of the surface, the value used could potentially cause under-torqueing or over-torqueing of the connection. The

program, in theory, could eliminate this problem by allowing a more precise estimation of CoF, which in turn would result in a more accurate torque value.

Being able to quantify and estimate this change in CoF could essentially provide a far more accurate value which in high-temperature, high-pressure circumstances could be the difference between a connection leaking or not. This reduces the opportunity for leak paths to occur at very high pressures and temperatures.

5.2.1 Archard's wear theorem

Wear occurs when two moving surfaces come into contact. The rate of wear and the amount of material removed during the sliding motion depends entirely on the situation that the two materials are in. Wear is also dependent on the type of lubrication that is experienced by the contact surfaces. Wear, friction and lubrication are dependent on each other. A classic wear model was based on Archard's theorem in which the wear resistance is proportional to the materials' hardness **(113)**. Archard stated that:

$$\frac{\boldsymbol{V}}{\boldsymbol{s}} = \boldsymbol{k}\frac{\boldsymbol{F_N}}{\boldsymbol{H}} \qquad \textbf{(5.1)}$$

Where $\boldsymbol{V}$ is the wear volume; $\boldsymbol{s}$ is the sliding distance; $\boldsymbol{k}$, the dimensionless wear rate which was used as a fitting parameter in the program; $\boldsymbol{F_N}$, the normal load; and $\boldsymbol{H}$ the hardness of the worn surface. This means that the wear volume is directly proportional to the normal force and inversely proportional to the hardness of the worn material (in this case the peened surface which is the

softer side). This equation therefore proposes the idea that the higher the normal force i.e. the higher the contact pressure, the greater the volume of material removed during sliding.

It can be rewritten as wear depth reduction rate as a function of sliding velocity, $\boldsymbol{v}$.

$$\frac{\boldsymbol{dh}}{\boldsymbol{dt}} = \boldsymbol{k}\frac{\boldsymbol{P}}{\boldsymbol{H}}\boldsymbol{v} \quad \textbf{(5.2)}$$

Where $\boldsymbol{P}$ is the contact pressure, $\boldsymbol{v}$ is the sliding velocity and $\boldsymbol{H}$ is the hardness. The wear coefficient $\boldsymbol{k}$ is regarded as a fitting parameter. The value for best fit of the surface roughness is $3x10^{-4}$ which is between the level of mild wear and severe wear.

As stated in the previous chapters, in order to achieve a representation of the sliding distance that the connection experiences during the make-up process, 100 mm long coupons and pins were manufactured with surface finishes representing the surface texture of the real products. The sliding distance of each test was 45 mm where the maximum force during the test was approximately 500 N. With the test procedure, the contact area was calculated using Equation (2.5) and this produced a contact pressure of roughly 70 MPa for the coupons. In a premium tubular connection, the thread load flank pressure is typically 70 MPa. In the wear model, the analysis was split into six sections, one for the loading and unloading portion of each of the three cycles. This gave a sliding distance of 270 mm which was representative of the linear

sliding distance of a 9” 7/8 diameter premium tubular connection during connection torqueing (make-up).

During the friction test (and in the make-up procedure), the surfaces come into contact and when this happens the peaks on the surface wear, therefore altering the characteristics of the surface. The load between the two surfaces in contact is shared between the asperities and the pressurised lubricant in the troughs on the surface. In simple terms, this means that:

$$\bar{p} = P_a A_a + P_v A_v \quad \textbf{(5.3)}$$

Where $\bar{p}$ is the total pressure during contact, P_a is the contact pressure between the asperities and P_v is the oil pressure in the valleys.

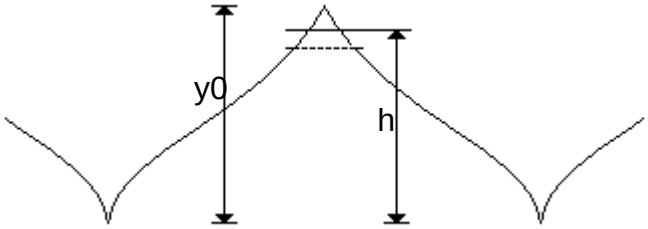

Figure 5-1: Normalised profile used to represent surface

To represent the real surface in a simplified manner, Christensen **(114)** introduced a model which was based on a stochastic or random rough surface. The surface was created primarily for model use, however it had the main characteristics of a real surface. This type of model was used to represent the real surface being investigated in the friction testing and was based upon a statistical distribution of height data. When two surfaces are touching, the area

of “real” contact is only a portion of the nominal contact area **(115)**. As contact pressure is equal to the force divided by the area, the actual contact pressure experienced on particular features (e.g. the peaks on the surface) is significantly higher than initially expected. This also means that on certain sections, particularly in the valleys of the asperities, the contact pressure is considerably lower than first believed. As this is a highly researched area of tribology, there are several techniques already available to investigate the contact area. To calculate the contact area, a function was implemented in MATLAB. This identified the surface height and shape of the asperities using statistical analysis of a Christensen model.

Figure 5-2 shows an example of the real ceramic peened surfaces of the pipe section used with the bronze plated surface and proprietary lubricant. These images were constructed using an Olympus LEXT 3D confocal microscope. Some shot blasting marks can be clearly observed on the surface and these occur in a very random pattern. These marks are created by means of shot blasting ceramic particles at the surface. This is used on the pipe section of the connection. The machining marks are no longer visible and the surface becomes almost isotropic compared the plated one.

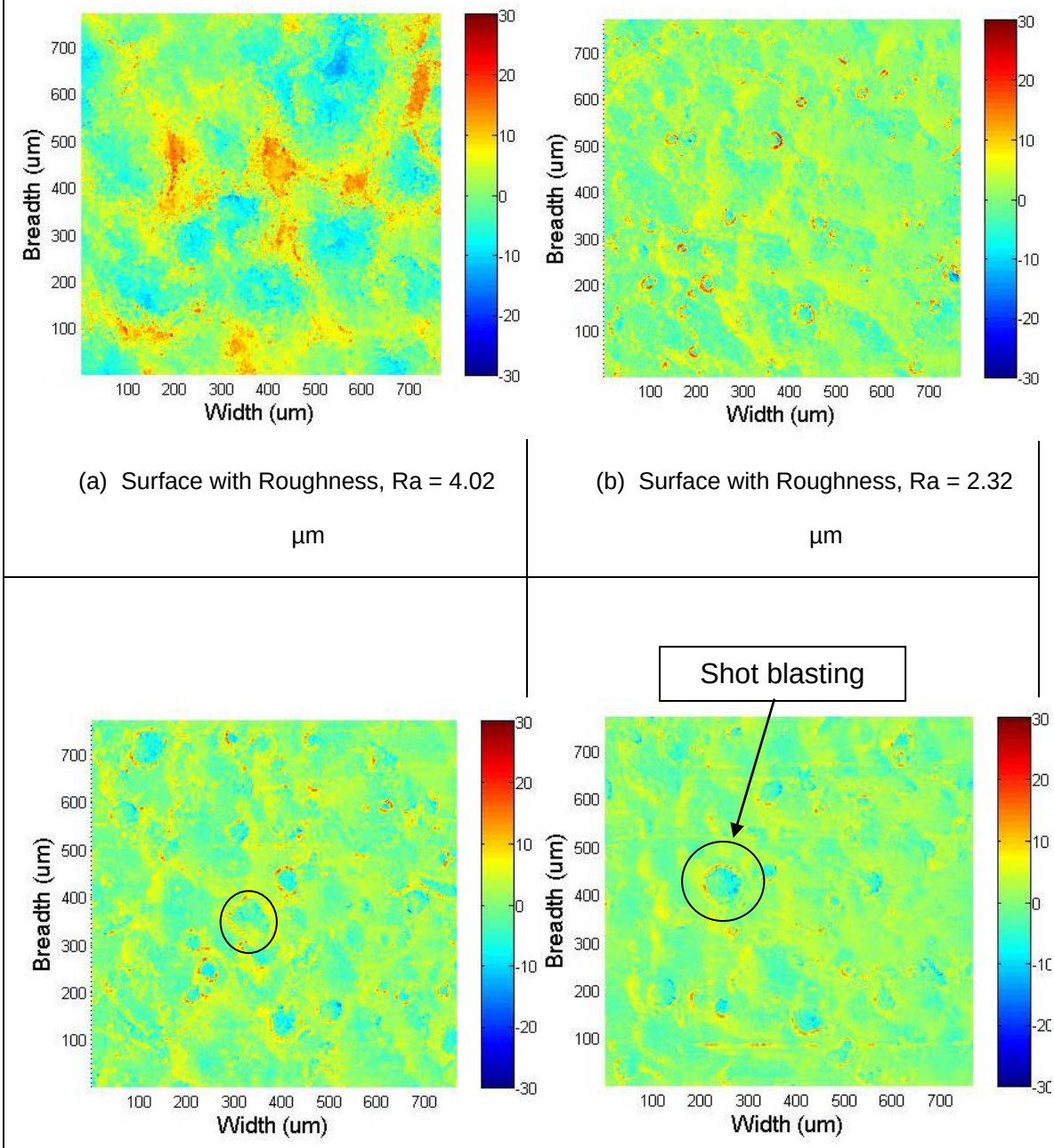

(a) Surface with Roughness, Ra = 4.02 µm

(b) Surface with Roughness, Ra = 2.32 µm

(c) Surface with Roughness, Ra = 2.21 µm

(d) Surface with Roughness, Ra = 1.95 µm

Figure 5-2: Olympus LEXT surface height images

One issue with the current manufacturing procedure is that there are no strict parameters set up to control the application process for peening. The length of time that the surface is shot blasted for is not defined, nor is the distance from

which blasting is performed. Variations of results in the process are dependent on the peening location and who performed it. Four different samples were compared in **Figure 5-3** and although the surface roughness of each sample was different, the pit percentage was very similar. Thus illustrating that the pit percentage was independent of the surface roughness and the samples had a similar percentage of surface pits. The surface area considered as a pit was similar in each case and the pressure in these valleys would not be affected by the shot blasting process characteristics.

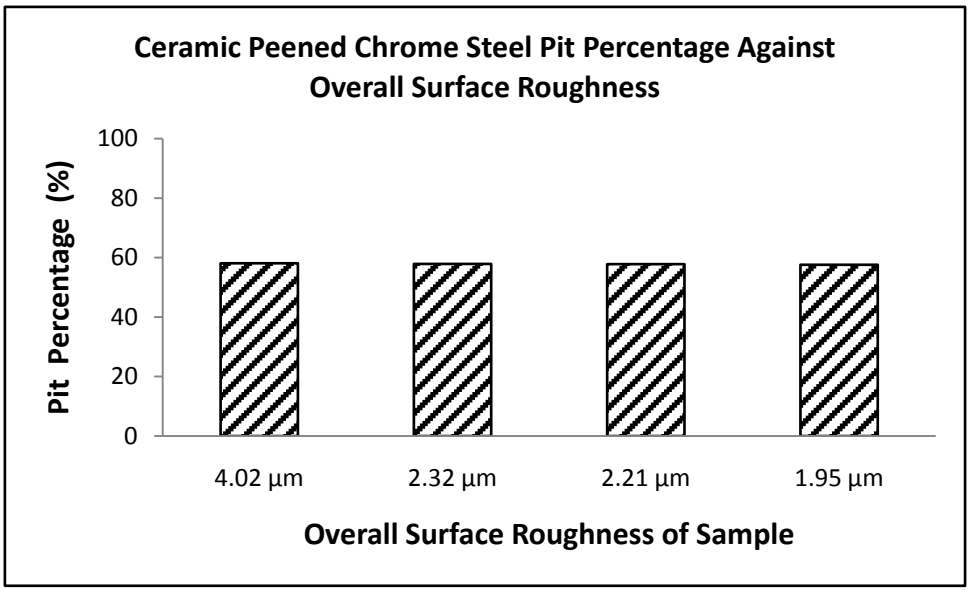

Figure 5-3: Comparison of surface characteristics between samples

Code was written to allow recognition of the height values in the areas around the highest peaks. This gave more information about the location of peaks and troughs and how high or low they were in relation to the surrounding environment. A value for what should constitute a pit was defined, and the same was done for a peak. This information then allowed the calculation of how much

of the surface was a valley and how much was a peak. This allowed conclusions of the ratio of valleys to peaks to be drawn.

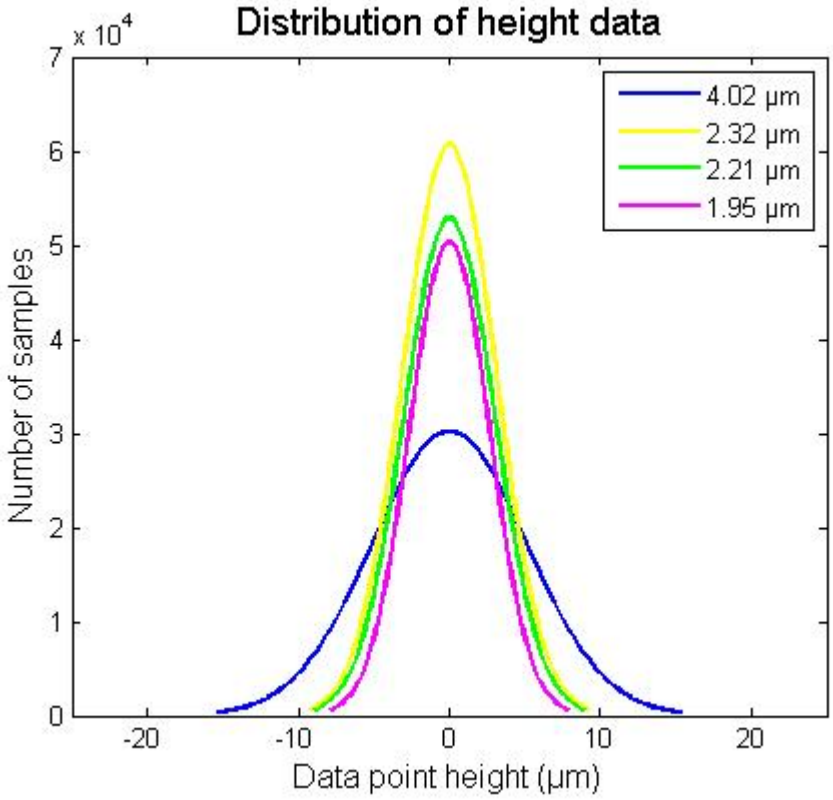

Figure 5-4: Height data distribution for 4 ceramic peened chrome steel samples

Figure 5-4 shows a distribution of the surface height data for four samples with different arithmetic average surface roughness values. Note that the total number of pixels of each measurement is the same. For the sample with the largest surface roughness, there are a larger number of higher peaks and deeper troughs. This is expected because, in this case, the deeper pits were probably produced due to larger peening media particles being blasted at the surface. Where the peaks are higher, the material movement must have been much larger than that of the smaller valleys and this movement of material produced the larger peaks on the surface. In the case of the other samples,

where the surface roughness is similar (approximately 2 μm), the number of baseline height values is higher and the number of larger peaks and troughs reduces. This means that in the cases of lower roughness values, the height of the surface is more concentrated around the base line which was altered by peening.

5.2.2 Asperity flattening and percolation

From Williams' "Engineering Tribology" **(1)** the load can be obtained using the equation:

$$\boldsymbol{W = \bar{p} * \pi^3 * \left(\frac{3R}{4E^*}\right)^2} \quad \textbf{(5.4)}$$

Where $\boldsymbol{\bar{p}}$ is the mean pressure, $\boldsymbol{W}$ is the normal load acting on the surface, $\boldsymbol{R}$ is the reduced radius of contact and $\boldsymbol{E^*}$ is the contact modulus. This equation was proven to be applicable for elastic deformation of a surface. Provided that the surface experiences elastic deformation, the following holds true.

Rearranging this gives the mean pressure to be:

$$\boldsymbol{\bar{p} = \frac{1}{\pi} * \left(\frac{16 * W * E^{*2}}{9 * R^2}\right)^{\frac{1}{3}}} \quad \textbf{(5.5)}$$

Work by Patir and Cheng **(116)** gave the following set of equations used to calculate the lubricant characteristics in a contact between two rough surfaces. Because the sliding speed is low, it is assumed that the lubricant flow rate, $\boldsymbol{q_x}$, is mainly driven by the pressure gradient as :

$$q_x = \phi_x \frac{h_t^3}{12\eta} \frac{dP_v}{dx} \quad \textbf{(5.6)}$$

Whereη is the oil viscosity, h_t is the mean oil thickness, P_v is the valley lubricant pressure and ϕ_x is the flow factor per unit width.

The flow factor per unit width for a rough contact is calculated using the equation:

$$\phi_x = \left[a_2(H_t - H_{tc})^2 + a_3(H_t - H_{tc})^3\right]/h_t^3 \quad \textbf{(5.7)}$$

Where

$$H_{tc} = 3\left[\left(1 - \left(0.47476/\gamma\right) + 1\right)^{-0.25007}\right] \quad \textbf{(5.8)}$$

$$a_2 = 0.051375(\ln(9\gamma))^3 - 0.0071901(\ln(9\gamma))^4 \quad \textbf{(5.9)}$$

$$a_3 = 1.0019 - 0.17927\ln(\gamma) + (0.047583\ln(\gamma))^2 - (0.016417\ln(\gamma))^3 \quad \textbf{(5.10)}$$

Where γ is the Peklenik number which identifies the roughness pattern of the surface, H_t is the ratio of the average film thickness h_t is the r.m.s surface roughness R_q, H_{tc} is the percolation threshold value of H_t. It is a measure of the remaining asperity height compared to initial surface height when the surface valleys are isolated **(117)**.

According to Hamrock and Dowson **(118)**, the central lubricant film thickness h_{cen} with a point contact can be derived from the relationship

$$h_{cen} = 3.34R\left(\frac{\eta u}{E' R}\right)^{0.64}\left(\frac{W}{E' R^2}\right)^{-0.22} \quad \textbf{(5.11)}$$

Where η is the viscosity of the lubricant and u the entraining speed (in this case half of the speed of sliding). The lubricant film thickness decreases with increasing load and hence the increase in the 'real' asperity-to-asperity contact ratio.

The ratio Λ of lubricant film thickness to combined r.m.s surface roughness is often used as a lubrication parameter and given by

$$\Lambda = \frac{h_{cen}}{\sqrt{{R_{q,1}}^2 + {R_{q,2}}^2}} \quad \textbf{(5.12)}$$

Where $R_{q,1}$ is the r.m.s roughness of top sample surface and $R_{q,2}$ of bottom sample surface. The values of Λ associated with the current tests are summarised in **Table 5-1**, based on a sliding velocity of 15 mm/s.

Table 5-1: Lubrication parameter for the tests performed at 15 mm/s

	Pin-on-pin Regime 1		**Coupon-on-coupon Regime 2**	
Surface treatments	As-machined	Ceramic peened	As-machined	Ceramic peened
Lamda ratio Λ for *W*=500N	0.426	0.356	0.754	0.648

The average amplitude based on the Christensen model of surface roughness **(114)** is about 3 times the r.m.s roughness. When $\Lambda > 3$, the lubricant film is larger than the average amplitude of surface roughness so that the contact surfaces will be separated by a full or hydrodynamic film. When $\Lambda < 0.3$, the average lubricant film thickness is below a tenth of the amplitude of the surface roughness so that the asperity-to-asperity contact ratio will be large, and boundary lubrication will be dominant. **Table 5-1** indicates that in many cases Λ is close to 0.3 with a maximum load of 500 N in current tests so that boundary lubrication dominates. It is expected the hydrodynamic factor is small compared to hydrostatic factor under these conditions. The oil removal from the contact will be dominated by the leakage driven by the hydrostatic pressure gradient. There are more sophisticated models available which can solve coupled hydrostatic and hydrodynamic flow in two-dimensions. For simplicity, the hydrodynamic effect is not included in the current model.

A schematic of the lubricant flow is shown in **Figure 5-5**. As a first approximation, the hydrostatic pressure gradient is assumed as constant:

$$\frac{dP_v}{dx} = \frac{P_v}{a} \qquad \textbf{(5.13)}$$

Where $P_v$is the hydrostatic pressure at the centre of the contact patch, and a is the radius of contact. The side leakage rate through the contact edge can be derived by combining this equation with Eq. 5.6:

$$q_x = \phi_x \frac{{h_t}^3}{12\eta} \frac{P_v}{a} \qquad \textbf{(5.14)}$$

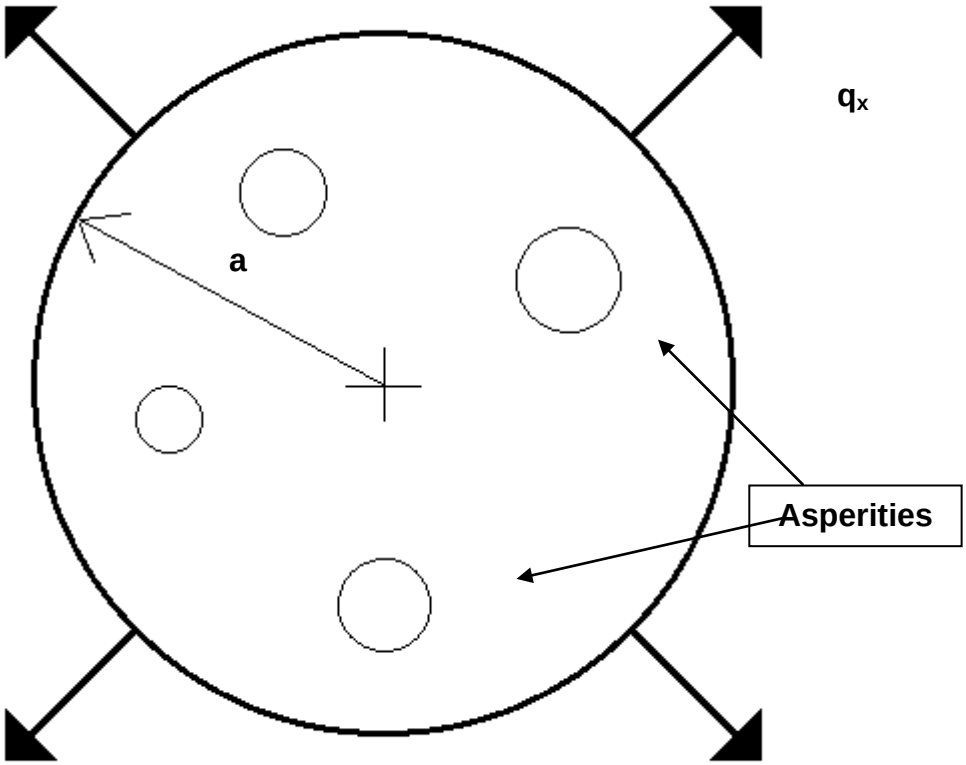

Figure 5-5: Contact area during friction test

For simplicity, it is assumed that the contact is circular and the surface roughness is isotropic. Therefore the flow rate is axisymmetric. The reduction in lubricant volume in contact patch due to leakage is given by:

$$\frac{dV}{dt} = 2\pi a q_x = \frac{\pi \emptyset_x h_t^{\,3} P_v}{6\eta} \qquad (5.15)$$

The volume reduction of the entrapped lubricant within the contact patch is also related to the reduction of asperity height due to wear described in section 5.2.1.

$$\frac{dV}{dt} = \pi a^2 (1 - A) k \frac{P_a}{H} v \qquad \textbf{(5.16)}$$

Therefore the pressure in the valleys can then be derived by combining Eq. 5.15 and 5.16 as:

$$P_v = \frac{6\eta a^2 \left(k \frac{P_a}{H} v\right)(1 - A)}{\phi_x {h_t}^3} \qquad \textbf{(5.17)}$$

As the sliding distance and wear area increases, the pressure in the valleys becomes more prominent than in the initial cycles. The proprietary lubricant has a viscosity of 50,000 cP (50 Pa.s). Solving Equations 5.3, 5.16 and 5.17 continuously with sliding distance will yield the variation of asperity height h, asperity contact ratio A, valley pressure $P_v$and asperity contact pressure P_a.

Figure 5-6 shows the difference between the pressure on the asperities and the pressure in the valleys for the first cycle of the friction test. The asperity pressure is greatly more significant than the valley pressure at the first stroke and becomes more prevalent in the second stroke as the contact ratio increases.

Another consequence of wear is the reduction in asperity height and the increase in the contact ratio with sliding distance. **Figure 5-7** shows a comparison between the sliding distance and the asperity height, and also the contact ratio. This comparison is for the first cycle, showing both loading and unloading. As the sliding distance increases, the asperity height reduces and as the sliding distance increases the contact ratio, i.e. the area of contact between the two surfaces, also increases.

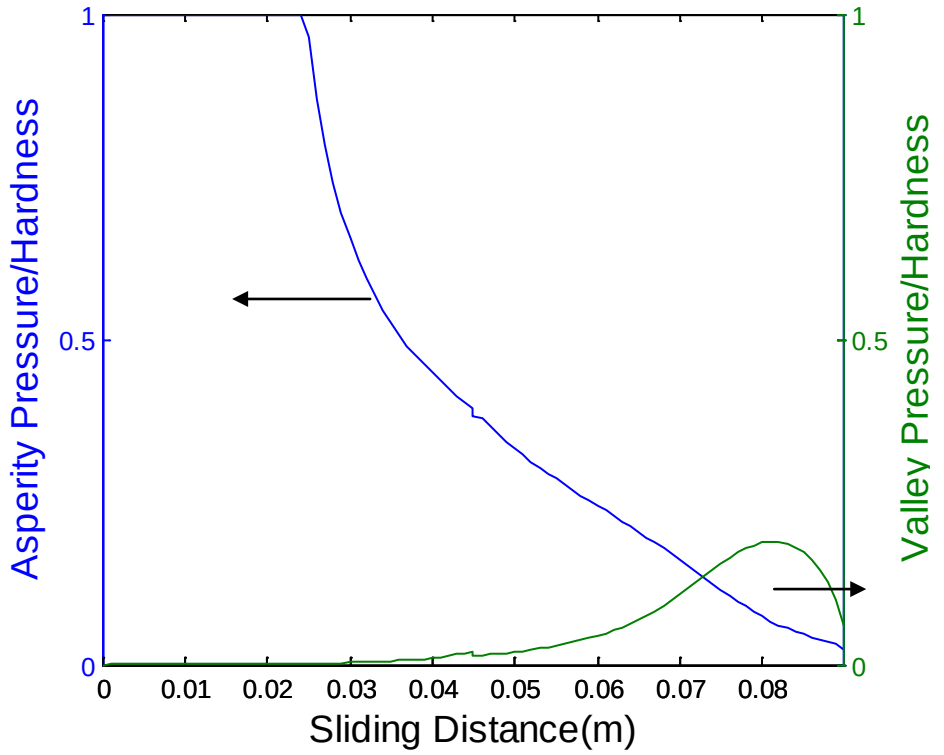

Figure 5-6: Cycle 1 – comparison of asperity and valley pressures for cycle 1 in friction test

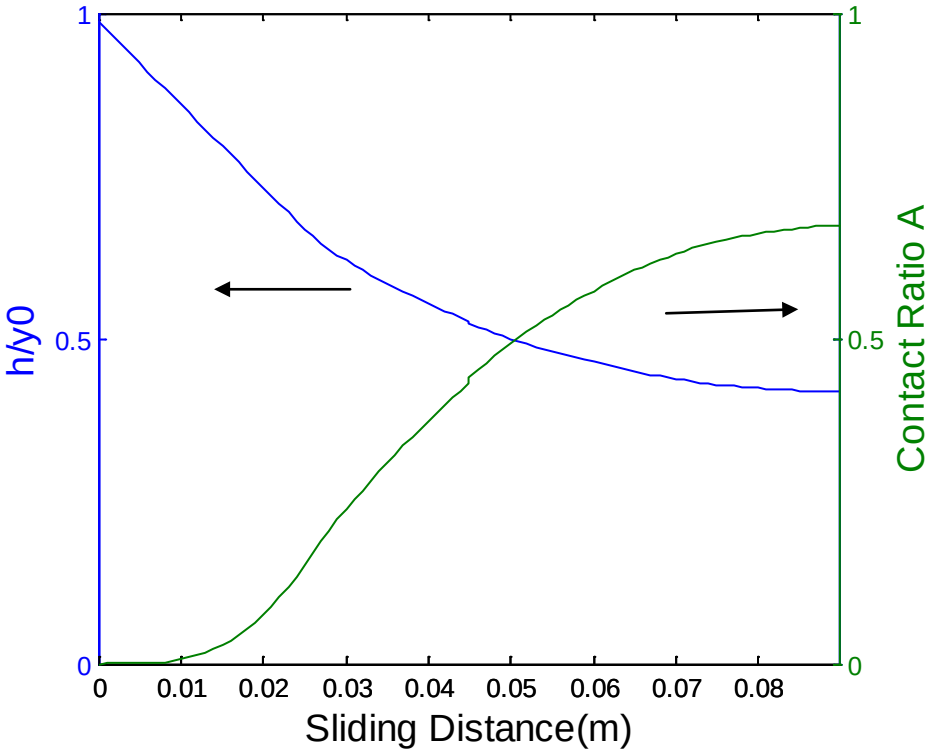

Figure 5-7: Comparison of asperity height and contact area for cycle 1 in friction test

Carbone et al **(119)** compared existing theories of contact between surfaces and evaluated the differences in accuracy. The authors looked at theories from the major contributors to contact theory and compared the advantages that were given to the knowledge.

It is noted that hydrostatic pressure remains low until the asperity contact percolation is reached which leads to rapid increase in lubricant pressure and decrease in asperity pressure. Hence the wear of the asperity will diminish. The percolation threshold depends on the Peklenik number. For a non-directional surface, the Peklenik number is 1. The real surface can be described as practically non-directional due to the spherical shape of the peened asperities on the surface, however the plated surface has initial machine marks in transverse to the sliding direction. Therefore the initial contact cannot be described as non-directional. After the first stroke of sliding, galling marks will be present on the plated surface. The surface will become more isotropic.

This allows for the prediction of the $\boldsymbol{R_q}$ value for the shot peened surface. As shown in **Figure 5-8**, the asperity wear diminishes after the first cycle so that surface roughness stays constant. This is because the contact percolation is reached and hence the valley pressure increases rapidly. This is in agreement with the results taken from the samples after the first cycle but the discrepancy increases after subsequent cycles. This indicates that the lubricant can still escape after the percolation threshold is reached. It has been demonstrated previously by Lo and Wilson **(120)** and Le et al **(82)** that lubricant can still be drawn out of ‘micro-pools’ by relative sliding. Nevertheless, the current model

does capture the mechanism which leads to the main reduction of the surface asperities. The focus is then switched to the study of the friction.

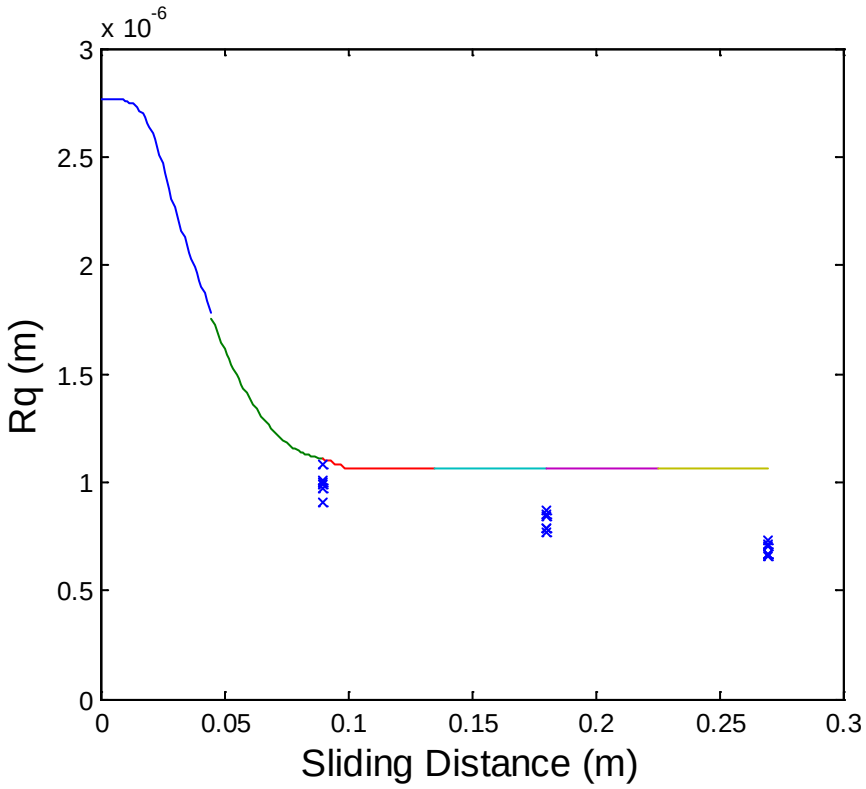

Figure 5-8: Effect of sliding distance on RMS roughness for surfaces with γ = 1

5.3 Friction model

As stated by Le et al **(121)**, a correct value for CoF is vital in the estimation of roll load and torque in rolling methods, however generally a constant value is used. This is true for most OCTG pipe connections. The value is taken from a set of API Standards and an accurate value is not predicted for each individual condition of the connection. According to the API 7G Recommended Practice **(122)**, CoF between mating surfaces, i.e. threads and shoulders, is predicted to be 0.07 - 0.08; this is true for thread compounds containing 40 – 60 wt% of finely metallic zinc. However, there is no information in this standard which

specifies the lubrication regime, contact pressure, sliding speed or surface roughness of either of the two mating surfaces.

It is therefore inaccurate to presume that all surfaces would have the same value of CoF associated with them. A new value is not calculated each time and therefore it is not dependent on how many times the connection has been made-up previously. This means that most likely, the value of torque calculated from the CoF is not accurate. Although this may cause no difference to pipes in some sections of the production string, the value could have catastrophic problems in the future where the depth of the wells and the associated temperature and pressure increase significantly. Although largely over-torqued connections should be noticeable to the inspector, if the plastic deformation is small, this can easily be missed.

A friction model was therefore produced to allow the calculation of the friction coefficient with changes in surface roughness after testing. From the experimental results it can be shown that as the sliding distance increases, the surface roughness reduces to a certain point. The same occurs with the friction; initially the surface roughness and friction are high but as the surface wears and the roughness reduces, stabilise to a more constant value.

Identifying the main features on the surface is a useful technique to help understand the structure of the surfaces in contact. The peened surface typically has the largest value of roughness and therefore the source of the value of CoF. It has been proven that for two surfaces of the same material, the

one with the highest roughness also has the highest CoF. From the SEM and microscopic images, the surface features can be visually identified. It was the work of Ahmed and Sutcliffe **(68)** that recognised the necessity for being able to quantify these features. They produced a MATLAB code which was capable of ascertaining which characteristics were peaks and which were troughs on the material surface. Providing that the correct threshold values were supplied in the code, algorithms were used to identify pits and roll marks in the surface.

This technique was modified to fit the surface characteristics of the samples used in the current project to identify the pits on the peened surfaces. The area fraction of pits was calculated for the initial shot peened sample and after each test cycle. The results are shown in **Figure 5-9**. It is found that the size of the pits decreases but the pit area ratio is approximately 0.50 even after the fourth cycle. This means that the large pits are broken into small pits but the area ratio remains more or less constant.

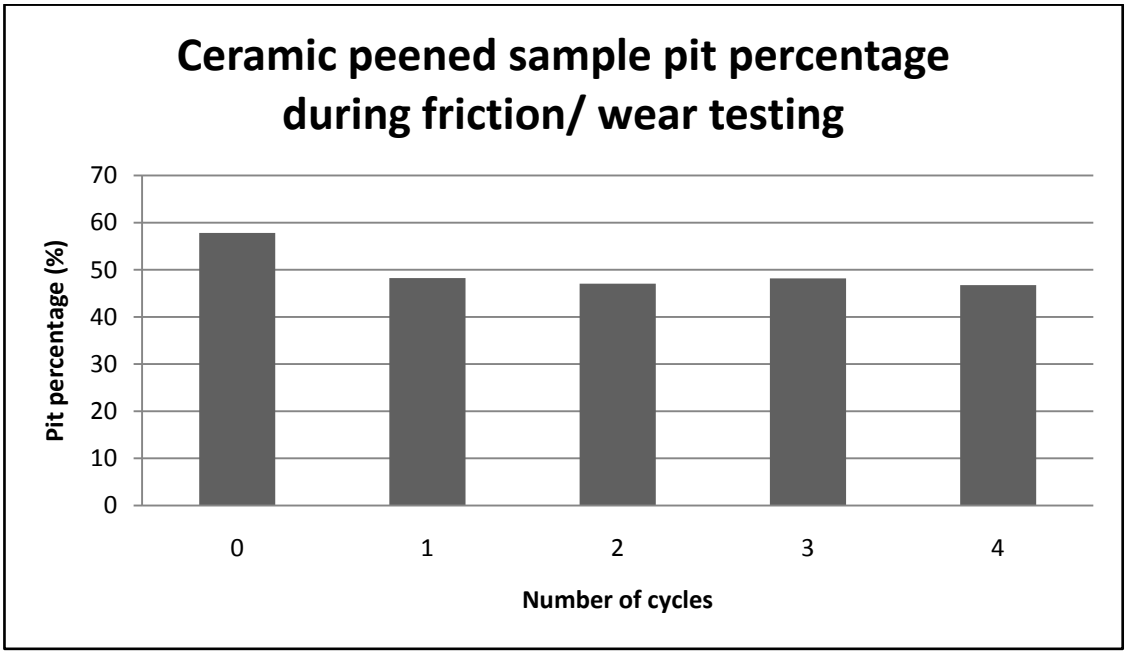

Figure 5-9: Ceramic peened sample pit percentage during friction/wear

Similar to the work done by Sutcliffe et al **(88)**, the steel material was shot blasted with beads of a chosen material, resulting in the creation of pits on the surface. Both are operated at low speed and in the boundary lubrication regime. During the sliding of two surfaces in contact, the same motion experienced by the connection during the make-up process, there is movement of the lubricating film between the two surfaces. The difference however is that there is bulk plastic deformation in the drawing process so that the asperity flattening is different. To understand this movement and appreciate how it works, the mechanism described in this paper was micro-plasto-hydrodynamic lubrication (MPHL). MPHL is where the lubricant is drawn from the craters by relative sliding due to the wedge effect while the surface is plastically stretched. This process results in the creation of a very thin film with boundary additives on to the asperity contacts.

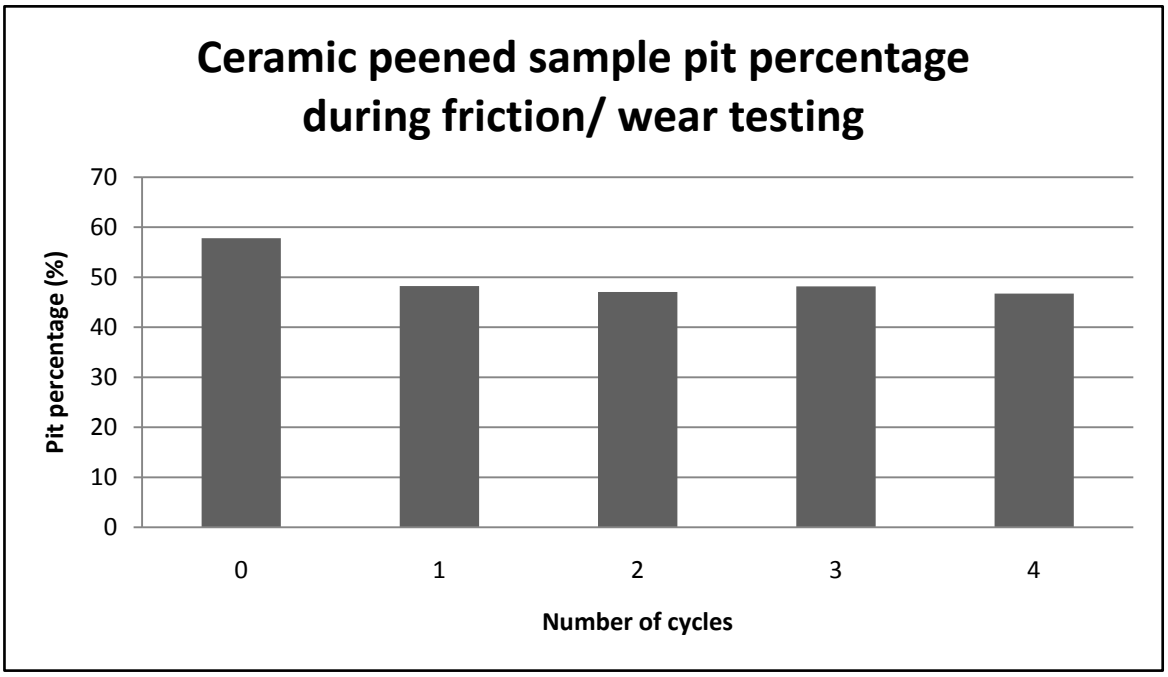

Figure 5-10: Pit percentage comparison for each cycle

The work done by Sutcliffe et al **(88)** was based upon the model by Lo and Wilson **(120)**, which was developed to help understand the lubricant flow in the "contact between a smooth tool and rough work-piece" **(88)**. Sutcliffe et al applied the model to cold rolling and drawing processes to predict how the surfaces react to the pressure change during movement.

When the lubricant in the pits is isolated as the asperity contact percolation is reached, it is assumed that it is a uniform pressure which is applied to the material surface as shown in **Figure 5-11** (a). When lubricant is drawn out of the pits, the valley pressure will drop while the asperity increases as shown in **Figure 5-11** (b). The localised pressure for (b) is significantly higher for the plateau section and lower in the troughs where the oil film was present. The maximum pressure of the plateau is however limited by the indentation limit of the material.

Using the same procedure as Sutcliffe et al **(88)**, the expression for the film thickness can be stated as:

$$\boldsymbol{h_1 = \frac{6\eta\alpha\overline{u}_1}{\theta\left(e^{-\alpha P_v} - e^{-\alpha P_p}\right)}} \qquad \textbf{(5.18)}$$

Where $\boldsymbol{\theta}$ is the pit angle, $\boldsymbol{\eta}$ is the viscosity of the lubricant, $\boldsymbol{\overline{u}_1}$ is the mean velocity at the edge of the pit, and $\boldsymbol{\alpha}$ is the pressure viscosity index.

This expression takes the pressures in the valleys $(\boldsymbol{P_v})$ and pressures on the asperities $\left(\boldsymbol{P_p}\right)$ into consideration, where the oil film thickness height was deemed much smaller than the depth of the valleys.

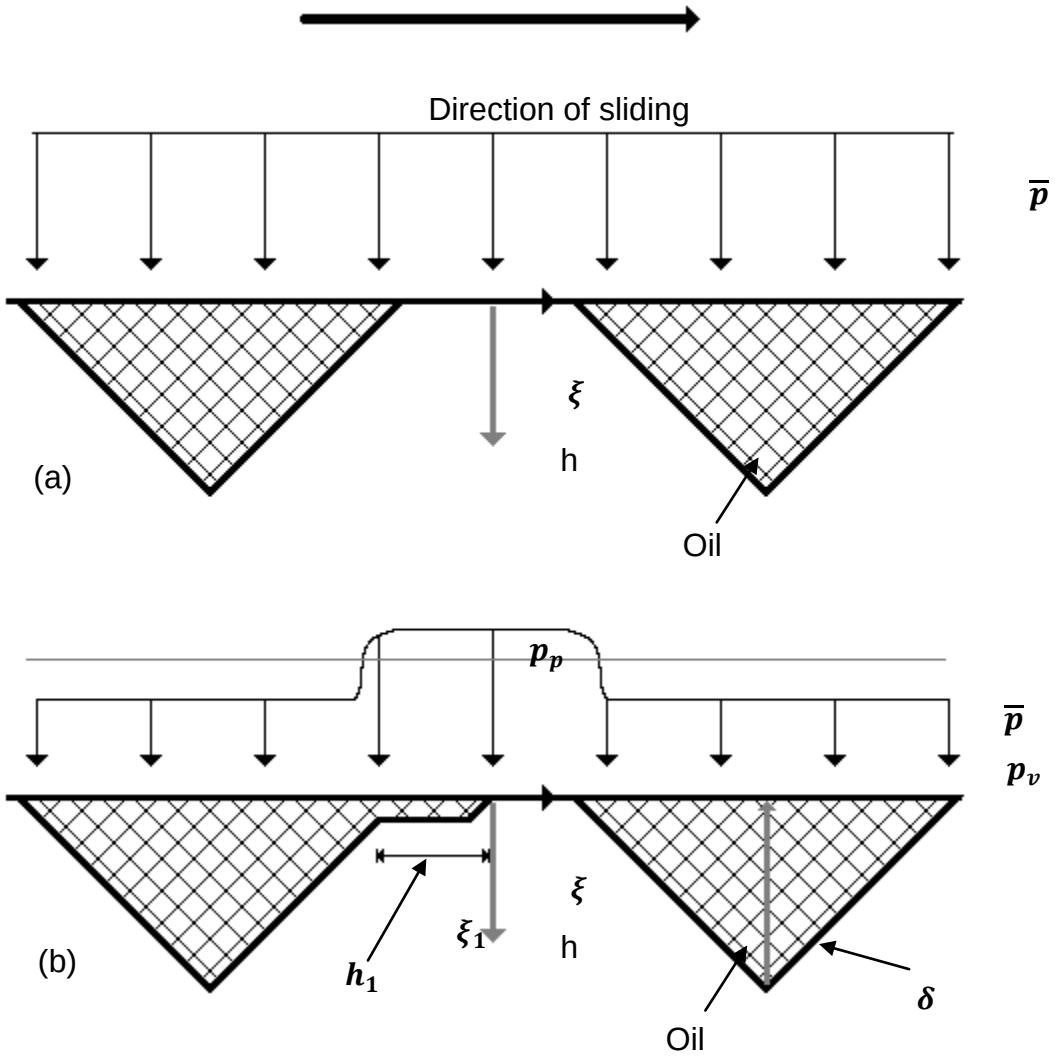

Figure 5-11: Micro-pit arrangement for (a) Geometric calculation of pressures using uniform contact pressure and (b) Hydrodynamic calculation of pressure where oil is drawn out (88, 120)

As a lower boundary estimation proposed by Le et al **(82)**, the film thickness on the plateau can be derived as:

$$h_1 = \frac{6\eta\alpha\overline{u}_1}{\theta\left(1 - e^{-\alpha P_p}\right)} \quad \textbf{(5.19)}$$

The average friction coefficient $\overline{u}_1$ can be calculated by combining the CoF on the plateau and within the valleys. This overall CoF is calculated using Equation

(5.20). This is done so by considering friction on the plateau. In this case, the CoF on the valleys is significantly lower than that on the plateau and is therefore regarded to as being negligible. Consequently, it is not included in this equation.

$$\boldsymbol{\mu = A_p \mu_p} \quad \textbf{(5.20)}$$

Where $\boldsymbol{A_p}$ is the area ratio of the plateau and $\boldsymbol{\mu_p}$ is the coefficient of friction on the plateau.

Equation (5.21) is used to calculate the CoF on the plateau. This incorporates the friction at the boundary contact $\boldsymbol{\mu_b}$ with the friction coefficient of the lubricant $\boldsymbol{\mu_v}$. Each is multiplied by the area ratio concerned with each section. $\boldsymbol{A_r}$ is the area ratio of the metal-to-metal contact and therefore $(\boldsymbol{1 - A_r})$ is the area ratio of the thin film lubricant.

$$\boldsymbol{\mu_p = A_r \mu_b + (1 - A_r)\mu_v} \quad \textbf{(5.21)}$$

The boundary friction coefficient $\boldsymbol{\mu_b}$is regarded as a fitting parameter. $\boldsymbol{A_r}$is determined by the lubricant film thickness and the surface roughness on the plateau which is given explicitly for each specific surface profile (**123**). The friction coefficient of the lubricant thin film is calculated using Eyring's equation.

$$\boldsymbol{\mu_v = \frac{\tau_0}{\bar{p}} sinh\left(\frac{(\eta v)}{\tau_0 h_1}\right)} \quad \textbf{(5.22)}$$

Where $\boldsymbol{\tau_0}$ is the Erying shear stress of the lubricant, $\boldsymbol{\bar{p}}$ is the mean contact pressure, $\boldsymbol{h_1}$ is derived by Equation 5.19.

The parameters used in the calculation of the average CoF are summarised in **Table 5-2**.

Table 5-2: Model parameters

Parameter	**Value**
Contact Modulus, E*	113 GPa
Contact Radius, R*	60 mm
Vicker's Hardness, H	2.6 GPa
Initial Surface Roughness of top sample, $R_{q,1}$	2.80 μm
Initial Surface Roughness to bottom sample , $R_{q,2}$	2.8 μm
Angle of Asperity, θ	10°
Area ratio on the plateau, Ap	0.45
Wear Rate, k	3 x 10^{-4}
Coefficient of Friction on the boundary layer, μ_b	0.6
Eyring's Shear Stress, τ_0	2 MPa
Viscosity, η	50 Pa.s
Viscosity pressure index, α	3.88 x 10^{-8} /Pa

In order to produce a model which was in line with the actual results obtained during the physical testing, a number of assumptions had to be made. One hypothesis was that the type of wear which occurred during the sliding was somewhere between severe and mild wear. Therefore, as severe wear occurs with a wear coefficient in the range of around 1x10^{-6} and mild wear at around 1x10^{-2}, using best fit parameters the wear coefficient used in the program was 3x10^{-4}. The initial coefficient of friction predicted on the boundary layer was 0.6 as this was assumed to be metal-to-metal contact. The proprietary synthetic film lubricant had a viscosity of 50 Pa.s which was obtained from the Data Sheet provided by the manufacturer. In order to determine the Eyring shear stress value, a lubricant with a similar viscosity was used as reference. The surface roughness of the sample was measured using the techniques noted in Chapter

3 prior to friction testing, and measurements were taken between each cycle during the tests. This gave a series of results along the sliding distance which could be compared with the outcome of the model. The area ratio on the plateau was obtained from the wear model results described in the model above. The contact radius was obtained from the size of the samples used in the friction tests. In this case, the coupons were used, which meant that the radius was 60 mm. The hardness value was obtained through testing and the results of this are shown in Table 4-2. The softer material (ceramic peened) surface was taken as the hardness value for the system because this is the surface which was changing during sliding. The angle of asperities was estimated to be approximately 10°. **Figure 5-12** shows the result of the friction model. The initial CoF is approximately 20% higher than the final CoF. The graph shows two different tests, both run at 15 mm/s. As friction calculation is not an exact science, there are a lot of variations in the final results. However, the general trend of reducing CoF with increasing sliding distance can be seen. The trend line has been calculated in MATLAB and shows the relationship between the sliding distance and CoF. This result mirrors what has been seen during the physical experiments, and the significance of these results may provide a system which could be used to determine CoF accurately without the need for large scale physical testing.

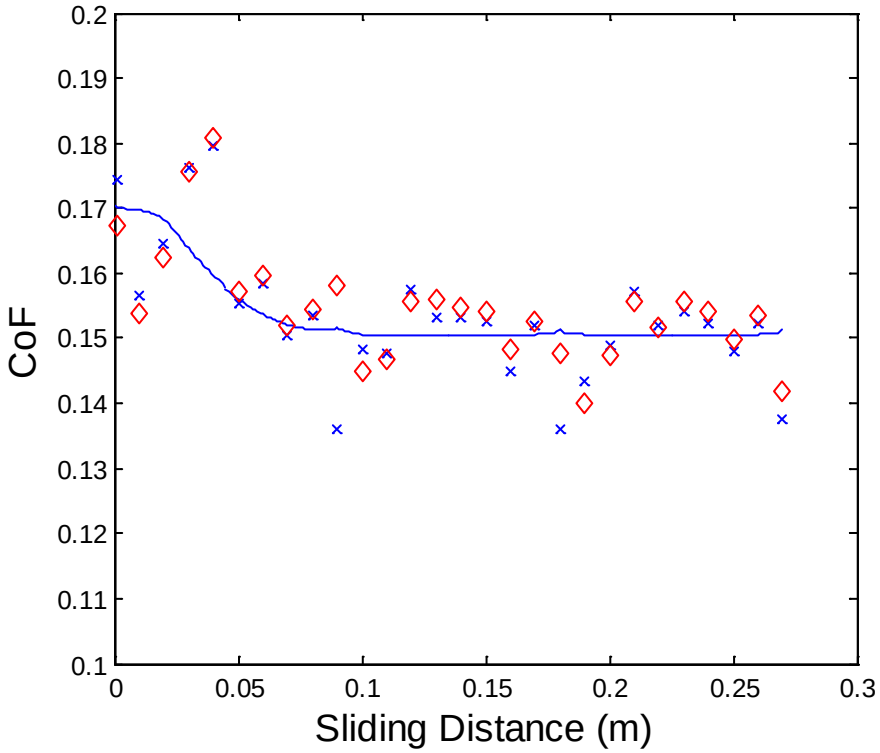

Figure 5-12: Friction model for Clear-Run system at 15 mm/s

5.4 Summary of friction and wear modelling

The work in this chapter provides a simplified model to predict the evolution of shot peened surface roughness due to asperity wear. The process is terminated as the asperity contact percolation is reached. The predictions of surface roughness are in good agreement with experimental measurements for the first cycle but discrepancy increases with test cycles. It was found that the asperity contact percolation was reached very quickly under typical operating conditions, so that lubrication is subsequently dependent on the 'micro-pool' mechanism. This is the main mechanism to keep the metal-to-metal contact 'irrigated' for the boundary lubrication to be effective. Therefore, an established 'micro-pool' lubrication mechanism was applied to calculate the thin film thickness on the asperity contacts. Combining this 'micro-pool' lubrication theory with the remaining surface roughness can predict the ratio of boundary contact and

hence the average CoF. The CoF predictions are in line with experimental measurements.

Chapter 6 : Discussion and Conclusions

Accurate calculation of friction is fundamental; it is, however, very complex and any minor changes in external circumstances can have major consequences on the final value of CoF. The subject of friction is not completely understood and there is not a prescribed method of calculation for every type of material under every condition available. This is because some theories work under certain circumstances and others do not. The American Petroleum Institute (API) has a standard value recommended for some of their procedures however its accuracy is uncertain. The main issue with their calculation is that the same value of CoF is used for every material type, without taking into consideration the roughness of the surface, the speed at which it is made up or even the type of materials that constitute the connection. This current value is satisfactory for present conditions. However, since the torque value used to make-up connections is highly dependent on this, there is the possibility for error. The outcomes of this project conclude that through investigation of the materials that form the manufacturer's premium tubular connections, there are variations in the final CoF. This was based on laboratory tests on different surface roughness values and by varying the contact pressure experienced by the materials, at the speeds associated with make-up.

Changes in all external conditions have the possibility to cause some effect on CoF. The significance of this change is subject to how the changes affect the lubrication between the two samples. The velocity of sliding, the type of lubricant, the surface roughness, type of surface peening and contact pressure

all cause different reactions to CoF. The largest effect comes from the initial surface roughness. The current procedure in the majority of the OCTG industry is to make the connection up three times for casings, and ten times for tubing before discarding the products. A value of torque is determined for each connection using the friction values and the connection size; however CoF is taken to be around 0.07-0.08 as standard. There is no consideration of changes in the CoF used in the calculation of torque the second or third time the connection has been made-up. The same torque value is reused each time. The work in this project concludes that the surface roughness and CoF reduce significantly after initial contact. This is caused by the flattening of asperities due to wear. Chapter 5 details a method of predicting the surface roughness and CoF during the make-up procedure. Such a model would improve connection success rate, and could save the company significant money should leakages or failures be caused by an insufficient seal between surfaces due to inadequate or excessive make-up torque.

The details of the CoF test results are shown and analysed in Chapter 4. The largest variations in the CoF are a result of the surface roughness. In the majority of cases, samples of the same roughness(no matter what type of media was used in peening) resulted in a similar CoF. Another typical conclusion is that as the initial surface roughness increases, CoF also rises. Regime 3 includes a smaller quantity of tests because the process was more difficult and there was a significantly larger expense in producing the test samples. This was beyond the scope of the HES project and budget. The new testing rig, produced to undertake the Regime 3 tests, was less reliable than the

test rig used for the other two regimes. This was due to the size and material required for manufacture. Although the values produced from the Regime 3 tests were of the magnitude expected, there was some uncertainty upon each individual value. The very low pressures, however, are less significant as it was the localised high stresses in the seal which were of main interest. It was not at these magnitudes of pressure that failure could occur. As the localised contact pressure between the samples used in the testing was significantly greater than the yield stress of the materials, the higher pressures were more of a concern to the industry. Nevertheless, the major subject of concern was in the differences in CoF after wear of the initial surface. Due to the procedure used to make-up the connection, and the fact that the torque applied to the connection was calculated using CoF, significant differences between the CoF value in the initial and final make-up cycles could have catastrophic consequences on the connection functionality. As a minor leakage can cost the industry and environment dearly, an investigation into the effect had to be done.

A simplified asperity flattening and friction model was presented in Chapter 5. The model allowed for the prediction of burnishing of the shot peened surface and the average CoF for the conditions of laboratory tests. Although the hydrodynamic flow of lubricant was simplified significantly, the prediction of the asperity flattening in the initial stage of sliding was in agreement with experimental measurements. An established ‘micro-pool’ lubrication mechanism was applied to estimate the ratio of asperity contact and the CoF. The results are in concurrence with the laboratory test results.

Chapter 7 : Future Work

7.1 Oil Country Tubular Goods Industry Standards

Further improvements in the standardisation of CoF testing are needed in the future to improve the accuracy of calculation of the torque used in make-up. The current method of using an industry standard value of 0.07 to 0.08 potentially has a degree of inaccuracy, and may cause problems with under or over-torqued connections in the future. Although there is a large amount of research being done into finding more sustainable ways of producing energy, the oil and gas industry remains at the forefront of energy production worldwide. As the sources are drained in the current wells, deeper drilling is required to keep up with current demand. As the wells deepen, the pressures and temperatures that the connections experience increase, and thus the connections need to be more accurate.

A standardised method of obtaining the working CoF is necessary to ensure that every OCTG connection producer uses the same technique. The American Petroleum Institute (API) already has a substantial number of Standards and Recommended Practices that each connection must satisfy in order to be approved by a classification society. However, even though there are recommendations about how this value should be obtained, there is no current method in any of these standards which determines how every CoF value must be attained. The costs associated with a proposal such as this are significantly, high and would require solid justification to prove that it was deemed necessary. The current project does show that the CoF changes with different external

circumstances, although in order to merit its significance, much larger scaled projects need to be done to ensure that improvements are made in the future.

7.2 Temperature investigation

Although the project produced an extensive range of CoF data, and looked at a wide variety of external circumstances, there was some additional work which could have been done which would have added further value to the project. Every CoF test was undertaken at room temperature (approximately 18 to 22ºC), as temperature was not one of the external circumstances in the initial project scope. The temperature may have had an effect on CoF, but the temperatures that the pipeline experiences in the field are much higher than those which were used within this testing procedure. As the pipes and couplings can be used in extremely hot and cold environments, further work could be done in the future to allow a range of temperatures to be investigated.

The current test rig would not be sufficient to undertake such testing and any improvements would have taken the project well beyond its scope and budget. One method of obtaining results for changes in temperature would be to heat up the samples in an oven (or cool them down by subjecting them to the solid form of carbon dioxide known as dry ice),prior to being placed in the test rig ready for the testing process to take place. The accuracy of such changes would be low and the temperature changes of the samples would most likely change the composition of the materials. The use of lubricants becomes another issue as heating up or cooling down of the lubricants changes the viscosity and freezing them would mean that they would not be able to be spread on the surface

easily. This is not comparable with what happens on the rig even with very low temperatures so would not be equivalent. The case is similar to that of the higher temperatures where most likely the lubricants would run off the surface prior to contact. This would result in a number of extra tests being undertaken with no improvements in results and the uncertainties of both the temperatures and the behaviour of the lubrication would have reduced the reliability of the project.

7.3 Development of the low pressure test

An enhanced testing process for the very low pressures would improve the testing results, as a larger and more accurate set of results would be available. A new load cell would have to be produced to improve the testing process. Instead of using 2 mm strain gauges and gluing them to the legs of the load cell, a much smaller set would be more accurate. This would have been a much more complicated job to undertake and, if the wiring was not accurate enough, would produce less reliable results. An alternative method would probably be more precise, however this would seriously increase the costs and time associated.

7.4 Helical motion

Although the complexity of producing such a test rig capable of helical motion is high, the results may be improved if the sliding between the two contacting surfaces was helical. The linear sliding motion used in this project was suitable for understanding the effect of external conditions on CoF. However, if helical motion was able to be replicated then the accuracy of the results would be

slightly higher. The cost and time associated in such a project was far beyond the scope and budget of the project.

Chapter 8 : Appendices

Appendix 1: Sketches and Drawings of the Test rig

The top and bottom sample holders were manufacturered by the technical staff of the University of Dundee and Plymouth University. These were made from an aluminium alloy called Dural and held the samples in place allowing contact during the testing process. **Figure 8-1** shows the configuration for the large pressure tests (Regime 1) carried out using the test rig. In this particular case, the sample geometry was cylindrical, producing the largest contact pressure.

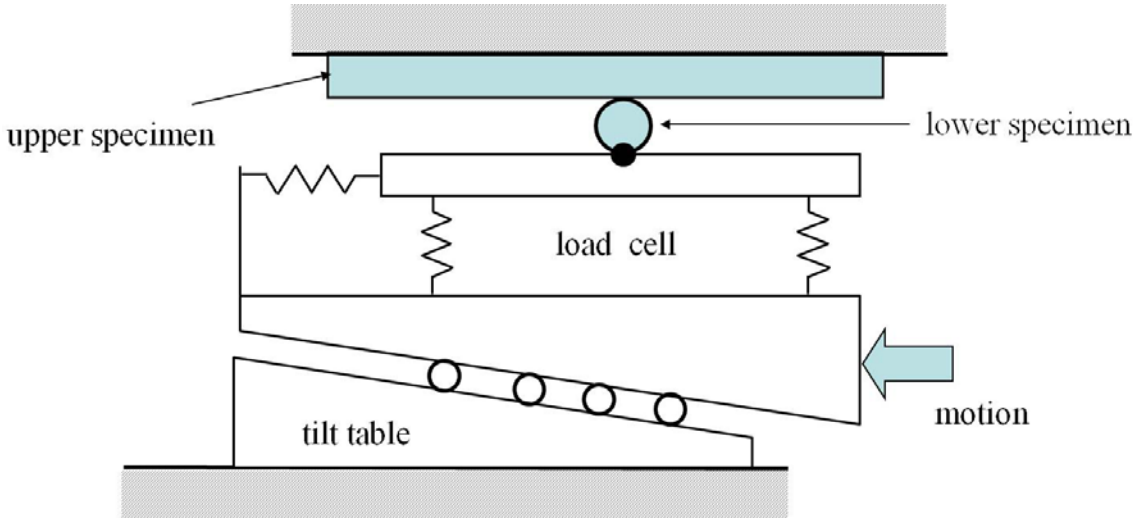

Figure 8-1: Test Rig Configuration

The test samples were produced using existing pipeline connections manufactured by HES. These best represent the profiles of the contact surfaces during make-up. A drawing of the coupon samples utilised in Regime 2 is shown in **Figure 8-2**. Laser cutting was used to produce these samples. **Figure 8-3** shows the pin samples used in Regime 2. These were turned on a milling machine during manufacture.

Appendix 2: Sample Drawings

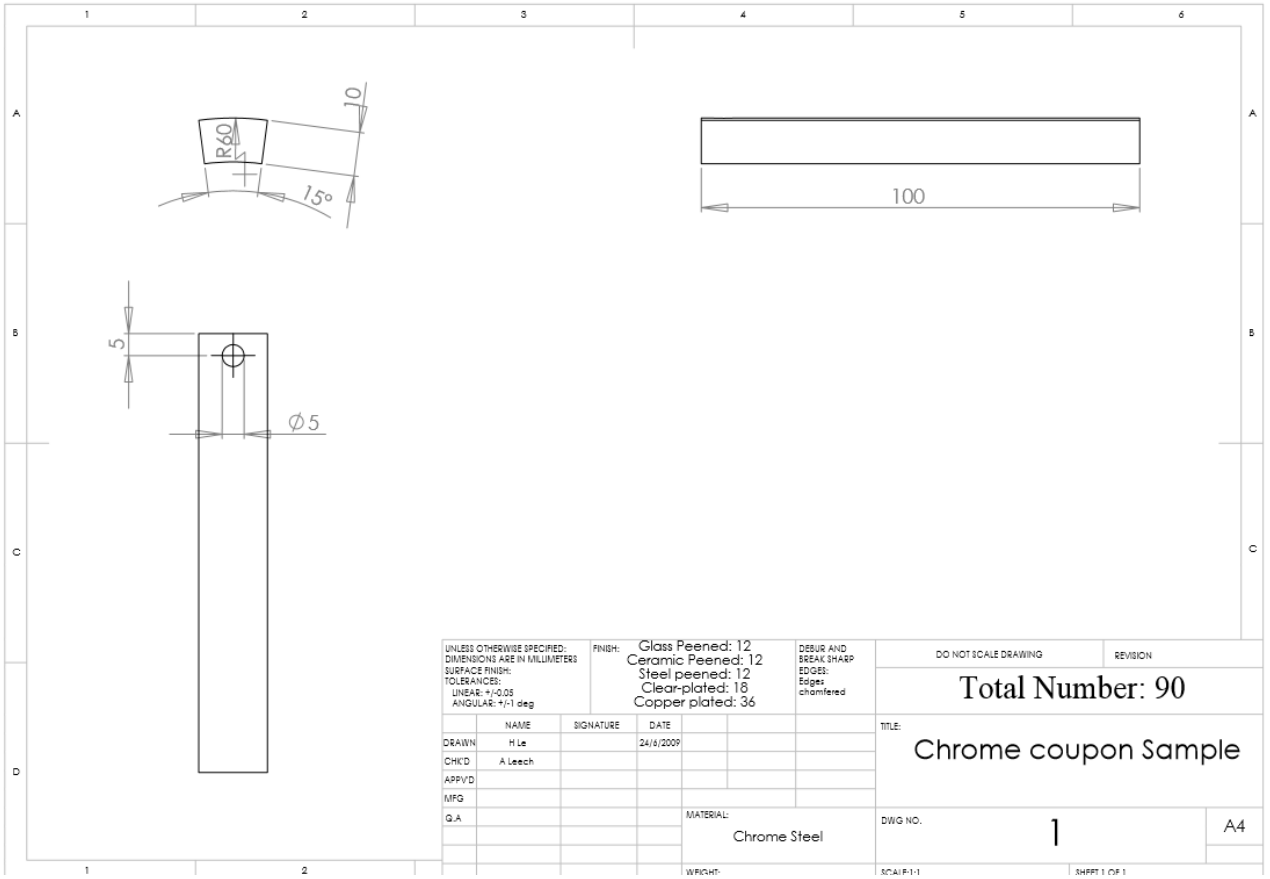

Figure 8-2: Coupon drawing for Regime 3 test samples

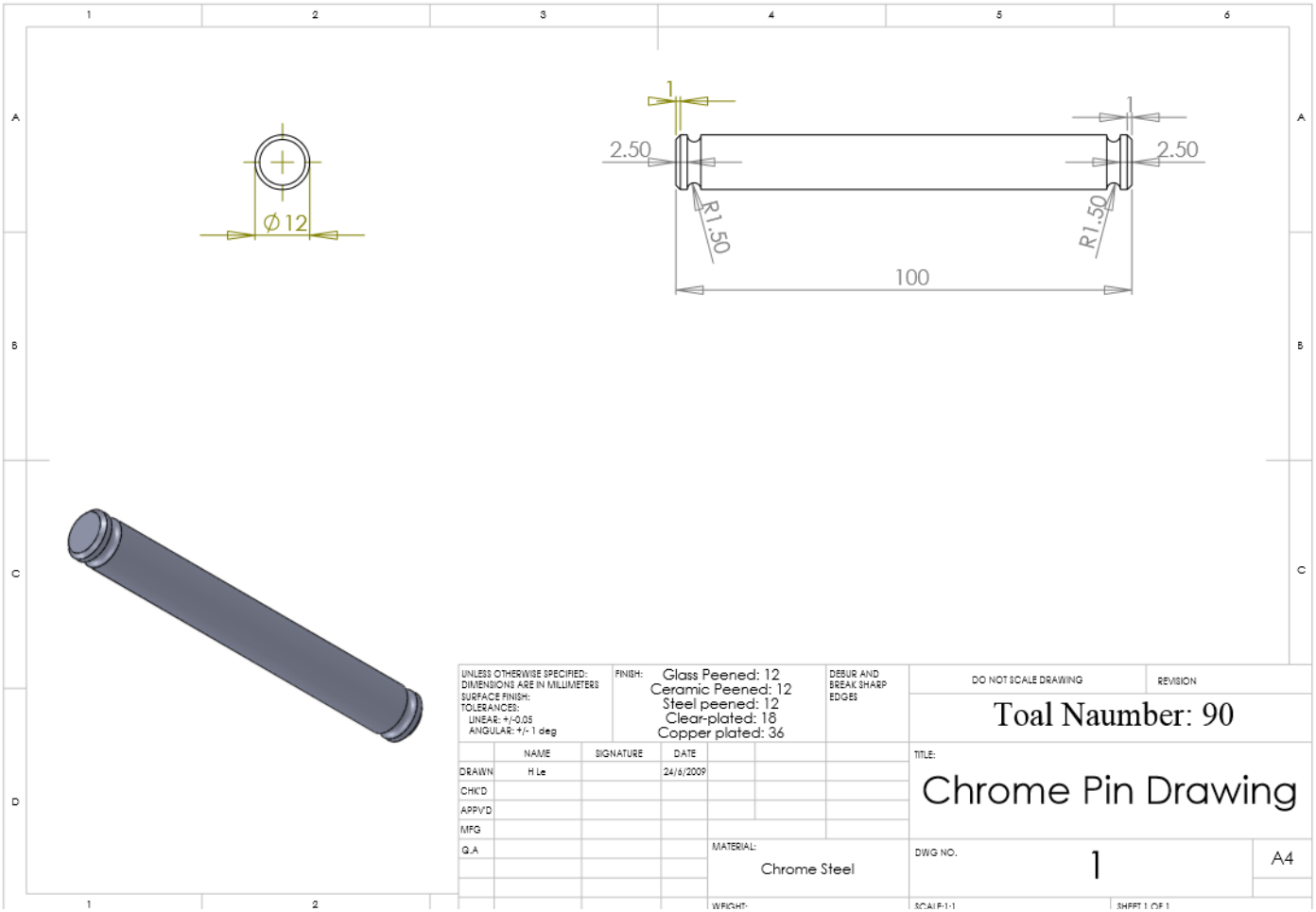

Figure 8-3: Pin drawing for Regime 1 test samples

Appendix 3: Regime 3 Load Cell Drawings

Appendix 3 contains drawings for each of the components used in the Regime 1 and 2 set-ups. The assembly shown in **Figure 8-4** shows the load cell which is made up of a top plate [**Figure 8-7]**, bottom plate [**Figure 8-6**] and legs (or rings) [**Figure 8-5**].

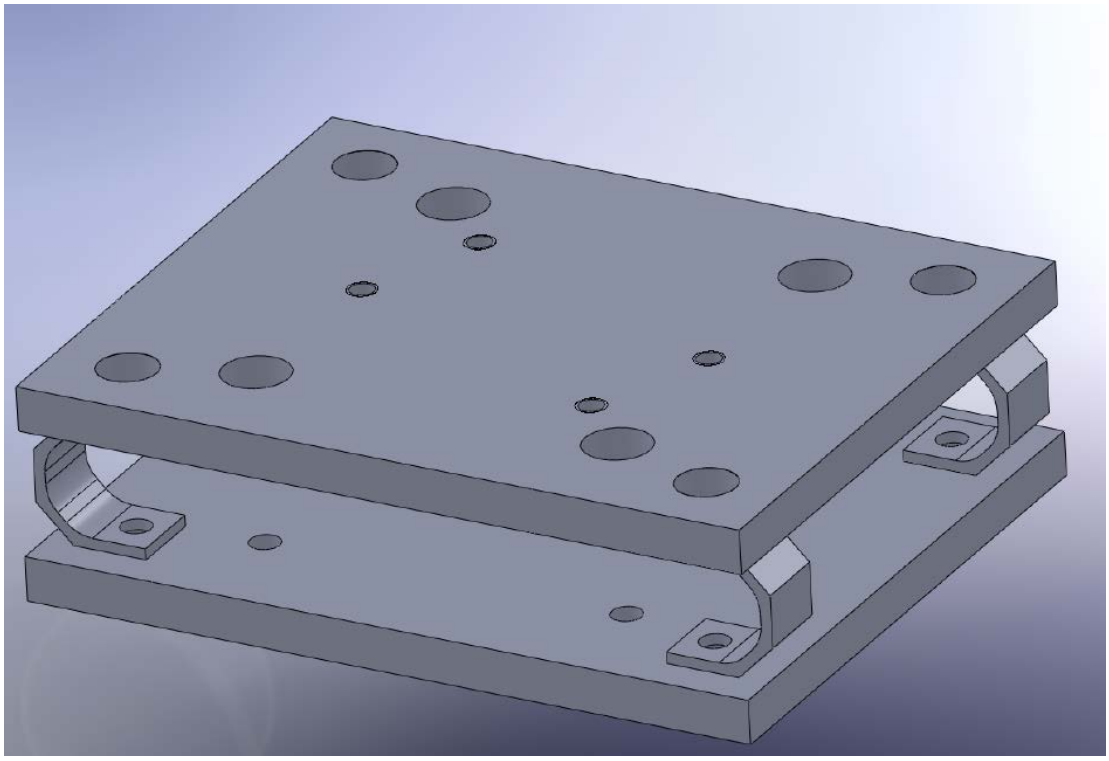

Figure 8-4: Load cell assembly

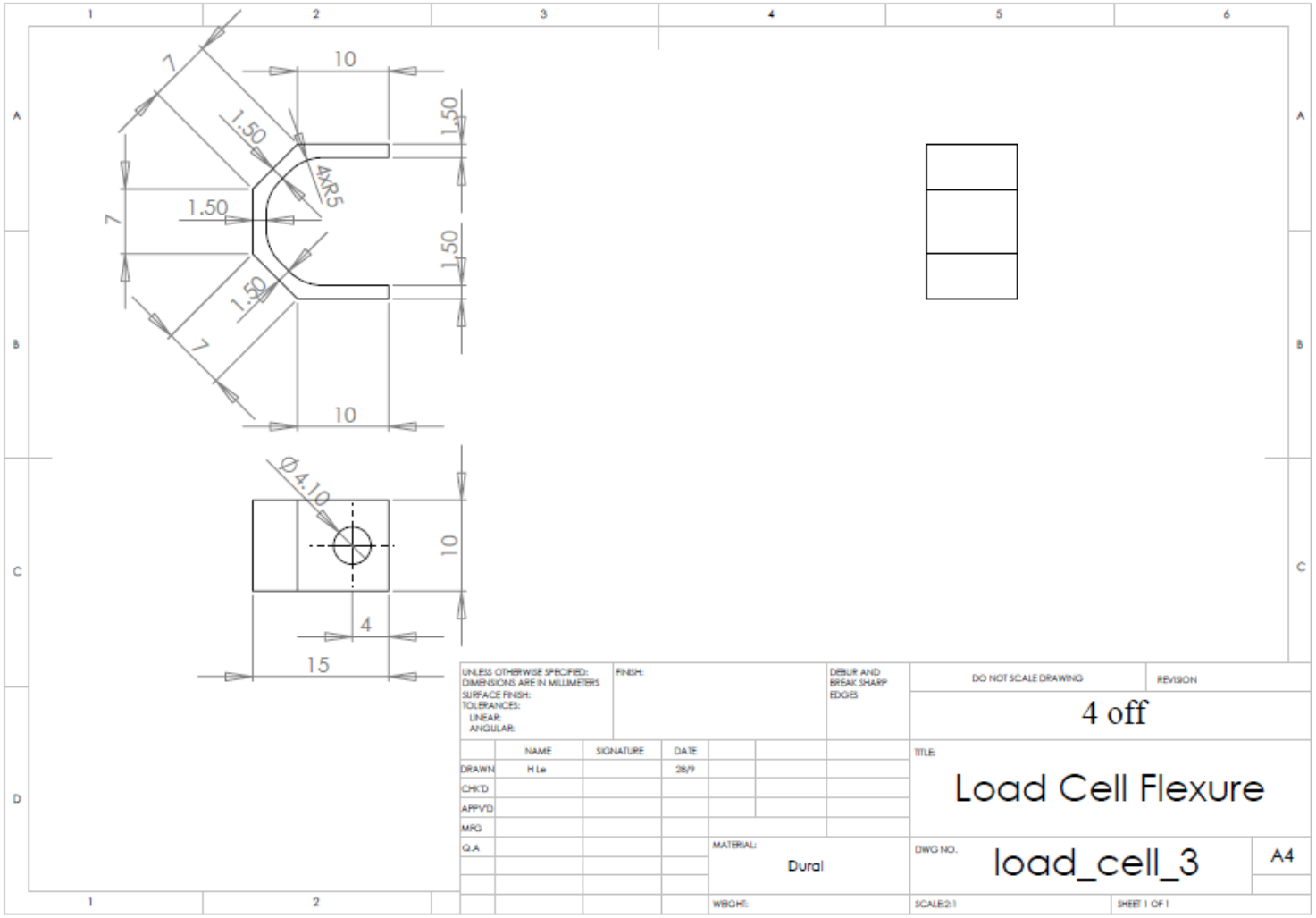

Figure 8-5: Legs (rings) of Regime 1 and 2 load cell

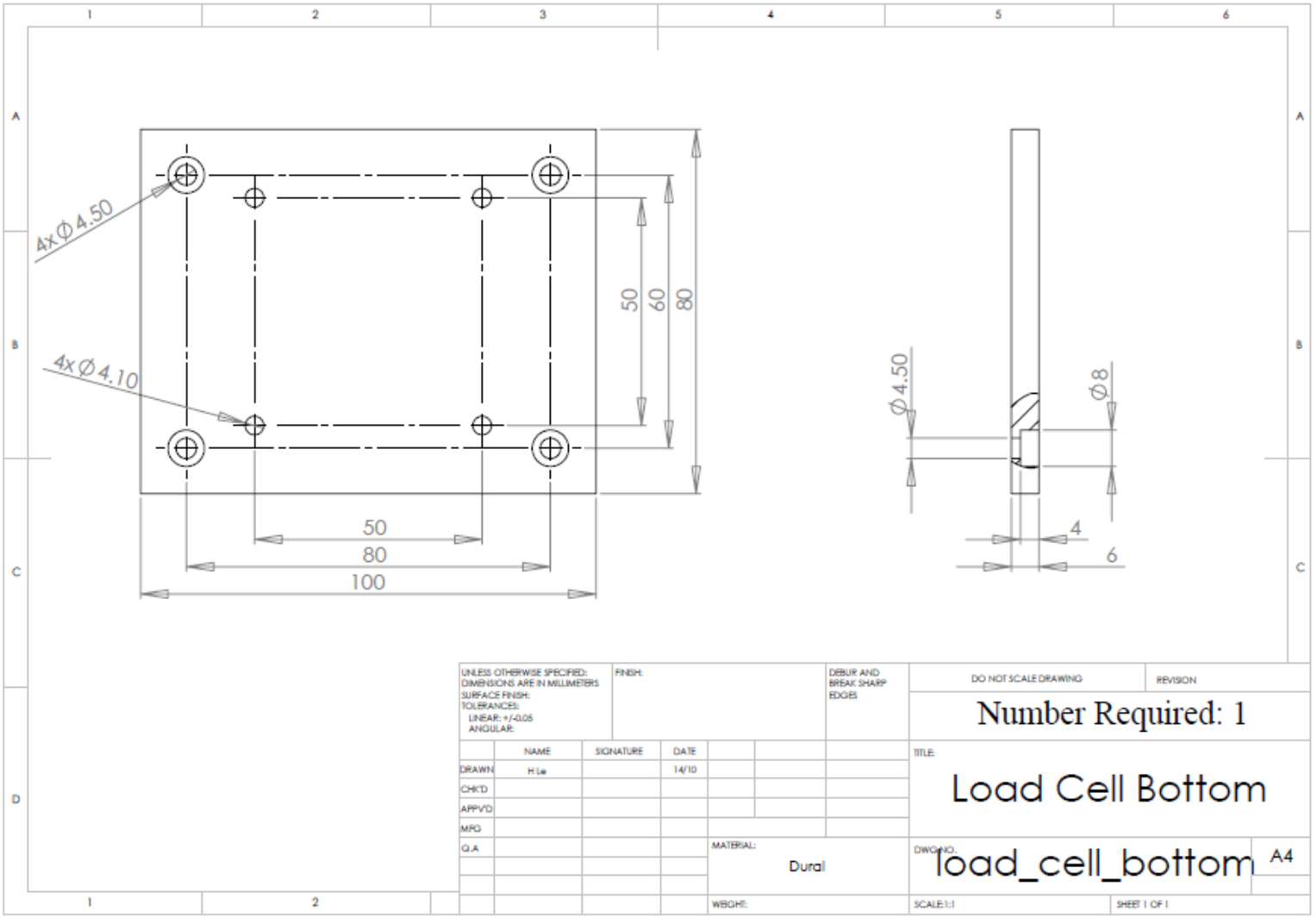

Figure 8-6: Bottom plate of Regime 1 and 2 load cell

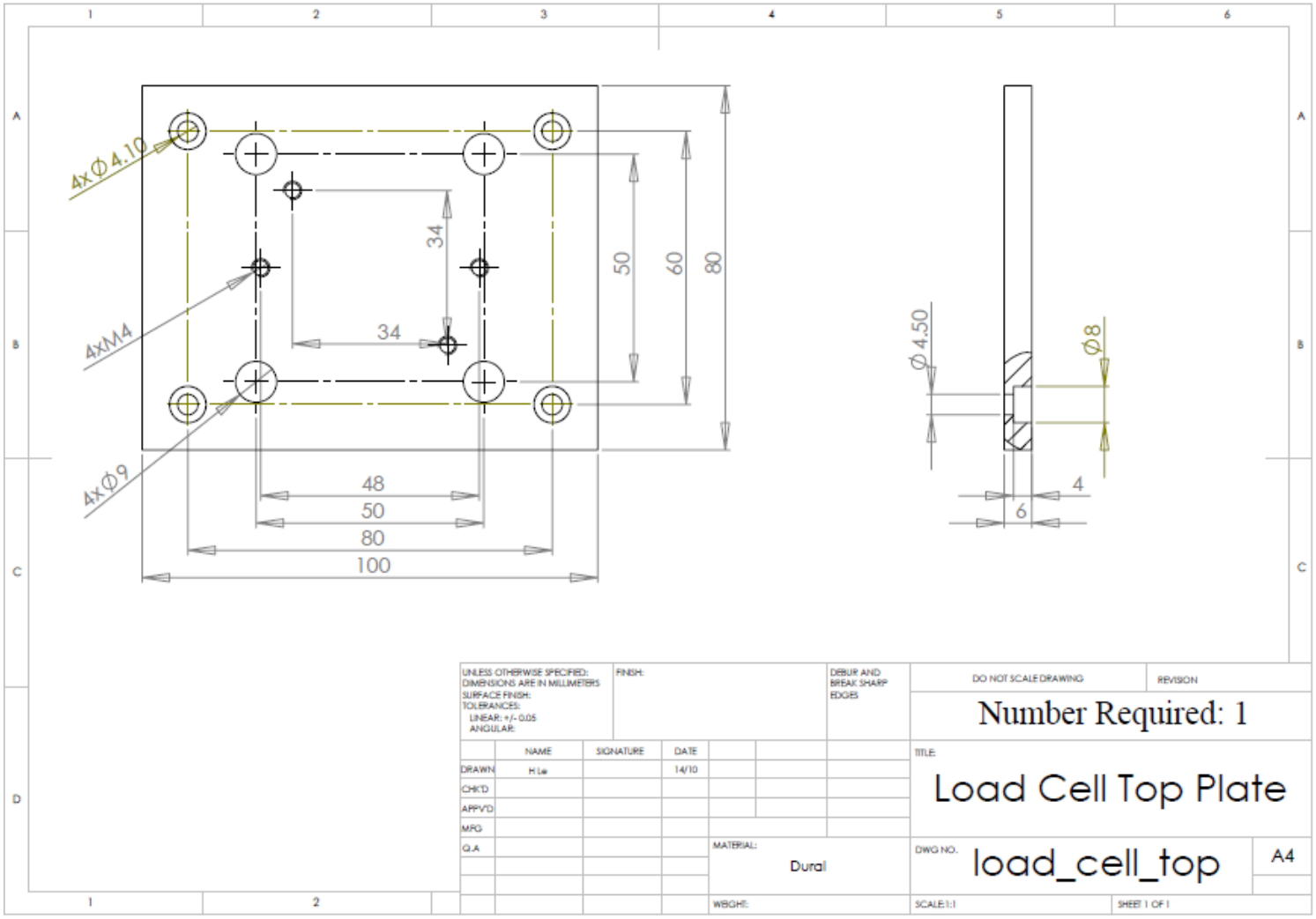

Figure 8-7: Top plate of Regime 1 and 2 load cell

The test rig is arranged as shown in **Figure 8-8**. There are two pole sections (shown in **Figure 8-9** and **Figure 8-10**) which hold the load cell, sample holders, motorised table and tilt table in place.

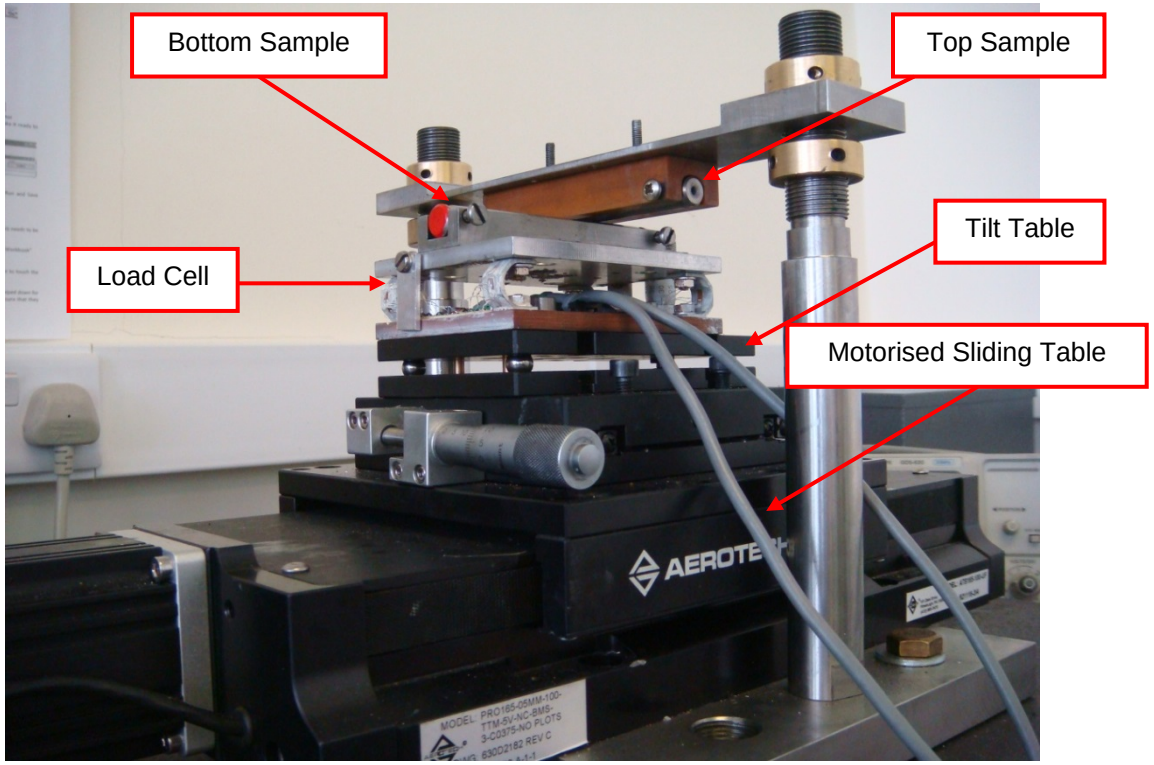

Figure 8-8: Load cell assembly

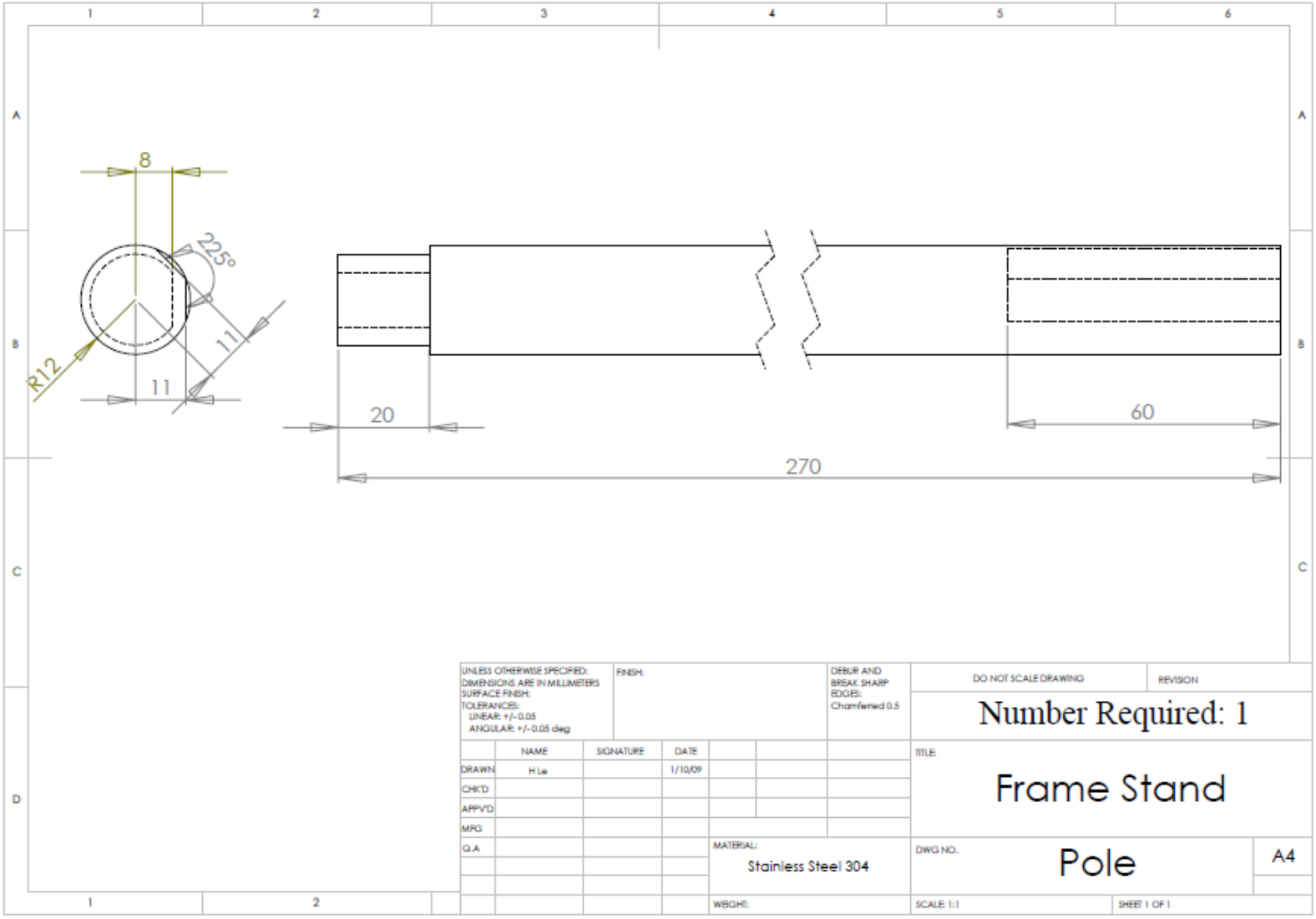

Figure 8-9: Pole for frame stand for test rig – Section 1

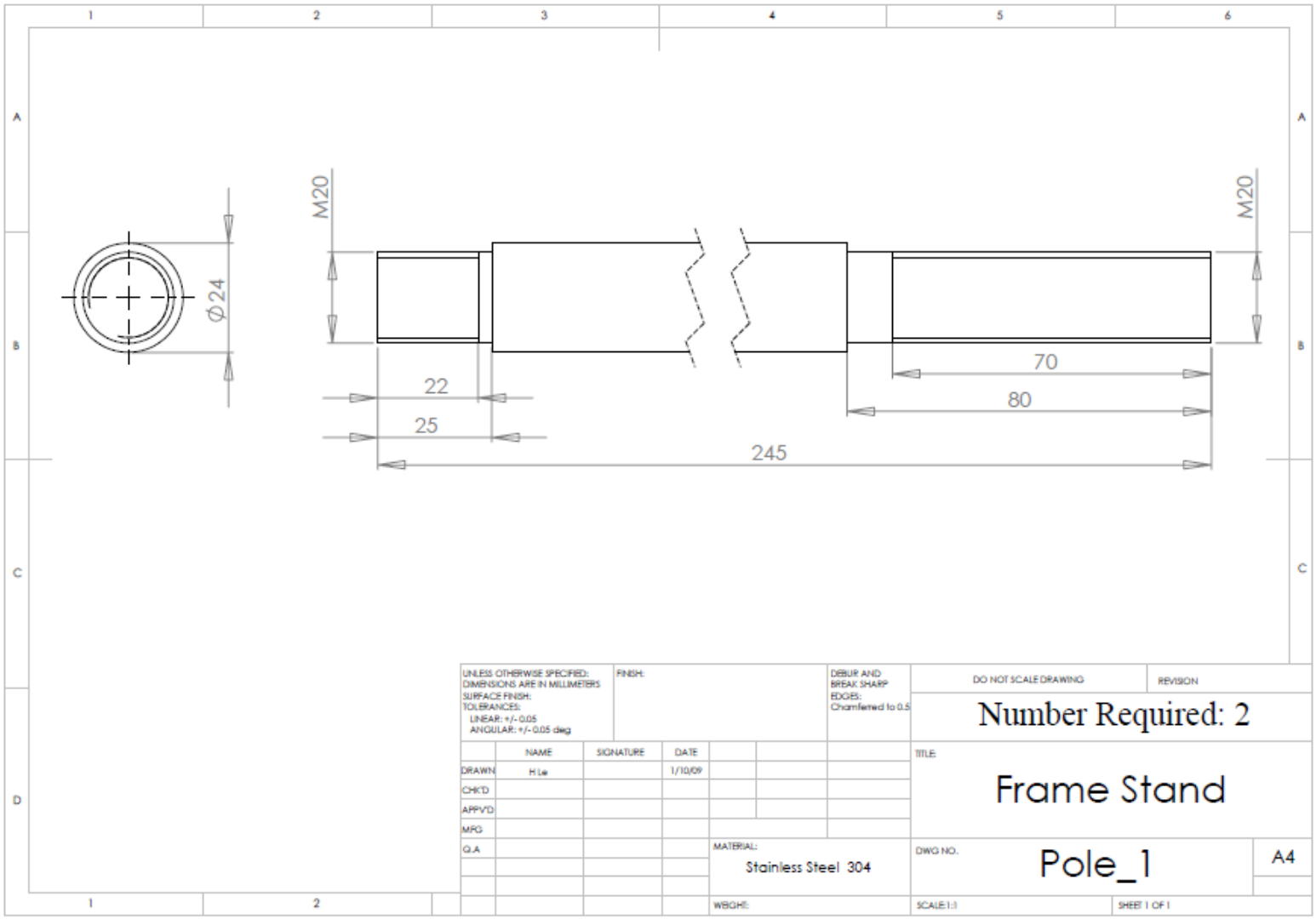

Figure 8-10: Pole for frame stand for test rig – Section 2

Appendix 4: Regime 3 Load Cell Drawings

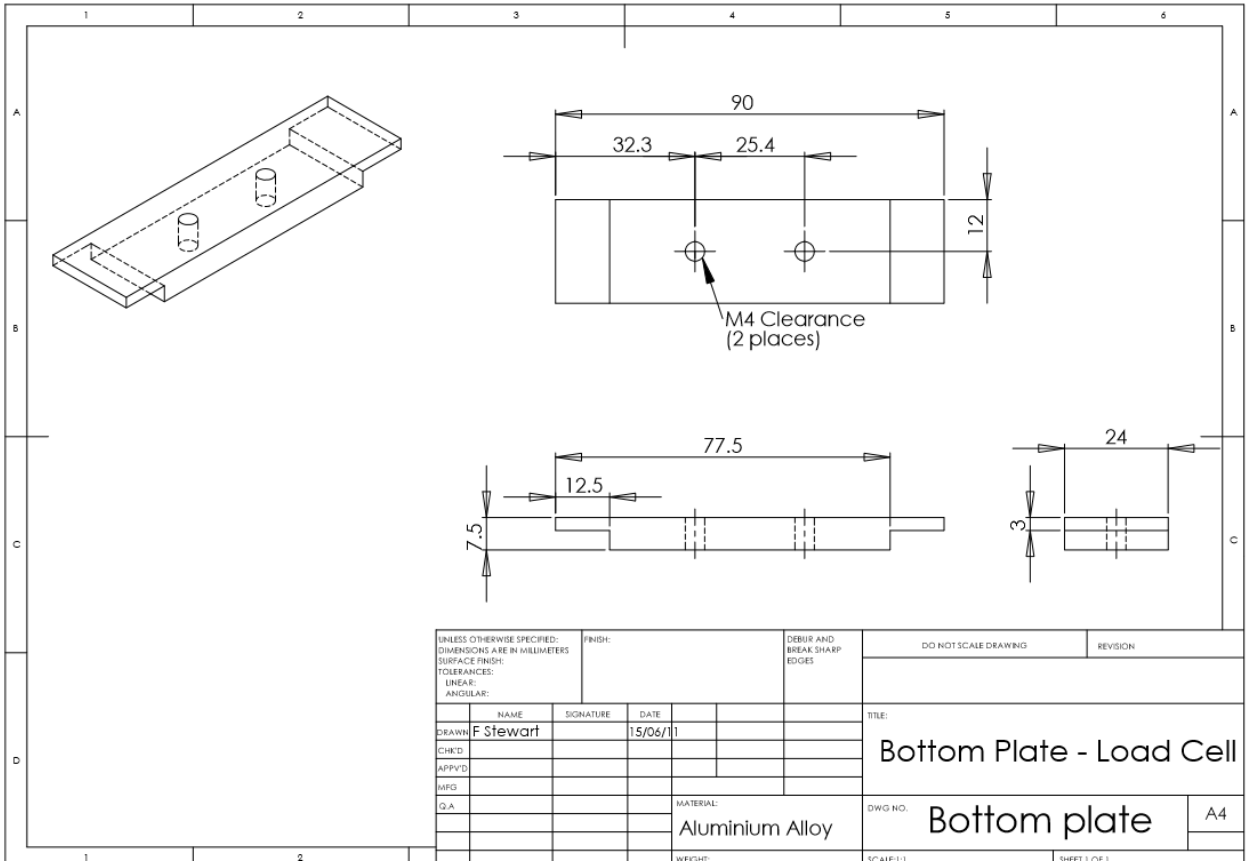

Figure 8-11: Bottom plate for Regime 3 test

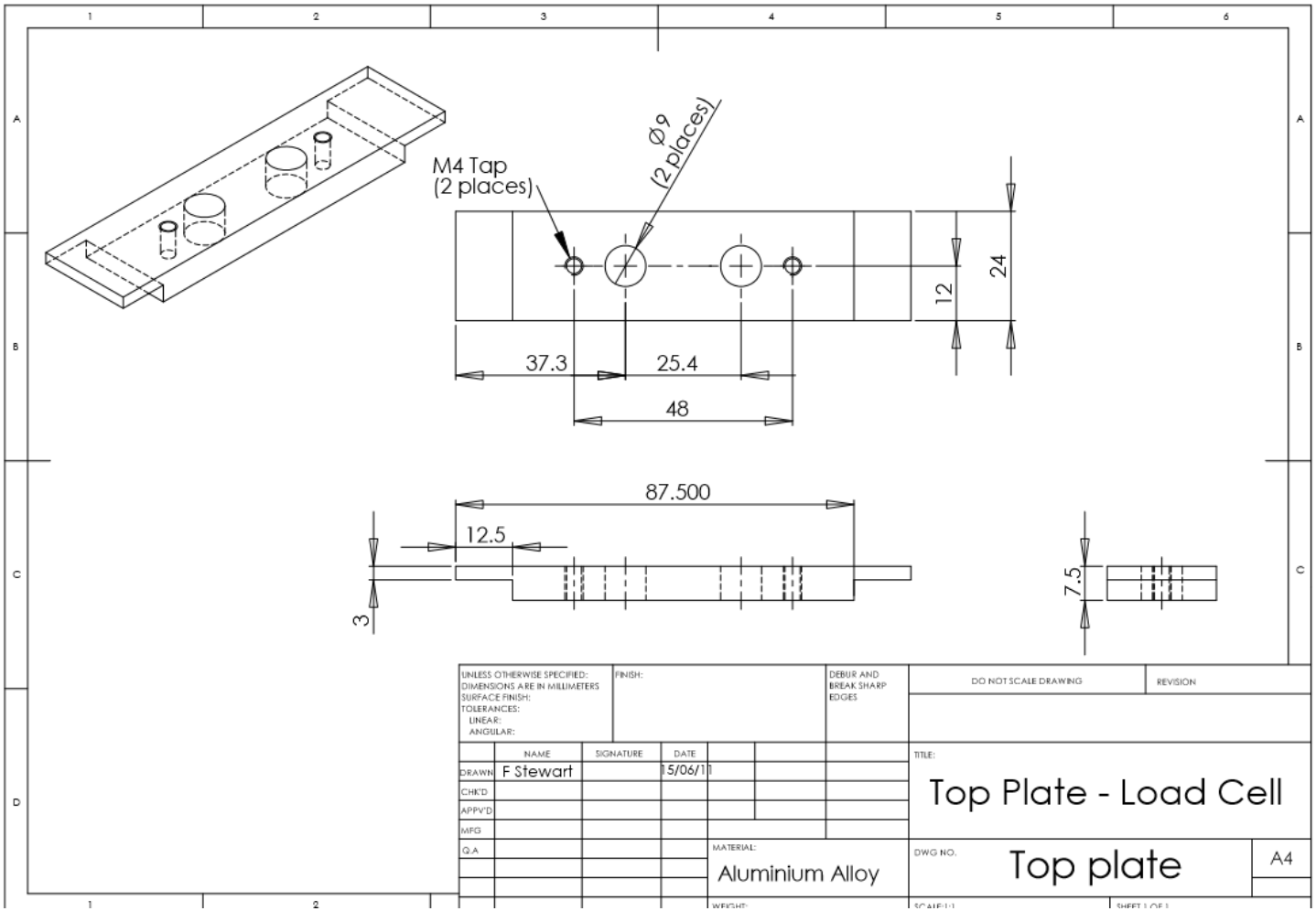

Figure 8-12: Top plate for Regime 3 test

Appendix5: Test Rig Operation Procedure

A test rig operating procedure is shown below.

Safety Note:
• Do not put fingers in contact area. • Do not stand too close to test rig.

- Turn on – Amplifiers, Motor, Computer

This takes approximately 30 minutes to warm-up properly to be ready to start.

1. Balance amplifiers

Place the samples into the test rig, securing them with the screws. Ensure that the samples are flat in the sample holder. When there is no load applied on the test rig, zero the reading on the oscilloscope. This is done by rotating the Position dials for both the Tangential and Normal Force signals.

2. Apply a thin layer of lubricant to both samples

Use a high quality acrylic paint brush to prevent any bristles shedding onto the samples which will affect the test. Each paintbrush is labelled for the individual lubricants. Ensure that these are used only for the specified lubricant.

3. Adjust the tilt table

Using the spirit level, check that sample is horizontal, ensuring that the top plate parallel to the table.

Check the samples are in contact with each other – by applying a minimum force (pressing down with one finger) on the top sample and confirm that the oscilloscope moves approximately half a division.

For the current assembly, a tilt of 12.8 gives 450 MPa (~ 8V). Before beginning experiments with an alternative set-up, the amount of tilt needs to be established. Obtain this value by using small

running distances. i.e. the full distance along the sample is 45 mm, so initially tilt the micrometer a limited amount e.g. moves it along 15mm to begin with, then increase until the user is fully confident that the load cell will not be overloaded.

4. Apply lubricant and lower top sample.

Apply lubricant to the surface of the sample, ensure that it is thinly spread across the area of contact during the test.

Check that the top sample is horizontal using the spirit level.

Check the samples are in contact – apply minimum force (by pressing down slightly) on the top sample and check that the oscilloscope moves approximately half a division.

5. Tighten the locking nuts gently until the two samples are locked tightly together and cannot move. Overdoing this can damage the load cell and not tightening it enough will give false results.

6. Ensure nothing is obstructing the motorised table

7. Set-up an Aerotech program to complete the required number of cycles of linear travel at the speeds desired (see later Appendix for programs)

8. In Labview, set up a program to record data from both the normal and tangential amplifiers for the full length of the test, first click the Run button on the Labview Program to start the recording.

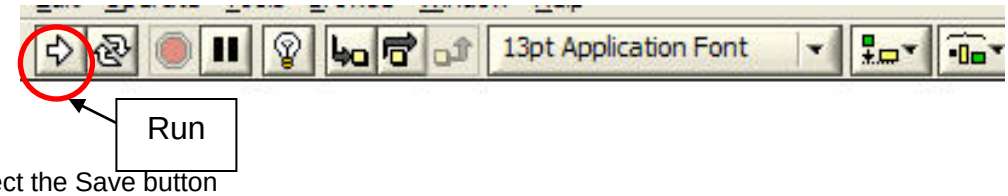

The select the Save button

9. Next click Run on the Aerotech program to begin movement of the linear motorised table.

The default folder in which Labview saves the program should be found and then when this is known read the results from folder

My Documents/ Labview Data

File name: Test

To allow Excel functionality, the file needs to be renamed and saved as “Microsoft Office Excel Workbook”, otherwise Excel functions and formulae will not work.

10. When the test is complete, loosen upper locking nuts to release the samples.

Do not touch the bottom locking nuts as these maintain the maximum pressure value used during the test.

Remove the samples from the sample holders.

Finally, clean everything using acetone or similar cleaner to ensure the test rig is ready to be used again.

Place the samples in a labelled box to ensure that they can be identified later.

Appendix 6: Aerotech Program

Aerotech design and manufacture accurate motion control, positioning tables/stages and positioning systems. Their software Soloist ID is a single axis motion controller which is used to power the motorised table. Due to its functionality, the power supply, amplifier and position controller are combined within the one system. The linear speed of the motorised table can reach up to 100 mm/s. The three codes used to control the motion for the 3 mm/s, 15 mm/s and 50 mm/s test are based upon a 45 mm contact sample length and are shown below.

Appendix 6a

3 mm/s Aerotech Soloist program

```
SETPOSCMD 100                ; Start 100mm from home position
REPEAT 3                     ; Repeat this 3 times
        FREERUN F 3  ; Move from R to L at3mm/s (i.e. Velocity = 3 mm/s)
        DWELL 15             ; Run for 15 s (45 mm)
        FREERUN F 0  ; Velocity = 0 mm/s - Pause to change direction
        DWELL 2              ; Pause for 2 s
        FREERUN F -3 ; Move from L to R at 3mm/s (i.e. Velocity = -3 mm/s)
        DWELL 15             ; Run for 15 s (45 mm)
        FREERUN F 0  ; Velocity = 0 mm/s - Pause to change direction
        DWELL 2              ; Pause for 2 seconds to repeat cycles or stop
ENDREPEAT    ; End of repeating section
```

Appendix 6b

15 mm/s Aerotech Soloist program

```
SETPOSCMD 100              ; Start 100 mm from home position
REPEAT 3                   ; Repeat this 3 times
        FREERUN F 15; Move from R to L at 15mm/s (i.e. Velocity = 15 mm/s)
        DWELL 3            ; Run for 3 s (45 mm)
        FREERUN F 0  ; Velocity = 0mm/s - Pause to change direction
        DWELL 3            ; Pause for 2 s
        FREERUN F -15      ; Move from L to R at 15 mm/s (i.e. Velocity = -3 mm/s)
        DWELL 3            ; Run for 3 s (45 mm)
        FREERUN F 0  ; Velocity = 0 mm/s - Pause to change direction
        DWELL 3            ; Pause for 2 seconds to repeat cycles or stop
ENDREPEAT    ; End of repeating section
```

Appendix 6c

50 mm/s Aerotech Soloist program

```
SETPOSCMD 100              ; Start 100 mm from home position
REPEAT 3                   ; Repeat this 3 times
        FREERUN F 50; Move from R to L at 50 mm/s (i.e. Velocity = 50mm/s)
        DWELL 0.9          ; Run for 0.9 s (45 mm)
        FREERUN F 0  ; Velocity = 0 mm/s - Pause to change direction
        DWELL 1            ; Pause for 2 s
        FREERUN F -50      ; Move from L to R at 50 mm/s (i.e. Velocity = -50 mm/s)
        DWELL 0.9          ; Run for 0.9 s (45 mm)
        FREERUN F 0  ; Velocity = 0 mm/s - Pause to change direction
        DWELL 5            ; Pause for 2 seconds to repeat cycles or stop
ENDREPEAT          ; End of repeating section
```

Appendix 7: Matlab Programme

Matlab Programme – “Christensen”

```
%Main program -Christensen surface model and Archard wear, updated 30/12/2012
close all
clear all
global asptype
global hmean0temp
global y0friction
asptype='christensen';

v1 = 0.29;              % Poissons ratio of peened sample - chrome steel
v2 = 0.29;              % Poissons ratio of plated sample - chrome steel
E1 = 2.05E11;           % Young's modulus of peened sample - chrome steel
E2 = 2.05E11;           % Young's modulus of plated sample - chrome steel
Estar = 1/(((1-v1^2)/E1)+((1-v2^2)/E2));     %plane stress modulus from the material properties of both substances=
Rq0=2.767E-6*sqrt(2);                  %Combined surface roughness of two surfaces - From heightmatrixworkingchange.m
file
Rq=Rq0/sqrt(2);         %Estimated plataeu surface roughness
K=3e-4;                 %Change this to suit, start with 0.001
Hv=2.6E9;               %Ceramic peened chrome steel hardness result from Birmingham
theta=10*pi/180;        %
alpha=3.88e-8;          %
lambda=100e-6;          %
y0=6*Rq0;               %Surface roughness amplitude
Wm=500;                 %Maximum load at largest sliding distance - For coupons - between 65-80 ksi (448-551 MPa)
R = 0.06;                   %1/R=1/R1+1/R2, R2=infinity because perpendicular, so R=R1 (R1=R2) - For coupons R=60mm
(0.06m), For pins R=6mm (0.006m)

gamma=3;                %Peklenik number - for non-directional surface, gamma=1

a2 = 0.051375*(log(9*gamma)).^3-0.0071901*(log(9*gamma)).^4;    %flow factor coefficient
a3 = 1.0019-0.17927*log(gamma)+0.042583*(log(gamma)).^2-0.016417*log(gamma)^3;%flow factor coefficient
Htc = 3*((1-((0.47476/gamma)+1).^(-0.25007)));%percolation threshold
eta = 50; %Viscosity - For ClearGlide, eta =50 Pa.s from 50,000CP
v=0.015;
v0=0.015;   %(m/s) - speed)
rho=1160;   % in kg/m^3 - As ClearGlide relative density from datasheetis 1.160
Pvtemp=0; dh=0; htemp=y0;  %initial valley pressure, asperity height change, asperity height

%Cycle 1 loading
dS=0.001;               %Change in sliding distance
S = [0:dS:0.045];       %Sliding distance (m) for cycle 1
Aa=zeros(1,length(S));      %Asperity contact areas
for i=1:length(S)
W(i)=Wm*(S(i)/0.045)+10;       %Load applied - increases as sliding distance increases
   Pbartemp=1/pi*(((16*W(i)*Estar.^2)/(9*R.^2)).^(1/3));   %Mean contact pressure
   [atemp,hmean,hvartemp]=aspparas(htemp,y0); %Contact area determined using "aspparas" program

      Patemp=(Pbartemp-Pvtemp*(1-atemp))/atemp;
Patemp=min(Patemp,Hv);
a=(3/4*W(i)*R/Estar)^(1/3);    %Contact radius
%a=0.5*a;
      Ht=hmean/Rq0;
if Ht>Htc
phix = (a2*(Ht-Htc).^2+a3*(Ht-Htc).^3)/Ht^3;
      Pvtemp = 6*eta*a*(1-atemp)*(a*dh/dS*v0)/(phix*(hmean).^3);
else
      Pvtemp=Pbartemp;
      Patemp=0;
end
            Pvtemp=max(Pvtemp,0);
            Pv(i)=Pvtemp;
Pbar(i)=Pbartemp;
   Pa=min(Patemp,Hv);         %Pa cannot be higher than the hardness of the material
```

```
   Pa=max(Pa,0);
dh=K*Pa*dS/(Hv);       %wear depth
Pabar(i)=Patemp;
hvar(i)=hvartemp;
htemp=htemp-dh;
h1(i)=htemp;
   Aa(i)=atemp;
end
KPH=(K*Pabar)/Hv;
Wh=S.*KPH;      %Wear increment

%Calculate Surface Roughness of plataeu (Rq) during cycle 1+
Rqtemp=sqrt(0.5*hvar);  % Rq of each surface
Rq1=Rqtemp;

%Cycle 1 unloading
S2=[0.045:dS:0.090];
for i=1:length(S2)
W2(i)=(((0-Wm)/(0.09-0.045))*S(i))+510;  %Load applied - increases as sliding distance increases

   vel2=v0;

   Pbartemp=1/pi*(((16*abs(W2(i))*Estar.^2)/(9*R.^2)).^(1/3));  %Mean pressure when L=a

   [atemp,hmean,hvartemp]=aspparas(htemp,y0);

      Patemp=(Pbartemp-Pvtemp*(1-atemp))/atemp;
      Patemp=min(Patemp,Hv);
      a=(3/4*W2(i)*R/Estar)^(1/3);  %Change this

ht=sqrt(hvartemp+0.25*y0^2);
      Ht=hmean/Rq;
if Ht>Htc
phix = (a2*(Ht-Htc).^2+a3*(Ht-Htc).^3)/Ht^3;
      Pvtemp = 6*eta*a*(1-atemp)*(a*dh/dS*vel2)/(phix*(hmean).^3);
else
      Pvtemp=Pbartemp;
      Patemp=0;
end
      Pvtemp=max(Pvtemp,0);
Pv2(i)=Pvtemp;

Pbar2(i)=Pbartemp;
   Pa=min(Patemp,Hv);     %Pa cannot be higher than the hardness of the material
   Pa=max(Pa,0);

dh=K*Pa*dS/(Hv);
Pabar2(i)=Pa;
   hvar2(i)=hvartemp;
   htemp=htemp-dh;
   h2(i)=htemp;
   Aa2(i)=atemp;
end

%Calculate Surface Roughness of plataeu (Rq) during cycle 1-
Rq2=sqrt(0.5*hvar2);

%Calculate Wear Height
KPH2=(K*Pabar2)/Hv;
Wh2=S2.*KPH2;      %Wear height

%Cycle 2 loading
S3=[0.090:dS:0.135];

for i=1:length(S3)

   vel3=v0;

W3(i)=Wm*(S(i)/0.045)+10;  %Load applied - increases as sliding distance increases
    Pbartemp=1/pi*(((16*abs(W3(i))*Estar.^2)/(9*R.^2)).^(1/3));  %Mean pressure when L=a
```

```
   [atemp,hmean,hvartemp]=aspparas(htemp,y0);
atemp=max(atemp,0.01);
      Patemp=(Pbartemp-Pvtemp*(1-atemp))/atemp;
      Patemp=min(Patemp,Hv);
      a=(3/4*W2(i)*R/Estar)^(1/3);  %Change this

ht=sqrt(hvartemp+0.25*y0^2);
      Ht=hmean/Rq;
if Ht>Htc
phix = (a2*(Ht-Htc).^2+a3*(Ht-Htc).^3)/Ht^3;
      Pvtemp = 6*eta*a*(1-atemp)*(a*dh/dS*vel3)/(phix*(hmean).^3);
else
      Pvtemp=Pbartemp;
      Patemp=0;
end
   Pvtemp=max(Pvtemp,0);
Pv3(i)=Pvtemp;
Pbar3(i)=Pbartemp;
   Pa=min(Patemp,Hv); %Pa cannot be higher than the hardness of the material
   Pa=max(Pa,0);
dh=K*Pa*dS/(Hv);
Pabar3(i)=Pa;
   hvar3(i)=hvartemp;
   htemp=htemp-dh;
   h3(i)=htemp;
   Aa3(i)=atemp;
end


%Calculate Surface Roughness of plataeu (Rq) during cycle 2+
Rq3=sqrt(0.5*hvar3);

%Calculate Wear Height
KPH3=(K*Pabar3)/Hv;
Wh3=S3.*KPH3;      %Wear heigh

%Cycle 2 unloading
S4=[0.135:dS:0.180];
for i=1:length(S4)
W4(i)=(((0-Wm)/(0.09-0.045))*S(i))+510;  %Load applied - increases as sliding distance increases

   Pbartemp=1/pi*(((16*abs(W4(i))*Estar.^2)/(9*R.^2)).^(1/3));  %Mean pressure when L=a

   vel4=v0;

   [atemp,hmean,hvartemp]=aspparas(htemp,y0);
atemp=max(0.01,atemp);%Contact area determined using "aspparas" program
      Patemp=(Pbartemp-Pvtemp*(1-atemp))/atemp;
      Patemp=min(Patemp,Hv);
      a=(3/4*W2(i)*R/Estar)^(1/3);  %Change this
ht=sqrt(hmean^2+0.25*y0^2);
       Ht=hmean/Rq;
if Ht>Htc
phix = (a2*(Ht-Htc).^2+a3*(Ht-Htc).^3)/Ht^3;
      Pvtemp = 6*eta*a*(1-atemp)*(a*dh/dS*vel4)/(phix*(hmean).^3);
else
      Pvtemp=Pbartemp;
      Patemp=0;
end
   Pvtemp=max(Pvtemp,0);
   Pvtemp=min(Pvtemp, Pbartemp);
Pv4(i)=Pvtemp;
Pbar4(i)=Pbartemp;
Pa=min(Patemp,Hv);
Pa=max(Pa,0);%Pa cannot be higher than the hardness of the material
dh=K*Pa*dS/(Hv);
Pabar4(i)=Pa;
hvar4(i)=hvartemp;
```

```
   htemp=htemp-dh;
h4(i)=htemp;
   Aa4(i)=atemp;

end

%Calculate Surface Roughness of plataeu (Rq) during cycle 2-
Rq4=sqrt(0.5*hvar4);

%Calculate Wear Height
KPH4=(K*Pabar4)/Hv;
Wh4=S4.*KPH4;      %Wear heigh

%Cycle 3 loading
S5=[0.180:dS:0.225];

for i=1:length(S5)

   vel5=v0;

W5(i)=Wm*(S(i)/0.045)+10;  %Load applied - increases as sliding distance increases
    Pbartemp=1/pi*(((16*abs(W5(i))*Estar.^2)/(9*R.^2)).^(1/3));  %Mean pressure when L=a

   [atemp,hmean,hvartemp]=aspparas(htemp,y0);
      Patemp=(Pbartemp-Pvtemp*(1-atemp))/atemp;
      Patemp=min(Patemp,Hv);
      a=(3/4*W2(i)*R/Estar)^(1/3);  %Change this

ht=sqrt(hvartemp+0.25*y0^2);
      Ht=hmean/Rq;
if Ht>Htc
phix = (a2*(Ht-Htc).^2+a3*(Ht-Htc).^3)/Ht^3;
      Pvtemp = 6*eta*a*(1-atemp)*(a*dh/dS*vel4)/(phix*(hmean).^3);
else
      Pvtemp=Pbartemp;
      Patemp=0;
end
   Pvtemp=max(Pvtemp,0);
Pv5(i)=Pvtemp;
Pbar5(i)=Pbartemp;
Pa=min(Patemp,Hv);
Pa=max(Pa,0);%Pa cannot be higher than the hardness of the material
dh=K*Pa*dS/(Hv);
Pabar5(i)=Patemp;
hvar5(i)=hvartemp;
htemp=htemp-dh;
h5(i)=htemp;
Aa5(i)=atemp;


end

%Calculate Surface Roughness of plataeu (Rq) during cycle 3+
Rq5=sqrt(0.5*hvar5);

%Calculate Wear Height
KPH5=(K*Pabar5)/Hv;
Wh5=S5.*KPH5;      %Wear heigh

%Cycle 3 unloading
S6=[0.225:dS:0.270];

for i=1:length(S6)

   vel6=v0;

W6(i)=(((0-Wm)/(0.09-0.045))*S(i))+510;  %Load applied - increases as sliding distance increases
    Pbartemp=1/pi*(((16*abs(W6(i))*Estar.^2)/(9*R.^2)).^(1/3));  %Mean pressure when L=a

   [atemp,hmean,hvartemp]=aspparas(htemp,y0);
```

```
atemp=max(0.01,atemp);%Contact area determined using "aspparas" program
        Patemp=(Pbartemp-Pvtemp*(1-atemp))/atemp;
        Patemp=min(Patemp,Hv);
        a=(3/4*W2(i)*R/Estar)^(1/3);  %Change this

ht=sqrt(hvartemp+0.25*y0^2);
        Ht=hmean/Rq;
if Ht>Htc
phix = (a2*(Ht-Htc).^2+a3*(Ht-Htc).^3)/Ht^3;
        Pvtemp = 6*eta*a*(1-atemp)*(a*dh/dS*vel6)/(phix*(hmean).^3);
else
        Pvtemp=Pbartemp;
        Patemp=0;
end
        Pvtemp=max(Pvtemp,0);
Pv6(i)=Pvtemp;

Pbar6(i)=Pbartemp;
    Pa=min(Patemp,Hv);     %Pa cannot be higher than the hardness of the material
    Pa=max(Pa,0);
dh=K*Pa*dS/(Hv);
Pabar6(i)=Patemp;
hvar6(i)=hvartemp;
htemp=htemp-dh;
h6(i)=htemp;
    Aa6(i)=atemp;

end

%Calculate Surface Roughness of plataeu (Rq) during cycle 3-
Rq6=sqrt(0.5*hvar6);

%Calculate Wear Height
KPH6=(K*Pabar6)/Hv;
Wh6=S6.*KPH6;      %Wear height

%Plot the results
%Show relationship between Sliding Distance and Wear Depth
%Show relationship between Sliding Distance and Contact Pressure
figure(1)
set(1,'Position', [400 500 480 400]);
plot(S,Pabar)
hold all
plot(S2,Pabar2)
hold all
plot(S3,Pabar3)
hold all
plot(S4,Pabar4)
hold all
plot(S5,Pabar5)
hold all
plot(S6,Pabar6)
hold all
xlabel('Sliding Distance (m)','FontSize',14);
ylabel('Contact Pressure (Pa)','FontSize',14);

%Show relationship between Sliding Distance and Mean Pressure on the plateau when L=a
figure(2)
set(2,'Position', [800 500 480 400]);
plot(S,Pbar)
hold all
plot(S2,Pbar2)
hold all
plot(S3,Pbar3)
hold all
plot(S4,Pbar4)
hold all
plot(S5,Pbar5)
hold all
plot(S6,Pbar6)
```

```
hold all
xlabel('Sliding Distance (m)','FontSize',14);
ylabel('Pbar (Pa)','FontSize',14);

%Show relationship between Sliding Distance and Contact Area using aspparas function
figure(3)
set(3,'Position', [1200 500 480 400]);
plot(S,Aa)
hold all
plot(S2,Aa2)
hold all
plot(S3,Aa3)
hold all
plot(S4,Aa4)
hold all
plot(S5,Aa5)
hold all
plot(S6,Aa6)
hold all
xlabel('Sliding Distance (m)','FontSize',14);
ylabel('Contact Area','FontSize',14);

%Show relationship between Sliding Distance and Surface roughness on the plateau
figure(4)
set(4,'Position', [5 30 480 400]);
plot(S,Rq1)
hold all
plot(S2,Rq2)
hold all
plot(S3,Rq3)
hold all
plot(S4,Rq4)
hold all
plot(S5,Rq5)
hold all
plot(S6,Rq6)
hold all
axis([0 0.3 0 3E-6])
%errorbar(0,2.767E-6,0.168E-6,'xr')
%1 Cycle
plot(0.09,0.974E-6,'bx')
plot(0.09,0.988E-6,'bx')
plot(0.09,0.994E-6,'bx')
plot(0.09,1.004E-6,'bx')
plot(0.09,1.079E-6,'bx')
plot(0.09,0.911E-6,'bx')

%2 Cycle
plot(0.18,0.868E-6,'bx')
plot(0.18,0.840E-6,'bx')
plot(0.18,0.787E-6,'bx')
plot(0.18,0.767E-6,'bx')
plot(0.18,0.855E-6,'bx')
plot(0.18,0.791E-6,'bx')

%3 Cycle
plot(0.27,0.736E-6,'bx')
plot(0.27,0.658E-6,'bx')
plot(0.27,0.663E-6,'bx')
plot(0.27,0.713E-6,'bx')
plot(0.27,0.705E-6,'bx')
plot(0.27,0.667E-6,'bx')
hold on

%errorbar(0.090,0.992E-6,0.054E-6,'xr')
%hold all

%errorbar(0.180,0.818E-6,0.042E-6,'xr')
%hold all
```

```
%errorbar(0.270,0.690E-6,0.032E-6,'xr')
%hold all

xlabel('Sliding Distance (m)','FontSize',14);
ylabel('Rq (m)','FontSize',14);

%Show relationship between Sliding Distance and Load Applied During Sliding
figure(5)
set(5,'Position', [400 30 480 400]);
plot(S,W)
hold all
plot(S2,W2)
hold all
plot(S3,W3)
hold all
plot(S4,W4)
hold all
plot(S5,W5)
hold all
plot(S6,W6)
hold all
xlabel('Sliding Distance (m)','FontSize',14);
ylabel('Load (N)','FontSize',14);
axis([0 0.27 0 3E-6])

%Show relationship between Sliding Distance and Load Applied During Sliding
figure(6)
set(6,'Position', [800 30 480 400]);
plot(S,h1)
hold all
plot(S2,h2)
hold all
plot(S3,h3)
hold all
plot(S4,h4)
hold all
plot(S5,h5)
hold all
plot(S6,h6)
hold all
xlabel('Sliding Distance(m)','FontSize',14);
ylabel('Asperity height (m)','FontSize',14);


%Show relationship between Sliding Distance and Pv
figure(7)
set(7,'Position', [0 30 480 400]);
plot(S,Pv)
hold all
plot(S2,Pv2)
hold all
plot(S3,Pv3)
hold all
plot(S4,Pv4)
hold all
plot(S5,Pv5)
hold all
plot(S6,Pv6)
hold all
xlabel('Sliding Distance(m)','FontSize',14);
ylabel('Asperity height (m)','FontSize',14);


Pabarcycle1=[Pabar Pabar2];
Pvcycle1=[Pv Pv2];

SD=[S S2];

%Show relationship between Sliding Distance and Pv
figure(8)
```

```
set(8,'Position', [0 30 480 400]);
ax = plotyy(SD,(Pabarcycle1/Hv),SD,(Pvcycle1/Hv),'plot');
hold all
set(ax, 'XLim', [0 0.09])
xlabel('Sliding Distance(m)','FontSize',14);
set(ax, 'YLim', [0 1])
set(get(ax(1),'Ylabel'),'String','Asperity Pressure/Hardness','FontSize',14)
set(get(ax(2),'Ylabel'),'String','Valley Pressure/Hardness','FontSize',14)
set(ax(1),'YTick',[0:.5:1])
set(ax(2),'YTick',[0:.5:1])

hcycle1=[h1 h2];
Aacycle1=[Aa Aa2];

figure(9)
set(9,'Position', [0 30 480 400]);
axh = plotyy(SD,(hcycle1/y0),SD,(Aacycle1/atemp(1)),'plot');
set(axh, 'XLim', [0 0.09])
set(axh, 'YLim', [0 1])
set(get(axh(1),'Ylabel'),'String','h/y0','FontSize',14)
set(get(axh(2),'Ylabel'),'String','Contact Ratio A','FontSize',14)
axis([0,0.09,0,1])
set(axh(1),'YTick',[0:.5:1])
set(axh(2),'YTick',[0:.5:1])
xlabel('Sliding Distance(m)','FontSize',14);



%Friction Model
%This is fine after a certain sliding distance, however an initial friction
%model is required for the first stroke.

CoFb =0.6; % friction coefficient on metal-on-metal contact
CoFv = 0.002; %Change this
tau0=2e6; %Eyring shesr stress
taua=0.2*Hv;
Ap=0.45; % plateau area ratio outside the pits
%Cycle 1+
for l=1:length(S);
vel1=v0;
hfriction=y0;
   y0friction=y0;
   hmphl=(6*eta*alpha*vel1)/(theta*(1-exp(-alpha*Hv)));
hcen=2.8*(eta*vel1/Estar/R).^0.65*(W(l)/Estar/R^2)^(-0.21)*R;
hmean0temp=hmphl;

%[atempfriction, hmeanfriction, hvartempfriction] = aspparas(hmean0temp,y0friction);
y0friction=6*sqrt(Rq1(l)^2+Rq^2);% asperity height on plateau
hfric=fzero('hafunc2',0);
[Ar, hmeanb, hvarb]=aspparas(hfric,y0friction); % hfric is the traugh height
%Ar=min(Ar,Pbar(l)/Hv)
temp=Ar;
tau0=2e6;
CoFv=tau0*asinh(eta*vel1/hmeanb/tau0)/Pbar(l); %Eyring model
CoFv=min(CoFv,CoFb);
CoFall(l)=Ap*(CoFb*Ar + CoFv*(1-Ar));
end

%Cycle 1-
for l=1:length(S);
vel1=v0;

hfriction=y0;
   y0friction=y0;
   hmphl=(6*eta*alpha*vel1)/(theta*(1-exp(-alpha*Hv)));
hcen=2.8*(eta*vel1/Estar/R).^0.65*(W(l)/Estar/R^2)^(-0.21)*R;
hmean0temp=hmphl;
%[atempfriction, hmeanfriction, hvartempfriction] = aspparas(hmean0temp,y0friction);
y0friction=6*sqrt(Rq2(l)^2+Rq^2);
hfric2=fzero('hafunc2',0);
```

```
[Ar, hmeanb, hvarb]=aspparas(hfric2,y0friction); % hfric is the traugh height
%Ar=min(Ar,Pbar(l)/Hv)
temp(l)=Ar;
tau0=2e6;
CoFv=tau0*asinh(eta*vel1/hmeanb/tau0)/Pbar2(l); %Eyring model
CoFv=min(CoFv,CoFb)
CoFall2(l)=Ap*(CoFb*Ar + CoFv*(1-Ar));
end

%Cycle 2+
for l=1:length(S);

vel1=v0;
hfriction=y0;
   y0friction=y0;
   hmphl=(6*eta*alpha*vel1)/(theta*(1-exp(-alpha*Hv)));
hcen=2.8*(eta*vel1/Estar/R).^0.65*(W(l)/Estar/R^2)^(-0.21)*R;
hmean0temp=hmphl;
%[atempfriction, hmeanfriction, hvartempfriction] = aspparas(hmean0temp,y0friction);
y0friction=6*sqrt(Rq3(l)^2+Rq^2);
hfric3=fzero('hafunc2',0);
[Ar, hmeanb, hvarb]=aspparas(hfric3,y0friction); % hfric is the traugh height
%Ar=min(Ar,Pbar(l)/Hv)
tau0=2e6;
CoFv=tau0*asinh(eta*vel1/hmeanb/tau0)/Pbar3(l); %Eyring model
CoFv=min(CoFv,CoFb);
CoFall3(l)=Ap*(CoFb*Ar + CoFv*(1-Ar));
end

%Cycle 2-
for l=1:length(S);
vel1=v0;
hfriction=y0;
   y0friction=y0;
   hmphl=(6*eta*alpha*vel1)/(theta*(1-exp(-alpha*Hv)));
hcen=2.8*(eta*vel1/Estar/R).^0.65*(W(l)/Estar/R^2)^(-0.21)*R;
hmean0temp=hmphl;
%[atempfriction, hmeanfriction, hvartempfriction] = aspparas(hmean0temp,y0friction);
y0friction=6*sqrt(Rq4(l)^2+Rq^2);
hfric4=fzero('hafunc2',0);
[Ar, hmeanb, hvarb]=aspparas(hfric4,y0friction); % hfric is the traugh height
%Ar=min(Ar,Pbar(l)/Hv)
tau0=2e6;
CoFv=tau0*asinh(eta*vel1/hmeanb/tau0)/Pbar4(l); %Eyring model
CoFv=min(CoFv,CoFb);
CoFall4(l)=Ap*(CoFb*Ar + CoFv*(1-Ar));
end

%Cycle 3+
for l=1:length(S);
vel1=v0;
hfriction=y0;
   y0friction=y0;
   hmphl=(6*eta*alpha*vel1)/(theta*(1-exp(-alpha*Hv)));
hcen=2.8*(eta*vel1/Estar/R).^0.65*(W(l)/Estar/R^2)^(-0.21)*R;
hmean0temp=hmphl;
%[atempfriction, hmeanfriction, hvartempfriction] = aspparas(hmean0temp,y0friction);
y0friction=6*sqrt(Rq5(l)^2+Rq^2);
hfric5=fzero('hafunc2',0);
[Ar, hmeanb, hvarb]=aspparas(hfric5,y0friction); % hfric is the traugh height
%Ar=min(Ar,Pbar(l)/Hv)
tau0=2e6;
CoFv=tau0*asinh(eta*vel1/hmeanb/tau0)/Pbar5(l); %Eyring model
CoFv=min(CoFv,CoFb);
CoFall5(l)=Ap*(CoFb*Ar + CoFv*(1-Ar));
end

%Cycle 3-
for l=1:length(S);
vel1=v0;
```

```
hfriction=y0;
    y0friction=y0;
    hmphl=(6*eta*alpha*vel1)/(theta*(1-exp(-alpha*Hv)));
hcen=2.8*(eta*vel1/Estar/R).^0.65*(W(l)/Estar/R^2)^(-0.21)*R;
hmean0temp=hmphl;

%[atempfriction, hmeanfriction, hvartempfriction] = aspparas(hmean0temp,y0friction);
y0friction=6*sqrt(Rq6(l)^2+Rq^2);
hfric6=fzero('hafunc2',0);
[Ar, hmeanb, hvarb]=aspparas(hfric6,y0friction); % hfric is the traugh height
%Ar=min(Ar,Pbar(l)/Hv)
tau0=2e6;
CoFv=tau0*asinh(eta*vel1/hmeanb/tau0)/Pbar6(l); %Eyring model
CoFv=min(CoFv,0.1);
CoFall6(l)=Ap*(CoFb*Ar + CoFv*(1-Ar));
end


figure(12)
set(12,'Position', [800 500 480 400]);
plot(Pbar,CoFall)
xlabel('Contact Pressure (Pa)','FontSize',14);
ylabel('CoF','FontSize',14);
hold on

figure(13)
set(13,'Position', [800 500 480 400]);
plot(S,CoFall)
axis([0 0.3 0.1 .2])
hold on
plot(S2,CoFall2)
plot(S3,CoFall3)
plot(S4,CoFall4)
plot(S5,CoFall5)
plot(S6,CoFall6)
xlabel('Sliding Distance (m)','FontSize',14);
ylabel('CoF','FontSize',14);



plot(0.001,0.174394,'bx')
plot(0.01,0.1567286,'bx')
plot(0.02,0.1646635,'bx')
plot(0.03,0.1760868,'bx')
plot(0.04,0.1794499,'bx')
plot(0.05,0.1553237,'bx')
plot(0.06,0.1585696,'bx')
plot(0.07,0.1503934,'bx')
plot(0.08,0.1535697,'bx')
plot(0.09,0.1360539,'bx')
plot(0.10,0.1481996,'bx')
plot(0.11,0.1476034,'bx')
plot(0.12,0.1576052,'bx')
plot(0.13,0.1531775,'bx')
plot(0.14,0.1533096,'bx')
plot(0.15,0.1527194,'bx')
plot(0.16,0.1449809,'bx')
plot(0.17,0.1518542,'bx')
plot(0.18,0.1361490,'bx')
plot(0.19,0.1432556,'bx')
plot(0.20,0.1489767,'bx')
plot(0.21,0.1572341,'bx')
plot(0.22,0.1520521,'bx')
plot(0.23,0.1539898,'bx')
plot(0.24,0.1523296,'bx')
plot(0.25,0.1479000,'bx')
plot(0.26,0.1523026,'bx')
plot(0.27,0.1374660,'bx')

plot(0.001,0.167287413,'rd')
```

```
plot(0.01,0.153870152,'rd')
plot(0.02,0.162574223,'rd')
plot(0.03,0.175694528,'rd')
plot(0.04,0.180901916,'rd')
plot(0.05,0.157059427,'rd')
plot(0.06,0.159603631,'rd')
plot(0.07,0.152118647,'rd')
plot(0.08,0.154478661,'rd')
plot(0.09,0.158215417,'rd')
plot(0.10,0.144952667,'rd')
plot(0.11,0.146642577,'rd')
plot(0.12,0.155636185,'rd')
plot(0.13,0.156082258,'rd')
plot(0.14,0.15486357,'rd')
plot(0.15,0.154213903,'rd')
plot(0.16,0.148241825,'rd')
plot(0.17,0.152666248,'rd')
plot(0.18,0.147748683,'rd')
plot(0.19,0.140042281,'rd')
plot(0.20,0.147417524,'rd')
plot(0.21,0.155760693,'rd')
plot(0.22,0.151802958,'rd')
plot(0.23,0.155593151,'rd')
plot(0.24,0.154101166,'rd')
plot(0.25,0.149883263,'rd')
plot(0.26,0.153534956,'rd')
plot(0.27,0.141938449,'rd')
hold on
```

Matlab program – “afunc”

```
%program afunc.m to find area as a function of h/y0
% for triangular and christensen asperities

function a=afunc(h,y0)
%h is measured from bottom of the asperity to platen level
%y0 is the total depth of the asperity
%x is measured from original mean position
%z is distance from mean position divided semi-height
global asptype
if(asptype(1:1)=='t')
a=min(max(1-h./y0,0.),1.);
else
z=h*2 ./y0-1;
z2=z.*z;z3=z2.*z;z4=z3.*z;z5=z4.*z;z6=z5.*z;z7=z6.*z;z8=z7.*z;
a=(16-35*z+35*z3-21*z5+5*z7)/32;
i=find(z>=1);
%if(length(i)>=1)
a(i)=zeros(size(i));
i=find(z<=-1);
%if(length(i)>=1)
a(i)=ones(size(i));
end
%end
```

Matlab Program – “Aspparas”

```
%program aspparas.m to find asperity geometric parameters for triangular
%and christensen asperities

function [a ,hmean,hvar]=aspparas(h,y0)

%a is the ratio of contact area
%h is measured from bottom of the asperity to platen level
%y0 is the total depth of the asperity assumed scalar here
%x is measured from original mean position
%z is distance from mean position/semi-height
```

```
%z=-1:0.001:1;
%h and z are measured from mean postion
%hmean is mean height over whole contact measured from platen
%assume h isnt negative

global asptype
a=afunc(h,y0);
%iap=find(h<=y0);
ia0=find(h>y0);
ia1=find(h<0);
%easiest to do all the values, and then overwrite for the zero areas

if asptype(1:1)=='t'
%zmean measured from base, hmean from plateau
zmean=y0/2*(1-a.*a);
hmean=h-zmean;
hvar=y0.*y0/12*(1-a).^3.*(1+3*a);
%if(length(ia0)>=1)
hvar(ia0)=y0.*y0/12*ones(size(ia0));
%end

else

%christensen
%z ex ex2 are measured from mean of original surface
%hmean from plateau
%hvar is variance
z=h*2 ./y0-1;
z2=z.*z;z3=z2.*z;z4=z3.*z;z5=z4.*z;z6=z5.*z;z7=z6.*z;z8=z7.*z;z9=z8.*z;
hmean=(y0/6)*3*(35+128*z+140*z2-70*z4+28*z6-5*z8)/256;
ex2=(y0/6)*(y0/6)*(16+105*z3-189*z5+135*z7-35*z9)/32+(y0/6)*(y0/6)*9*z2.*a;
ex=h-y0/2-hmean;
hvar=ex2-ex.*ex;
%if(length(ia0)>=1)
%hmean(ia0)=h(ia0)-y0/2;
hvar(ia0)=y0.*y0/36*ones(size(ia0));
%end
end

hmean(ia0)=h(ia0)-y0/2;
hmean(ia1)=zeros(size(ia1));
hvar(ia1)=zeros(size(ia1));
```

References

1. Williams JA. Engineering Tribology. 2005 ed. Cambridge: Cambridge University Press; 2005. 488 p.
2. Abel P, Ferrante J. Modern Tribology Handbook, Volume One - Principles of Tribology: CRC Press; 2000.
3. Dowson D. History of Tribology. London: Longman Group Limited, 1979.
4. Ludema KC. Friction, lubrication, wear: textbook in tribology. Florida, USA: CRC Press; 1996. 257 p.
5. Arnell RDD, Peter; Halling, J; Whomes, Terence;. Tribology Principles and Design Applications. First Edition ed: Palgrave Macmillan; 1991.
6. Wilson WA. Word origins in science and technology: An etymological notebook Lexitheque Sudsexe; 1994. 586 p.
7. Rabinowicz E. Friction and wear of materials. 2nd Edition ed. New York, USA: John Wiley & Sons, Inc; 1995 1995. 315 p.
8. Vitintin JK, M; Dohda, K; Jahanmir, S;. Tribology of mechanical systems: A guide to present and future technologies. New York: ASME Press; 2004.
9. Beek Av. Tribology-ABC Delft, Netherlands2012 [26/03/2012]. Available from: http://www.tribology-abc.com/abc/history.htm.
10. Pugh B. A tribology text for students - friction and wear. London, UK: Butterworth & Co Ltd; 1973. 206 p.
11. Bowden FP, Tabor D. Friction: an introduction to tribology. Guildford, UK: Biddles Ltd; 1974. 178 p.
12. O'Connor JJR, E.F;. The MacTutor History of Mathematics archive St Andrews, UK2012 [28/03/12].
13. Halling J, Nuri KA, Teer DG, Howarth RB, Whomes TL, Davies PB. Principles of Tribology. London, UK: The Macmillan Press Ltd.; 1978. 401 p.
14. Bush AW, Gibson RD. The elastic contact of a rough surface. Journal of Wear. 1975;35:87-111.
15. Hertz H. Uber die Beruhrung fester elastischer Korper (On the contact of elastic solids). Journal für die reine und angewandte Mathematik. 1882;92:156-71.
16. Wisniak J. Guillaume Amontons. Revista CENIC Ciencias Quimicas [CENIC Journal Science & Chemistry]. 2005;36(3):187-95.
17. Bowden FP, Tabor D. The Friction of Lubrication of Solids: Part II. London, UK: Oxford University Press; 1964. 544 p.
18. Press OU. Oxford Online Dictionary Oxford, UK: Oxford University Press; 2011 [cited 2011 05/12/11].
19. Davis JR. ASM Materials Engineering Dictionary. 5th Edition ed. USA: ASM International; 2006.
20. Plint G, editor Tribology Testing. Cambridge Tribology Course; 2010; Cambridge, UK.
21. Plc H. Hunting Energy Services: Hunting Plc; 2013. Available from: http://www.huntingplc.com/.
22. Chapman RE. Petroleum Geology: Elsevier Science Publishers B,V; 1983.

23. Bellarby J. Well Completion Design. Elsevier, editor. Amsterdam, The Netherlands: Elsevier; 2009.
24. Perrin D. Well Completion and Servicing. petrole Ifd, editor. Rueil-Malmaison, France1999.
25. Macini P. Encyclopedia of Hydrocarbons. Italy: Treccani.IT; 2008.
26. Steel J. JFE Bear data sheet Handa, Japan: JFE Steel; 2013.
27. Guangjie Y, Zhenqiang Y, Qinghua W, Zhentong T. Numerical and experimental distribution of temperature and stress fields in API round threaded connection. Engineering Failure Analysis. 2006;13:1275-84.
28. Kent S, Amiel G, Faucon B. North Sea Gas Leak Could Cost Billions. The Wall Street Journal. 2012.
29. Gosden E. Total's Elgin gas leak costing $2.5m a day. The Telegraph. 2012.
30. Duggan TV. Applied engineering design and analysis. 1st Edition ed. London: Iliffe; 1969. 391 p.
31. Institute AP. API Test 5A3 3rd Edition; Recommended Practice on Thread Compounds for Casing, Tubing, Line Pipe, and Drill Stem; API Standards Catalogue. Englewood, Colorado, USA: American Petroleum Institute; 2010. p. 210.
32. Bezensek B. Finite Element Analysis of the Seal During Make-up. 2010.
33. Bengisu MT, Akay A. Stick-slip oscillations: Dynamics of friction and surface roughness. Journal of the Acoustical Society of America. 1998;105(1):195-204.
34. Coulomb CA. Memoires de Mathematique et de Physique de l'Academie Royale des Sciences: Theorie des machines simples. Paris: Academie Royale des Sciences, 1785.
35. Ford IJ. Roughness effect on friction for multi-asperity contact between surfaces. Journal of Physics D: Applied Physics. 1993;26:2219-25.
36. Nayak PR. Random process model of rough surfaces. Journal of Wear. 1973;26(3):305-33.
37. Menezes PL, Kishore, Kailas SV. Influence of roughness parameters on coefficient of friction under lubricated conditions. Sadhana. 2008;33(3):181-90.
38. Sedlacek M, Podgornik B, Vizintin J. Influence of surface preparation on roughness parameters, friction and wear. Journal of Wear. 2009;266:482-7.
39. Bradley AB, Nagasaku S, Verger E. Premium Connection Design, Testing and Installation for HPHT Sour Wells. SPE High Pressure-High Temperature Sour Well Design Applied Technology Workshop; 17-19 May; The Woodlands, Texas, USA2005. p. 1-8.
40. Standardisation IOf. ISO 13679. Petroleum and natural gas industries - Procedures for testing casing and tubing connections: ISO; 2002.
41. Schwind B. Mobil qualifies three tubling.casing connection product lines. Hart's Petroleum Engineer International. 1998:59-62.
42. Baragetti S, Clerici P, Matteazzi S. Friction and tightening force of conical threaded connections: experiments in various conditions. Int J Mater Prod Tec. 2003;19(5):414-30.
43. Van Wittenberghe J, De Pauw J, De Baets P, De Waele W, Wahab MA, De Roeck G. Experimental determination of the fatigue life of modified threaded pipe couplings. Procedia Engineer. 2010;2(1):1849-58.
44. De Baere I. Design of a three- and four-point bending setup for fatigue testing of fibre-reinforced thermoplastics.

45. Meng Q, Gao L, Liu F, Yang P, Fisher J, Jin Z. Contact mechanics and elastohydrodynamic lubrication in a novel metal-on-metal hip implant with an aspherical bearing surface. Journal of Biomechanics. 2010;43(849-857).
46. Shafiei M, Alpas AT. Effect of sliding speed on friction and wear behaviour of nanocrystalline nickel tested in an argon atmosphere. Journal of Wear. 2008;265:429-38.
47. Farhat ZN, Ding Y, Northwood DO, Alpas AT. Effect of grain size on friction and wear of nanocrystalline aluminium. Materials Science and Engineering. 1996;A206:302-13.
48. Kato K. Wear in relation to friction - a review. Journal of Wear. 2000;241:151-7.
49. Leslie J. An experimental inquiry into the nature and propagation of Heat. London1804. 562 p.
50. Greenwood JA, Williamson JBP. Contact of Nominally Flat Surfaces. Proceedings of The Royal Society of Mathematical, Physical and Engineering Sciences. 1966;295:300-19.
51. Johnson KL. Contact mechanics. Cambridge Cambridgeshire ; New York: Cambridge University Press; 1985. xi, 452 p. p.
52. Jackson RL, Green I. On the modeling of elastic contact between rough surfaces. Tribology Transactions. 2011;54:300-14.
53. Zavarise G, Borri-Brunetto M, Paggi M. On the resolution dependence of micromechanical contact models. Journal of Wear. 2007;262:42-54.
54. Carbone G. A slightly corrected Greenwood and Williamson model predicts asymptotic linearity between contact area and load. Journal of the Mechanics and Physics of Solids. 2009;57:1093-102.
55. Greenwood JA. A simplified elliptic model of rough surface contact. Journal of Wear. 2006;261:191-200.
56. Buczkowski R, Kleiber M. Elasto-plastic statistical model of strongly anisotropic rough surfaces for finite element 3D-contact analysis. Journal of Computer Methods in Applied Mechancs and Engineering. 2006;195:5141-61.
57. Kim H, Kardes N. Friction and lubrication. In: Altan T, Tekkaya AE, editors. Sheet Metal Forming - Fundamentals: ASM International; 2012.
58. Hironaka S. Boundary Lubrication and Lubricants. Three Bond: Technical News. 1984.
59. Singer IL, Pollock HM. Fundamentals of Friction: Macroscopic and Microscopic Processes. Netherlands: Kluwer Academic Publishers; 1992.
60. Qasim SA, Gulzar M, Malik MA. Influence of surface roughness factor in modeling isothermal piston skirts lubrication in initial engine start up. World Congress on Engineering2012.
61. Teodoriu C, McDonald H, Bollfrass C. Friction considerations in rotary shouldered threaded connections. 26th International Conference on Offshore Mechanics and Arctic Engineering; San Diego, California, USA: ASME; 2007.
62. Farr AP, editor Torque Requirements For Rotary Shouldered Connections And Selection of Connections For Drill Collars. ASME Petroleum Mechanical Engineering Conference; 1957; Tulsa, Oklahoma, USA: ASME Petroleum Division.
63. Jeng Y-R. Experimental study on the effects of surface roughness on friction. 35th STLE/ASME tribology conference; Fort Lauderdale, Florida, USA: STLE/ASME; 1989.

64. Qiao H-B. A study on friction and wear characteristics of nanometer Al2O3/PEEK composites under the dry sliding condition. Journal of Tribology International. 2006;40:105-10.
65. Burton RA. Effects of two-dimensional, sinusoidal roughness on the load support characteristics of a lubricant film. Journal of Basic Engineering. 1963;85(2):258-62.
66. Kudenatti RB, Basti DP, Bujurke NM. Numerical solution of the MHD Reynolds equation for squeeze film lubrication between two parallel surfaces. Applied Mathematics and Computation. 2012;218:9372-82.
67. Christensen H. The Oil Film in a Closing Gap. Proceedings of the Royal Society of London. 1962;266.
68. Ahmed R, Sutcliffe MPF. Identification of surface features on cold-rolled stainless steel strip. Journal of Wear. 2000;244:60-70.
69. Blencoe KA, Williams JA. The friction of sliding surfaces carrying boundary layers. Tribol Lett. 1997;3(1):121-3.
70. Blencoe KA, Williams JA. Friction of sliding surfaces carrying boundary films. Wear. 1997;203:722-9.
71. Georges JM, Mazuyer D, Tonck A, Loubet JL. Lubrication with a Thin Colloidal Layer. J Phys-Condens Mat. 1990;2:Sa399-Sa403.
72. Georges JM, Mazuyer D. Pressure Effects on the Shearing of a Colloidal Thin-Film. J Phys-Condens Mat. 1991;3(47):9545-50.
73. Le HR, Sutcliffe MPF, Williams JA. Friction and material transfer in micro-scale sliding contact between aluminium alloy and steel. Tribol Lett. 2005;18(1):99-104.
74. Blencoe KA, Roper GW, Williams J. The influence of lubricant rheology and surface topography in modelling friction at concentrated contacts. P I Mech Eng J-J Eng. 1998;212(J6):391-400.
75. Kapoor A, Williams JA, Johnson KL. The Steady-State Sliding of Rough Surfaces. Wear. 1994;175(1-2):81-92.
76. Sacher A. Slip Resistance and the James Machine 0.5 Static Coefficient of Friction-Sine Qua Non*. ASTM Standardization News. 1993:53.
77. Melhuish D, Wegand J. Coefficient of friction, the development of a standard portable device for the US Naval Fleet. Tri-Service Corrosion Conference; Springfield, Virginia, USA2007.
78. Khan ZA, Hadefield M, Wang Y. Pressurised chamber design for conducting rolling contact experiments with liquid refrigerant lubrication. Materials and Design. 2005;26(8):680-9.
79. Williams JA. Engineering tribology. New York: Cambridge University Press; 2005. xix, 488 p. p.
80. Podgornik B, Hogmark S, Pezdirnik J. Comparison between different test methods for evaluation of galling properties of surface engineered tool surfaces. Wear. 2004;257(7-8):843-51.
81. Imperial Scientific Industries. Pin on Disc Testers [Webpage]. http://www.tribotesters.com/pin_on_disc.htm; 2011 [cited 2011 20/8/2011]. Available from: http://www.tribotesters.com/pin_on_disc.htm.
82. Stewart F, Le HR, Williams JA, Leech A, Bezensek B, Roberts A. Characterisation of friction and lubrication regimes in premium tubular connections. Tribology International. 2012;53:159 - 66.

83. Carper HJ, Ertas A, Issa J, Cuvalci O. Effect of Some Material, Manufacturing, and Operating Variables on the Friction Coefficient in Octg Connections. J Tribol-T Asme. 1992;114(4):698-705.
84. Le HR, Williams JA, Luo JK. Characterisation of tribological behaviour of silicon and ceramic coatings under repeated sliding at micro-scale. Int J Surf Sci Eng. 2008;2(1-2):1-13.
85. Higounenc O. Correlation of shot peening parameters to surface characteristic. 9th International Conference and Exhibition on Shot Peening; Paris, France: Institute for Industrial Technology Transfer; 2005. p. 28-35.
86. Amaral R, Chong LH. Surface Roughness. 2002.
87. Mylonas GI, Labeas G. Numerical modelling of shot peening process and corresponding products: Residual stress, surface roughness and cold work prediction. Journal of Surface & Coatings Technology. 2011;205(19):4480-94.
88. Sutcliffe MPF, Le HR, Ahmed R. Modeling of micro-pit evolution in rolling or strip-drawing. Journal of Tribology. 2001;123:33-40.
89. Inc. VI. Surface Measurement Parameters for Wyko Optical Profilers. In: Inc. VI, editor. Tucson, Arizona: Veeco Instruments Inc.; 2002.
90. Research W. Wolfram Mathworld - Kurtosis: Eric Weisstein; 2013 [08/01/2013]. Available from: http://mathworld.wolfram.com/Kurtosis.html.
91. DeCarlo LT. On the meaning and use of Kurtosis. Journal of Psychological Methods. 1997;2(3):292-307.
92. Mate C, M. Tribology on the Small Scale -A Bottom Up Approach to Friction, Lubrication, and Wear. Oxford: Oxford University Press; 2008.
93. Rugar D, Hansma P. Atomic Force Microscopy. Physics Today. 1990;43(10):23-30.
94. Kossek S, Flowers M. Scanning Tunneling Microscopy Phoenix, Arizona, USA: Nanoscience Instruments Inc.; 2011. Available from: http://www.nanoscience.com/education/STM.html.
95. Meyer E. Atomic Force Microscopy. Journal of Progress in Surface Science. 1992;41:3-41.
96. Binnig G, Quate CF. Atomic Force Microscope. Physical Review Letters. 1986;56(9):930-4.
97. Facility AMMR. Sydney, Australia: Australian Learning and Teaching Council; 2011 [17/01/2013]. Available from: http://www.ammrf.org.au/myscope/confocal/confocal/.
98. Compact Oxford Dictionary Thesaurus, and Wordpower Guide. New York, USA: Oxford University Press Inc.; 2001. Oxford Dictionary.
99. OLS3000 OL-. LEXT Confocal Scanning Laser Microscope Manual. Japan: Olympus; 2008.
100. Swapp S. Scanning Electron Microscopy (SEM) Northfield, Minesota, USA: Carleton College; [18/01/2013]. Available from: http://serc.carleton.edu/research_education/geochemsheets/techniques/SEM.html.
101. Schweitzer J. Scanning Electron Microscope West Lafayette, Indiana, USA: Purdue University; 2012 [cited 2013 22/01/2013]. Available from: http://www.purdue.edu/rem/rs/sem.htm.
102. Kirk D. Residual stresses in shot peened components. The Shot Peener magazine. 2004.

103. ZirPro S-G. ZIRBLAST Safety Data Sheet No. DS MS BE 11 GB. In: S.E.P.R. SEdPR, editor. ZIRBLAST Shot Peening Media. Cedex France: Saint-Gobain ZirPro; 2001. p. 2.
104. Bowen J. Micro-hardness Measurements. 2012.
105. Al-Samarai RA, Haftirman, Ahmad KR, Al-Douri Y. Effect of Load and Sliding Speed on Wear and Friction of Aluminum – Silicon Casting Alloy<div data-canvas-width="8.85720006108284" data-font-name="Times New Roman" dir="ltr" style="font-size: 35.4288px; font-family: sans-serif; left: 746.683px; top: 139.037px; transform: scale(0.88572, 1); transform-origin: 0% 0% 0px;">. International Journal of Scientific and Research Publications. 2012;2(3):1-4.
106. Leech A. Discussion on maximum pressures in premium tubular connections. In: Stewart F, editor. 2013.
107. Institute AP. APi Spec 5L - Specification for Line Pipe. American Petroleum Institute; 2000.
108. Inc. MIC. Shot Peening Applications. Metal Improvement Company Inc.; 2001.
109. Zwörner O, Hölscher H, Schwarz UD, Wiesendanger R. The velocity dependence of frictional forces in point-contact friction. Journal of Applied Physics A: Materials Science & Processing. 1998;66(S1):263-7.
110. Wang Q, Zhou F, Chen K, Wang M, Qian T. Friction and wear properties of TiCN coatings sliding against SiC and steel balls in air and water. Journal of Thin Solid Films. 2011;519:4830-41.
111. Le HR, Sutcliffe MPF. A friction model for cold strip rolling with two-wavelength surface roughness in the "mixed" lubrication regime. Journal of Tribology. 2003;125:670-7.
112. MathWorks. MathWorks - MATLAB Overview Natick, Massachusetts, U.S.A.: MathWorks; 2013 [cited 2013 11/01/2013]. Available from: http://www.mathworks.co.uk/products/matlab/.
113. Kwon DH, Park ES, Huh MY, Kim HJ, Cae JC. Wear behaviour of Fe-based bult metallic glass composites. Journal of Alloys and Compounds. 2011;509(1):105-8.
114. Christensen H. Stochastic model for hydrodynamic lubrication of rough surfaces. Proceedings of the Institution of Mechanical Engineers. 1969-1970;184:1013-25.
115. Persson BNJ. Elastoplastic Contact between Randomly Rough Surfaces. Physical Review Letters. 2001;87(11):116101-1 - -4.
116. Patir N, Cheng HS. Average Flow Model for Determining Effects of 3-Dimensional Roughness on Partial Hydrodynamic Lubrication. J Lubric Tech-T Asme. 1978;100(1):12-7.
117. Li W-L, Chein W-T. Parameters for Roughness Pattern and Directionality. Tribol Lett. 2004;17(3):547-51.
118. Hamrock BJ, Dowson D. Elastohydrodynamic Lubrication of Elliptical Contacts for Materials of Low Elastic-Modulus I - Fully Flooded Conjunction. J Lubric Tech-T Asme.100(2): 236-45 1978.
119. Carbone G, Bottiglione F. Asperity contact theories: Do they predict linearity between contact area and load? Journal of Mechanics and Physics of Solids. 2008;56:2555-72.
120. Lo SW, Wilson WRD. A theoretical model of micro-pool lubrication in metal forming. Journal of Tribology. 1999;121:731-8.

121. Le HR, Sutcliffe MPF. Rolling of thin strip and foil: application of a tribological model for "mixed" lubrication. Journal of Tribology. 2002;124:129-36.
122. Institute AP. API RP 7G - Recommended Practice for Drill Stem Design and Operation Limits 16th Edition. American Petroleum Institute; 2009. p. 154.
123. Le HR, Sutcliffe MPF. A multi-scale model for friction in cold rolling of aluminium alloy. Tribol Lett. 2006;22(1):95-104.